Orientation-dependent segregation and oxidation at Fe0.85Al0.15 random alloy surfaces

Zongbei Dai

THÈSE DE DOCTORAT
DE L'UNIVERSITÉ PIERRE ET MAIRE CURIE

Spécialité : Physique
Ecole Doctorale de Physique et Chimie des Matériaux

réalisée au sein de
l'Institut des NanoSciences de Paris

Presentée par

DAI Zongbei

pour obtenir le grade de :
DOCTEUR DE L'UNIVERSITÉ PIERRE ET MARIE CURIE

Sujet de la thèse :

Orientation-dependent segregation and oxidation at $Fe_{0.85}Al_{0.15}$ random alloy surfaces

Soutenue le 15 Décembre 2017 devant le jury composé de:

M. LEDIEU Julian	Chargé de Recherches (IJL, Nancy)	Rapporteur
M^{me} GALTAYRIES Anouk	Maître de Conférences (ENSCP, Paris)	Rapporteur
M. LEROY Frédéric	Professeur (CINAM, Marseille)	Examinateur
M. CARRIER Xavier	Professeur (LRS, Paris)	Examinateur
M. LAZZARI Rémi	Directeur de Recherches (INSP, Paris)	Directeur de thèse

December 20, 2017

CONTENTS

Contents

ABSTRACT

$Fe_{0.85}Al_{0.15}$ single crystals of ferritic composition (random bcc A_2 alloy) have been chosen as a model system to study the orientation dependence of segregation and oxidation that happen at the surface of industrial Al-alloyed steels during recrystallisation annealing before hot-dip galvanisation. The three low-index orientations (110), (100) and (111) have been compared through a surface science approach involving Low-Energy Electron Diffraction (LEED), X-ray photoemission (XPS), Scanning Tunnelling Microscopy (STM) and Grazing Incidence X-ray Diffraction (GIXD).

Carbon segregation and contamination from ultra-high vacuum were two major difficulties to overcome. Upon annealing the (110) surface, transient carbon segregation was observed in the form of self-organised stripes running along [001] direction and separated by ~ 5 nm. Two types of C 1s fingerprints were evidenced and assigned to graphitic and chemisorbed carbon. The XPS quantification of the former parallels the maximum of stripe coverage at ~ 850 K before its decay at higher temperatures at the onset of Al segregation. The strong reactivity of (100) and (111) surfaces requires specific cautions in measurement protocols.

According to photoemission, if sputtered surfaces have a composition close to the nominal one, all clean surfaces of $Fe_{0.85}Al_{0.15}$ are prone to intense Al segregation in the temperature range 700-1000 K. After 1000 K, a steady state regime is reached and the impacted depth is around 2-3 nm with an average composition close to the ordered CsCl B_2 structure in agreement with the tendency of long-range order in Fe-Al. But on a structural point of view, all the surfaces behave in different ways. The (110) surface develops a 2 nm large pseudo-hexagonal reconstruction that is imaged in STM and that corresponds to an incommensurate in-plane modulation of the lattice parameter. The (100) surface is always (1×1) terminated with a marbled-like appearance assigned to an electronic and chemical contrast. At last, despite a smoothing at large scale, the (111) surface is locally rough with the development of nanometric-size three-fold protrusions/pits due to segregation-induced faceting involving (111) vicinal surfaces. The segregation trend is rationalised through *ab initio* calculations.

The oxidation with O_2 of all the surfaces in the Knudsen's regime at high temperature leads to a selective oxidation of Al and to the growth of alumina films of self-limited thickness

in the range of 1-2 nm. Iron stays metallic. Covering oxides are found on (110) and (100) faces while the growth is more 3D on (111). Photoemission analysis of the profile of segregation shows quite distinct behaviours. Subsurfaces of (110) and (111) are depleted in Al and adopt the $D0_3$ structure. On the other hand, the profile of segregation is insensitive to oxidation on (100) face. All the experimental fingerprints of the oxide at (100) and (110) orientations are very close to previous findings in particular on NiAl. At (110) surface, a two-domain alumina grows with a (18.5×10.5) Å^2 nearly rectangular rotated unit cell as seen by diffraction with a nearly perfect $(2 \times 1)_{ox}$ matching. While the average composition of $Al_2O_{2.6}$, the two oxide Al 2p components and the unit cell are twin of those of the oxide at NiAl(110), much fewer anti-phase domain boundaries are observed probably due to the composition freedom of the subsurface provided by the random alloy. The oxide film at (100) surface presents two (2×1) domains in the form of nanometric-sized orthogonal stripes; a likely explanation is the formation of a distorted θ-Al_2O_3 structure. The lack of any oxide ordering at (111) surface is assigned to the strong tendency of this orientation to nanofacet.

ABSTRACT IN FRENCH

Des cristaux de $Fe_{0.85}Al_{0.15}$ de composition ferritique (alliage aléatoire de type A_2) ont été choisis comme système modèle pour étudier la dépendance en orientation de la ségrégation et de l'oxydation qui se produisent à la surface d'aciers industriels alliés à l'Al durant le recuit de recristallisation avant la galvanisation. Les trois surfaces de bas indices (110), (100) et (111) ont été comparées dans une approche de science des surfaces impliquant la diffraction d'électrons lents (LEED), la photoémission X (XPS), la microscopie à effet tunnel (STM) et la diffraction rasante de rayons X (GIXD)

La ségrégation de carbone et la contamination à partir du vide ont constitué deux difficultés majeures à surmonter. Lors d'un recuit de la surface (110), une ségrégation transitoire de carbone a été observée sous forme de bandes auto-orgnisées orientées suivant la direction [001] et séparées par $\sim$ 5 nm. Deux types de signature C 1s ont été mises en évidence et attribuées à du carbone graphitique et chemisorbé. La quantification XPS de la première suit le maximum de taux de couverture des bandes à $\sim$ 850 K avant de décroitre à plus hautes températures au seuil de ségrégation de l'Al. La forte réactivité des surfaces (100) et (111) requiert des précautions spécifiques en termes de protocoles expérimentaux.

D'après la photoémission, si les surfaces bombardées ont une composition proche de la valeur nominale, toutes les surfaces de $Fe_{0.85}Al_{0.15}$ sont sujettes à une intense ségrégation d'Al dans la gamme de température 700-1000 K. Après 1000 K, un régime stationnaire est atteint et la zone affectée est de 2-3 nm d'épaisseur avec une composition proche de l'alliage ordonné de structure CsCl B_2. Mais d'un point de vue structural, toutes les surfaces se comportent différemment. La surface (110) développe une reconstruction pseudo-hexagonale de 2 nm qui est imagée par STM et qui correspond à une modulation incommensurable de paramètre de maille. L'orientation (100) est toujours terminée (1×1) avec une apparence marbrée à l'échelle atomique ce qui est attribué à un contraste électronique et chimique. Enfin, en dépit d'un lissage à grande échelle, le surface (111) est localement rugueuse et présente des structures nanométriques triangulaires dues à un facetage induit par la ségrégation sous forme de surfaces (111) vicinales. La tendance de ségrégation est rationalisée au travers de calculs *ab initio*.

L'oxydation par O_2 de toutes les surfaces en régime de Knudsen à haute température

conduit à une oxydation sélective d'Al et à la croissance de films d'alumine d'épaisseur auto-limitée de 1-2 nm. Le fer reste métallique. Des oxydes couvrants sont trouvés sur les faces (110) et (100) alors que la croissance est plus 3D sur la face (111). L'analyse par photoémission du profil de ségrégation montre des comportements assez distincts. Les sous-surfaces des orientations (110) et (111) sont déplétées en Al et adoptent la structure $D0_3$. D'un autre côté, le profil de ségrégation est insensible à l'oxydation sur la face (100). Toutes les caractéristiques expérimentales des oxydes sur les orientations (100) et (110) sont très proches des résultats de la litérature en particulier sur NiAl. Sur la surface (110), d'après la diffraction rasante, l'alumine croit sous forme de deux domaines ayant une maille de (18.5×10.5) Å^2 presque rectangulaire mais tournée avec une concidence $(2 \times 1)_{ox}$ presque parfaite avec le substrat. Alors que la composition moyenne $Al_2O_{2.6}$, la présence de deux composantes Al 2p oxyde et la cellule élémentaire sont des caractéristiques jumelles de l'oxyde sur NiAl(110), beaucoup moins de parois d'anti-phase sont observées probablement en raison de la liberté de composition de la sous-surface permise par l'alliage aléatoire. L'oxyde à la surface (100) comporte deux domaines (2×1) sous forme de bandes nanométriques; un explication plausible est la formation d'une d'alumine de structure θ. L'absence d'ordre à la surface (111) est attribuée à la forte tendance de cette orientation à se nano-facetter.

CHAPTER 1

INTRODUCTION

1.1 The industrial context

The environmental imperative of reduction of CO_2 emission (Fig. 1.1-a) leads the automotive industry to decrease vehicle mass [1]. For example, according to weight saving plan of the PSA car manufacturer, the reduction should be of 50 kg by 2020 with respect to 2015 for B class vehicles. In response to that challenge, steel industry develops generations of new highly alloyed steels that show improved formability and crash worthiness compared to the conventional grades. The use of high strength thinner gauge steel sheet results in reduction of the car weight and the fuel or electrical consumption while keeping mechanical properties and safety intact at an affordable price. A whole family of so-called Advanced High-Strength Steel (AHSS) (Fig. 1.1-b) has been developed in the recent years with a large range of mechanical properties that can be tuned with the chemical composition and multiphase microstructures resulting from precisely controlled heating and cooling processes [1]. Next to silicon and manganese, aluminium is one of the often used alloying elements for new highly alloyed steel grades. It leads not only to the improvement of elasticity limits, but also to the increase of stiffness performance due to its low density.

The manufacturing of AHSS products for automotive industry challenges industrial operations in each process step. During production process, before hot-dip galvanizing (Fig. 1.1-c), cold rolled strips undergo recrystallization annealing at $\sim$ 1070 K in order to remove remaining stresses and metal texture produced during the rolling operation. Despite the reducing atmosphere of the furnace (N_2 - 5 vol.% H_2) which is suitable to thermodynamically prevent oxidation of iron, the alloying elements that are more prone to oxidation undergo oxygen-induced segregation at the surface leading to a steel sheet extensively covered by oxides such as alumina, silica or MnO_x [4, 5]. A strong industrial concern is that the bad wetting of these oxides by zinc [6] degrades the efficiency of galvanization which is the historical method to prevent corrosion; zinc being less noble or anodic than iron, it sacrificially corrodes to protect the steel substrate. Galvanization of oxide-covered steel faces a new paradigm since it

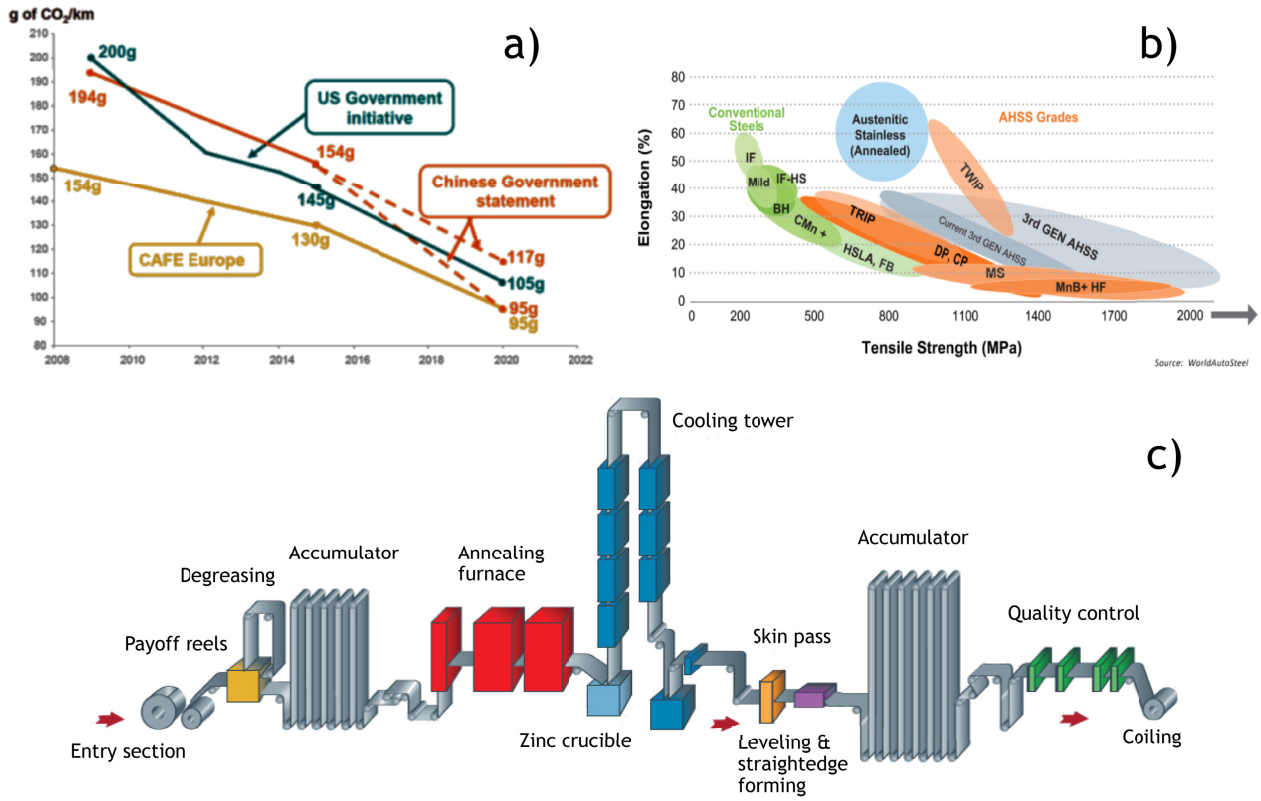

Figure 1.1: a) Worldwide convergence of objectives for CO_2 emission of cars per km [2]. b) Global formability diagram for today's Advanced High-Strength Steel grades including a comparison to traditional low-strength and high-strength steels [1]. c) Scheme of the industrial process of hot-dip galvanization of steel sheets [3].

switches from what is close to a reactive interface with a bare iron surface [1] to a high-energy interface with wide bandgap oxides.

In order to improve the coatability of the steel strips, the production process can be modified via two complementary strategies which consist in (i) optimizing the conditions of the galvanization or using physical vapor deposition techniques to control adhesion at the zinc/oxide interface [3, 7–10] and (ii) modifying the morphology and composition of the oxide layer to control upstream the surface oxidation of steel [3]. The present thesis is based on the second strategy which requires a precise knowledge of the physics and chemistry underlying the formation of the oxide layer.

[1] An interfacial alloy is formed between zinc and iron.

1.2 The research strategy

In this fundamental work, a binary FeX alloy has been examined to pinpoint the behaviour of the alloying element X. It has been chosen to study samples containing aluminium at a given composition (15 atomic per cent of Al) in the form of $Fe_{0.85}Al_{0.15}$ single crystals of different crystallographic orientations for the following reasons:

- *FeAl alloy as a model of alloyed-steel*: obviously complex on the material side through the presence of multiple elements and its polycrystalline structure, the oxidation of steel is also complicated by the gaseous environment in which it occurs. The reducing H_2+N_2 atmosphere used for the recrystallization annealing contains many redox couples, in particular H_2O/H_2. A detailed analysis of alloyed steel being far out of grasp, a tractable alternative is to study binary FeX alloys and their oxidation with only one agent, namely here O_2.

- *Surface oxidation in the form of film*: alloys containing either silicon or manganese are much less easy to model since the oxidation of silicon leads to amorphous oxides while the oxidation of manganese results in different oxides corresponding to the various valences of the element. Moreover, they often appear as oxide clusters and not covering films. Instead, the Al-alloyed iron is of interest since the oxidation of FeAl crystals leads to the growth of crystalline films of aluminium oxide at surfaces with thicknesses of a few nanometres [3] which makes the system adapted to the fundamental surface science approach that is foreseen herein.

- *Application as light-weight alloys*: generally speaking, iron aluminides are very promising light-weight alloys [11] since aluminium, which is one of the alloying elements that improves the elasticity limit of steel, increases the stiffness (elasticity limit/density ratio) performance due to its low density. The subject thus relates to other scopes of application than the automotive industry, in particular the aircraft industry. Moreover, alumina films act as corrosion barriers at low and medium temperatures.

- *Ferrite phase in both model alloy and steel*: $Fe_{0.85}Al_{0.15}$ alloys were chosen because they nicely account for the selective oxidation observed at the surface of industrial Al-alloyed steel grades which have a similar Al content [3]. Indeed, at annealing temperatures of $\sim$ 1070 K, both Fe-Al alloy matrix and Al-alloyed steel correspond to the ferrite phase. Accordingly to the phase diagram, no phase transition in temperature is expected. Consequently, those alloys are test beds in applied research.

- *Orientation-dependent behaviour*: single crystals of similar composition are expected to allow to rationalise the effects of changes in surface orientation, in order to explain the selective oxide distribution observed at the surface of textured Al-alloyed ferrite matrices. Finally, $Fe_{0.85}Al_{0.15}$ crystals of various orientations are commercially available.

In parallel to this industrial context, during the past twenty-five years, aluminium oxide thin films were extensively studied in surface science [12] for both academic and applied issues. Aluminium-based alloys were mostly used to prepare thin alumina films that were conductive enough to allow surface science analysis while being able to mimic catalyst supports.

In this context, seminal works [13, 14] were followed by a massive number of papers dealing with the oxide-covered NiAl crystals of various compositions and orientations (see Chap. 3) until the resolution of the unusual atomic structure of the oxide film on NiAl(110) [15]. The strong contrast in affinity to oxygen of nickel with respect to aluminium insures the formation of surface alumina upon oxidation while nickel is not oxidised at all. Conversely, although they oxidise in a rather similar way than NiAl, crystals of FeAl alloys have attracted much less attention as a support of alumina thin films. A likely reason is that, in FeAl alloys, the relative affinity of iron and aluminium for oxygen is such that there are conditions in which iron is oxidised [16]. Moreover, the use of a random alloy and not of a defined compound asks for the role of inward concentration gradient underneath the oxide, namely the profile of segregation, and its actual role in the film formation. Those points discouraged those who were in search of well-defined alumina thin films on iron-aluminium alloys that can be used as model surfaces. Interestingly, in line with the present work, there is nowadays a growing interest about the surface oxidation of those alloys viewed as structural materials [17].

Conversely, there is some consensus that the structures of all aluminium oxide films that are formed at the surface of Al-containing alloys in ultra-high vacuum condition bear strong similarities. Besides the case FeAl(110) [16] and NiAl(110) [14], the structure of the aluminium oxide grown at the Cu-9 at.% Al(111) [18] was found to be similar to that formed at the NiAl(110) surface [18] as well as the oxide formed on Al-covered Ni(111) [19]. The differences of bulk atomic structure and symmetry of the used substrates (cubic-face centred or cubic centred) and of the aluminium contents question the actual role of the substrate in the final atomic structure of the oxide.

In this thesis, the orientation dependence of aluminium segregation and oxidation at the surface of $Fe_{0.85}Al_{0.15}$ have been tackled with a surface science approach by combining X-ray photoemission, diffraction techniques and near-field microscopy. The low index (100), (110) and (111) surfaces have been compared, clean and after high temperature oxidation. By restricting to ultra-high vacuum treatment, although of interest, the thickening of the oxide layer at higher oxygen chemical potential and the formation of the corresponding transient alumina structures [20], the competition between iron and aluminium oxidation and the switch from external to internal oxidation as described by the Wagner theory [21] have not been addressed in this work.

1.3 Outline of the thesis

The manuscript is divided in five chapters. After the present introduction, the experimental set-up (Sect. 2.1) and techniques used (LEED: Low-Energy Electron Diffraction Sect. 2.3, XPS: X-ray Photoemission Spectroscopy Sect. 2.5, STM: Scanning Tunnelling Microscopy Sect. 2.4, GIXD: Grazing Incidence X-Ray Diffraction Sect. 2.6) are briefly introduced in Chap. 2.

Chap. 3 starts with a presentation of the phase diagram of the FeAl intermetallic alloy, the description of the corresponding common atomic structures and the question of diffusion

and segregation in this material. The most common low index surfaces are then introduced with the crystallographic convention used afterwards. The emphasis is then put on surface science studies already performed on FeAl. In a second part, a state of the art of the different structures of bulk alumina is given. All previous works performed on well-crystallised oxide layers on aluminium alloys are then reviewed in particular on the well-studied nickel-aluminium alloys.

Preparation of a clean surface is a prerequisite in any surface science study. Impurity contents of $Fe_{0.85}Al_{0.15}$ single crystals and reactivity towards residual vacuum are two obstacles that impeded a straightforward study of the intrinsic properties of surfaces. Chap. 4 describes the transient formation of carbon stripes on the (110) surface that paralleled the aluminium segregation in the first stages of sample preparation, as well as the carbon contamination due to the residual gases in the vacuum chambers.

Once highlighted the pitfalls of surface preparation, the analysis of the intrinsic behaviour of clean surfaces is described in Chap. 5. Recrystallisation annealing of all $Fe_{0.85}Al_{0.15}$ surfaces yields an intense aluminium segregation that is explored with photoemission. Dedicated modelling of the angular dependence of core level intensities (Sect. 5.1) is developed to derive the profile of aluminium concentration. A depth of a few nanometres is affected and the surface composition is close to FeAl. This surface enrichment in aluminium is accompanied by the appearance of a long-range hexagonal-like superstructure on the (110) surface which is explored by LEED and GIXD (Sect. 5.2). In parallel, (100) and (111) surfaces seem (1×1) terminated. Near-field microscopy (Sect. 5.3) points at an obvious increase of terrace size of sputtered surfaces and straightening of step edges with annealing temperature. The hexagonal nanometre-sized superstructure is imaged on the (110) surface while the (100) appears flat with a marbled electronic contrast and the (111) surface is nanofacetted and rough at the atomic scale with some tendency to form locally a double periodicity. Finally, the strong trend of aluminium segregation is confirmed by *ab initio* calculations.

High temperature oxidation of the three orientations is addressed in Chap. 6. Analysis of core levels demonstrates that, in the present conditions, iron is not oxidised and a self-limited continuous aluminium oxide is formed. All surfaces are alternately analysed in a common way. Al 2p core levels are decomposed in metallic and oxide components through a careful fitting. Firstly, the dependence with emission angle of the ratio between metallic aluminium and iron is used to obtain the profile of segregation under the oxide. Oxidation seems to induce a subsurface depletion in aluminium except on the (100) surface. The knowledge of the actual profile of segregation is mandatory to deduce oxide film thickness and stoichiometry which turn out to be different on the three surfaces. LEED shows that all oxide films are crystalline except for (111) orientation, mainly because of the open character of the body-centred (111) surface. On the (110) surface, the complex diffraction pattern can be indexed with two domains as seen with STM exhibiting a large and nearly rectangular unit cell which is very similar to that found on NiAl(110). Accurate lattice parameters determination with GIXD points at a nearly coincidence on a (1×2) oxide supercell with traces of a superstructure due to segregation underneath. LEED and STM demonstrates that the oxide formed on (100)

surface is a twin of that formed on NiAl(100). Two chemical environments of oxidised aluminium are present for (110) and (111) while only one is present for (100). The chapter ends with a comparison of the oxides formed on all terminations with results from the literature.

Beyond a quick summary, the conclusion points at unanswered questions and tries to draw some perspectives of study.

CHAPTER 2

EXPERIMENTAL TECHNIQUES AND SET-UPS

This chapter aims at a brief introduction of the experimental set-up, the sample preparation and the characterization techniques used all along this work. The questions of orientation dependence of segregation and of oxidation at the surface of a $Fe_{0.85}Al_{0.15}$ crystal were tackled on the low-index (100), (110) and (111) surfaces using a surface science approach. The vacuum environment (Sect. 2.1) enabled the characterization of atomically clean surfaces with the following techniques:

- Low-Energy Electron Diffraction (LEED, Sect. 2.3) to explore surface crystallinity,
- Scanning Tunnelling Microscopy (STM, Sect. 2.4), to analyse the surface morphology,
- X-ray Photoemission Spectroscopy (XPS, Sect. 2.5), to determine the chemical states of elements and composition profiles.

Complementary measurements were performed at the European Synchrotron Radiation Facility (ESRF) with Grazing Incidence X-ray Diffraction (GIXD, Sect. 2.6).

2.1 The ultra-high vacuum set-up at INSP

Experiments were carried out in Ultra-High Vacuum (UHV) conditions (pressure $<10^{-9}$ mbar). UHV is essential to keep samples free of contaminants for a period long enough to be able to characterise the intrinsic properties of the surfaces. Indeed, assuming a sticking coefficient close to one, the kinetic theory of gases shows that it only takes one second at a pressure of around 10^{-6} Torr to create one absorbed monolayer. This defines the Langmuir unit (L) of exposure as used hereafter which amounts to 10^{-6} Torr·s ($\sim 1.33\times10^{-6}$ mbar·s) [22–24] [1].

[1] No correction from gauge ionisation sensitivity was accounted for in this study.

Aside a load-lock system for a fast entry of the samples, the experimental system used at Institut des NanoSciences de Paris (INSP) (Fig. 2.1) consists of two chambers (preparation and analysis, base pressures of $5 \cdot 10^{-11}$ up to $3 \cdot 10^{-10}$ mbar) where different *in situ* techniques are combined:

- photoemission spectroscopy with an Omicron EA 125 (5 channeltrons) hemispherical analyser under non-monochromatic Al-Kα (1486.6 eV) and Mg-Kα (1253.6 eV) X-ray excitations (XPS); the analysis chamber made-out of μ-metal is shielded against external magnetic field and the X-ray source is a DARX-400 from Omicron;
- near-field microscopy, herein Scanning Tunnelling Microscopy (STM) with an Omicron VT-AFM head operating under Matrix electronics;
- electron diffraction with a reverse 4 grids device (LEED; ErLEED 150 from SPECS).

The chambers are pumped by ionic pumps (Varian StarCell) with pumping speed of 500 $l \cdot s^{-1}$ (analysis) and 300 $l \cdot s^{-1}$ (preparation) associated with Ti sublimators and turbomolecular pumps (Pfeiffer, 200 $l \cdot s^{-1}$) back-pumped with two-stage rotary pumps (Pfeiffer 10 $m^3 \cdot h^{-1}$). Pressures are measured by hot filament Bayard-Alpert gauges in each chamber and by combined Pirani-Penning gauges on turbomolecular pumps. On a leak-free system, a careful bake-out of around 24-48 hours at 135°C allows to outgas the walls of the chamber, by removing in particular adsorbed water, to reach the final pressure which composition is essentially made of hydrogen, water and carbon monoxide as checked by a Residual Gas Analyser (RGA, Pfeiffer 200 amu). Flow of ultra-pure gases (research grade O_2 and Ar) are controlled through series of leak valves connected to manifold ancillary gas pipes which are baked-out and carefully flushed several times before any use.

In the preparation chamber, the sample mounted on an Omicron plate made-out of refractory material (Ta, Mo) can be cleaned by Ar^+ bombardment with a gun (SPEC IQE11/35) having a fixed focalisation (spot of 1 cm^2 at sample position; beam energy around 1000 eV, incident angle 60° from normal). The usual ion current around 10 μA allows for the removal of around one monolayer per minute assuming a sputtering yield of one. At the same position, the sample can be annealed up to high temperature (1700 K) on a home-made electron-bombardment furnace. Temperature is systematically measured directly on the supporting plate and the sample with an optical pyrometer (Impac IGA 140) with an emissivity set at 20 %; a calibration between pyrometer, thermocouple directly spot welded on the plate and heating power was performed to minimise the error on temperature determination due to emissivity. Samples are transferred between the different parts of the experimental chambers with a magnetic rod equipped with the Omicron fork. On the 5-axis manipulator of the analysis chamber, the sample can be heated up to 1100 K and analysed by XPS and LEED. The sample can be transferred from this position to the microscope via a wobble-stick.

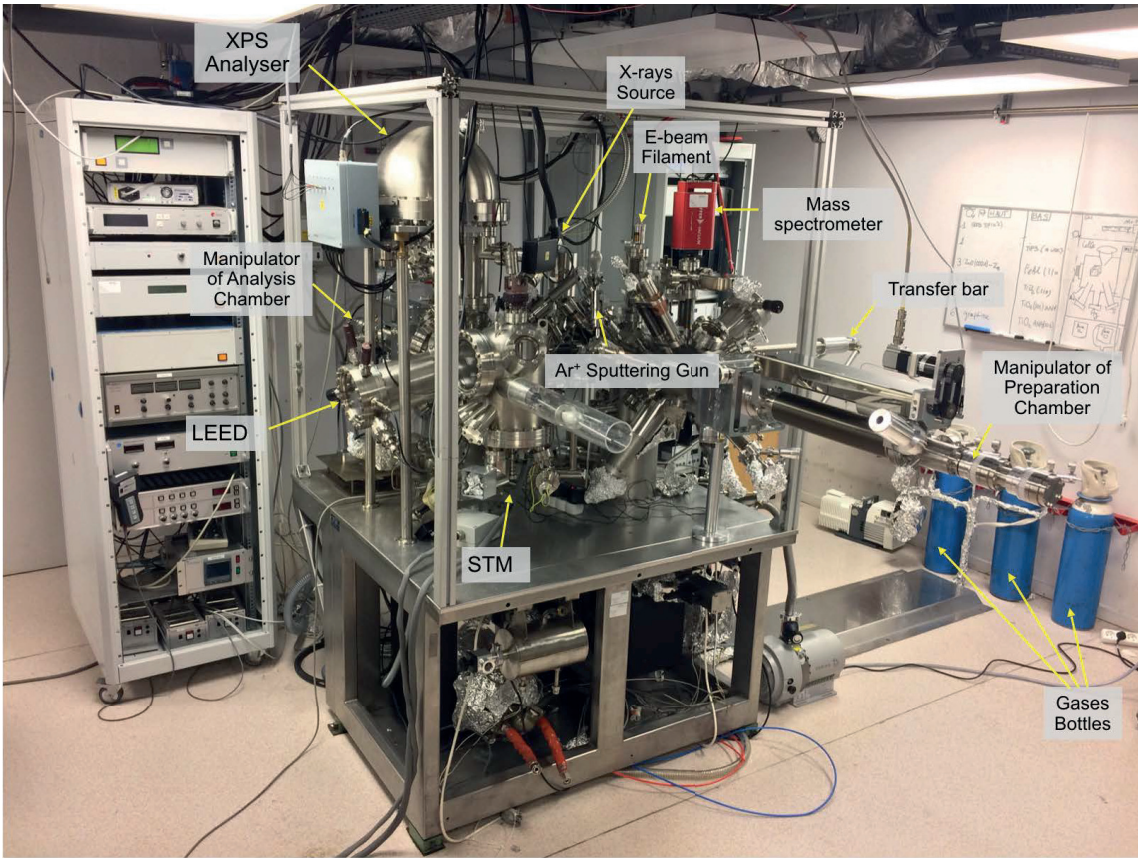

Figure 2.1: Overview of the ultra-high vacuum system at INSP used during this thesis.

2.2 Surface preparation and film synthesis

$Fe_{0.85}Al_{0.15}$ single crystals cut along low index (100), (110) and (111) orientations have been studied throughout this work. According to the phase diagram, such a composition corresponds to a random A_2 body centred alloy (see Sect. 3.1). The bulk composition was checked *a posteriori* (on (110) crystal only !) by X-ray diffraction (see Sect. 2.6) through the Vegard's law dependence of the lattice parameter [25] ($a = 2.8914$ Å). Crystals of disk shape ($\phi = 6$ mm, thickness 2 mm) have a miscut below 0.1° and are polished down to the lowest achievable roughness by the supplier [26]. They have been mounted through a Ta wire inserted in a groove in the thickness of the sample and spot-welded on the support plate, letting the surface fully free.

Since segregation and sample history is an issue for random alloys (see Sect. 3.3), a common protocol of surface preparation has been adopted. Samples have been cleaned by intensive cycles of Ar^+ sputtering (beam energy 1000 eV) for 20-45 minutes at room temperature. From the tabulated sputter yield (normal incidence, 1000 eV Ar^+) [27], a slight preferential sputtering of Fe (1.70 atom/ion) over Al (1.53 atom/ion) is expected at the opposite of the common belief of the literature which argues [2] about Fe enrichment. Indeed, the composition

[2] Without convincing proofs!

found on sputtered surface is close to the nominal one (see Chap. 5). Sputtering has been followed by a given cycle of heating: (i) ramping up to the final temperature within a couple of minutes, (ii) annealing plateau of 15-20 mins, (iii) fast cooling down. To test segregation effect, the plateau temperature has been increased from 673 K to 1273 K (see Chap. 5). However, in most cases, the annealing did not exceed 1200 K to avoid Al evaporation problems as already reported above this temperature [28, 29]. Sample cleanliness and crystallographic quality were systematically checked by XPS and LEED. Bulk contamination and strong surface reactivity of bare surfaces were two major difficulties in this work as described in Chap. 4.

Surface oxidation (see Chap. 6) was achieved by introducing molecular oxygen during the annealing plateau at a pressure between 10^{-7} mbar and a few 10^{-6} mbar to reach a given exposure (expressed in Langmuirs) during the fixed annealing duration. Introduction of oxygen at the beginning, middle or end of the annealing plateau did not change the final results. A few tests of two-step oxidation (exposure at room-temperature followed by annealing) commonly applied to growth thin oxide films on NiAl were also performed on the (110) orientation.

2.3 Low-Energy Electron Diffraction

In surface science, Low-Energy Electron Diffraction (LEED) is the usual technique for checking the crystallographic quality, the symmetry and the reconstruction of the surface. The strong interaction between electrons of kinetic energy between 30 and 200 eV having a wavelength around the Angstrom makes this diffraction technique extremely surface sensitive. The determination of an atomic structure in diffraction experiments falls naturally into two parts [23, 24]:

- the determination of the periodicity of the system and thus the basic unit of repetition or the surface unit mesh which requires an analysis of diffraction spot symmetry and positions;
- the location of the atoms within this unit cell which requires a careful analysis of spot intensities, and more precisely their variation with beam energy in LEED; this dynamic LEED analysis was applied in the literature to tackle the question of segregation at the FeAl surface [28–34].

A clean surface with large crystalline domains should be characterised by sharp spots with high contract and low background intensity. Any crystallographic imperfections or disordered phases will increase the background intensity, because of diffuse scattering from these statistically distributed defects.

2.3.1 Experimental set-up

A common reverse LEED optics consists in an electron gun, grids and a collector (fluorescent screen) (Fig. 2.3.1). The electron gun produces an electron beam with primary energies of $\sim$ 20 to 200 eV. These latter impinge on the surface of the sample at normal incidence and diffracted beams are collected in the backward direction. After a first grounded grid to

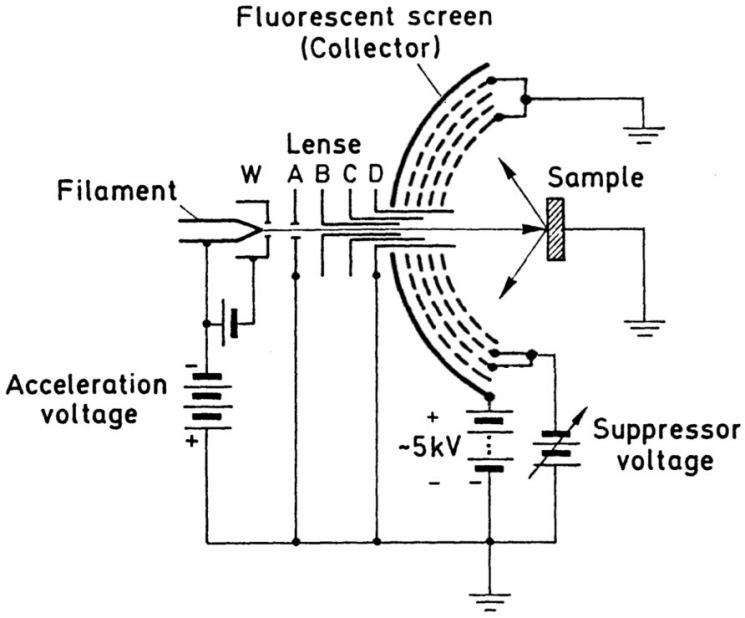

Figure 2.2: Schematic of a four-grids LEED optics.

produce a zone free of potential between sample and apparatus, the next one is polarised at a value close to the beam energy to get rid of inelastic electrons. The elastic ones are then re-accelerated up to several keV before reaching the fluorescent screen. According to de Broglie's relation, the wavelength λ of electrons $\lambda(\text{Å}) \approx \sqrt{140.4/E}$ (eV) in a LEED experiment is in the Angstrom range, *i.e.* the same magnitude as the interatomic distances in a solid.

LEED diffraction pattern only provides surface information originating from an area with a radius smaller than coherence length due to the instrument Δr_c:

$$\Delta r_c \simeq \frac{\lambda}{2\beta\sqrt{1+(\Delta E/2E)^2}}. \tag{2.1}$$

It is limited by the divergence or angular spread 2β of the beam (the so-called transverse coherence) and by the wavelength or energy spread ΔE (the so-called longitudinal coherence) given mainly by the temperature of the emitting filament. Thus for a kinetic energy of ~ 100 eV, if the angular spread of the primary beam is $\sim 10^{-2}$ rad, and the energy width is of ~ 0.5 eV, the coherence length is about 100 Å which corresponds to a coherently illuminated area of ~ 300 nm^2 [23]. Therefore imperfections, in particular terrace size, will not contribute to the peak broadening above this limit.

2.3.2 Ewald's construction in 2D

If a low energy electron beam of wavelength λ and wavevector $\mathbf{K}_i$ impinges on a two-dimensional net of scattering centres, a number of scattered waves $\mathbf{K}_s$ are produced within the elastic condition $K_i = K_s = 2\pi/\lambda$. The bulk Laue's conditions of diffraction on a crystal of unit cell vectors $(\mathbf{a}, \mathbf{b}, \mathbf{c})$:

$$\mathbf{a}\cdot\Delta\mathbf{k} = 2\pi h \qquad \mathbf{b}\cdot\Delta\mathbf{k} = 2\pi k \qquad \mathbf{c}\cdot\Delta\mathbf{k} = 2\pi l \tag{2.2}$$

would require that the wave vector transfer $\Delta\mathbf{k} = \mathbf{K}_s - \mathbf{K}_i = h\mathbf{a}^* + k\mathbf{b}^* + l\mathbf{c}* = \mathbf{G}$ is a vector of the reciprocal lattice. $(\mathbf{a}^*, \mathbf{b}^*, \mathbf{c}^*)$ are the reciprocal space lattice vectors and (h, k, l) integers. However, the strong interaction of low kinetic electrons with matter gives rise to a limited probing depth that releases the Laue's condition perpendicular to the surface. In other words, if $\mathbf{c}$ is assumed to be normal to the surface and $\mathbf{a}, \mathbf{b}$ are in plane, the reciprocal space seen by electrons consists of continuous rods, the so-called Crystal Truncation Rods (CTR) and the Laue's condition of constructive interference impacts only the parallel component $\Delta\mathbf{k}_{\parallel}$ of the wavevector transfer: $\Delta\mathbf{k} = G_{\parallel} = h\mathbf{a}^* + k\mathbf{b}^*$.

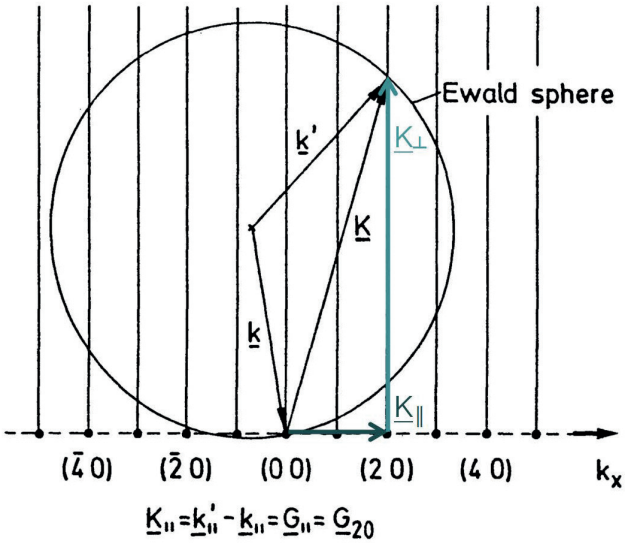

Figure 2.3: Ewald's construction based on 1D reciprocal lattice points. The reciprocal space of a surface is made of Crystal Truncation Rods normal to the surface which intersections with the Ewald's sphere give the directions of the diffracted beams. CTRs are labelled here with their surface indexes.

In terms of Ewald's sphere construction (Fig. 2.3) which is a geometrical interpretation of the Laue's conditions, scattering will be observed along directions where the CTRs drill the Ewald's sphere which is a sphere of radius $K_i = 2\pi/\lambda$. Of course among the half space, only the scattered wavevectors $\mathbf{K}_s$ intersecting the LEED screen will be observed. Usually in surface crystallography, the periodicity of the bulk crystal is described through a surface unit cell $(\mathbf{a}_S, \mathbf{b}_S)$ with the repeating unit cell vector $\mathbf{c}_S$ normal to it; the corresponding surface indexes (h_S, k_S) label the diffraction spots. The analysis of a LEED pattern [23, 24] can provide:

- the symmetry of a superstructure (i) due to a reconstruction of the surface compared to the bulk surface unit cell $(\mathbf{a}_S, \mathbf{b}_S)$ or (ii) due to an adsorbed film. The unit cell lattice vectors of the superstructure is usually defined through a matrix M_S from the bulk surface unit cell. In the simplest cases, it involves a dilatation (m along $\mathbf{a}_S$ and n along $\mathbf{b}_S$) and a rotation Θ and is noted $(m \times n)R\Theta$. If m, n are integers, the superstructure is said commensurate with the substrate, but incommensurate cases are not unusual. The corresponding matrix of transformation M_S between "bulk" surface and superstructure unit cells is also often used to characterise this latter.

- information regarding the crystalline quality of the substrate (such as faceting, roughness etc. . .) through spot broadening or splitting. In our case, only qualitative informa-

tion can be obtained since a quantitative analysis would require a spot profile analysis apparatus.

2.4 Scanning Tunnelling Microscopy

Scanning Tunnelling Microscopy (STM) is a direct real-space imaging technique that is based on the tunnelling effect principle between a metallic tip and a sample. The tip is scanned over the surface with sub-nanometre resolution in all directions while measuring/regulating the current at the near vicinity of the surface. The strength of STM in achieving atomic resolution is the extreme sensitivity of the current on sample/tip distance. Conductive sample is a prerequisite but insulators can be imaged in the form of thin films deposited on a conductive substrate.

2.4.1 Instrumentation

The schematic diagram of a STM is shown in Fig. 2.4. The essential element consists of a probe tip, usually made of W or PtIr, attached to a piezodrive which involves three mutually perpendicular piezoelectric transducers along *x, y, z*. Upon applying a voltage, they expand or contract through piezoelectric effect (of the order of $\mathrm{nm \cdot V^{-1}}$). Using the coarse motors [3] and the z piezo, tip and/or sample are brought to a distance of a few angstroms at which the electron wavefunctions of the tip and sample overlap. A bias voltage applied between them causes an electrical current to flow through the vacuum junction [35]. Sawtooth voltages that are applied on the x and y piezoelectric components enable the tip to scan the x y plane under tunnelling condition reconstructing a "topographic" image of the surface of the sample. In STM, there are two imaging modes (Fig. 2.5). At constant current, as used in this thesis, the tunnelling current is kept constant via a feedback circuit that adjusts the height while scanning. In constant-height mode, the tip moves in a horizontal x y plane, leading to a change in the tunnelling current accordingly to local topography and local electronic states of the sample.

In order to achieve atomic resolution, effective vibration isolation is critical since a typical corrugation amplitude in STM within a crystallographic plane is of the order of a fraction of Angstrom. In our microscope, this is achieved through a heavy and rigid bench for the high frequency vibrations and by a low-frequency vibration isolation stage holding the microscope based on suspension springs combined with eddy-current damping [35]. Another important issue to be solved is the electronics and control of the STM. Since the tunnelling currents occurring in STM are typically from 0.01 to 50 nA, the current should be amplified with a low-noise circuit. Besides the current amplifier, a feedback circuit is necessary to control an equilibrium z position and control the tip-sample distance. The feedback loop is negative that is to say if the tunnelling current increases when scanning, then a voltage is applied to the z piezoelectric transducer to withdraw the tip from the sample surface, and vice versa.

[3] Which are actually piezoelectric motors that work on the slip/stick principle when actuated with a sawtooth voltage.

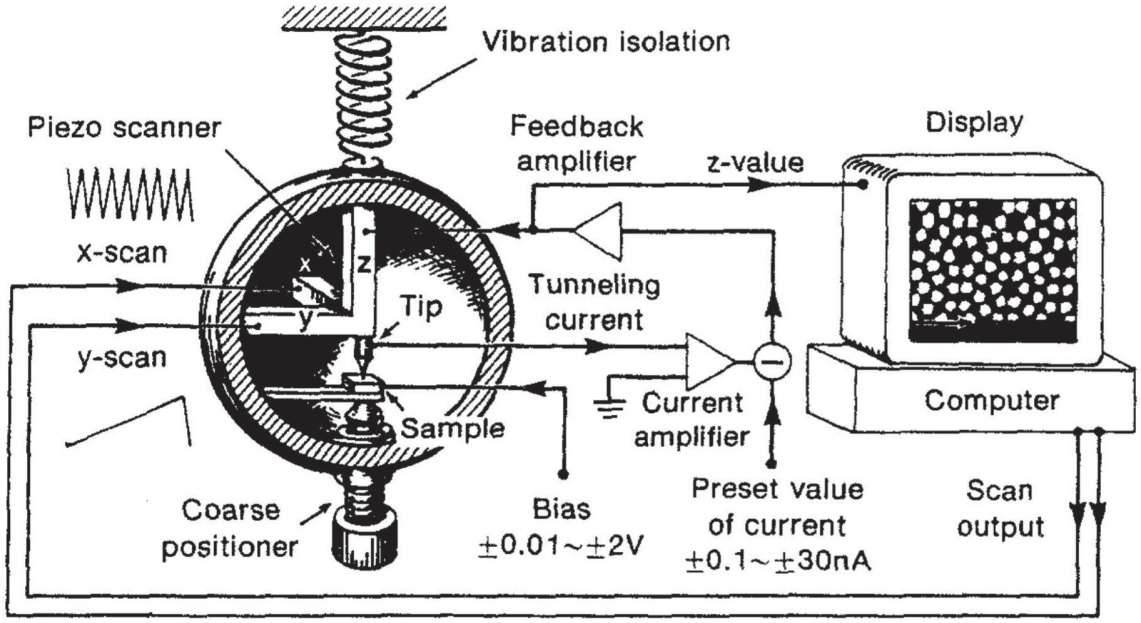

Figure 2.4: Schematic diagram of a scanning tunnelling microscope. From Ref. [35].

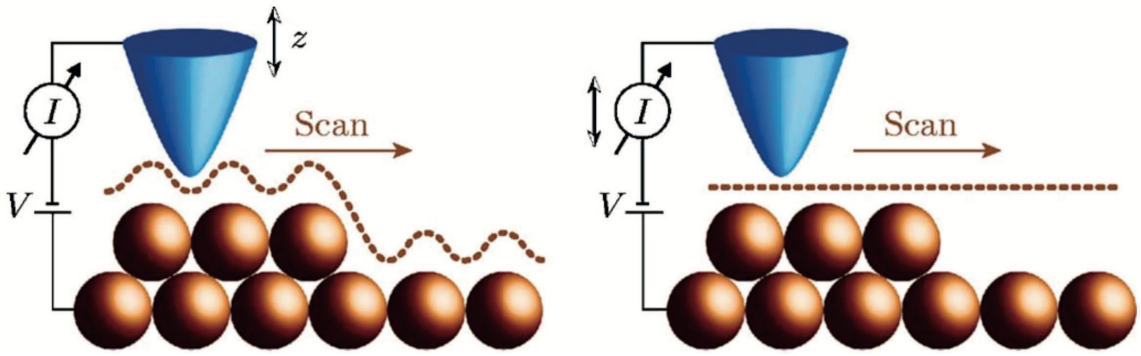

Figure 2.5: The STM imaging modes [36]: (left) constant-current mode, (right) constant-height mode.

2.4.2 Basics of STM theory

In order to understand the unprecedented resolution achieved by STM, a number of theoretical methods have been developed over the years up to atomic simulations of the whole tip/sample system. The first one is known as the elementary one dimensional model [35]. The other two early theories are the corrugation function model, the so-called the Stoll's formula (1984) [37] and the s-wave-tip model developed by Tersoff and Hamann (1983, 1985) [38,39]. Both grasp the main physics underlying the imaging *i.e.* the extreme sensitivity of tunnelling current on distance and the importance of density of electronic states of the sample and the tip.

In one-dimensional model, the movement of an electron of mass m having an energy E confined in one dimension by a potential barrier [$U(z) = 0$ if $z < 0$ and $U(z) = U$ if $z > 0$] is described by the Schödinger's equation:

$$E\Psi(z) = -\frac{\hbar^2}{2m}\frac{d^2}{dz^2}\Psi(z) + U(z)\Psi(z), \tag{2.3}$$

where $\Psi(z)$ is its wave function. When $E > U$, the solution of Eq. 2.3 is propagative and reads:

$$\Psi(z) = \Psi(0)e^{\pm ikz}, \tag{2.4}$$

where the wavevector is $k = \frac{\sqrt{2m(E-U)}}{\hbar}$ ($p_z = \hbar k$). When $E < U$, *i.e.* in the forbidden region in classical mechanics, the wave function exponentially decays with distance z since k becomes imaginary:

$$\Psi(z) = \Psi(0)e^{-kz}. \tag{2.5}$$

The possibility to observe an electron at $z > 0$ being proportional to $|\Psi(0)|^2 e^{-2kz}$ is nonzero outside the potential barrier. This basic interpretation of metal-vacuum-metal tunnelling is at the basis of the calculation of the tunnelling current at a tip/vacuum/sample junction in a STM experiment (see Fig. 2.4.2) with a barrier value ϕ given by the work function of tip and sample (assumed to be the same herein). ϕ gives the minimum energy needed to remove an electron from the substrate Fermi level into vacuum; typical values of metals are in the range of 4 to 5.5 eV [40].

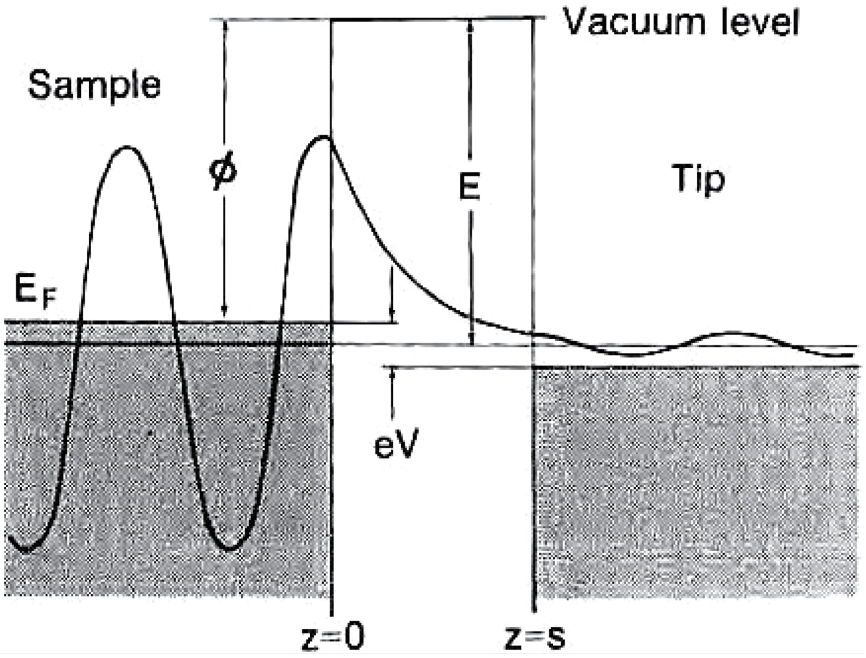

Figure 2.6: Schematic diagram of metal-vacuum-metal tunnelling [35]. Metals are indicated by the grey shadowing and represent the metal sample (left) and the tip (right). The middle region corresponds to the vacuum.

Under a bias voltage V applied to the sample, the junction is polarised and the tunnelling current is the probability of overlap of the wavefunction Ψ_n of an electron in state n:

$$w \propto |\Psi_n(0)|^2 e^{-2kz}, \tag{2.6}$$

where the decay constant $k = \frac{\sqrt{2m(\phi - eV)}}{\hbar}$ is in the range of 1 Å^{-1}. The tunnelling direction of the current changes when reversing the bias. When a positive bias is applied on the sample, electrons tunnel from the tip to unoccupied states of the sample, whereas if the bias is negative,

electrons tunnel from occupied states of the sample to the tip. Therefore, the bias polarity determines whether unoccupied or occupied electronic states of the sample surface are probed.

The tunnelling current is proportional to the number of states on the sample surface within an energy interval. For metals and alloys, the number is finite and proportional to the Local Density Of States (LDOS) at the set point. For semiconductors and insulators, it can be very small or even null if the bias applied is smaller than the band gap. Taking all the sample states Ψ_n in the energy interval eV, the tunnelling current can be expressed as:

$$I \propto \sum_{E_n=E_F-eV}^{E_F} |\Psi_n(0)|^2 e^{-2kz}. \tag{2.7}$$

If the bias voltage V is small enough compared with the work function of the sample and tip, the density of states does not vary obviously within the energy interval eV. Then Eq. 2.7 can be written as the LDOS of the sample at the Fermi level and at the centre of the tip apex. LDOS is the number of electrons per unit volume per unit energy, having a given energy at a given point in space. The LDOS $\rho_S(z, E)$ can be written as:

$$\rho_S(z, E) \equiv \frac{1}{\epsilon} \sum_{E_n=E-\epsilon}^{E} |\Psi_n(z)|^2. \tag{2.8}$$

At $(z = 0, E = E_F)$ within the bias voltage windows eV,

$$eV \cdot \rho_S(0, E_F) \equiv \sum_{E_n=E_F-eV}^{E_F} |\Psi_n(0)|^2. \tag{2.9}$$

Therefore, the tunnelling current reads:

$$I \propto eV \cdot \rho_S(0, E_F)e^{-2kz} \equiv eV \cdot \rho_S(z, E_F), \tag{2.10}$$

which means that a topographic STM image obtained by scanning the tip over the surface under constant tunnelling current is a contour of a constant LDOS of the surface of the sample. It is independent of the electronic states of tip.

If accounting for the whole junction including the tip electronic state by solving two separate equivalent subsystems (sample/vacuum and vacuum/tip) following the approach of Bardeen [35,41,42], the tunnelling current appears as the convolution of the Density Of States (DOS) of two electrodes:

$$I \propto \int_0^{eV} \rho_S(E_F - eV + \delta)\rho_T(E_F + \delta)d\delta. \tag{2.11}$$

ρ_S and ρ_T are the DOS of sample and tip and E_F is Fermi level at equilibrium.

2.4.3 Tip preparation and image treatment

Tip is an essential component of an STM experiment since the tunnelling current is determined by the convolution of the electronic states of the sample and of the tip, and its ultimate atomic apex controls the resolution. In our experiments, reproducible STM imaging could be obtained with different W tips. They have been prepared via continuous electrochemical etching in a KOH solution (concentration $\sim$ 4.5 mol/L). A potential of around 7 V is applied between a W wire ($\Phi = 0.36$ mm) partially immersed in the solution and a stainless steel ring ($\Phi = 40$ mm) touching the surface of the solution. The overall etching reaction $W(s) + 2H_2O + 2OH^- \rightarrow WO_4^{2-} + 3H_2(g)$ happens at the meniscus between the wire and the solution until the neck is so thin that the remaining portion of the wire falls in the solution. This generates a fresh atomic W tip. The external circuit detects the sudden increase of resistivity and stops the etching process to avoid damaging the tip apex. After thorough rinsing with deionised water and/or pure alcohol, tip shapes are optically controlled [4] and mounted onto dedicated gold coated tip holders [43, 44]. Tip are "cleaned" and "conditioned" *in situ* through pulses of increasing voltage and duration until stable and good imaging conditions are achieved in particular on steps of metallic substrates.

The obtained STM images have been treated using the Gwyddion software [45] a modular program for SPM (Scanning Probe Microscopy) data visualization and analysis. The main used image treatments are:

- a flattening of the image (tilt correction) through the average plane followed by a further interpolation line by line along the scan direction; eventually flattening is performed over selected area of the image to enhance the contrast from terraces;
- filtering through 2D Fast Fourier Transform to remove noise having specific spatial frequencies if needed;
- drift compensation between up/down images;
- 2D auto-correlation function or Fourier transform to seek for periodicity;
- line profiles and statistical analysis such as roughness or slope analysis.

2.5 X-ray Photoemission Spectroscopy

2.5.1 Basic principles

Photoelectron spectroscopy is based on the photoelectric effect during which electrons in a solid can be ejected by a radiation which energy exceeds the binding energies (BEs) in the material. The analysis in kinetic energy of the intensity of photoelectrons gives access to information regarding material composition and chemical states of elements. Depending on the excitation energy, laboratory photoemission can be divided into two techniques: Ultraviolet and X-ray Photoelectron Spectroscopy (UPS and XPS) respectively. XPS is also known

[4] Symmetric and short apexes are preferred although this is not a guarantee of good imaging conditions.

as Electron Spectroscopy for Chemical Analysis (ESCA) [46, 47]. UPS is dedicated to the analysis of the valence band.

Taking the Fermi level common to the sample and the spectrometer as an energy reference, the kinetic energy of the elastically emitted photoelectrons can be calculated from energy conservation by combining the emission (Fig. 2.7) and the energy levels involved (Fig. 2.8):

$$E_K = h\nu - E_B - \Phi_{sp}. \tag{2.12}$$

$h\nu$ is the photon energy, E_K the kinetic energy of the emitted photoelectron, E_B its binding energy and Φ_{sp} is the work function of the spectrometer. Eq. 2.12 indicates that photoemission can provide a picture of the filled states in the probed material, deep core levels in XPS and valence band in UPS. In our set-up, Φ_{sp} was determined by using Ag 3d core level as a reference ($E_B = 368.2$ eV).

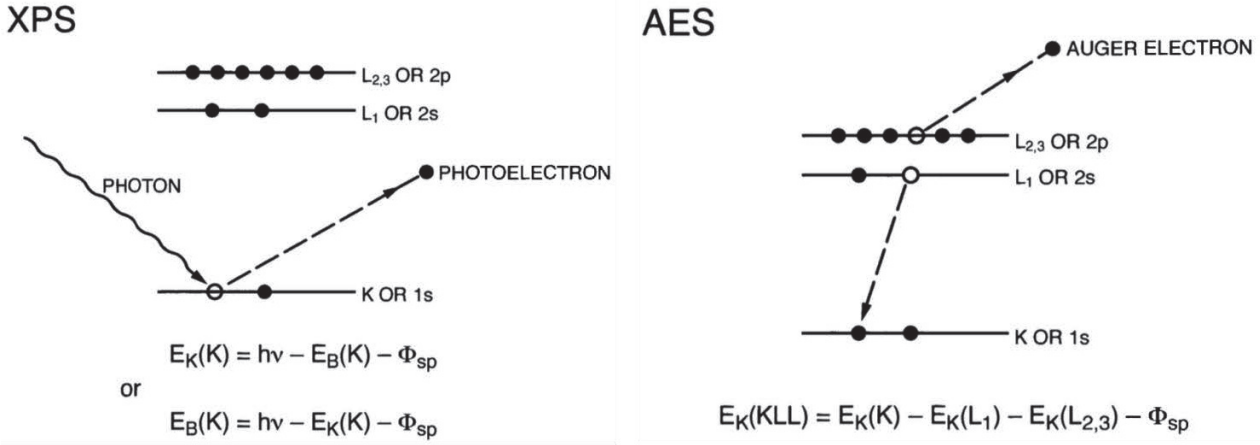

Figure 2.7: Scheme of the main processes involved in an XPS experiment [48]: photoemission (left) and Auger process (right). XPS involves the emission of a single photoelectron from a given core level ($1s$ or K shell here) via X-ray excitation. Auger emission is a three-electron process. After emission of the initial photoelectron, an other electron (L core level here) fills the vacancy and an electron of an upper orbital (L core level here) is emitted with a kinetic energy equal to the excess energy. The Auger transition, given as an example, is labelled KLL.

After photoionization, the hole created by the emitted photoelectron (Fig. 2.7) can be filled by the decay of an electron from an outer orbital followed by the subsequent emission of an electron of a higher lying orbital which kinetic energy carries the excess energy. This so-called Auger process is labelled by the three energy levels involved in the transition. For example, for a KLL series, the initial core level hole is in the K shell and the last two holes are in the L shell:

$$E_K(KL_1L_{2,3}) = E_B(K) - E_B(L_1) - E_B(L_{2,3}) - \Phi_{sp} + \Delta E_{rel}. \tag{2.13}$$

Where ΔE_{rel} stands for the relaxation in energy, that is involved in the Auger process. The relation (Eq. 2.13) is at the heart of Auger Electron Spectroscopy (AES) for which a series

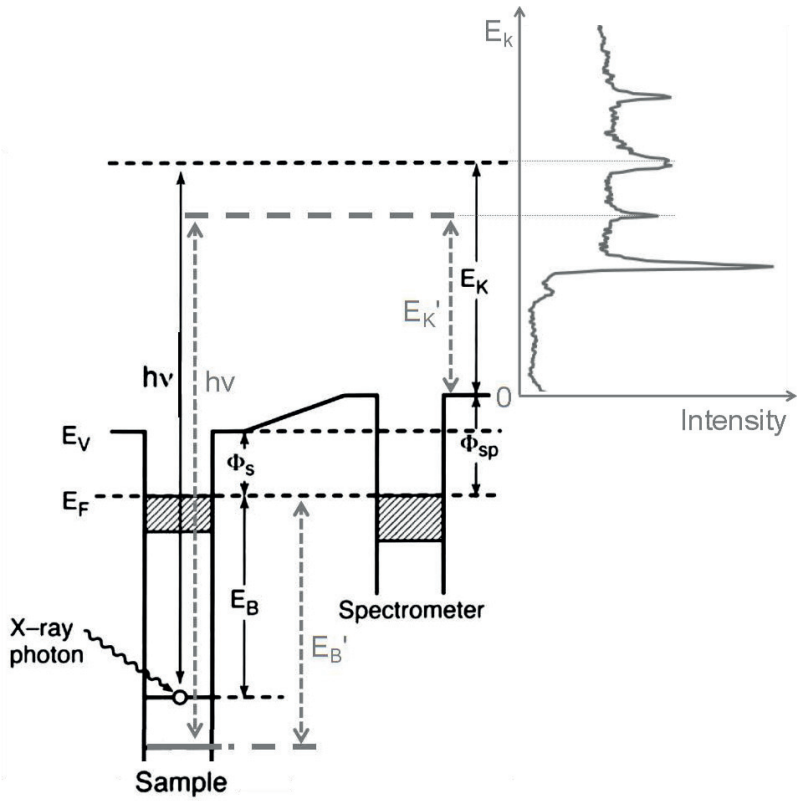

Figure 2.8: Link between schematic band level alignment between sample and spectrometer and photoemission spectrum in kinetic energy. Φ_s is the work function of the sample *i.e.* the minimum energy required to extract an electron from the Fermi level to infinity [49].

of relaxations follow the creation of a core hole (generally by an impinging electron or an impinging photon).

2.5.2 Instrumentation

The main components for a typical laboratory XPS apparatus shown in Fig. 2.9 are the X-ray source, the sample support system (manipulator), the energy analyser, the electron detector (multiplier) and the driving electronics converter.

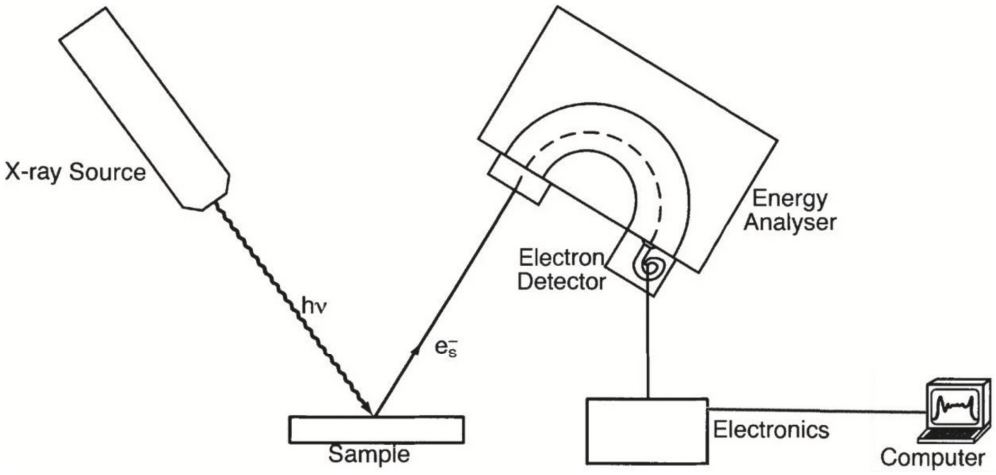

Figure 2.9: Main components for a typical XPS apparatus [48].

In the source, the emission of X-rays is produced by bombarding with high energy electrons (around 10 keV and 200 W in DARX-400) a cooled metallic target containing Mg or Al. For both elements, the X-ray emission spectrum due to the refilling of K-level holes is dominated by Kα_1 and Kα_2 lines [50, 51]. In a non-monochromatised source, these intense lines are superimposed with:

- satellite peaks (Kα_3, Kα_4 ...) which positions and relative intensities (see Tab. 2.1) are characteristic of a given anode material;
- Bremsstrahlung radiation (also called braking radiation) which is produced by the deceleration of the electrons as they strike the target;
- cross talk between anode (less than 1 % for our source) due the contamination of the anode material by the other one.

These drawbacks increases the complexity of the analysis and limit the resolution to around 0.85 eV for Al-Kα and 0.7 eV for Mg-Kα. The ionization cross section *i.e.* the probability of absorbing a photon and creating a hole on a given level has been calculated and are tabulated for our excitation energies [52]. Since our source is non-polarised and located at the "magic" angle of $\arccos(1/\sqrt{3}) = 54.7°$, no assymetry in the ionization cross section have to be taken into account [52, 53].

Line	$\alpha_{1,2}$	α_3	α_4	α_5	α_6	β
Mg displacement, eV	0	8.4	10.2	17.5	20.0	48.5
Mg relative height	100	8.0	4.1	0.55	0.45	0.5
Al displacement, eV	0	9.8	11.8	20.1	23.4	69.7
Al relative height	100	6.4	3.2	0.4	0.3	0.55

Table 2.1: X-ray satellite energies and intensities for given X-ray sources [50].

Once the photoelectrons escape from the surface of the sample into the vacuum, they are collected and separated according to their kinetic energy and subsequently converted into a spectrum. Thus the electron energy analyser is the heart of XPS system and is the critical component in determining sensitivity and resolution [48]. The ejected electrons first pass through a set of electrostatic lenses that refocus the beam and are then decelerated down to (or accelerated up to) the so-called pass energy E_p before entering the hemispherical analyser (Omicron EA 125). The voltage difference applied between the inner and outer hemispheres acts as a band pass filter. The analyser only transmits electrons with an energy matching E_p which are then collected by the detector. The resolution can be improved by reducing the pass energy (at the expense of the total number of counts), entrance slit width and the acceptance angle of the lens system. The latter also govern the probed area.

The analyser can be run in:

- at Constant Retard Ratio (CRR) by keeping constant the ratio of pass energy and kinetic energy and therefore the transmission of the analyser,

- at Constant Analyser Energy (CAE) *i.e.* at constant pass energy and therefore resolution throughout the whole range of binding energy. This mode was systematically used in this work and leads to a higher transmission at low kinetic energy.

The resolution of the analyser can be written approximately as:

$$\Delta E = E_p \left(\frac{d}{2R_0} + \alpha^2 \right). \tag{2.14}$$

E_p is the pass energy, d is the slit width, R_0 is the mean radius of the hemispheres, and α is the half entry angle of electrons. Tab. 2.2 gathers typical parameters used for quick/wide scans ($E_p = 50$ eV) and for better resolved ($E_p = 20$ eV) scans. As determined in the lit-

	E_p (eV)	Slit width (mm)	Scan range (eV)	Calculated analyser ΔE from supplier (eV)	Step size (eV)	Dwell time (s)
XPS broad scan	50	6	$\sim 1 - 1300$	1.5	0.5	0.2
XPS narrow scan	20	6	~ 20	0.6	0.05	0.5

Table 2.2: Typical scan parameters and resolution used along this work.

erature [54], the transmission function of our analyser is close to the theoretical one for an hemispherical analyser *i.e.* $T \sim E_p/E_K$. This value was used for all our data analysis.

In our case, the detectors are multiple-channel detectors that are placed across the exit plane of the analyser. The amplification factor is 10^8. The small current pulse present at the output of the channeltrons (5 on our EA 125) is filtered and passed into the preamplifier unit. Then it is transmitted to a pulse counter for processing and an electron energy spectrum is produced.

2.5.3 Data interpretation

A typical spectrum of X-ray photoemission is made of sharp peaks corresponding to the core levels and broader lines due to the Auger transitions overlapped with a continuous background of secondary electrons due inelastic processes and Bremsstrahlung emission in a non-monochromatic source [47, 50, 51]. The binding energies of core levels are sensitive to the chemical state and to the environment of the emitting atoms. Fig. 2.10 shows a wide photoemission scan of the clean and oxidised $Fe_{0.85}Al_{0.15}$ surface for a Al-Kα excitation [5] with all the peaks labelled. Our work focused mainly on C 1s ($E_B \simeq 285$ eV), Al 2p ($E_B \simeq 73$ eV), Fe 3p ($E_B \simeq 53$ eV) and O 1s ($E_B \simeq 531$ eV) for the quantification of segregation and chemical state analysis. To characterise iron, Fe 3p was preferred over Fe 2p despite its lower ionization cross section to minimise differences of analyser transmission function compared to Al and to maximise escape depth.

[5] This source was systematically used during this work.

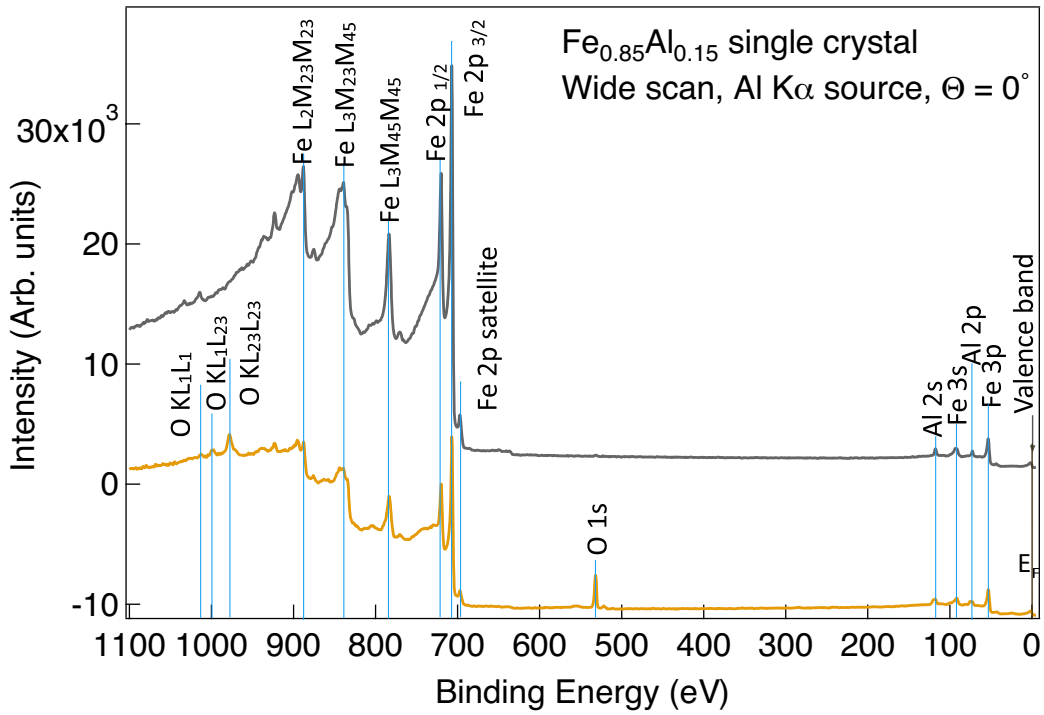

Figure 2.10: Al-Kα wide scan of a clean and oxidised $Fe_{0.85}Al_{0.15}$ where the main photoemission core levels and Auger transitions are pointed. Notice the increase of background at low kinetic energy due to inelastic electrons.

2.5.3.1 Core level characteristics in a photoemission spectrum: lineshape and data fitting

Core level lines are either singlets or doublets in case of spin-orbit splitting. A vacancy created by photoionisation couples with an unpaired electron in the originally incompletely filled shell and generates a splitting of the orbital (case of p, d, f orbitals). The coupling in the final state between the spin angular momentum **s** and the non zero orbital angular momentum **l** is described by a new total electronic angular momentum $\mathbf{j} = \mathbf{s} + \mathbf{l}$. For example, for Fe 3p orbital, the allowed values are $j = 1/2; 3/2$ giving rise to two photoelectron lines labelled Fe $3p_{3/2}$ and Fe $3p_{1/2}$. For different orbitals, the relative peak intensity is related to the degeneracy of the final state; it is given by $[2(l - \frac{1}{2}) + 1]/[2(l + \frac{1}{2}) + 1]$ and summarised in Tab 2.3. Of course, no splitting is expected for a s level ($l = 0$). In our data fitting, theoretical ratio between the two components of a doublet was kept constant.

Core level	2p	3d	5f
j	$\frac{1}{2}$: $\frac{3}{2}$	$\frac{3}{2}$: $\frac{5}{2}$	$\frac{5}{2}$: $\frac{7}{2}$
Intensity Ratio	1:2	2:3	3:4

Table 2.3: Relative peak intensity of doublets due to spin-orbit splitting in photoemission.

Core level lineshape maybe complex due to the combination of several physical and instrumental effects [46, 47]:

- X-ray excitation profile,
- broadening of the core level hole state due to its finite lifetime and thermal effect,
- surface potential inhomogeneities, surface charging of the sample, band bending in case of non-metallic sample,
- response function of the electron energy analyser.

If the X-ray source emission and the finite lifetime broadening are inherently Lorentzian, peak shapes are generally mixed with an additional Gaussian broadening, mainly due to the instrument. This latter is accounted for through a Voigt function *i.e.* a convolution of Gaussian $G(E)$ and Lorentzian $L(E)$ functions:

$$V(E) = \mathcal{A} \int_{-\infty}^{+\infty} L(E')G(E - E')dE', \tag{2.15}$$

where:

$$G(E) = \sqrt{\frac{\ln 2}{\pi}} \frac{1}{\gamma_G} \exp\left[-\frac{E^2 \cdot \ln 2}{\gamma_G^2}\right], \tag{2.16}$$

$$L(E) = \frac{1}{\pi\omega_L} \frac{\gamma_L}{((E - E_0)^2 + \gamma_L)}. \tag{2.17}$$

$2\gamma_G$ and $2\gamma_L$ are full widths at half maximum (FWHMs) of the Gaussian and Lorentzian components, E_0 the peak position and $\mathcal{A}$ the peak area.

But the profile may be greatly influenced by many-body phenomena such as electron-hole pair excitations near the Fermi level and plasmon excitations of the cloud of valence electrons. For solids with a large DOS at the Fermi level like metals, these excitation processes lead to a skewed peak shape toward higher binding energies [46, 47]. For energies of only a few electron-volts from the peak energy, where the valence band density of states may be considered roughly constant, the combined effect of these electron-hole pair excitations and the lifetime broadening is described by a formula derived by Doniach and Sunjic [55]:

$$DS(E, \alpha) = \mathcal{A}\gamma_{ds} \frac{\cos\left[\pi\frac{\alpha}{2} + (1 - \alpha)\arctan\left(\frac{E-E_0}{\gamma_{ds}}\right)\right]}{[(E - E_0)^2 + \gamma_{ds}^2]^{\frac{1-\alpha}{\gamma_{ds}}}}. \tag{2.18}$$

α is an asymmetry parameter and γ_{ds} is related to the peak FWHM. $\alpha = 0$ corresponds to the Lorentzian shape. Of course, $DS(E, \alpha)$ should be convoluted with a Gaussian to account for instrumental broadening.

Another important feature of the spectra is the background due to inelastic electrons, which subtraction is crucial for data interpretation. The often used Shirley background assumes a background proportional to the integral up to a given kinetic energy of the actual signal; it naturally accounts for the increase in the overall measured background that happens for each subsequent core level [56]. Beside this continuous background, other satellite

peaks may be present due to the losses suffered by the outgoing electrons, such as quantified plasmon losses and shake-up/shake-off satellites due to the interaction with valence electrons.

During this thesis, photoemission spectra were fitted using the XPSMania macro package for Igor Pro created by F. Bruno. Peaks were fitted through Levenberg-Marquadt χ^2 minimization with Voigt profiles and with Doniach-Sunjic shape for metallic component. The background was of Shirley's type.

2.5.3.2 Quantification and intensity analysis

Through modelling of intensities, photoemission can provide a quantification of coverage, atomic density or film thickness [46, 47, 50, 51]. For a thin layer of thickness dz buried at a depth z in a semi-infinite substrate, the photoelectron intensity I at kinetic energy E_K is given by:

$$I \sim FAD\Omega T(E_K)\sigma(E_K)\exp\left[-z/\lambda(E_K)\cos\Theta\right]n(z)dz, \tag{2.19}$$

where:

- F is the average flux of X-rays on the sample,
- A is the sample area illuminated by X-rays viewed by the analyser,
- D is the detector efficiency,
- Ω is the acceptance solid angle of the analyser,
- $T(E_K)$ is the analyser transmission function which is close to the inverse of the kinetic energy for a perfect hemispherical analyser [54],
- $\sigma(E_K)$ is the photo-ionisation cross-section of the corresponding core level,
- $\lambda(E_K)\cos\Theta$ is the electron escape depth which depends on the collection angle Θ and the Inelastic Mean Free Path (IMFP) $\lambda(E_K)$ for photoelectrons in the sample; it comes into play through an exponential damping of Beer-Lambert type;
- $n(z)$ is the atomic density of the probed element.

Depending on the material characteristics, the value $\lambda(E_K)$ were obtained herein from the TPP-2M predictive formula of Tanuma, Powell and Penn [57–65] as implemented in the QUASES-IMFP-TPP2M software [66].

While absolute intensity determination through reference sample is difficult, quantification can still be achieved by simply looking at the ratio of peak areas acquired during a given run since the ionization cross section, IMFP and transmission function are known quantities and the remaining ones F, A, D, Ω can be assumed to be constant as poorly dependent on the kinetic energy. The ratio $I/T(E_K)\sigma(E_K)$, called the corrected intensity, contains information related to the profile of concentration of the probed atom. The strategy of analysis depends on the sample geometry (see Fig. 5.3 for examples) and the question at hand implies the

z-integration of the above equation while accounting for any damping by overlayers. Two classical cases are tackled hereafter: the homogeneous mixture and the thin film on top of a bulk.

2.5.3.2.1 Bulk alloy If an element A is homogeneously mixed with an element B in a solid solution $A_{1-x}B_x$ (Fig. 5.3-a), the atomic concentration of the two elements are given by $n_A \sim 1-x$ and $n_B \sim x$. Therefore, the atomic ratio x can be determined from the measured intensities I_A, I_B of given core levels of the elements A and B by directly integrating Eq. 2.19:

$$\frac{I_B}{I_A}\frac{T_A\sigma_A}{T_B\sigma_B} = \frac{x}{1-x}\frac{\lambda_B^{AB}}{\lambda_A^{AB}}, \tag{2.20}$$

where T_i $(i = A, B)$ is the analyser transmission function at the corresponding electron kinetic energy, σ_i the photo-ionization cross section of the core level under consideration and λ_i^{AB} the inelastic mean free path of the photoelectrons from atom i in $A_{1-x}B_x$. The formula is independent of the collection angle Θ.

2.5.3.2.2 Thin film on a substrate For a thin film of thickness t of material B (density n_B) on top of a semi-infinite substrate A (density n_A) (Fig. 5.3-a), the signals can be derived by integrating Eq. 2.19:

$$\begin{aligned}
\frac{I_A}{T_A\sigma_A} &\sim n_A \int_{-\infty}^{0} \exp\left(z/\lambda_A^A \cos\Theta\right) dz \times \exp\left(-t/\lambda_A^B \cos\Theta\right) = n_A\lambda_A^A \cos\Theta \exp\left(-t/\lambda_A^B \cos\Theta\right) \\
\frac{I_B}{T_B\sigma_B} &\sim n_B \int_{-t}^{0} \exp\left(z/\lambda_B^B \cos\Theta\right) dz = n_B\lambda_B^B \cos\Theta \left[1 - \exp\left(-t/\lambda_B^B \cos\Theta\right)\right].
\end{aligned} \tag{2.21}$$

λ_i^j $(i, j = A, B)$ corresponds to the inelastic mean free path of core level i in material j. Notice that a further damping $\exp\left(-t/\lambda_A^B \cos\Theta\right)$ of the substrate signal in the film has been added in the previous equation. The other parameters have the above defined meanings. The ratio I_B/I_A of intensity yields a transcendental equation that can be solved easily by dichotomy to obtain (d, n_B) from the knowledge of n_A. Measurements at several collection angles allow to further constrain the modelling and check the validity of the underlying model.

2.6 Grazing Incidence X-Ray Diffraction

Grazing Incidence X-Ray Diffraction (GIXD), also known as Surface X-ray Diffraction (SXRD), was used to study the crystallography of the reconstruction and of the oxide layer on the $Fe_{0.85}Al_{0.15}(110)$ surface.

2.6.1 Principle

The principle of GIXD (Fig. 2.11) [67–71] is to shine a well collimated X-ray beam of wavelength λ of the order of the Angstrom at grazing incidence α_i and to collect scattered/diffracted beams along the two directions, in-plane $(2\theta_f)$ and out-of-plane (α_f), leading

to a wave vector transfer:

$$\begin{aligned} q_x &= k_0[\cos(\alpha_f)\cos(2\theta_f) - \cos(\alpha_i)] \\ q_y &= k_0[\cos(\alpha_f)\sin(2\theta_f)] \\ q_z &= k_0[\sin(\alpha_f) + \sin(\alpha_i)] \\ k_0 &= 2\pi/\lambda. \end{aligned} \tag{2.22}$$

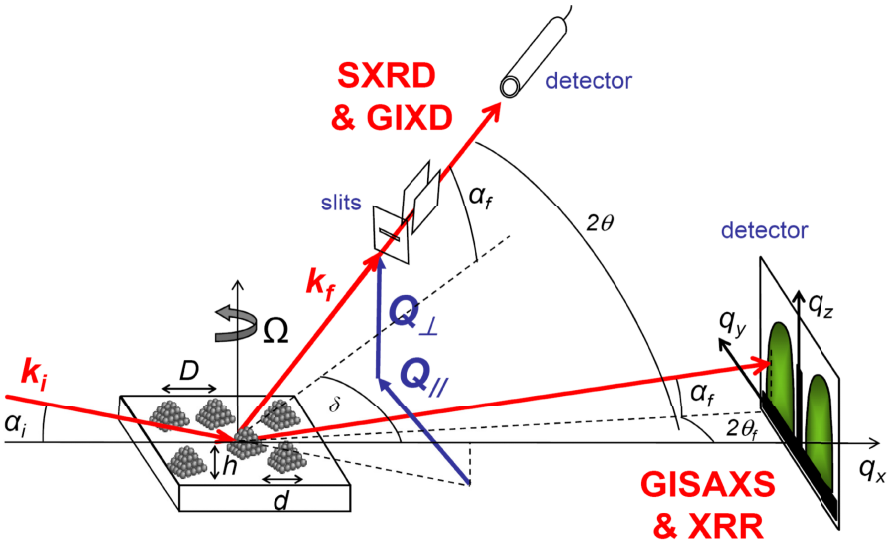

Figure 2.11: Grazing incidence X-ray scattering geometry [71]. The incident beam of wave vector $\mathbf{k_i}$ makes a small incident angle α_i with respect to the sample surface. The intensity is recorded at wide angles as a function of the angles $2\theta_f$ and α_f describing the in-plane and out-of plane angles between the incident $\mathbf{k_i}$ and scattered $\mathbf{k_f}$ wave vectors, respectively. The sample can be rotated by an angle ω around its surface normal. 2θ is the usual total scattering angle. SXRD and GIXD correspond to large values of the scattering angles. The direction of the exit wave vector $\mathbf{k_f}$ is defined by slits, parallel and perpendicular to the surface, behind which lies the detector, which can be punctual or linear, or even two-dimensional. Looking close to the origin of reciprocal space allows probing nanometre length structures with Grazing Incidence Small-Angle X-Ray Scattering (GISAXS) or XRR (X-Ray Reflectivity).

By scanning at fixed incidence, the position of the detector along $(2\theta_f, \alpha_f)$, it is possible to explore the reciprocal space of the sample. GIXD exploits the phenomenon of total external reflection of hard X-rays to reduce the penetration depth and to enhance the contribution of the surface compared to the bulk. Indeed, the index of refraction of matter in the hard X-rays regime $n = 1 - \delta + i\beta$ is slightly lower than one ($\delta \sim 10^{-5}$) leading to total external reflection below the critical angle $\alpha_c = \sqrt{2\delta}$ ($\alpha_c \sim 0.1 - 0.3°$). Fresnel calculations show that the total reflection (Fig. 2.6.1-a) observed for $\alpha_i < \alpha_c$ parallels a drastic reduction of the penetration depth Λ (Fig. 2.6.1-c) up to a value $\Lambda_c = 1/2k_0\alpha_c$ and an enhancement of transmission coefficient (Fig. 2.6.1-b) due to the propagation of an evanescent wave parallel to the surface. Typically Λ_c is in the range of the nanometre. Due to the time reversal principle, the same phenomenon holds true for the out-going diffracted beam *i.e* for α_f. In a GIXD experiments, one can probe:

- the intensity of the Crystal Truncation Rods (CTRs) which originate from the spreading of the signal in between bulk Bragg peaks due to the existence of a surface; their quantitative analysis and that of in-plane structure factors allows to determine atomic positions (relaxation, rumpling etc.. . .); this requires a precise integration of intensity;
- the presence of reconstruction which appear as extra-CTRs in between those of the substrate; they have a q_z extension much larger as they originate from a finite small thickness;
- the epitaxy and eventually the atomic structure of thin films or nanoparticles.

Usually, like in LEED, a point of the reciprocal space $\mathbf{q}$ is defined by its coordinates (h_S, k_S, l_S) in the $(\mathbf{a}_S^*, \mathbf{b}_S^*, \mathbf{c}_S^*)$ basis which first two components are linked to the surface unit cell $(\mathbf{a}_S, \mathbf{b}_S)$ of the substrate while the third component is along the surface normal $\mathbf{c}_S$.

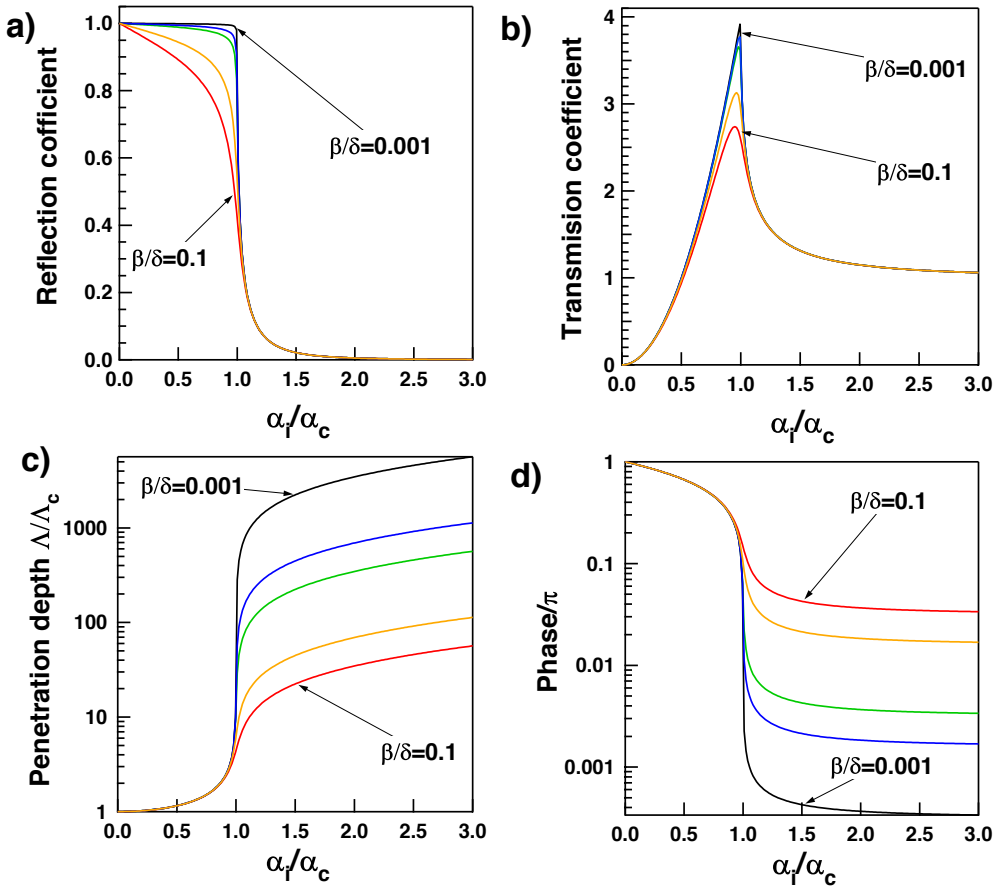

Figure 2.12: Fresnel quantities as function of the incident angle α_i normalised by the critical angle of the substrate $\alpha_c = \sqrt{2\delta}$ for absorption β/δ=0.001, 0.005, 0.01, 0.05, 0.1: a) the reflection coefficient $R = |r|^2$, b) the transmission coefficient $T = |t|^2$, c) the penetration depth Λ normalised to $\Lambda_c = 1/2k_0\alpha_c$, d) the phase shift at reflection. From Ref. [71].

2.6.2 Experimental set-up

The low amount of diffracting matter favors the use of a brilliant and collimated beam coming from a synchrotron source [67–71]. GIXD experiments have been performed at the European Synchrotron Radiation Facility (ESRF, Grenoble) on the INS (In situ Nanostructure and Surface) surface diffraction end-station of the bending magnet french beamline (BM32) [72]. The

X-ray optics includes mainly one mirror and a double Si crystal monochromator. The X-ray energy was set at $E = 18$ keV ($\lambda = 0.6888$ Å) (i) to avoid absorption and fluorescence by the substrate and the film,(ii) to have the highest accessible range of reciprocal space and (iii) to match the maximum of intensity of the bending magnet. The incidence $\alpha_i = 0.14°$ was fixed just below the critical angle of $Fe_{0.85}Al_{0.15}$ for total external reflection at the corresponding energy ($\alpha_c = 0.173°$ [73]) to minimise bulk signal. The X-ray beam was sagittally focused on the sample with horizontal ($H = 0.4$ mm) and vertical ($V = 0.3$ mm) sizes (Full Width at Half Maximum, FWHM), corresponding to divergences of $\delta_H = 1$ mrad and $\delta_V = 0.13$ mrad, respectively.

In the INS set-up, the sample (Fig. 2.6.2) is mounted vertically on the head of a six-circles diffractometer of "z-axis type" which holds the UHV-chamber (base pressure $1 \cdot 10^{-10}$ mbar) and allows for a precise positioning of the incoming beam α_i and of the outgoing in-plane ($2\theta_f$) and out-of-plane (α_f) scattered beam angles. The X-ray beam enters and exits the chamber through a large 0.5 mm thick X-ray transparent beryllium window; several slits in particular in vacuum reduces the background scattering. The alignment of the rotation axis ω of the sample normal is set by an hexapod (cradle-like settings) and rotation movement is transmitted through differential pumping. The detector arm which moves along $(\alpha_f, 2\theta_f)$ holds a 2D MaxiPix detector (1280×256 pixels) with pixel size of 55 μm which is put at a distance of 700 mm behind a vertical slit of 5 mm. It allows to measure directly portion of reciprocal space. Integration of signal along Region of Interests on the detector gives rise to a vertical resolution of 0.08° for in-plane scan. The UHV chamber is equipped with several surface science facilities such as ion gun for sample cleaning, Auger spectrometer and a reflection high-energy electron diffraction set-up for a rapid analysis of reciprocal space. Samples can be annealed by electron bombardment of the molybdenum holder; the temperature is estimated by pyrometry. The clean $Fe_{0.85}Al_{0.15}(110)$ surface and the oxide layers were prepared *in situ* following the same recipes as those used in the laboratory.

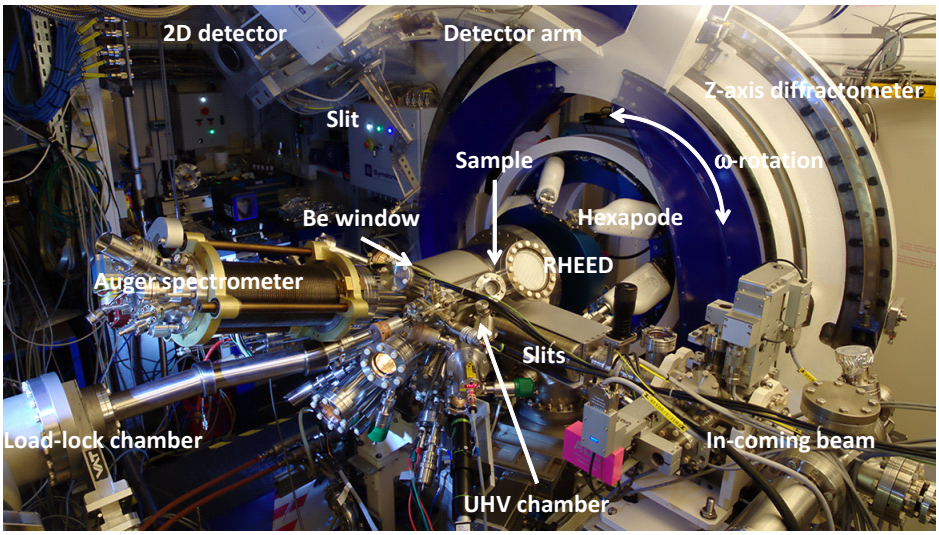

Figure 2.13: Picture of the z-axis diffractometer INS of the BM32 beamline. The main components are indicated in the figure.

CHAPTER 3

STATE OF THE ART OF ALUMINIUM METALLIC ALLOYS AND THEIR OXIDATION

This thesis focusses on the segregation and the oxidation behaviour of the low index orientations of $Fe_{0.85}Al_{0.15}$ single crystals. This chapter aims at acquainting the reader to the existing literature.

3.1 Bulk order in $Fe_{1-x}Al_x$ alloys

Like other transition metal aluminides (such as NiAl), Fe-Al alloys have been recognised as potential candidates for a variety of high temperature structural applications (e.g. turbine blades in aircraft) due to their excellent oxidation and corrosion resistances as well as specific mechanical properties [11]. The versatility of alloys stems primarily from the ability to manipulate their exact chemical composition giving profound control over their chemical and physical properties. Alloying elements may affect localised regions of strong compositional inhomogeneity, such as microstructural features (e.g. the distribution and interaction of dislocations, the cohesion of grain boundaries, or the formation and distribution of small-scale precipitates), which determine the mechanical behaviour of a material. Also, this concerns the region which mediates any interaction of a material with its environment, *i.e.* its surface.

The bulk phase diagram of $Fe_{1-x}Al_x$ alloy (x is the atomic percentage) brings out the formation of several compounds or solid solutions with different structures. In the simplified diagram of Fig. 3.1, several stable phases [74–77] appear as function of aluminium content x and temperature:

- a liquid phase at high temperature,
- the γ-Fe cubic face centred (fcc) characterized by a γ-loop at low Al content (1-2%),

- the A_2 phase which is a body centred cubic (bcc) solid solution, also called random alloy in which long-range order (LRO) is absent but short-range order (SRO) is possible under certain conditions,
- the B_2 phase, a long-range ordered bcc solid solution with CsCl structure,
- five common stable compounds, namely the Heussler $D0_3$ phase (of BiF_3 type, bcc with LRO), ϵ (uncertain phase), $FeAl_2$, Fe_2Al_5, $FeAl_3$ respectively (see Ref. [77] for the complex Al-rich part of the phase diagram).

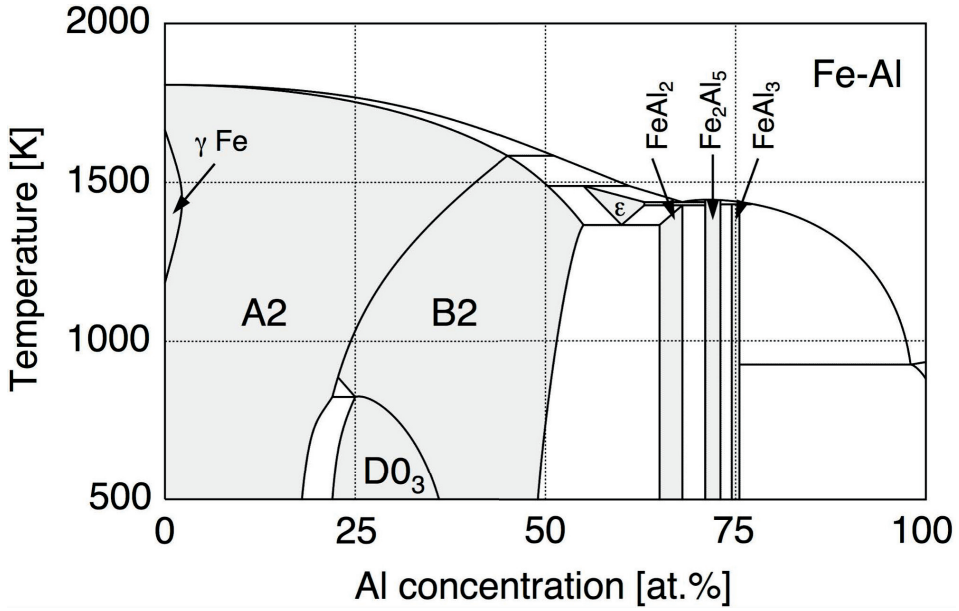

Figure 3.1: Fe-Al binary phase diagram where the most important compounds (shaded area) are labelled with their Strukturbericht symbol [74, 78–80] and/or their formula.

The ball models of the most relevant cubic structure with $0 \leq x \leq 0.5$, namely A_2, B_2 and $D0_3$ are shown in Fig. 3.2 and their space groups and lattice parameters are given in Tab. 3.1. At the peculiar concentration used in this study $Fe_{0.85}Al_{0.15}$, the alloy is in the random A_2 structure up to its melting point; in other words, no bulk structural transition is expected up ~ 1700 K which allows safe high temperature annealings. The B_2 phase exists in wide range of composition $0.23 \leq x \leq 0.55$ depending on temperature; at room temperature, it extends from $x = 0.4$ to $x = 0.48$. In the range $0.2 \leq x \leq 0.35$, Fe-Al system adopts a LRO $D0_3$ structure which is derived at $Fe_{0.75}Al_{0.15}$ composition from B_2-CsCl by replacing half of the Al atoms by Fe. The evolution of the cubic lattice parameter a_B with x [25] was shown to follow a Vegard's law of random alloy from 2.86 Å to 2.90 Å at $x = 0 - 0.2$ before being nearly constant up to $x = 0.5$ in the B_2 phase. At the composition studied herein, $a_B = 2.8914$ Å. This evolution of parameter is marginal (1.4 %) leading to reduced problem of lattice mismatch; this also holds for the bcc sublaticce of the $D0_3$ structure.

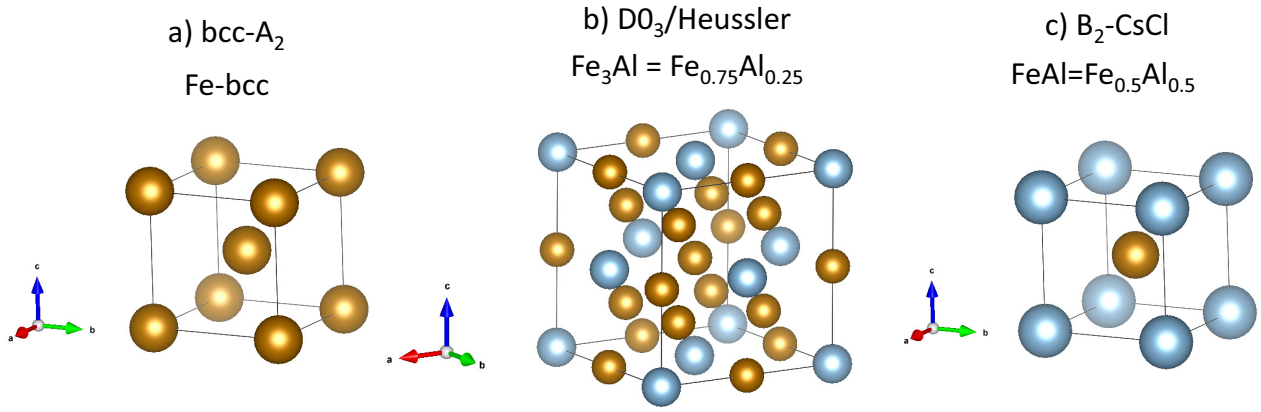

Figure 3.2: Ball models of the main atomic structure of iron rich $Fe_{1-x}Al_x$ intermetallics. Fe atoms are in brown and Al atoms in light blue.

Composition	Fe	$Fe_{0.85}Al_{0.15}$	$Fe_{0.75}Al_{0.25}$ (Fe_3Al)	$Fe_{0.5}Al_{0.5}$ (FeAl)
Structure type	bcc	bcc	$D0_3$	CsCl
Space group	$I(m\bar{3}m)$	$I(m\bar{3}m)$	$F(m\bar{3}m)$	$P(m\bar{3}m)$
Lattice parameter (Å)	2.8665	2.8914	5.80	2.90

Table 3.1: Atomic structure of the iron rich $Fe_{1-x}Al_x$ intermetallics. Lattice parameters are from Ref. [25].

Obviously, owing to the large domain of existence in x, each ordered lattice is able to incorporate excess atoms while retaining its positional translation symmetry through randomly distributed defects. The simplest ones are (i) antisites defects *i.e.* excess of A on B sublattice or vice-versa and (ii) vacancies. Antisites are much more energetically favorable for the FeAl B_2 structure on both side of the composition domain, Al-rich and Al-poor [81, 82]; there is nearly no vacancies. The formation enthalpy of Fe-Al alloys is quite high (0.26 eV per unit cell in $Fe_{0.50}Al_{0.50}$) [79, 83] demonstrating a favourable mixing trend.

Beyond composition, the degree and assumed type of order in Fe-Al alloys is temperature dependent. Two order-disorder transitions appear $D0_3 \leftrightarrow B_2$, $B_2 \leftrightarrow A_2$. The condition for the existence of a complete disordered solid solution is quite demanding (such as high temperature close to melting point); thus a degree of SRO always exist in A_2 $Fe_{1-x}Al_x$ through a correlation between each lattice site and its immediate surrounding, not only to first nearest neighbours but also to second ones [32]. In diffraction, SRO appears through diffuse scattering that has been analysed by neutron scattering in the case of $Fe_{0.8}Al_{0.2}$ to extract effective pair interactions [75]. It turned out that second neighbour contributions are sizeable compared to first neighbour ones; Al atoms have a trend to be surrounded by Fe as first neighbours and a strong preference for Al as second neighbours at low temperature [75, 79]. This trend appears obviously through the existence of B_2 and $D0_3$ structures in the phase diagram. The increasing presence of antisites seems to shift the order-disorder B_2-A_2 transition from close

to the melting temperature at $x = 0.5$ down to 750 K.

3.2 Crystallography of $Fe_{1-x}Al_x$ low index surfaces

For a better understanding of the following chapters, it is worth introducing the bulk truncation along the low index surfaces of the main crystal structures found in the bulk phase diagram of $Fe_{1-x}Al_x$ in the range $x = 0 - 0.5$, namely A_2, B_2 and $D0_3$. As this work deals with a surface science analysis, an emphasis will be put on their surface unit cell. As usual, the surface unit cells $(\mathbf{a}_S, \mathbf{b}_S, \mathbf{c}_S)$ for which $\mathbf{c}_S$ is normal to the considered face is used to describe the crystallography of a given truncation. Later on, in diffraction analysis, the reciprocal space will be defined in the surface unit cell with the corresponding (h_S, k_S, l_S) indexes. Hereafter, the B and S subscript will stand for bulk and surface related quantities.

3.2.1 Cubic centred A_2 random alloy

Figs. 3.3, 3.4, 3.5 show the bulk truncation along (100), (110) and (111) orientations of a cubic centred A_2 random alloy. As reminder, the bulk unit cell parameter of $Fe_{0.85}Al_{0.15}$ is $a_B = 2.8914$ Å [25]. The surface lattice vectors (Figs. 3.3, 3.4, 3.5-a) are defined from the bulk ones $(\mathbf{a}_B, \mathbf{b}_B, \mathbf{c}_B)$ as:

- (100): $\mathbf{a}_S = \mathbf{a}_B$, $\mathbf{b}_S = \mathbf{b}_B$, $\mathbf{c}_S = \mathbf{c}_B$;
- (110): $\mathbf{a}_S = -\mathbf{a}_B + \mathbf{b}_B$, $\mathbf{b}_S = \mathbf{c}_B$, $\mathbf{c}_S = \mathbf{a}_B + \mathbf{b}_B$ ($a_S = \sqrt{2}a_B = 4.09$ Å and $b_S = a_B = 2.89$ Å); the selected surface unit cell is centred but a primitive one, rotated by 45° can also be defined by $\mathbf{a}_{S,P} = (\mathbf{a}_S + \mathbf{b}_S)/2$ and $\mathbf{b}_{S,P} = (-\mathbf{a}_S + \mathbf{b}_S)/2$; both will be used later on;
- (111): $\mathbf{a}_S = (-4\mathbf{a}_B + 2\mathbf{b}_B + 2\mathbf{c}_B)/3$, $\mathbf{b}_S = (2\mathbf{a}_B - 4\mathbf{b}_B + 2\mathbf{c}_B)/3$, $\mathbf{c}_S = (\mathbf{a}_B + \mathbf{b}_B + \mathbf{c}_B)/2$ ($a_S = b_S = 2\sqrt{2}a_B/\sqrt{3} = 4.72$ Å)

While all atoms are coplanar on (100) and (110) faces (see Figs. 3.3, 3.4), the (111) surface of body centred compound is opened and atomically rough; it includes three atomic planes (Fig. 3.5-b) defining a physical monolayer. The distance between atomic planes giving the monoatomic steps (see Figs. 3.3, 3.4, 3.5-c) is $a_B/2 = 1.45$ Å, $a_B/\sqrt{2} = 2.04$ Å, $a_B/2\sqrt{3} = 0.83$ Å for $(100), (110), (111)$ faces, respectively. The density of atoms per unit of surface is given by: $n_S = 1/a_B^2$, $n_S = \sqrt{2}/a_B^2$, $n_S = 3\sqrt{3}/4a_B^2$ for $(100), (110), (111)$ faces leading to the hierarchy $n_S(100) < n_S(111) < n_S(110)$. This coverage will be used to define the monolayer for each orientations; this corresponds to 1.20×10^{15} atm·cm^{-2} on (100), 1.55×10^{15} atm·cm^{-2} on (111) and 1.69×10^{15} atm·cm^{-2} on (110).

3.2.2 CsCl B_2 ordered alloy

Compared to the A_2 cubic centred random alloy, the ordered B_2 has the same cubic structure but with one type of atom at the nodes of the cube and the other one at the centre (CsCl structure). This "centring" leads to an higher level of complexity for the low index faces as shown in Fig. 3.6:

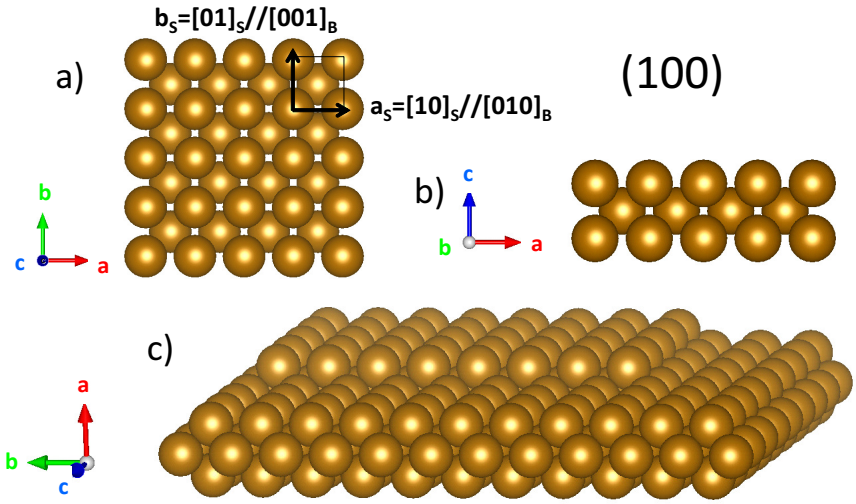

Figure 3.3: Ball model of the (100) face of cubic centred A_2 $Fe_{1-x}Al_x$ random alloy. The brown balls stand for the average atom and the bulk cubic unit cell vector $(\mathbf{a}_B, \mathbf{b}_B, \mathbf{c}_B)$ are shown with coloured arrows. a) Top view along the $[001]_B$ direction with the surface unit cell indicated by bold arrows. b) Side view along $[010]_B$. c) View in perspective showing a monoatomic terrace with steps along the surface unit cell directions.

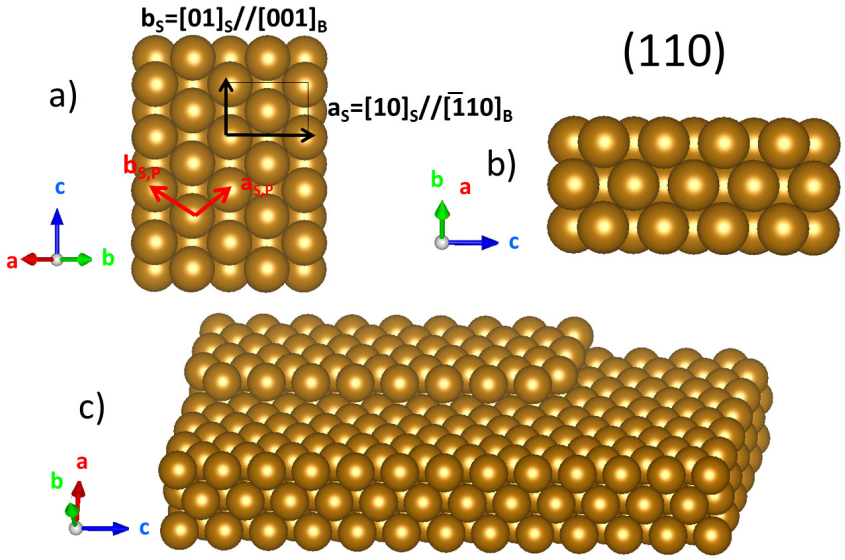

Figure 3.4: Same as Fig. 3.3 but for the (110) orientation. a) Top view along $[110]_B$. The primitive unit cell is shown by red arows. b) Side view along $[1\bar{1}0]_B$. c) View in perspective with a monoatomic step.

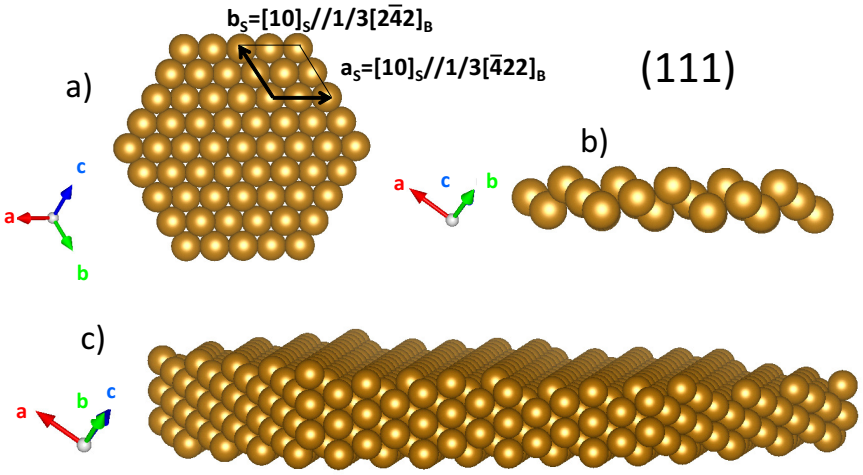

Figure 3.5: Same as Fig. 3.3 but for the (111) orientation. a) Top view along $[111]_B$. b) Side view along $[01\bar{1}]_B$. c) View in perspective with a three consecutive monoatomic steps.

- (100): the bulk truncation (100) face is either terminated by a pure Al or Fe atoms with coplanar atoms; Al and Fe planes alternate along the $[100]_B$ direction;
- (110): the (110) face is mixed with 50 % of Al and 50 % of Fe with coplanar atoms;
- (111): like for A_2 structure, the (111) is terminated by three planes alternatively made out of Fe and Al; therefore the last plane is 100 % Fe or Al and they alternate along the $[111]_B$ direction; the surface unit cell is larger than for A_2-(110).

3.2.3 $D0_3$ Heussler Fe_3Al phase

The bulk truncation of the $D0_3$ Heussler Fe_3Al ($Fe_{0.75}Al_{0.25}$) is even more complex than the A_2 structure (see Fig. 3.7):

- (100): the (100) bulk termination is made out of either a mixed 50 %-50 % Fe-Al plane or a pure Fe one. All atoms are coplanar. The last plane can be seen as a $c(2 \times 2)$ superstructrure of the bcc(100) surface.
- (110): (110) planes are mixed with exactly the bulk composition 75 % Fe - 25 % Al.
- (111): along the $[111]_B$ direction , pure Al or Fe planes alternate with the same density following the sequence Al-Fe-Fe-Fe.

3.3 The surfaces of the $Fe_{1-x}Al_x$ alloy

The surface structures presented above (Sect. 3.2) are only truncations of the bulk infinite crystal. Breaking bonds to create a surface along a given crystallographic direction and reducing locally the coordination of atoms leads to atomic rearrangements such as [31, 84]:

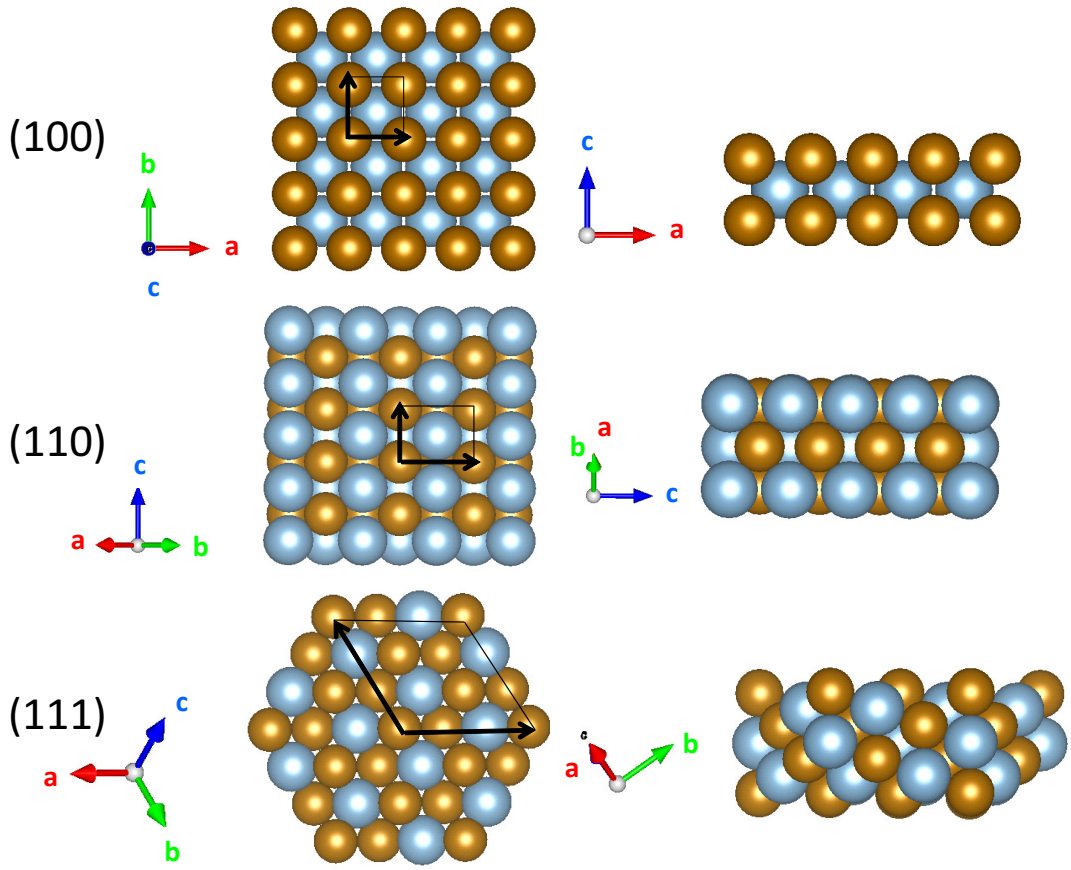

Figure 3.6: Low index (100), (110) and (111) surfaces of FeAl in CsCl B_2 ordered alloy structure. The brown and blue balls stand for Fe and Al atoms, respectively and the bulk cubic unit cell vector $(\mathbf{a}_B, \mathbf{b}_B, \mathbf{c}_B)$ are shown with coloured arrows. Left column corresponds to top views along the $[100]_B, [110]_B, [111]_B$ while the right column shows a side view. The surface unit cell is indicated by black arrow.

- normal relaxations: the interlayer spacings of top layers change but preserve the same lateral symmetry; in metals, it is usually inward for the first layer and followed by an damped oscillatory behaviour at deeper layers;
- surface reconstruction: a geometrical in-plane reordering induces a symmetry-breaking compared to bulk truncation (see Sect. 2.3).

Surface segregation is one of the driving forces of reconstructions on both ordered and disordered metallic alloys [85–87]. It consists in an enrichment with a given constituent through diffusion in the vicinity of a surface. For instance, $Fe_{1-x}Al_x$ surfaces are always enriched in Al. For ordered alloys, such an effect can produce new ordered phases or some disordered antisite phase with respect to the bulk. Regarding random alloys with substitutional disorder, a variable concentration of enriched element can be found in near-surface layers (the so-called segregation profile which may be oscillatory) before converging towards the bulk concentration as depth increases [31]. If the interplay between segregation, LRO, SRO and crystal

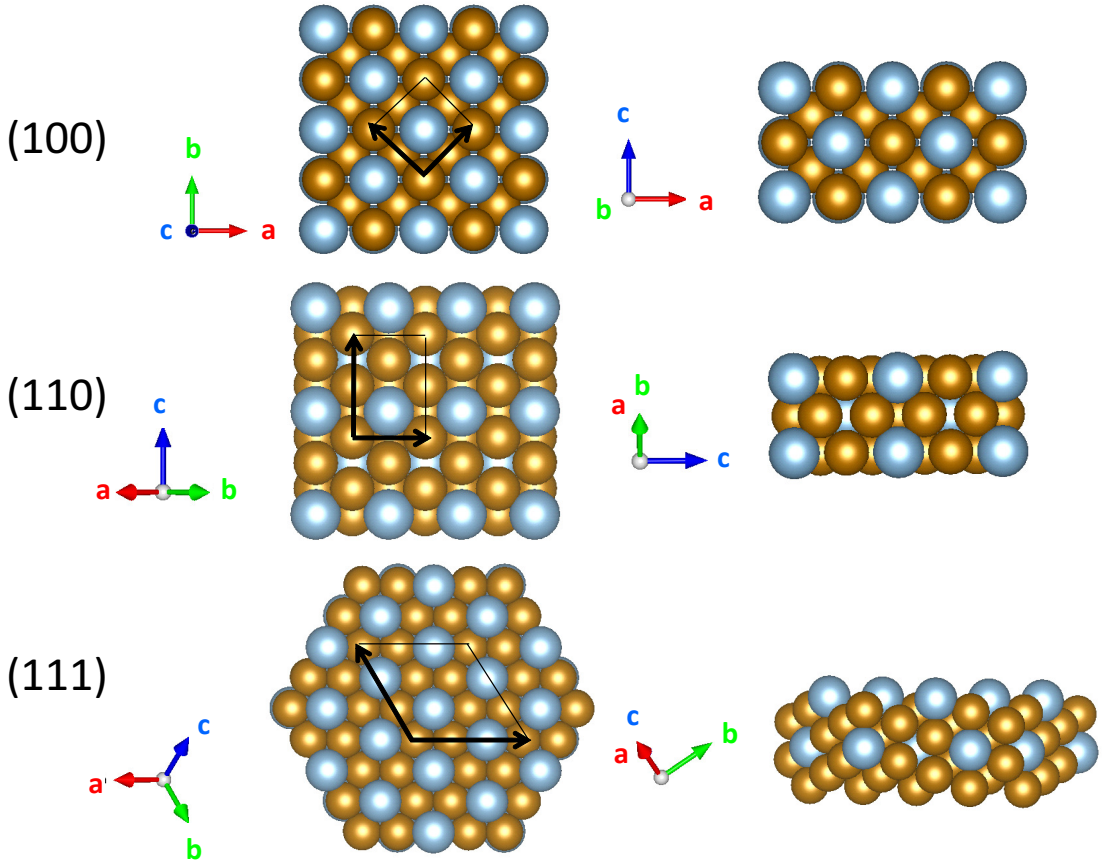

Figure 3.7: Same as Fig. 3.6 but for low index surface of Heussler $D0_3$ ordered alloy.

structure can be quite complex (see review Ref. [85–87]), the commonly accepted driving forces of surface segregation are:

- a reduction of the surface free energy; in this respect, surface energies of pure phases can serve as a guideline: that of Al surface is much lower than that of Fe for all orientations [88–90] (see Tab. 3.2);
- a reduction of surface stress due to different atomic sizes between the solvent and solute;
- a decrease of the elemental heat of vaporisation which reflects in the broken bond model the bond strength of the element under consideration;
- the reaction of one of the alloying element with an adsorbate, among which for instance oxygen; one speaks about induced preferential segregation;
- preferential sputtering may induce an artificial enrichment in one of the elements; ion bombardment is a mandatory step in the preparation of a clean surface; some authors [28, 30–32, 91–94] claimed at preferential sputtering of Al (without clear proof although predicted ones are similar [27, 95]!) leading to a depletion in Al at the surface (see Sect. 5.1.2.2).

	Structure	Surface	Theory ($J.m^{-2}$)	Experiments ($J.m^{-2}$)
Al	fcc	(111)	1.199	1.143, 1.160
	(4.049 Å)	(100)	1.347	
		(110)	1.271	
Fe	bcc	(110)	2.430	2.417, 2.475
	(3.001 Å)	(100)	2.222	
		(211)	2.589	
		(310)	2.393	
		(111)	2.733	

Table 3.2: Surface energies of several orientations for Al and Fe. Calculated values with the full charge density within the full potential linear muffin-tin orbitals are from Ref. [90] while experimental values are from Ref. [88].

The last comment points at the underlying question of the actual equilibrium between bulk and (sub)surface in surface science studies [29, 34] and therefore of the history of the sample after intensive cycles of preparation. In our experiments, we checked the reproducibility of the composition of the surface after sputtering/annealing through ratio of intensities of photoemission peaks (see Sect. 5.1.2.2).

However, if the large surface energy and heat of vaporisation of transition metals compared to Al favours segregation, it can be counterbalanced by a large (absolute) heat of formation of the alloy (the larger this quantity, the less favourable the interchange of constituents). This argument explains (i) why Fe-Al alloys are more prone to Al segregation than Ni-Al or Co-Al ones [30] ($\Delta H(\mathrm{FeAl}) = -25.1$ kJ/mol, $\Delta H(\mathrm{Fe_3Al}) = -13.0$ kJ/mol, $\Delta H(\mathrm{NiAl}) = -58.9$ kJ/mol, $\Delta H(\mathrm{CoAl}) = -54.2$ kJ/mol) and (ii) why Ni-Al alloys are found nearly bulk terminated compared to Fe-Al ones (see below). Finally, ordering tendency in the alloy will hamper segregation since the latter favours the occupation of neighbouring lattice sites by the same atomic species while ordering causes exactly the opposite [87].

In Chaps. 5-6, the profile of segregation (before and after oxidation) and the reconstructions on $\mathrm{Fe_{0.85}Al_{0.15}}$(100), (110) and (111) surface will be analysed with core level photoemission and LEED. The following sections aim at introducing the state-of-the-art on $\mathrm{Fe_{1-x}Al_x}$ surfaces.

Auger spectroscopy [96] evidenced a clear trend of Al segregation in polycrystalline $\mathrm{Fe_{0.8}Al_{0.2}}$ sample with an activation energy of ~ 2 eV/atom assigned to the diffusion coefficient of Al. It was found that all the surface orientations of $\mathrm{Fe_{1-x}Al_x}$ are characterised by Al surface segregation phenomena somewhat more pronounced for the more opened surfaces although no clear trend exist at least for FeAl [30]. This is in stark contrast with NiAl for which bulk terminations are observed. The onset of the phenomenon is around 600-800 K [28–30, 32, 93, 96] and depends on bulk composition. Most of the surface science studies on single crystals have been performed by a German group [28–34, 92] from the University of Erlangen using Auger spec-

troscopy and dynamic LEED, *i.e.* variation of spot intensities with beam energy to determine atomic positions, relaxations as well as profile of concentration in the first layers. Multiple scattering effects due to the strong electron surface interactions render the quantitative LEED analysis quite complex all the more that a coupling exists in the refinement between element-dependent vibrational amplitudes and compositions. Therefore, results should be taken with caution as it was recognised by the authors themselves [33].

3.3.1 $Fe_{1-x}Al_x(100)$

The ordered B_2-$Fe_{0.53}Al_{0.47}(100)$ (a_B=2.903 Å) surface [28,30,92] is found depleted in Al after room temperature sputtering. Upon annealing at increasing temperature, Auger spectroscopy evidences an onset of Al segregation around 623 K with a fast equilibration kinetic that depends more on the annealing temperature than on the annealing time. This finding is quite general for all the studied surfaces [28–30, 32, 93, 96]. The LEED pattern (Fig. 3.8) displayed the following transitions:

$$\text{diffuse}(1\times1) \underset{623-683\ K}{\longrightarrow} c(2\times2) \underset{>683\ K}{\longrightarrow} (1\times1) \tag{3.1}$$

with a high temperature surface average composition [1] of $Fe_{0.38}Al_{0.62}$ and pure Al termination [92, 97] while the c(2 × 2) superstructure corresponds to a surface average composition of $Fe_{0.51}Al_{0.49}$ based on LEED/Auger analysis [28, 30, 34, 92] on top of a thick metastable film (at least 6 layers) of $D0_3$ Fe_3Al [92] (Fig. 3.9).

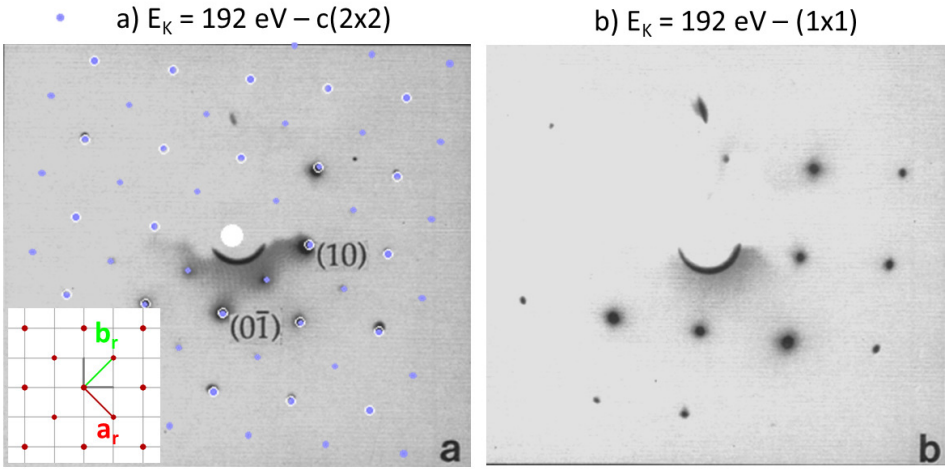

Figure 3.8: LEED patterns obtained after annealing a $Fe_{0.53}Al_{0.47}(100)$ surface: a) at low temperature (673 K) and b) at higher temperature leading to a) c(2 × 2) and b) (1 × 1) reconstruction. From Ref. [28].

Similarly, $Fe_{0.97}Al_{0.03}$, $Fe_{0.85}Al_{0.15}$ and $Fe_{0.70}Al_{0.30}(100)$ display an intermediate c(2 × 2) LEED pattern after annealing [32, 93]. The structure of $Fe_{0.85}Al_{0.15}$-c(2 × 2) seems to be

[1] Over the probing depth of Auger transitions of Al and Fe at 68 eV and 47 eV.

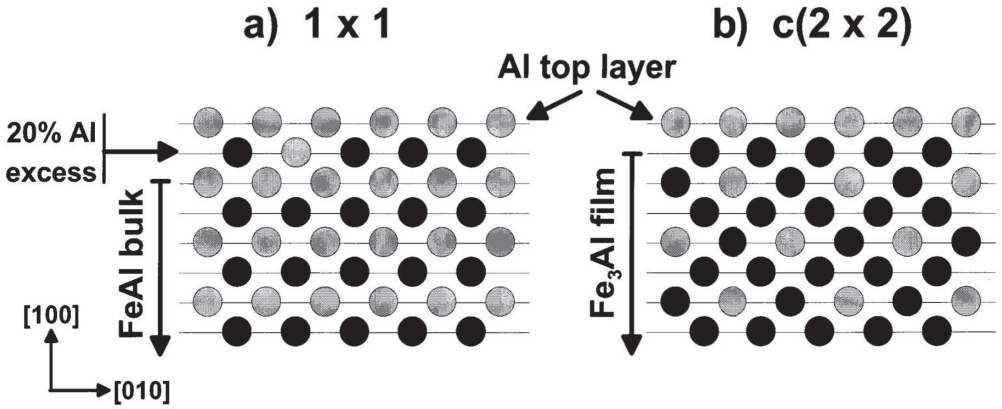

Figure 3.9: Atomic structure of the $Fe_{0.53}Al_{0.47}(100)$ surface derived from dynamic LEED with a) (1×1) and b) $c(2 \times 2)$ structures. Both are Al terminated, with 20% Al enrichment in the second layer for the (1×1) surface and with more than 6 layers of interfacial Fe_3Al ($D0_3$) film sandwiched between a complete Al layer and FeAl bulk for the $c(2 \times 2)$ surface. From Refs. [30, 31].

equivalent with that of $Fe_{0.97}Al_{0.03}$ but with a poor contrast in the LEED pattern [29, 32, 93]. The corresponding refined stacking and compositional models of $c(2 \times 2)$ surface region with top 4 layers are shown in Fig. 3.10-a. If an STM image of $Fe_{0.85}Al_{0.15}(100)$ surface annealed at $\sim$ 700 K indeed shows locally a $c(2 \times 2)$ superstructure demonstrated by the antiphase boundaries (Fig. 3.10-b [32]), no LEED determination could be obtained for this reconstruction. The $c(2 \times 2)$ structure of $Fe_{0.70}Al_{0.30}(100)$ is quite close to that observed on $Fe_{0.53}Al_{0.47}$ with a nearly full aluminium capping. It should be noted that, the same $c(2 \times 2)$ superstructure forms on Fe-Al alloys with different bulk atomic arrangements (see phase diagram Fig. 3.1), *i.e.* (i) for $x = 0.03, 0.15$ on top of a randomly occupied A_2 lattice, (labelled as $c(2 \times 2)^I$) and (ii) for $x = 0.30, 0.47$ on top of a $D0_3$ lattice ($x = 0.3$) or a thick $D0_3$ layer ($x = 0.47$) (labelled as $c(2 \times 2)^{II}$). This latter reconstruction is observed up to $\sim$ 700 K which corresponds to the phase transition from $D0_3$ to B_2. These structures have been determined mainly from dynamic LEED with some Auger/STM input for decisive pieces of information in terms of composition [28–31, 92, 93].

For the $Fe_{0.85}Al_{0.15}(100)$ surface above 1100 K, the faint $c(2 \times 2)$ phase is replaced by a (1×1) phase with an Al segregation beyond half a monolayer [32, 93]. The surface Al concentration can reach up to 75% as derived from low energy ion scattering data; the corresponding structural model although questioned later on by the same authors due to correlations in LEED analysis [33] is shown in Fig. 3.11 as well as the corresponding STM image. On all (100) terminated surfaces [32], the oscillatory behaviour of the composition was assigned to the favourable nearest neighbour interactions.

To sum up, a compositional schematic diagram of the equilibrium phases of above-mentioned $Fe_{1-x}Al_x(100)$ surface regions after annealing at high temperatures is shown in Fig. 3.12 [29]

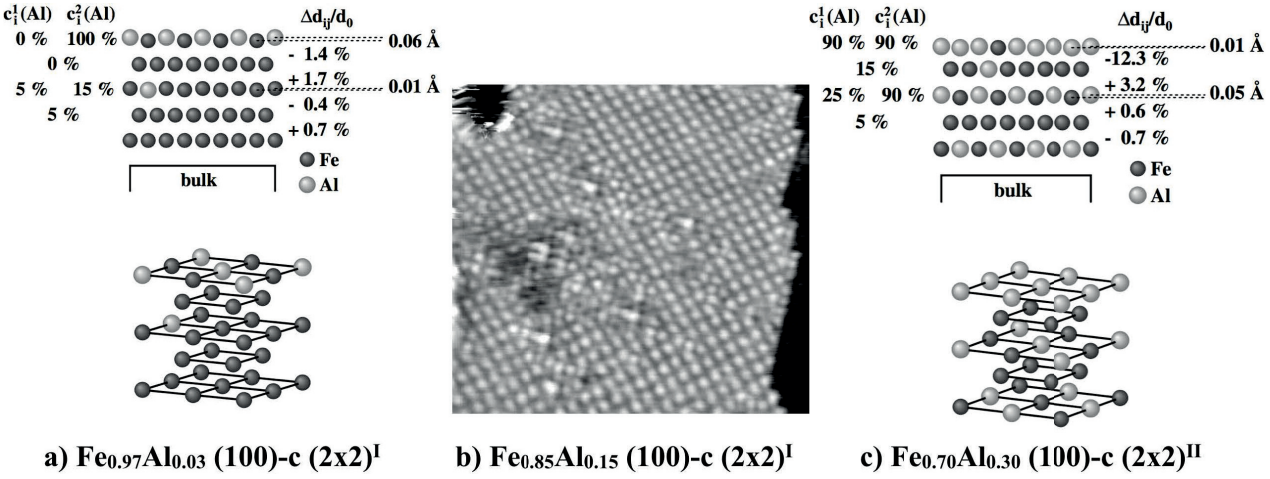

Figure 3.10: Structural models of a) $Fe_{0.97}Al_{0.03}(100)$-c$(2 \times 2)^I$, c) $Fe_{0.70}Al_{0.30}(100)$-c$(2 \times 2)^{II}$ and b) the STM image of $Fe_{0.85}Al_{0.15}(100)$ with a local c$(2 \times 2)^I$ (Size 100×100 Å^2, $U_b = -0.5$ mV, $I_t = 2.1$ nA). Herein sublattices with c(2×2) periodicity are denoted I and II, respectively. Interlayer spacings $\Delta d/d$ and atomic concentrations c_i are given in figure. From Refs. [29, 32].

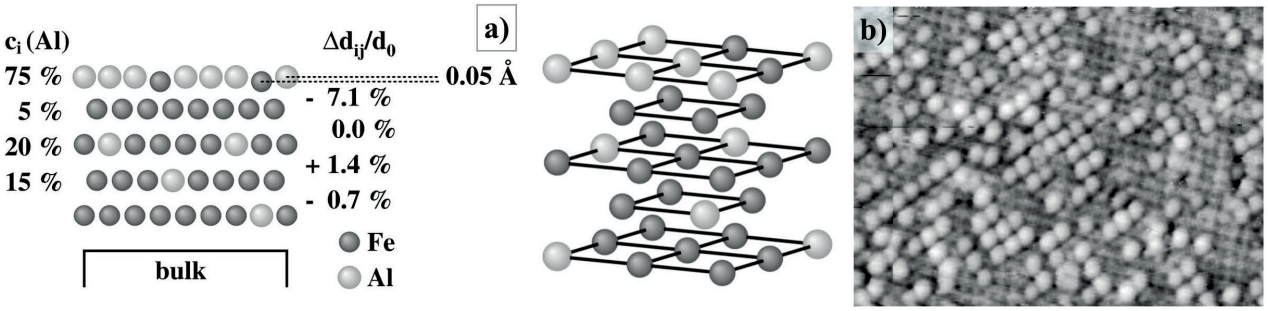

Figure 3.11: a) Structural models of $Fe_{0.85}Al_{0.15}(100)$-(1×1) and b) room temperature STM image of this surface (100×83 Å, $U_b = -6$ mV, $I_t = 0.46$ nA). According to authors, a clear chemical contrast is achieved between Fe (protruding atoms) and Al (dark indentations). From Ref. [32].

in terms of reconstruction, subsurface bulk structure and capping layer.

3.3.2 $Fe_{1-x}Al_x(110)$

To our knowledge, very few studies of (110) orientation of B_2 FeAl have been reported [28, 30, 31, 94, 98–101].

Annealing at ~ 673 K the sputtered Al-depleted surface of $Fe_{0.53}Al_{0.47}(110)$ results in Al segregation with a (2×1) superstructure (Fig. 3.13-a) which is supposed to be a thick Fe_3Al layer on top of FeAl [30, 31].

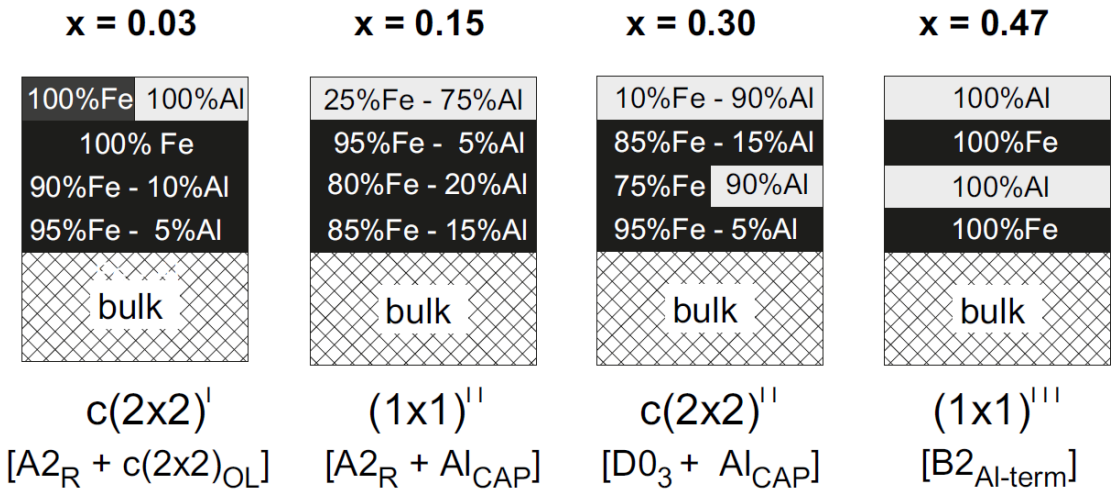

Figure 3.12: The compositional schematic diagram of equilibrium FeAl(100) surface region deduced from full dynamical LEED intensity analyses. Split shadings within a layer manifest that two sublattices of c(2×2) symmetry are observed [29]. Schematic stacking is given below each figure: (R) randomly, (OL) overlayer, (CAP) capping, (Al-term) Al terminated. From Ref. [29].

A higher temperatures (673-873 K or $>$ 1073 K), a superstructure which is commensurate along the $[1\bar{1}0]$ direction but not along the [001] direction appears [28,30,94,98,99] (Fig. 3.13-b). It is characterised by a matrix $M_s = \begin{bmatrix} 1 & 0.7 \\ 0 & 1.41 \end{bmatrix}$ due to a quasi-hexagonal arrangement of atoms imaged in STM [94, 99] and limited to the last plane according to diffraction [98]. Diffraction [98] concludes that Fe protudes over Al. The STM image of Fig. 3.14-b is interpreted as Fe atoms surrounded by 6 Al atoms. The periodicities of the superstructure as defined by the distance between two successive Fe atoms based on STM measurements are 4.2 Å and 8.22 Å along [001] and $[1\bar{1}0]$ directions respectively, indicating the commensurability along $[1\bar{1}0]$ direction (4.1 Å for the substrate). The stoichiometry of the superstructure is close to $FeAl_2$ with an estimated Al concentration of the last plane of 0.67 according to Auger spectroscopy [98] and X-ray diffraction (XRD) results [28, 30]. Relaxations have been also calculated [100].

In the intermediate regime of temperature (873-973 K), unexplained severe streaking along the $[1\bar{1}0]$ direction was observed in LEED by Graupner and coworkers [28] (Fig. 3.13-c). While these authors [28, 30] argue that a (1×1) bulk terminated surface does not exist, it was observed either after annealing at $\geq$ 1073 K in Ref. [101] (Fig. 3.13-d) or at annealing of around 673 K by STM in Ref. [94] (see Fig. 3.14-a).

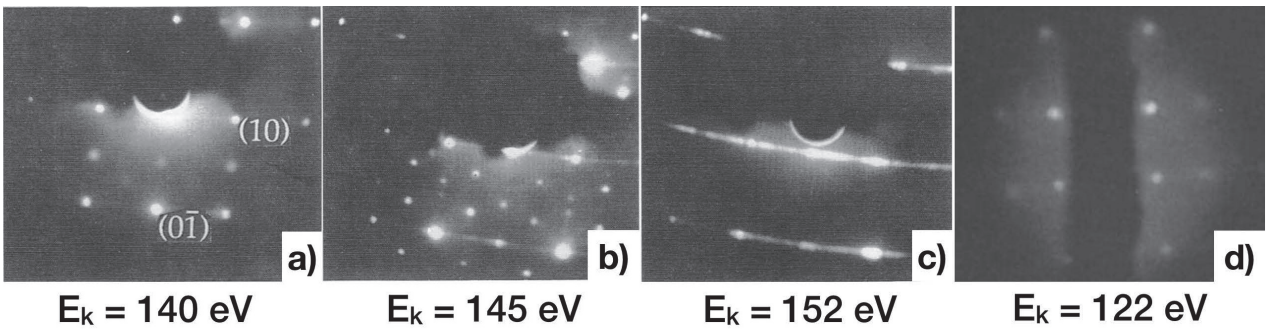

Figure 3.13: LEED patterns of $Fe_{0.53}Al_{0.47}(110)$ surface after annealing at a) 673 K with a (2×1) pattern; b) 673-873 K or $>$ 1073 K with a complex superstructure; c) 873-973 K with unknown streak phases along $[1\bar{1}0]$ direction [28]. d) LEED pattern of $Fe_{0.60}Al_{0.40}(110)$ annealed at $\geq$ 1073 K showing a (1×1) arrangement [101].

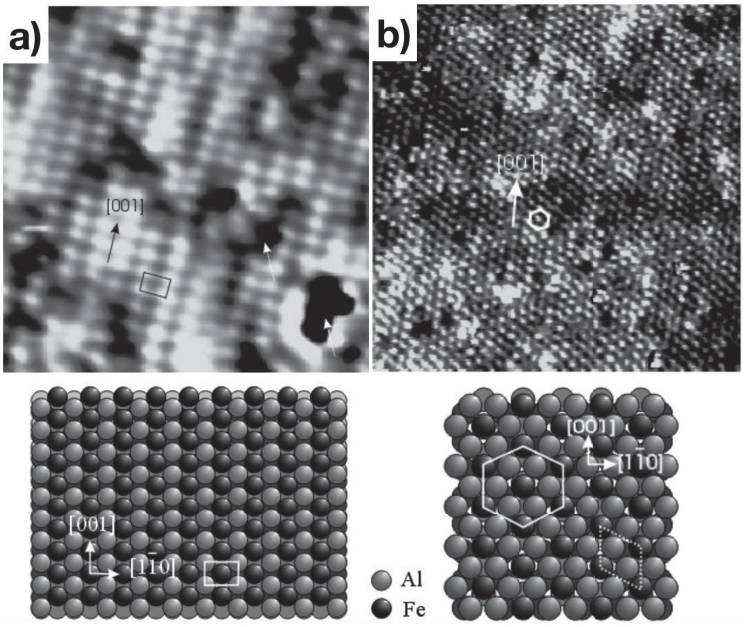

Figure 3.14: STM images of $Fe_{0.53}Al_{0.47}(110)$ after annealing at a) 673 K showing a truncated bulk (1×1) surface (4.7×4.7 nm^2, $I_t = 3.96$ nA, $U_b = 331$ mV) with some vacancies; b) at 1123 K, with a $FeAl_2$ superstructure on top (15×15 nm^2, $I_t = 5.41$ nA, $U_b = 30.2$ mV). The unit cells are labeled, and the corresponding ball models are shown below. The unit cell of stoichiometric $FeAl_2$ is one Fe atom surrounded by six Al atoms. Only one type of atoms (Fe) is imaged. From Ref. [94].

3.3.3 $Fe_{0.50}Al_{0.50}$(111), (210), (310)

The more open (111), (211) and (310) surfaces of FeAl were studied only in Ref. [30]. Upon annealing the (111) orientation, in parallel to Al segregation observed through Auger spectroscopy (average concentration c_{Al}), a series of reconstructions has been found:

$$\text{diffuse}(1\times1) \underset{573\ K,c_{Al}=0.6}{\longrightarrow} (\sqrt{3}\times\sqrt{3})R30^\circ \underset{873\ K,c_{Al}=0.7}{\longrightarrow} (2.4\times2.4)R30^\circ \underset{973\ K,c_{Al}=0.75}{\longrightarrow} (3\times3)+(3\times6)/(6\times6) \tag{3.2}$$

In contrast to the other orientations, c_{Al} increases continuously and almost linearly with temperature. This proves the existence of a severe multilayer Al segregation which can be explained already by the specific open structure of bcc(111). Based on LEED and average Auger compositions, it was assumed that, like on other surfaces, the $(\sqrt{3} \times \sqrt{3})R30^\circ$ corre-

sponds to a reconstruction on a thick Fe_3Al $D0_3$ slab while the (3×3) was assigned to a regular array of pyramids with microfacets having a lower energy. A tentative model for the close-packed microfaceted (3×3) surface is shown in Fig. 3.15-c. However, it should be noticed that the corrugated amplitude of FeAl(111) surface is comparable with the escape depth of Auger electrons increasing the uncertainty in the determination of near-surface concentration on which these conclusions are based [30].

The (210) displays a (1×3) reconstruction while the (310) is not stable at all and microfacets along the [100] direction.

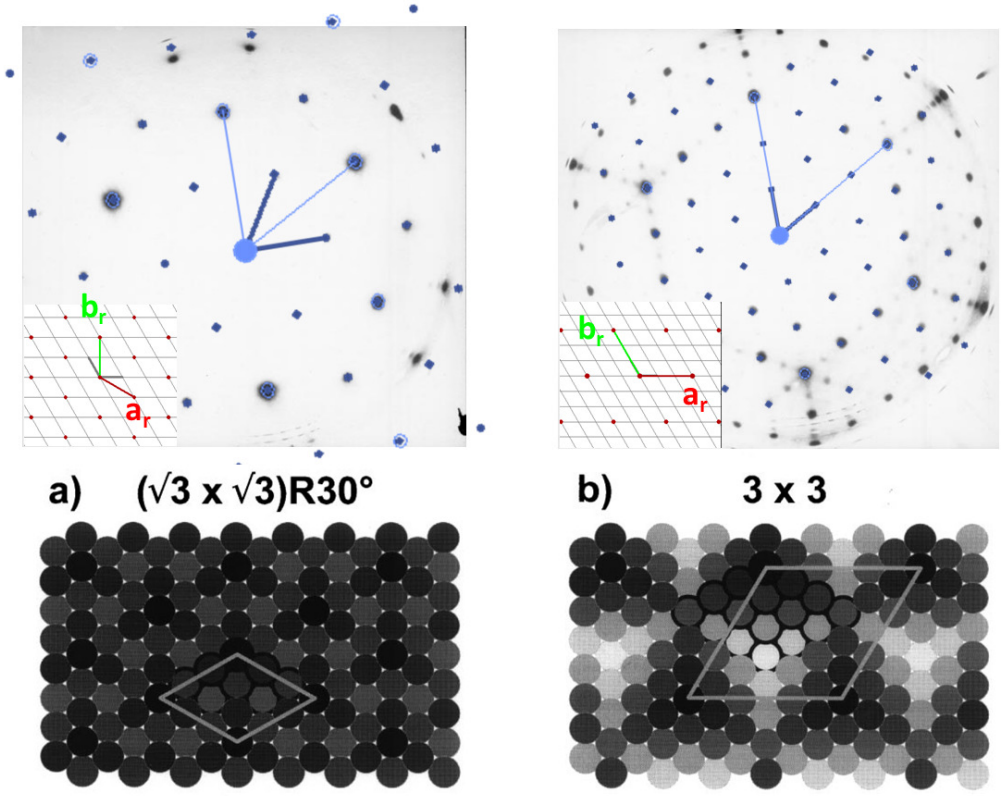

Figure 3.15: LEED patterns and proposed ball models of an annealed $Fe_{0.50}Al_{0.50}(111)$ surface ($E_K = 42$ eV). a) $(\sqrt{3}\times\sqrt{3})R30°$ superstructure obtained after annealing at 753 K; b) (3×3) superstructure formed at $\geq$ 973 K. Patterns have been overlapped with simulated LEED; the insets show the corresponding direct space. The atoms marked in bold represent close-packed Al microfacets forming pyramid-like microstructures. Interpreted from Refs. [30, 31].

3.3.4 Conclusion

Although, according to bulk properties, Fe-Al is an ordering system which should favour bulk termination, its surfaces are dominated by strong segregation effects. Al being the element with the lowest bulk binding energy, it segregates to the surface in a way that depends on

the composition, bulk atomic structure, temperature and crystal orientation. The (1×1) termination is not the rule, except after sputtering, and a rich set of reconstructions has been observed in which a strong coupling between chemical and substitutional disorder happens. Even ordered Fe-Al compositions are prone to segregation.

Sometimes it may be hard to state whether a certain stoichiometric state or chemical order that is reached is stable or still metastable and only frozen [31]. Transient states are often observed; through the comparison of several $Fe_{1-x}Al_x$ compositions, some authors [34] concluded at a two-step equilibration model according to which a thermal equilibrium happens much faster between the top Al-enriched layer and the subsurface atomic slab than between this latter and the bulk. During the course of annealing, the altered layer is ruled by bulk like atomic interaction and follows the actual phase diagram in the sequence $A_2 \rightarrow D0_3 \rightarrow B_2$.

3.4 Oxides at the surfaces of aluminium metallic alloys

In this section, the literature on the aluminium oxide thin films formed at the surfaces of metallic (alloy) substrates is briefly reviewed (see review [12]). After a starter on the necessary description of the atomic structures of the alumina polymorphs on which rely most of the surface science analysis, the emphasis is put on the most studied substrates (in particular NiAl) and the effects of orientation and reduced dimensionality on the structure of the formed ultrathin alumina films. The section ends with a summary of the common characteristics of those films.

3.4.1 The bulk alumina polymorphs

Alumina is a ceramic material with a high melting point (2323 K) and a large band gap (8.8 eV) that has numerous applications as a catalyst by itself, a support of catalytically active metallic nanoparticles, a soft abrasive, an electrical insulator or a tunnelling barrier [102, 104]. Alumina presents a great variety of polymorphs which consist in oxygen sub-lattice in which the Al cations occupy tetrahedral and/or octahedral distorted sites. The type of oxygen stacking and the differences in occupation probability of these vacancy sites determine the crystal structure. The most common polymorphs and their characteristics are gathered in Tab. 3.3; some of atomic structures are represented in Fig. 3.16. Depending upon the stacking sequence, three groups of alumina can be distinguished:

- ABAB... stacking: the oxygen sub-lattice has a hexagonal compact (hcp) structure; α-alumina is the most representative of this group;
- ABCABC ... stacking: the oxygen sub-lattice has a face centred cubic structure (fcc); γ-alumina is among those;
- Disordered stacking: the oxygen sub-lattice has neither a hcp nor a fcc structure (ex: β-alumina).

The distance between oxygen atoms in the packed hexagonal planes is in the range of 2.75 Å for all the compounds. The distance between O planes is around 2.2 Å while the Al-O distance

Alumina phase	Crystal system	Space group	Lattice parameters	Oxygen sub-lattice	Occupied anionic sites
α-Al_2O_3	Trigonal	$R\bar{3}c$	a = 4.759 Å, c = 12.991 Å	hcp	Octa (100 %)
κ-Al_2O_3	Orthorhombic	$Pna2_1$	a = 4.84 Å, b = 8.33 Å c = 8.95 Å	hcp	Octa (75 %)/Tetra (25 %)
γ-Al_2O_3	Cubic	$Fd\bar{3}m$	a = 7.93 Å	fcc	Octa (63 %)/Tetra (37 %)
θ-Al_2O_3	Monoclinic	C12/m1	a = 5.64 Å, b = 2.92 Å c = 11.83 Å, $\beta = 104°$	fcc	Octa/Tetra
δ-Al_2O_3	Tetragonal	-	a = 7.96 Å, c = 11.70 Å	fcc	Octa/Tetra
β-Al_2O_3	Hexagonal	-	a = 5.60 Å, c = 22.5 Å	fcc	Octa/Tetra
a-Al_2O_3	-	-	-	Random	Tetra

Table 3.3: Crystal structures of the most important alumina polymorphs. "Octa" and "Tetra" stands for octahedral and tetrahedral sites, respectively.

is distributed between 1.65 and 2 Å.

On a thermodynamic point of view, the most stable phase is α-Al_2O_3 known as corundum. α-Al_2O_3 is the final product of the dehydration sequence of trihydroxides $Al(OH)_3$ (gibbsite) and the aluminium oxide-hydroxides AlOOH (boehmite). During dehydration, several transient phases occur depending on the temperature. But the followed reaction pathways depend on temperature, precursors and atmosphere (vacuum/water content); reaction sequences are irreversible and all the transition aluminas are stable at room temperature. Some structures do not have an exact Al_2O_3 stoichiometry due to partial occupancy of sites; some of them are even still debated on a crystallographic point of view.

Although being rhombohedral, α-Al_2O_3 is often described in a hexagonal unit cell containing 18 planes of pure Al or O that stack along the [0001] direction with the sequence O-Al-Al where the distance between planes in Al-Al bilayer is 0.485 Å. The distance between successive O plane in the hcp stacking is c/6=2.165 Å. In this structure, Al atoms occupy only distorted octahedral sites with two Al-O bond lengths (1.86 and 1.96 Å). γ-Al_2O_3 has a defect spinel structure with Al ions distributed between octahedral and tetrahedral sites. θ-Al_2O_3 alumina is closely related to γ-Al_2O_3. Through a slight change of the arrangement of the Al ions in the interstices, the lattice becomes monoclinic instead of cubic. The local geometry of the ion configuration (bond lengths and angles) is the same of those of γ-Al_2O_3. The last alumina to mention is amorphous aluminium oxide a-Al_2O_3. Even if it lacks long-range order, it has a significant short-range order like in glass; it can be described as oxygen clusters with aluminium in their tetrahedral vacancies.

3.4.2 Surface structures of α-Al_2O_3

On a surface science point of view, only the various surfaces of the thermodynamically stable α-Al_2O_3 polymorph have been studied in the literature due to the availability of large scale and good quality single crystals. Studies have been reviewed in Refs. [70, 105, 106]. The discussion will be restricted herein to the most stable (0001) orientation. Due to the stacking

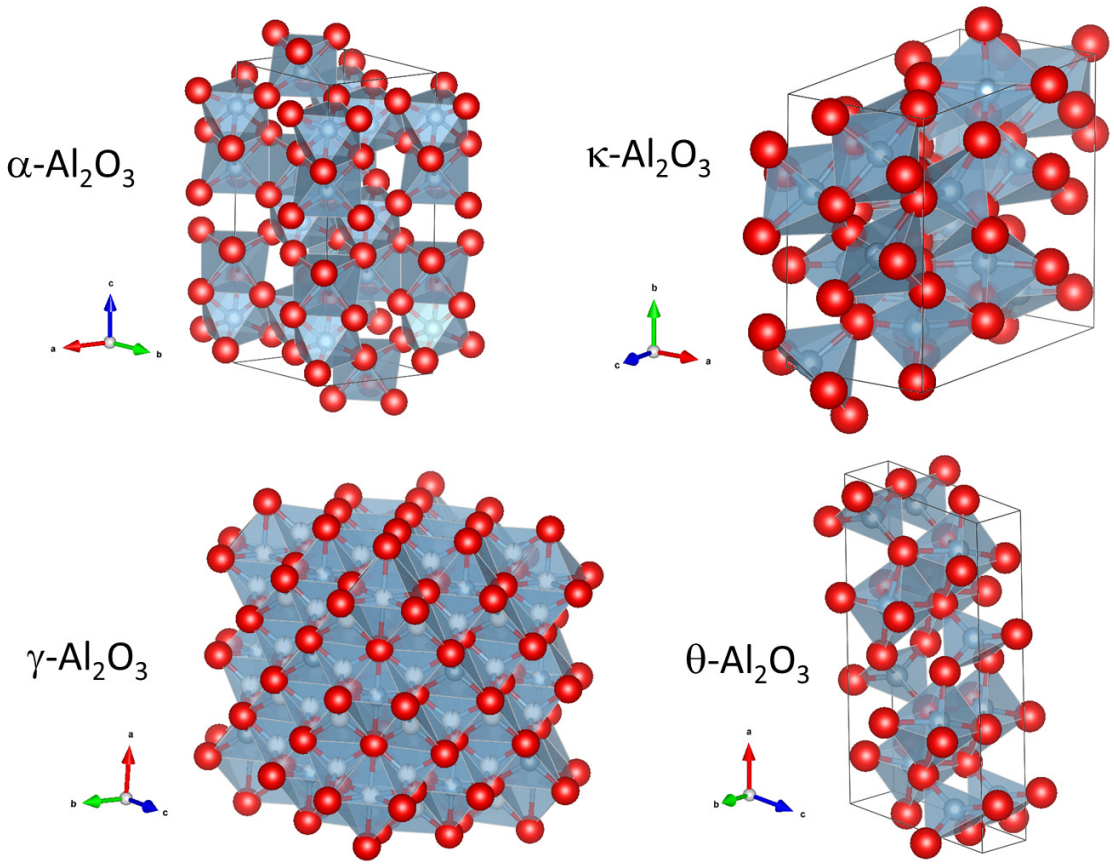

Figure 3.16: Ball models of a few bulk alumina atomic structures showing the coordination polyhedra of the cations. Red spheres stand for oxygen anions and blue ones for aluminium cations. Al cations are either surrounded by a distorted octahedron or by a tetrahedron made out of O nearest neighbours. Partial occupancy of sites is not uncommon.

sequence along the [0001] direction of the corundum structure, three bulk terminations can be obtained: (i) with a single Al plane (Al/O/Al/...sequence), (ii) with a single O layer (O/Al/Al/...sequence) and (ii) with a Al bilayer (Al/Al/O/...sequence). Through simple electrostatic arguments, only termination (i) with only one Al plane is self-compensated on chemical and polarity points of views [107] (*i.e.* without a dipolar moment perpendicular to the surface that increases dramatically the surface energy). Theoretical and experimental studies agree that the (1×1) (0001) surface prepared in ultra-high vacuum conditions is Al terminated with a strong inward relaxation (~ 50 %) followed by sizeable ones for the next planes [108]. On the other hand, hydroxylated surfaces are terminated by an OH-plane [109]. High temperature annealing under vacuum leads to a series of O-deficient reconstructions:

$$(1\times1) \underset{1473\ K}{\longrightarrow} (\sqrt{3}\times\sqrt{3})R30^\circ \longrightarrow (2\sqrt{3}\times2\sqrt{3})R30^\circ \underset{1573\ K}{\longrightarrow} (3\sqrt{3}\times3\sqrt{3})R30^\circ \underset{1673\ K}{\longrightarrow} (\sqrt{31}\times\sqrt{31})R\pm9^\circ$$

Only the last reconstruction $(\sqrt{31} \times \sqrt{31})R \pm 9^\circ$ [110] has been solved by surface X-ray diffraction [70, 111]. It is terminated by 5 Al planes upon removal of the last two O planes

of the corundum structure. The structure of the last two Al planes is very close to that of Al(111).

3.4.3 Alumina thin films on metallic alloys

In binary alloys $A_{1-x}B_x$, if the species B possesses a higher oxygen affinity compared to A, the oxidation tends to produce a BO_y compound at the surface, through the so-called selective or preferential oxidation [12, 112]. This oxidation is accompanied by a depletion in B and enrichment in A in the near surface region. If the $A_{1-x}B_x$ is a defined compound, the species in excess may dissolve in the bulk to keep the stoichiometry ratio under the oxide while for a random alloy, a gradient of concentration builds up. The prototypical examples are (i) chromia on M-Cr alloys, M being Fe [113], Co [114, 115], Ni [116, 117]; and (ii) alumina on M-Al alloys, M being Fe [20, 118–120], Ni [15, 121, 122], Cu [18, 123] and Co [124, 125]. Single crystal alloy substrates are preferred platforms to grow well-defined epitaxial thin films and to rationalise the effect of crystallographic orientations and the interplay with segregation; they also offer the opportunity to form oxide films with atomic structures that are metastable in the bulk form or without bulk equivalent. Moreover, film thickness quite often provides enough conductivity to employ surface science characterisation techniques based on charged species.

In this thesis, the orientation dependence of the structure, the composition and the morphology of alumina thin films have been probed on $Fe_{0.85}Al_{0.15}$(100), (110) and (111) surfaces. As explained in Chap. 1, this study is motivated by the upstream control of selective aluminium oxidation on Al-alloyed steel that is detrimental during the hot-dip galvanization process [3, 9, 10]. On the contrary, the use of structural alloys for high temperature applications [11] is quite demanding for the formation of a stable protective alumina against corrosion [126].

Alumina ultrathin films on metallic substrates can be prepared following different strategies [12]:

- surface oxidation of Al- [127–130] or Al-alloyed (NiAl [121, 131–133], Ni_3Al [134–136], FeAl [16, 20, 99, 137, 138], CuAl [18, 123, 139] and CoAl [124, 125]) single crystal surface,
- growing alumina on other metallic substrate such as Ni(111) [140, 141], Co(0001) [142], Cu(111) [141]) via (i) reactive deposition of Al in an oxidising atmosphere or (ii) post-oxidation after deposition of Al followed by a thermal treatment in an oxidising agent.

In the following, the studies done on surface oxidation on aluminium metallic alloys will be briefly reviewed in connection with the present work. In particular, those studies performed on Al(111) surface (Sect. 3.4.3.1) and single crystal alloy surfaces, such as NiAl and Ni_3Al(110), (100), (111) (Sect. 3.4.3.2), Cu-9 at.% Al(111) (Sect. 3.4.3.4), CoAl(100) (Sect. 3.4.3.5) and FeAl(110), (100), (111) surfaces (Sect. 3.4.3.6) [13–16, 18, 99, 121–125, 127–130, 132–134, 137–139, 143–196] provide keys to understand the work performed herein on $Fe_{0.85}Al_{0.15}$ single crystals.

3.4.3.1 Alumina grown on Al crystal

Alumina film formed on Al(111) surface via oxidation method is not well crystallised and its thickness is self-limited [12, 127–130, 143]. Indeed, the low melting temperature of aluminium (933 K) severely limits recrystallisation annealing. The self-limited thickness is often described in the frame of the Cabrera-Mott model [197]. According to it, an electric field is formed across the oxide film due to the potential difference of the metal-oxide and the oxygen-oxide work functions resulting from electron tunnelling between the Fermi level of the substrate and acceptor levels of chemisorbed oxygen at the surface. The generated electric field due to this potential difference reduces the energy barrier for the migration of the ions through the oxide. But as the tunnelling current decreases with thickness, the oxidation stops at a saturating thickness.

Cai *et al.* [128, 129] studied the oxidation kinetics of Al(111) by molecular oxygen in the pressure range of 1×10^{-8} to 5 Torr at room temperature. The kinetics for dissociative oxygen adsorption can be fitted by a Langmuir isotherm. Oxide growth rate as well as film thickness increase with gas pressure. But, film thickness saturates at ~ 12.4 Å beyond 1 Torr of oxygen pressure [128, 129]. Oxygen populates surface and then subsurface sites [127, 143] but in the explored temperature range, oxygen pressure weights more than oxidation temperature for oxide growth rate. Kiejna *et al.* [143] used first-principle density-functional calculations to explore the structure of oxygen adsorption sites on Al(111). They found that for on-surface sites, O atoms (1 monolayer) prefer to be chemisorbed in hcp hollow sites, and for subsurface, the most stable structure is O-(1×1) in tetrahedral sites below the top-most Al layer. Thus these two O layers induce a very large increase in the mean interplanar distance of top-most layers that consequently deteriorate the surface crystalline structure [12, 143].

3.4.3.2 Ni_xAl

Thin oxide films on Ni_xAl ($x = 1, 3$) single crystal have been intensively studied not only *per se* as an alloy for high temperature applications [11] but also mostly as a support in fundamental surface science studies of catalytic activity of metallic nanoparticles [12,198,199]. Well-ordered and crystallised alumina films can be formed on all the low index surfaces (111), (110), (100) of the ordered compound NiAl and Ni_3Al [13–15, 121, 122, 132–134, 145, 146, 148, 149, 151–164, 164–166, 168–188]. At the opposite of our study on a random alloy, the use of an ordered alloy sets the composition of the substrate underneath the oxide. NiAl crystallises in the CsCl B_2 structure where Ni atoms occupy the corner of a cube and the Al its centre or vice-versa ($a_B = 2.89$ Å). Ni_3Al adopts a cubic $L1_2$-Cu_3Au type structure ($a_B = 3.56$ Å [172, 173]) where Ni atoms occupy the centres of the faces of the cube while Al atoms are located at the corners. The relaxed surfaces of $Ni_3Al(111)$ and (110) alloys have Al atoms located above Ni atoms [174, 175]. Annealing the crystal to above 1070 K is required to restore stoichiometric Ni_3Al composition after ion bombardment [174, 176].

3.4.3.2.1 NiAl(110) Alumina ultrathin film formed on a NiAl(110) surface by high temperature or two-step (exposure followed by annealing) oxidation in the low UHV exposure regimes was the one most extensively studied system [13–15, 145, 146, 148, 149, 151, 152]. The

NiAl(110) surface unit cell is a centred rectangle with cmm symmetry with zigzag Ni and Al atoms in equal amount. After ion bombardment and flash-annealing to 1300 K, clean NiAl(110) surface is characterised by a rumpling: Al atoms stick out of the top-most layer by 0.2 Å and Ni atoms relax inward towards the second layer by 0.12 Å. These outward relaxed Al atoms are detected through a -0.13 eV shift on the Al 2p spectra [148, 149].

Besides the lack of Ni oxidation, photoemission shows that the oxide film thickness on NiAl(110) is limited to two bilayers (5-11 Å by photoemission [13, 200, 201] and has a large band gap (6.7 eV) but lower than bulk alumina phases [13, 192]. The surface unit cell of ultrathin films was determined through LEED [13, 14] in particular in the Spot Profile Analysis of Libuda *et al.* [14]. As confirmed extensively later by STM [14, 131, 153, 154, 158, 202], the LEED pattern (Fig. 3.17-a, b) reveals that the oxide film is composed of two domains having a quasi-rectangular large unit cell rotated by $\sim 24°$ from the $[1\bar{1}0]$ direction. One domain may be favoured on vicinal substrate via a stress relief mechanism [131]. The unit cell parameters were found as $a_{ox} = 17.9$ Å, $b_{ox} = 10.55$ Å, $\gamma_{ox} = 88.7°$; close values have been obtained by Surface X-Ray Diffraction [121] $a_{ox} = 18.01$ Å, $b_{ox} = 10.59$ Å, $\gamma_{ox} = 91.15°$. The film is commensurate with the substrate along the $[1\bar{1}0]$ direction and incommensurate along the other one [001]. Ni atoms in excess after oxidation are dissolved in the bulk of the crystal [13, 145, 146, 148] or annihilated by diffusing Ni vacancies [112].

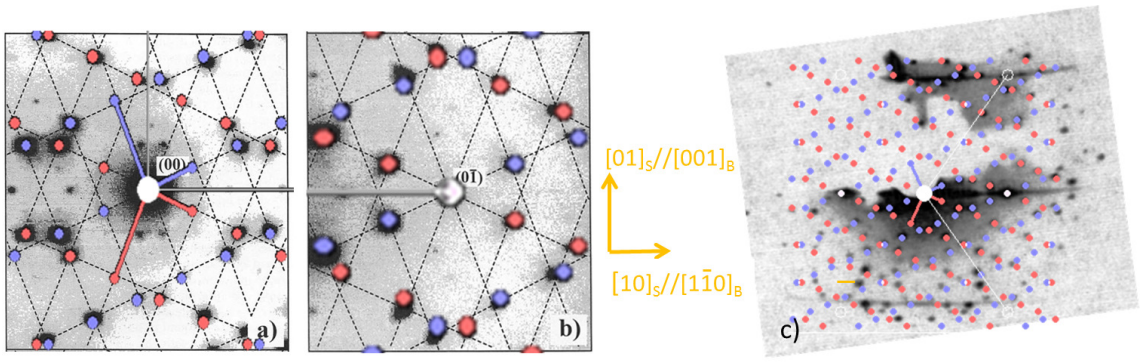

Figure 3.17: LEED patterns of the oxide layer on NiAl(110) [14] around a) $(00)_S$ and b) $(0\bar{1})_S$ reflections, and c) on FeAl(110) [16]. They have been overlapped with a simulation with an indexing corresponding to a quasi-rectangular unit cell with two domains (blue/red points) corresponding to the matrix of $\begin{bmatrix} 4 & 2.53 \\ -1 & 3.37 \end{bmatrix}$ from the rectangular surface unit cell. In Figs. a, b, several additional weak spots due to double diffraction appear, which do not coincide with the indicated oxide lattice. Interpreted from Refs. [14, 16].

The initial studies concluded at a structure close to that of α- or γ-alumina through a comparison to vibrational fingerprints of Electron Energy Loss Spectroscopy with known aluminium compounds [13], Transmission Electron Microscopy [203] or STM imaging of the compact (111) planes [204]. Later on, a surface X-ray diffraction study [121] pointed at the formation of a well-ordered ultrathin κ-Al_2O_3-like layer with a strong distorted double layer

structure. This latter was assigned to hexagon-like arranged oxygen ions interacting strongly with NiAl(110) substrate. Aluminium ions occupy equally octahedral and tetrahedral sites but with two bonds that are unphysically short (Al-Al, 2.08 Å, Al-O, 1.51 Å).

This model was challenged by Kresse *et al.* [15] who concluded that the alumina film on NiAl(110) is related to neither bulk α-corundum nor to γ- or κ- alumina. By combining atomically resolved STM and *ab initio* calculations, they concluded at a bilayer film with a stacking sequence and stoichiometry of $4(Al_4^{2+}O_6^{2-}Al_6^{3+}O_7^{2-})$, corresponding to interfacial Al (Al_i), interfacial O (O_i), surface Al (Al_s) and surface O (O_s) ions. The oxide unit cell (white rectangles in Fig. 3.18), with 16 NiAl surface unit cells beneath, is nearly commensurate along the diagonal of the oxide unit cell (yellow line). In this structure, 24 surface Al atoms are arranged nearly in hexagons (Fig. 3.18-e) together with 28 coplanar oxygen atoms (Fig. 3.18-c). Among these 24 surface Al atoms, 12 are tetrahedrally coordinated and 12 pyramidally coordinated with surface O atoms (Fig. 3.18-a, f). The 16 interfacial Al atoms are in pentagon-heptagon pairs (blue lines, Fig. 3.18-a, c, d); one interfacial Al atom shares one valence electron with Ni atom underlying and two valence electrons with the oxide film. In Fig. 3.18-d, the interface structure is visualised and the thickness of alumina film (Fig. 3.18-b) is around $\sim$ 5 Å. The average surface Al-Al distance around 3.03 Å is in accord with the well known $(\sqrt{31} \times \sqrt{31})R \pm 9°$) high temperature reconstruction of α-$Al_2O_3(0001)$ [111]. The proposed model matches perfectly data from the literature in particular core level shifts [151], STM [15], atomic resolved Atomic Force Microscopy [154–156, 205], vibrational spectroscopy [13, 15] and diffraction [121]. A similar structure was also observed during oxidation of Al deposits on Ni(111) [19, 140].

Martin *et al.* [151] extended previous photoemission analysis of this layer [13, 144, 150]. Based on the model proposed in Ref. [15], a study via high-resolution core level spectroscopy and Density Functional Theory calculation distinguished oxygen and aluminium atoms residing at the surface and interface. As seen in Fig. 3.19 and Tab. 3.4, Al $2p_{3/2}$ spectra can be decomposed into 4 components, corresponding to the NiAl substrate (72.5 eV), to the interfacial Al atoms between the oxide and the NiAl substrate (72.4 eV), to the interfacial Al atoms in the oxide layer (73.5 eV) and to the surface Al atoms (74.77 eV) respectively, in agreement with previous results [206]. The O 1s core level can be decomposed into two components; the weaker has a 19 % intensity of the larger component and derives from surface O atoms bounded to interfacial Al atom underneath [151].

These alumina layers on NiAl(110) possess three kinds of defects, which are oxide step edges, reflection domain boundaries and antiphase domain boundaries (Fig. 3.20) [14, 121, 153, 156–159, 202, 205]. Oxide step edges are introduced by the atomic steps of the substrate, reflection domain boundaries separate domains orientated differently due to the 2-fold symmetry of the substrate, while antiphase domain boundaries are between domains with the same orientation, which are identified as straight (along the small oxide unit cell vector) and zigzagged (along the diagonal of the oxide unit cell) types [153, 156]. Antiphase domain boundary occur between translation related domains which equivalent sites are related by a displacement vector that cannot be expressed as an integer multiple of the surface lattice constant. They

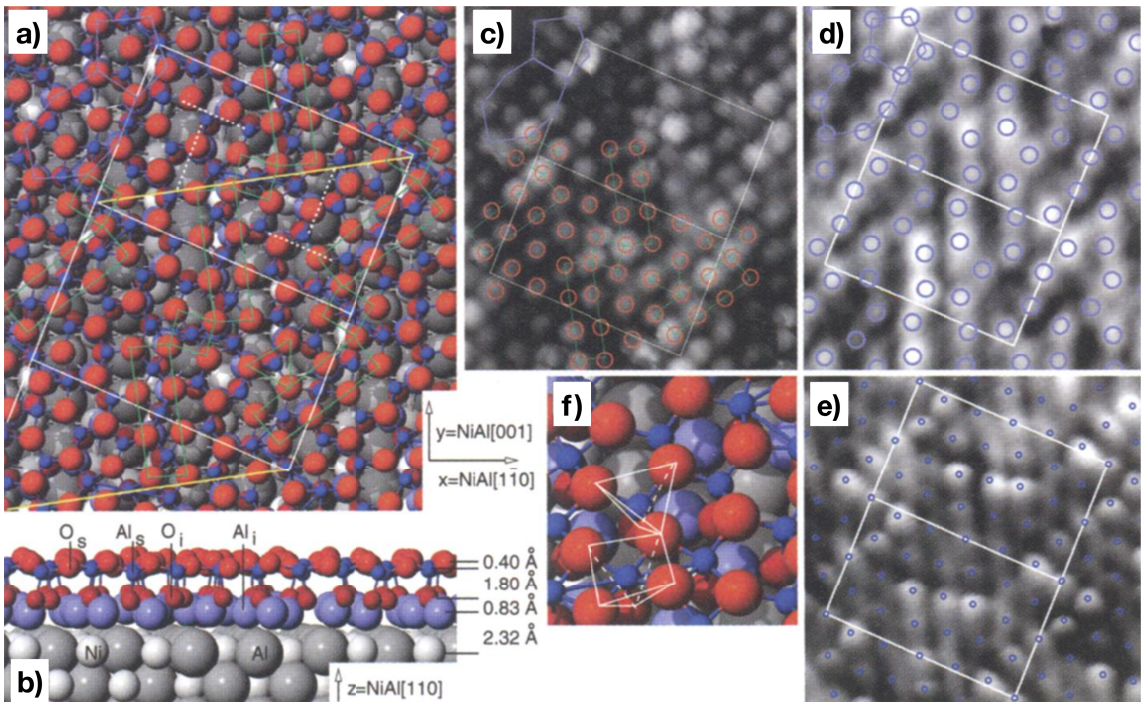

Figure 3.18: Top view (a) and side view (b) of alumina/NiAl(110) model based on *ab initio* calculation and STM. Dark blue balls are Al_s atoms while violet ones are Al_i atoms; larger and smaller red balls are O_s and O_i atoms respectively. (c) to (e) are experimental STM images. (c) -2.5 mV/1.4 nA and (d) -0.2 V/0.9 nA are conducted at room temperature while (e) -0.5 V/0.3 nA is at low temperature. (a) Two unit cells are marked by white rectangles, and the green rectangles and squares are the arrangement of surface O atoms. (c)-(d), O atoms and Al atoms are presented with red and blue circles respectively. (d) Closeup of surface structure showing the coordination of the tetrahedral and pyramidal Al atoms. From Ref. [15].

Atom	Experiment CLS (eV)	Calculation CLS (eV)
Al bulk	0.00 (72.5)	0.00
Al interface	-0.10	-0.60 to -0.30
Al interface	1.00	1.00 to 1.40
Al surface	2.27	1.71 to 2.67
O interface	0.00	-0.41 to 0.54
O surface (1)	0.00	-0.41 to 0.54
O surface (2)	1.23	1.05 to 1.14

Table 3.4: Experimental and calculated Al 2p $_{3/2}$ and O 1s core level shifts. O(2) correspond to atoms with Al atoms underneath which are quite distant with other surface O atoms; they give rise to the weaker O 1s component in Fig. 3.19-a [151].

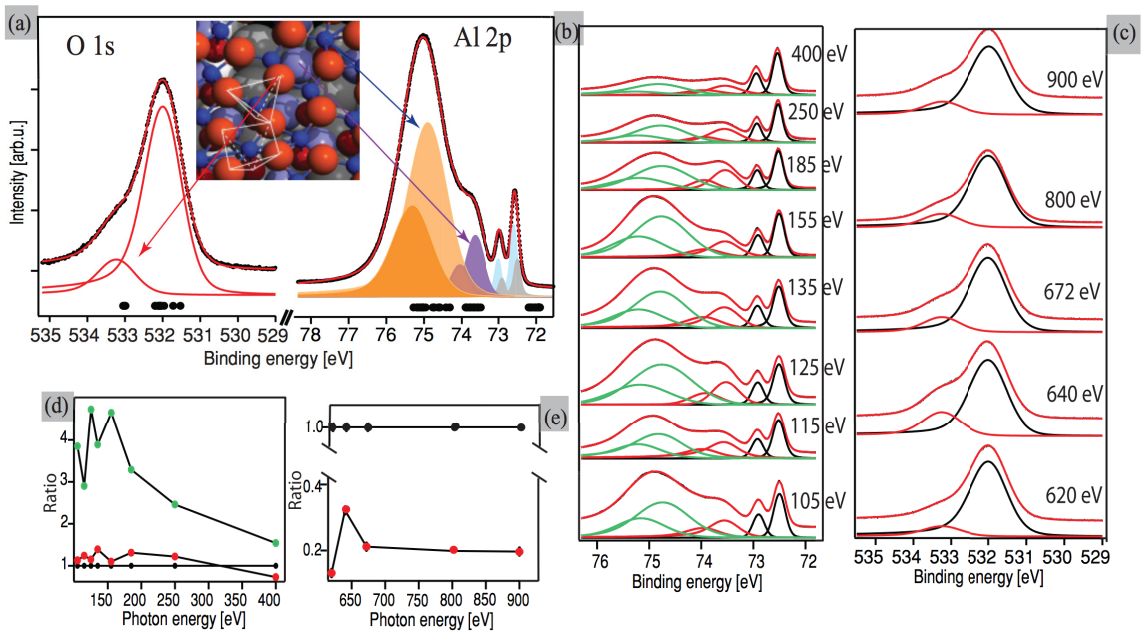

Figure 3.19: High-resolution core level spectra of an ultrathin alumina film formed on NiAl(110). a) right: Al 2p spectra (recorded at 130 eV) is decomposed into 4 visible components, each with a 0.4 eV spin-orbit splitting with a ratio of 0.5. These components correspond to (1) Al atoms of NiAl substrate (light blue), (2) interfacial Al atoms between oxide and substrate (grey), (3) interfacial Al atoms in the oxide overlayer (violet), (4) surface Al atoms of the oxide (orange). a) Left: O 1s spectra (recorded at 900 eV) is fitted with two components with a 1.23 eV binding energy difference and an intensity ratio of 0.19; the less intense one originates from the O atoms with interfacial Al atoms beneath that reside more distant to the other O atoms. d)e) Evolution with photon energy of ratios of Al 2p and O 1s peaks. From Ref. [151].

are believed to lower the strain energy in the film [153, 158, 202] and to be oxygen deficient F^{2+} like centre [158] with stoichiometry $(NiAl)^{2-}(Al_{19}O_{28}Al_{28}O_{32})^{2+}$. They are preferential nucleation sites for metallic clusters due to their specific electronic structure [158] leading to unoccupied states in the band gap of the oxide [158, 207, 208].

Finally, another preparation method through multistep selective oxidation [209] leads to an atomically flat film with a hexagonal superstructure quite different from the previously described one. Based on STM, it was assigned to α-alumina. At last, much thicker epitaxial film of γ-$Al_2O_3(111)$ (several nm) can be obtained through harsher oxidative conditions at high pressure [210, 211].

3.4.3.2.2 NiAl(100) Owing to the CsCl-B_2 structure, bulk truncated NiAl(100) is either Al- or Ni-terminated. The actual structure of the clean surface depends strongly on annealing temperature and duration [147, 160, 161]. Blum *et al.* [161] found that a defective Al terminated surface can be obtained by a prolonged annealing at temperatures lower than 500 K

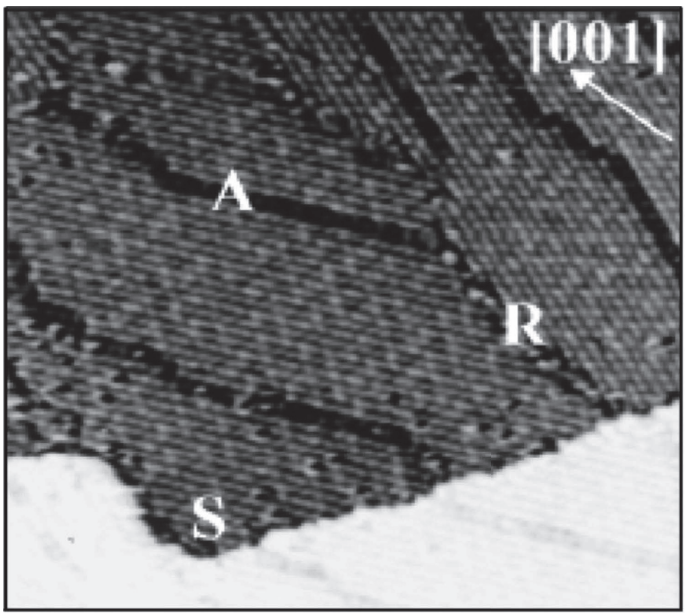

Figure 3.20: STM image (500 × 500 Å^2) of an alumina film on NiAl(110) showing a step edge (S), a reflection domain boundary (R) and an antiphase domain boundary (A). Sample bias = -1.3 V, I = -0.4 nA. From Ref. [159].

with a (1 × 1) LEED pattern, while the same pattern with a Ni terminated surface appears after flashing to 1400 K and rapid cooling to room temperature. Annealing at 800 K generates a c($\sqrt{2} \times 3\sqrt{2}$)R45° LEED pattern that is characteristic of an Al terminated missing row surface structure [161]. However, the same pattern is also believed to be due to O, C or N contamination [162, 163].

Fortunately, oxide formation at NiAl(100) is unaffected by the initial composition of the surface [164] but depends mainly on oxygen pressure, temperature and annealing duration [165]. All starting surfaces c($\sqrt{2} \times 3\sqrt{2}$)R45° [165, 166] or Ni-terminated/Al-terminated (1×1) [162,163] produce epitaxial θ-Al_2O_3-like alumina with a two-domain (2×1, 1×2) LEED pattern and a thickness close to 1 nm. This structural model was initially proposed based on lattice mismatch arguments with all the known alumina compounds [162] and on vibrational fingerprints in High Resolution Electron Energy Loss Spectroscopy [163]. The corresponding structure is displayed in Fig. 3.21. The monoclinic θ-Al_2O_3 of lattice parameters a_{ox} = 5.64 Å, b_{ox} = 2.91 Å, c_{ox} = 11.83 Å, $\beta_{ox} = 104°$ consist in fcc oxygen sublattice where Al^{3+} ions occupy tetrahedral and octahedral interstices equally. This epitaxy corresponds to the Bain classical orientation relationship between the fcc oxygen sublattice and the bcc NiAl. The mismatch amounts to 2.5 % in one direction ($2a_{\mathrm{NiAl}}$ = 5.78 Å) and 1 % along the other direction (b_{NiAl} = 2.89 Å), which explains the (2×1, 1×2) observed LEED pattern very well [162, 163]. The structure was confirmed by X-ray diffraction [147] but with some strong distortions from the bulk θ-alumina; Al prefers tetrahedral sites at the interface and octahedral sites at the surface. Diffraction evidenced a Stranski-Krastanov like growth with 0.76 nm thick layer covered by 2 nm high islands.

STM imaging yields to a morphology in the form of orthogonal strips running along the [010] and [001] directions with a mean width of 27 Å and a periodicity of 45 Å [164–168]. This lateral anisotropy is assigned to a stress build-up due to the lattice mismatch. As shown by

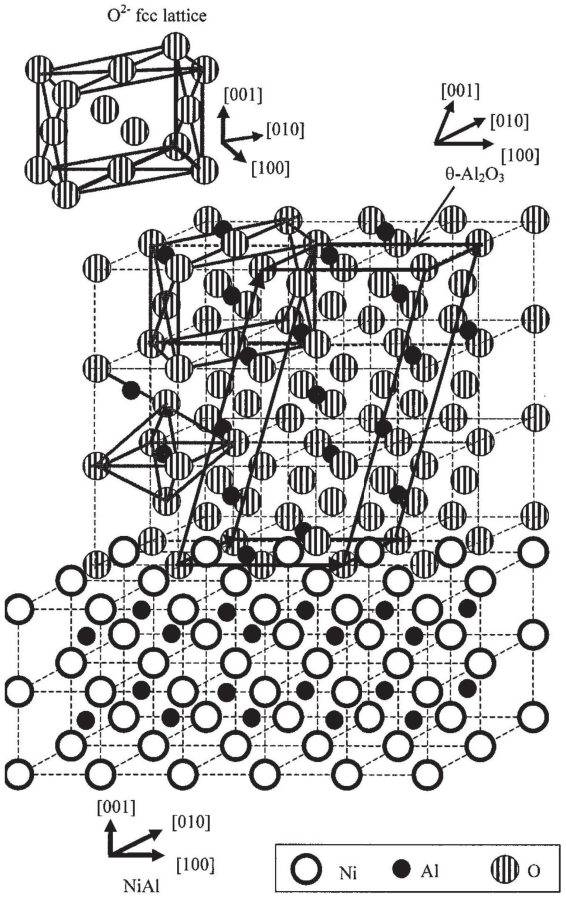

Figure 3.21: Structural model of θ-Al_2O_3/NiAl(100), showing the Bain epitaxy relationship between oxygen fcc sublattice and NiAl(100) bcc lattice, that is $(001)_{\text{NiAl}} \parallel (001)_{\text{O-lat}}$ and $[100]_{\text{NiAl}}/[010]_{\text{NiAl}} \parallel [110]_{\text{O-lat}}$. The height of θ-Al_2O_3 unit cell is 11.83 Å. From Refs. [163, 166].

Spot Profile Analysis LEED, the self organised arrangement of parallel oxide stripes results in a (9×1) superstructure in which the stripes themselves expose a (2×1) superstructure. Atomic resolution in STM [166] (Fig. 3.22) reveals the underlying square oxygen sublattice of the Al_2O_3 layer parallel to the substrate, with a close-packed double rows of O^{2-} ions and Al^{3+} ions occupying every other row. This structure is fully consistent with the proposed θ-alumina structural model (Fig. 3.21). Laboratory photoemission evidenced only one Al 2p oxide component shifted by 2.7-2.9 eV from the metallic one [212].

3.4.3.2.3 NiAl(111) The termination of the open NiAl(111) surface depends on the preparation conditions. A clean surface is terminated by a Ni plane with Al in the second layer with double steps and has a (1×1) LEED pattern. When annealed up to 1300 K with a coverage of a fraction of monolayer of oxygen contamination, the surface switches to large flat Ni-terminated terraces covered by triangular islands (size $\simeq$ 2.5 nm, height $\simeq$ 0.8 Å) with azimuthal ordering with respect to the substrate separated by double atomic steps with an average height of 1.7 Å. Annealing at 1400 K can avoid oxygen contamination, generating Ni-terminated surface [169]. Usually, the sample is annealed to 1500 K to remove oxide on NiAl(111) [132].

Franchy *et al.* [132] conducted high temperature oxidation experiments (at 900-1100 K) on oxygen-saturated surfaces covered by amorphous alumina obtained by exposing to O_2 at room

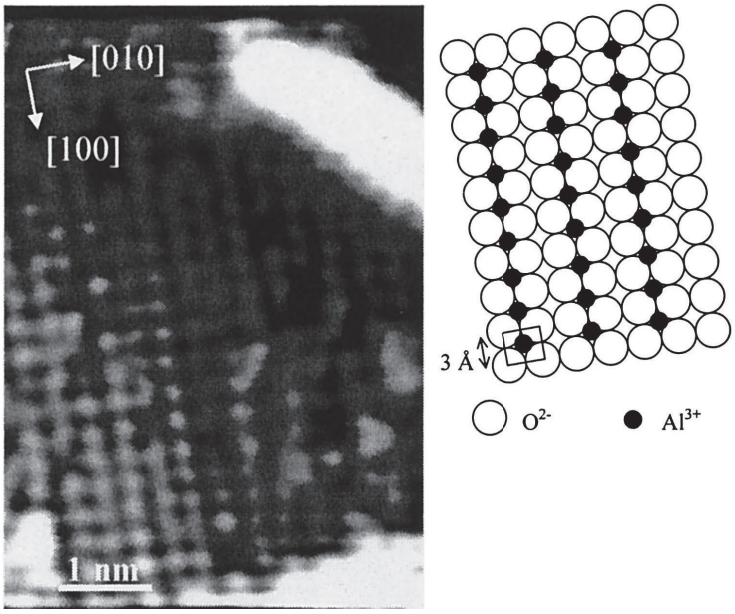

Figure 3.22: Atomic resolution STM image of the oxide overlayer on NiAl(100) after 500 L of oxidation followed by 2 h of annealing at 1025 K (U_b = 2 V, I_t = 1 nA). The observed peridodicity matches the oxygen sublattice of the bulk θ-Al_2O_3 structure. From Ref. [166].

temperature. A γ'-Al_2O_3 film is formed but when the annealing temperature is $\geq$ 1100 K, γ'-Al_2O_3 film transforms into α-like Al_2O_3 [132]. Similar transformation of allotropic phases are interpreted as θ- to α-Al_2O_3 transformation [170] at $\sim$ 1300 K, because γ'- and θ-Al_2O_3 can be regarded as the same structure in the sense of bond angles and bond lengths. Note also that oxidation at $\geq$ 1100 K can also produce a surface faceting with (110) facets and (111) terraces on which the oxide islands grow [132].

Beyond stable α-Al_2O_3 formation, a new oxide phase with spinel $NiAl_2O_4$ stoichiometry was detected by Loginova *et al.* at $\sim$ 1400 K after repeated cycles of oxidation, annealing and cleaning procedures [171]. The $NiAl_2O_4$ phase is a 3-fold dendritic structure with a size of several micrometers and a height of 250-400 nm, showing a milky-looking appearance at the macroscopic scale.

3.4.3.2.4 $Ni_3Al(110)$ As mentioned before, on a clean $Ni_3Al(110)$ surface, the topmost Al atoms are situated above Ni atoms at a distance of 0.055 Å while the Ni atoms are only slightly above Al atoms in the layer beneath [174].

Upon exposure of the surface at pressures of $2 \times 10^{-8} - 1 \times 10^{-6}$ mbar (exposure$\sim$ 8 L) at 970 K, disordered AlO_x overlayer forms on top and oxygen activates Al segregation [176]. When exposed to 2500 L (10^{-6} Torr) of O_2 at 800 K followed by annealing to 1100 K, the mixture of NiO and AlO_x formed at 800 K are transformed into metallic Ni and Al_2O_3 due to the reduction of NiO and Al segregation [177]. But none of the studies above put forward a clear structural model for alumina/$Ni_3Al(110)$. Yet Qin *et al.* [179] proposed theoretically a κ-like structure for a 7 Å thick alumina film (*i.e.*, three O-layers) which is produced by annealing the as-formed alumina film (exposed with 500 L of O_2 at 900 K) to 1100 K. The relaxed computed model obtained via *ab initio* methods is shown in Fig. 3.23. The bottom O-layer is chemisorbed on a plane of Al(111) and the film has a κ-alumina on the first two

planes followed by interfacial O(111)+Al(111) layer on top of $Ni_3Al(110)$ substrate [178–180].

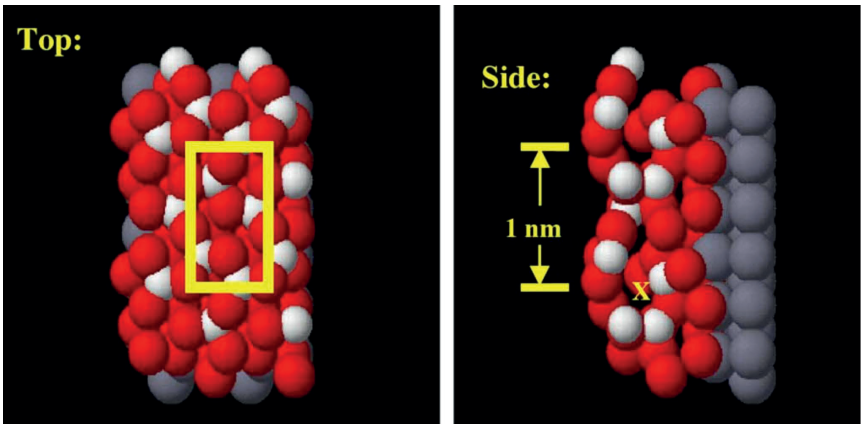

Figure 3.23: Top and side views of the relaxed slab (alumina/$Ni_3Al(110)$) computed using Density Functional Theory. The (2×1) unit cell (left) is shown as a yellow rectangle. X marks the largest interstitial sites. O-ions are red balls, Al-ions are white balls and metallic Al atoms in the model substrate are in grey. From Ref. [179].

3.4.3.2.5 $Ni_3Al(100)$ Oxidation on $Ni_3Al(100)$ surface at 1100 K with 2000 L of O_2 leads to the formation of a well ordered strongly distorted γ'-Al_2O_3 thin film (thickness $\sim$ 10 Å) growing with its (111) plane parallel to the (100) surface of the substrate [181]. The corresponding very complex LEED pattern (Fig. 3.24) is explained by a hexagonal structure with a lattice constant around 3 Å with two domains perpendicular to each other. Extra-spots are assigned to a hexagonal superstructure of lattice constant 17.5 Å [181]. Similar LEED results were previously obtained upon high temperature oxidation above 800 K [182]. The 17.5 Å periodicity is assigned to simple dislocation lines that could be described as (5×1) reconstruction.

3.4.3.2.6 $Ni_3Al(111)$ Clean $Ni_3Al(111)$ surface annealed at $\geq$ 1000 K leads to a (2×2) unit cell the lattice constant of which is $\sim$ 5.1 Å [183–185]. The corresponding LEED pattern and structural model are shown in Fig. 3.25.

The structure of the film depends on the annealing temperature and amorphous oxide is formed at low temperature [122, 183]. Oxidation performed on the $Ni_3Al(111)$ (2×2) surface at high temperature ($\geq$ 1000 K) [122, 134, 183, 185–188] leads to a well ordered alumina with a thickness of around 5 Å including two compact planes of oxygen. The LEED pattern reveals the presence of two domains of hexagonal symmetry (lattice parameter of around 3 Å) rotated by $\sim 24°$ and $\sim 37°$ with respect to the substrate. This structure relationship with the substrate was assigned to a distorted γ'-Al_2O_3 [183, 185] with its (111) plane parallel to the substrate. The assignment is confirmed by specific vibrational fingerprints [183].

STM imaging pointed [122,186] at the existence of two different hexagonal superstructures at the nanometric scale depending on the bias voltage. Above 3 V, a so-called "network" of $b_{net} = 2.6$ nm lattice parameter appears while around 2.3 V a "dot" superstructure of $b_{dot} = 4.5$ nm is observed; both of them are linked by a $(\sqrt{3} \times \sqrt{3})R30°$ transformation. The

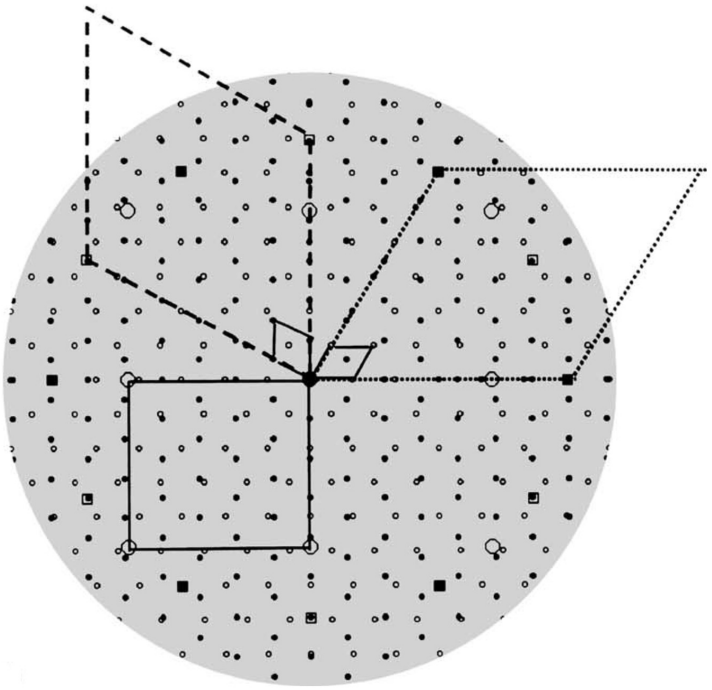

Figure 3.24: Calculated LEED pattern of γ-$Al_2O_3/Ni_3Al(100)$ by considering a model of alumina consisting of two domains with hexagonal structure (holes and filled squares) with a lattice constant of 3 Å and an angle of 90° between them and two extra domains with hexagonal structure (small holes and filled circles) with a lattice constant of 17.5 Å and angle between them of 90°. The later can be resolved in STM observation. The square indicates the substrate unit cell [181].

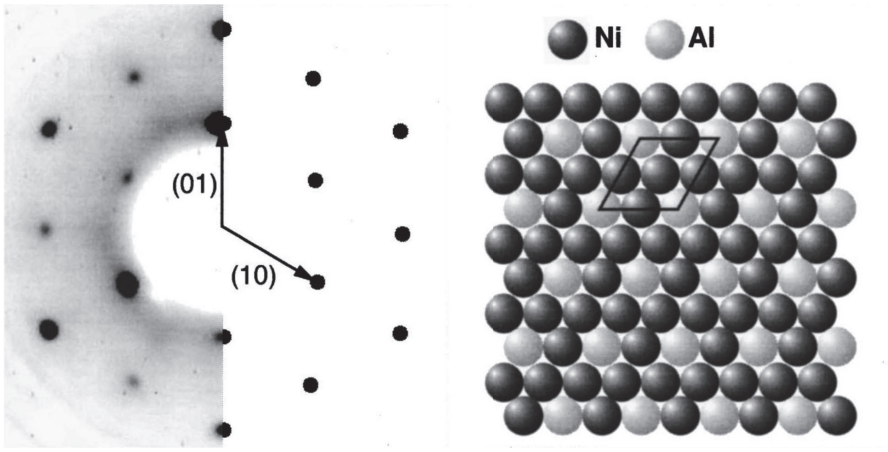

Figure 3.25: LEED pattern (E_K = 93 eV) and real space model of the clean $Ni_3Al(111)$ surface. The pattern is split vertically in experimental image (left) and a schematic representation (right). The surface unit cell is indicated by a rhombus. From Ref. [183].

film are very uniform and without apparent defects.

Further STM studies with atomic resolution and Spot Profile Analysis-LEED with a better reciprocal space resolution [187] disclosed that the "dot" superstructure is the actual real superstructure of the alumina film with an unit cell of $(\sqrt{67} \times \sqrt{67})R47.78°$ with a parameter b_{dot} = 4.16 nm [187] or b_{dot} = 4.14 nm [134] while the "network" structure is just a $(1/\sqrt{3} \times 1/\sqrt{3})R30°$ reconstruction with b_{net}=2.40 nm [187] or b_{net}=2.39 nm [134]. More accurate imaging could be obtained via dynamic Scanning Force Microscopy (SFM) [188] which showed

that six dark spots are arranged around the corner of the "dot" structure and the "network" structure covers the entire surface with a honeycomb-like atomic feature (Fig. 3.26) [188]. The commensurability of the substrate, dot structure and network structure is shown in Fig. 3.27. While the dot structure is commensurate with the (2×2) substrate (integer numbers in the transformation matrix), the network structure is incommensurate [187,188]. Finally, the main structural element of the oxide film is a lattice of hexagons (side length of 0.29 nm) that is pinned onto the 0.51 nm grid of the substrate [188]. It is assigned to a distorted hexagonal network of oxygen rotated by 30° from the substrate [185]. This large scale superstructure drew some attention also as a potential candidate to grow organised array of nanoparticles through preferential nucleation [213].

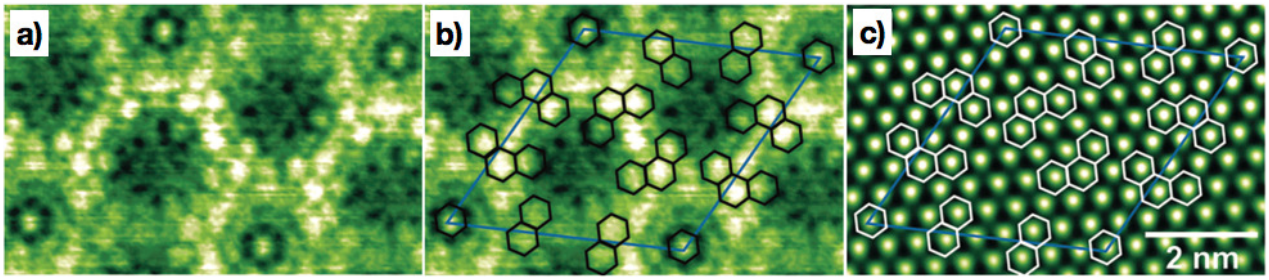

Figure 3.26: a) AFM imaging of the well ordered oxide film on a (2×2) $Ni_3Al(111)$ surface. b) Same image, with all recognizable hexagonal features. c) The open hexagons are centred on a hexagonal lattice with 0.51 nm periodicity, which is the aluminium sublattice of Ni_3Al substrate. From Ref. [188].

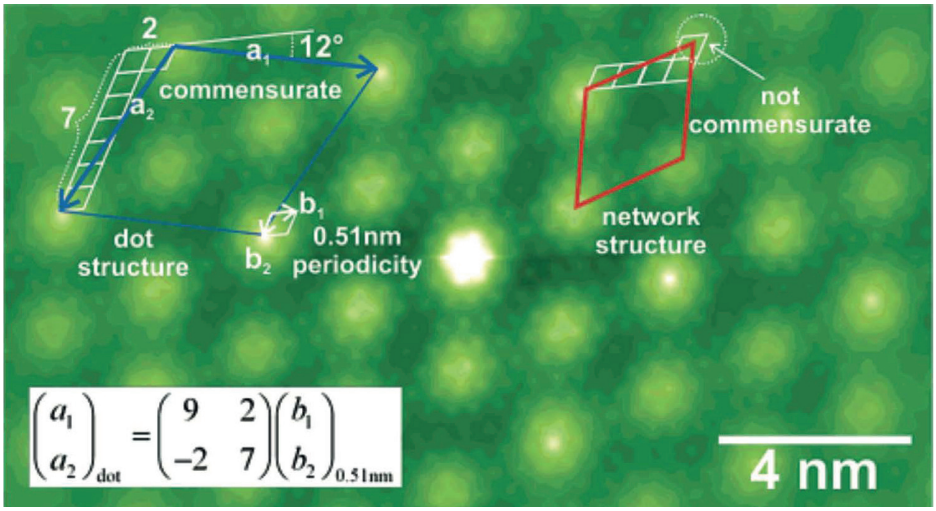

Figure 3.27: Real space unit cells of the $Ni_3Al(111)$ substrate (0.51 nm, white), the dot (blue) and the network (red) structures of the oxide. In contrast to the network structure, the dot structure is commensurate with the substrate lattice [188].

3.4.3.3 Al deposited on Ni(111)

NiAl surface alloys on Ni(111) [19, 140, 214–216] have also been used as substrates for the growth of ordered alumina thin films. Alloyed layers are obtained by progressive annealing up to 800 K of Al deposits of various amounts on Ni(111) leading to the formation of a relaxed

epitaxial NiAl(110) (B_2-CsCl structure) with three domains at 120° (NiAl[001]‖Ni[1$\bar{1}$0]) on top of a 18 (111) layers of Ni_3Al (fcc-$L1_2$ structure) in strained epitaxy on Ni(111). In the range of a few Al monolayers deposit, only the Ni_3Al epitaxial layer is observed while above 800 K, the alloy layer decomposes and Al diffuse into the bulk of Ni.

A well-ordered alumina film is obtained through a two-step recipe, after oxygen exposure at room temperature and annealing at 1000 K of $Ni_3Al(111)$ alloy layer on Ni(111) [216]. Ion beam analysis concludes at a stoichiometry close to Al_2O_3, a self-limited film thickness of 2.5 ML (two compact planes of oxygen) with a $(5\sqrt{3} \times 5\sqrt{3})R30°$ LEED structure quite different from that observed on $Ni_3Al(111)$ (see Sect. 3.4.3.2.6). The difference is assigned to the absence of Al in the substrate, this latter has diffused deeply in the bulk upon annealing treatment. However, LEED and STM analysis of Prévot *et al.* [140] indicates that the actual unit cell corresponds to a sixton rectangle (18.2×10.5 Å^2) inscribed into an hexagon with a ratio between the two sides of the mesh of $\sqrt{3}$. This value is assigned to a specific hexagonal arrangement of oxygen atoms in the plane. This hypothesis was further confirmed by an accurate X-ray diffraction determination of the atomic structure [19] that found an atomic arrangment very close to that proposed by Kresse for NiAl(110) [15] within small distortions and sharing similarities with η-Al_2O_3. The lack of registry and of modifications of the interfacial substrate atom positions lead Prévot *et al.* [19, 140] to suggest that the oxide film structure common to many substrates of different symmetries and crystalline structure is a paradigm of a free-standing oxide layer (NiAl(110)-Sect. 3.4.3.2.1, Cu-9 at.%Al(111) and γ-Al_4Cu_9(110)-Sect. 3.4.3.4, FeAl(110)-Sect. 3.4.3.6).

3.4.3.4 Cu-9 at.% Al(111) and γ-Al_4Cu_9(110)

Cu-9 at.% Al is a random alloy that crystallises in the fcc structure. When annealed at above 650 K, Al segregation generates a $(\sqrt{3} \times \sqrt{3})R30°$ superstructure, the corresponding LEED pattern and atomic model of which are displayed in Fig. 3.28 [18, 123, 189, 190].

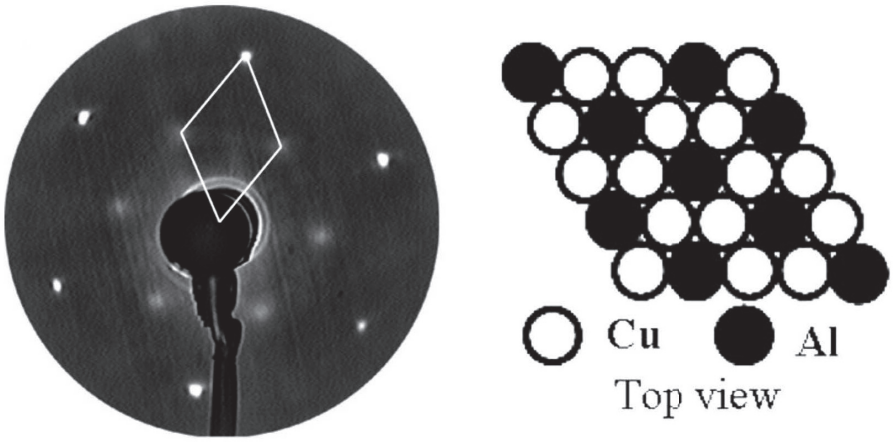

Figure 3.28: LEED pattern (left) and atomic model in real space (right) of clean Cu-9 at% Al(111) surface annealed at 953 K (E_K=90 eV; the reciprocal cell of $(\sqrt{3} \times \sqrt{3})R30°$ superstructure is marked. From Refs. [18, 190].

Starting from this surface, oxidation at $\geq$ 900 K leads to an ordered alumina film with a $(7/\sqrt{3} \times 7/\sqrt{3})R30°$ superstructure related to γ-Al_2O_3[100](111) ‖ [1$\bar{1}$0]Cu-9 at.%Al(111)

with a thickness of $\sim$ 4 Å [139, 191]. However, at the opposite to Refs. [139, 191], LEED analysis and atomic resolved STM study of this layer [18] point at a crystallographic structure with properties very similar to that of films obtained on NiAl(110). The film is formed by three domains with a large rectangular unit cell (18.2 $\times$ 10.6 Å) rotated by 18° and 30° with respect to the close-packed rows of the substrate. Beyond the matching of the unit cell with the structural model proposed by Kresse [15, 18] which is different from γ type alumina, a good agreement is also obtained on the atomic positions in STM (Fig. 3.29). 28 surface O atoms are arranged in squares and triangles with a p2gg symmetry while 16 interface Al atoms are arranged in heptagon and pentagon pairs, which agrees exactly with the structure on NiAl(110) [15, 18].

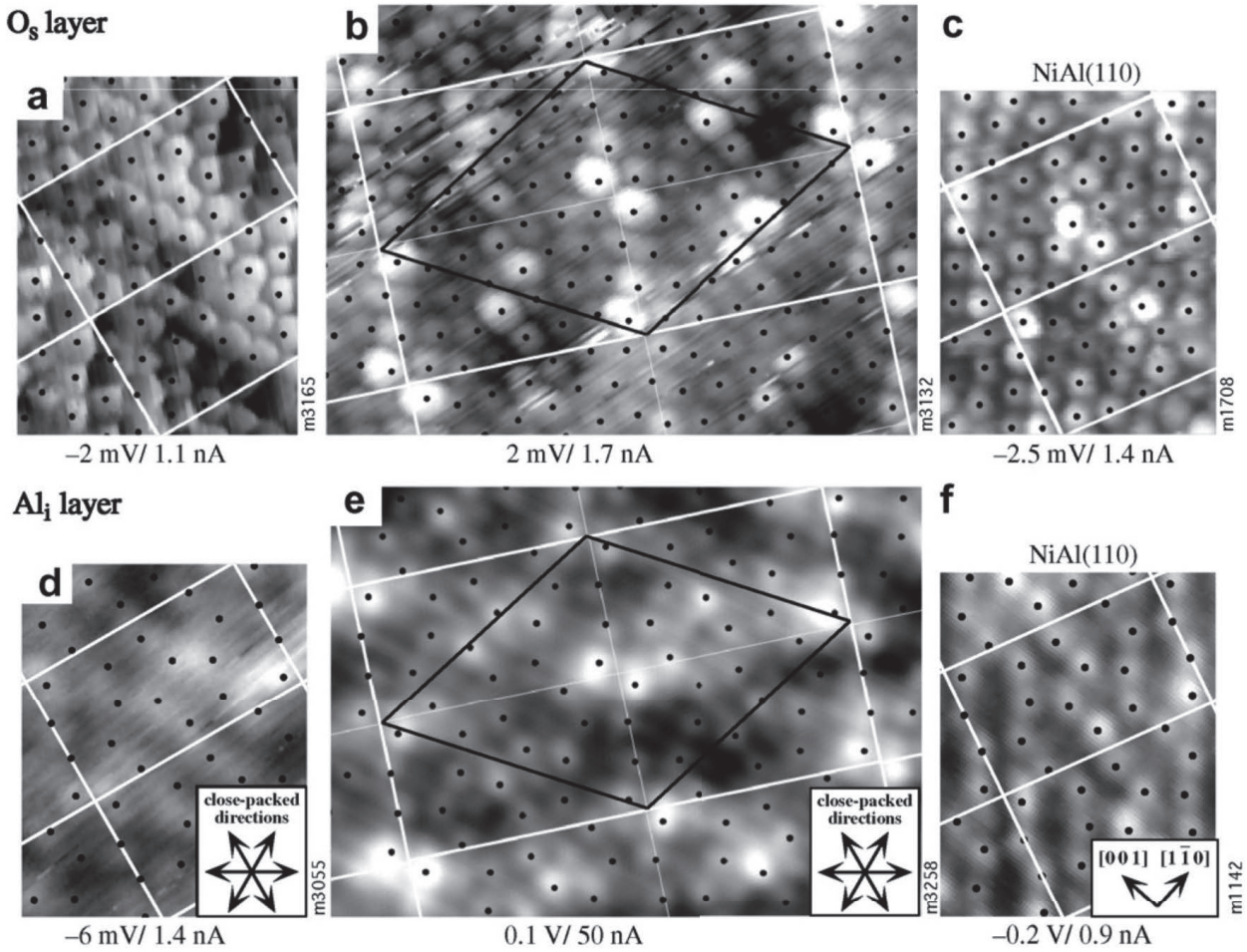

Figure 3.29: Atomic resolved STM images of an oxidised Cu-9 at.% Al(111) (100 L of O_2 at 953 K). a-c) The surface O layer and d-f) the interface Al layer visible at higher tunneling resistance. The left images (a,d) display the first (incommensurate) oxide structure and the centre images (b,e) show the second (commensurate) one. As a matter of comparison, the oxide on NiAl(110) is shown on right side. The dots mark the atomic positions of the alumina calculated on NiAl(110) [15]. In (b,e) the primitive unit cell is drawn in black and the four rectangular building blocks are marked in white. From Ref. [18].

The chemical states of alumina/Cu-9 at.% Al(111) were probed through core level and valence band photoemission. Core levels demonstrate the inertness of Cu; only Al is oxidised. Four components of Al $2p_{3/2}$ peak are presented after oxidation at 910 K: top Al layer of the clean alloy ($E_B = 72.40$ eV), Al in the bulk ($E_B = 72.58$ eV), the interface Al between alloy and epitaxial alumina ($E_B = 73.63$ eV) and Al in the alumina ($E_B = 74.90$ eV) [123]. The valence band spectra obtained with low energy photons at grazing emission reveal that, the position of the valence band maximum of alumina is 4.4 eV below the Fermi level of the substrate [123]. This value is considered being reasonable for Al interface termination from the reported results of first-principles calculations and similar to the well-ordered alumina on NiAl(110) [123, 192].

Amazingly a similar oxide structure as determined from LEED and STM has been obtained on the cubic Complex Metallic Alloy (CMA) γ-Al_4Cu_9(110) [217]. CMAs [218] are characterised by a unit cell containing from a few tens to several thousands atoms arranged into highly symmetric clusters; they share some similarity with quasi-crystals. Small oxide domains with the sixton rectangular unit cell (18.2×10.5 Å^2) rotated by $\pm 23.5°$ have been observed after annealing at 925 K the surface oxidised at room temperature. Heptagonal-pentagonal atomic arrangements characteristic of the Kresse's structure [15] appear on STM images.

3.4.3.5 CoAl(100)

CoAl crystallises in a cubic CsCl-B_2 lattice structure with a parameter of 2.86 Å [193]. The clean surface has a (1×1) LEED pattern with 40-100 nm wide terraces separated by 2.8 Å double atomic steps and it is enriched in Al after annealing at 1470 K for 10 min [124, 125].

High temperature oxidation of CoAl(100) at $\geq$ 800 K produces a well ordered θ-Al_2O_3 film showing a two-domain (2×1) LEED pattern having an epitaxial relationship identical to that of θ-Al_2O_3/NiAl(100) (Bain orientation, Fig. 3.30-b), thus leading to a small mismatch value of ~ 1 % along a_{ox}-axis and ~ 2 % along b_{ox}-axis directions [125, 162, 163]. Due to the substrate symmetry, the film presents two orthogonal domains as seen in STM (Fig. 3.30-a) with a self-limited thickness of ~ 10 Å [125] and has a band gap of ~ 4.5 eV [125, 194].

Besides θ-Al_2O_3 phase, it was reported also that phase transformations occur within alumina grown on CoAl(100): (i) single γ or four cubic γ' alumina leading to a $(2\sqrt{2} \times 2\sqrt{2})R45°$ superstructure [195], (ii) intermediate phases of alumina with a $c(2\sqrt{2} \times 6\sqrt{2})R45°$ LEED pattern, and (iii) α-like alumina [196]. It should be noted that the phase transformations were achieved by very specific treatments [195, 196].

3.4.3.6 $Fe_{1-x}Al_x$

The surface science studies of the oxidation of Fe-Al alloys are scarce maybe because of the intense segregation phenomena observed at their surfaces (see Sect. 3.3). Moreover, they are limited to ordered phases: B_2 (CsCl) $Fe_{0.53}Al_{0.47}$(110) (100) (111) [16, 93, 99, 137] and $D0_3$

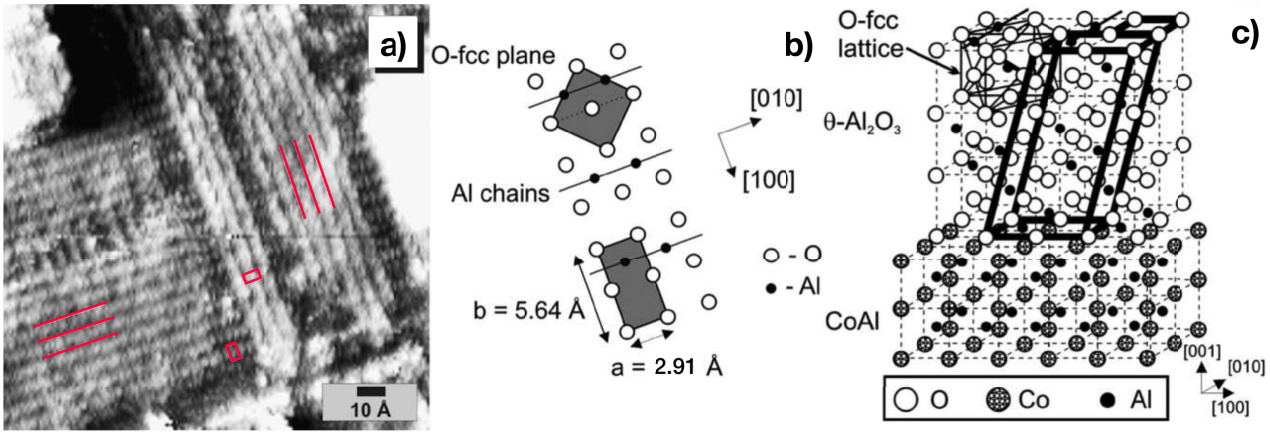

Figure 3.30: a) STM image of a CoAl(100) exposed to 10 L of O_2 at 800 K (U_b = 2.00 V, I_t = 0.2 nA). The two orthogonal domains of the oxide film are denoted by the red stripes. For each domain a unit cell is outlined. b) Top view model of the θ-Al_2O_3 surface plane with lattice parameters a_{ox} = 5.64 Å, b_{ox} = 2.91 Å. c) Structural model of the θ-Al_2O_3 grown on CoAl(100) where a monoclinic θ-Al_2O_3 unit cell and the close-packed oxygen fcc lattice are highlighted. For the sake of clarity, only the octahedral occupation of Al^{3+} ions are shown. From Ref. [125].

$Fe_{0.75}Al_{0.25}$(110) [219].

On $Fe_{0.53}Al_{0.47}$ [16], high temperature annealings (> 773 K) (with direct exposure to oxygen or with prior oxygen adsorption) are required to achieve ordered phases. Indeed, room temperature oxidation gives rise only to an amorphous oxide. For UHV exposures, the amorphous oxide has a thickness in the range 6 Å on all orientations. Electron spectroscopies clearly demonstrate that only Al is oxidised; Fe stays in its metallic state (Fig. 3.35-c), except at high oxidation rates for which the oxide thickness is larger ($\sim 10 - 30$ Å). This is in agreement with the hierarchy of enthalpy of formation of the aluminium and iron oxides ($\Delta H(Al_2O_3) = -1676$ kJ/mol, $\Delta H(Fe_2O_3) = -826$ kJ/mol, $\Delta H(Fe_3O_4) = -1118.4$ kJ/mol, $\Delta H(FeO) = -278.0$ kJ/mol) [22]). At room temperature, the oxygen uptake of a clean surface [16] follows a two-step regime, the first one corresponding to the reaction of available Al atoms at the surface, the second to a much slower thickening of the oxide film through a Cabrera-Mott process [197]. All films are found thermally unstable above 1073-1173 K, an instability assigned to Al evaporation from the interface between the oxide overlayer and the substrate.

3.4.3.6.1 $Fe_{0.53}Al_{0.47}$(110) In the range of 773-1173 K, the formation of well-ordered oxide film is observed; it grows in island mode at low exposure (10 L) before covering the whole surface (1000 L) [16]. According to the authors [16], the LEED pattern of the film shares some similarities with that observed on NiAl(110) although the LEED overlap is not fully convincing (see Fig. 3.17) [2]. By a simple analogy with NiAl(110), Graupner *et al.* claimed that the

[2] As we will see in Chap. 6.2.2.1, it is difficult to determine precisely such a large unit cell with a conventional LEED.

film structure involves a quasi-rectangular unit cell with two domains (due to the two-fold symmetry of the substrate) given by the matrix $M_s = \begin{bmatrix} 3.37 & -1 \\ 2.53 & 4 \end{bmatrix}$ and $\begin{bmatrix} -3.37 & -1 \\ -2.53 & 4 \end{bmatrix}$. The film thickness is evaluated around 6 ± 1 Å. Besides the two-domain diffraction spots in the LEED pattern, a streak phase (Fig. 3.31-b) is always observed (i) on surface oxidised at 773-973 K and (ii) at higher temperature but for large exposure (10^4 L) indicating a total disorder along $[1\bar{1}0]$ direction but a long-range order along [001] direction. No explanation was given for this structure; but a similar streak phase was observed in our measurements on the clean surface and assigned to C contamination (see Chap. 4).

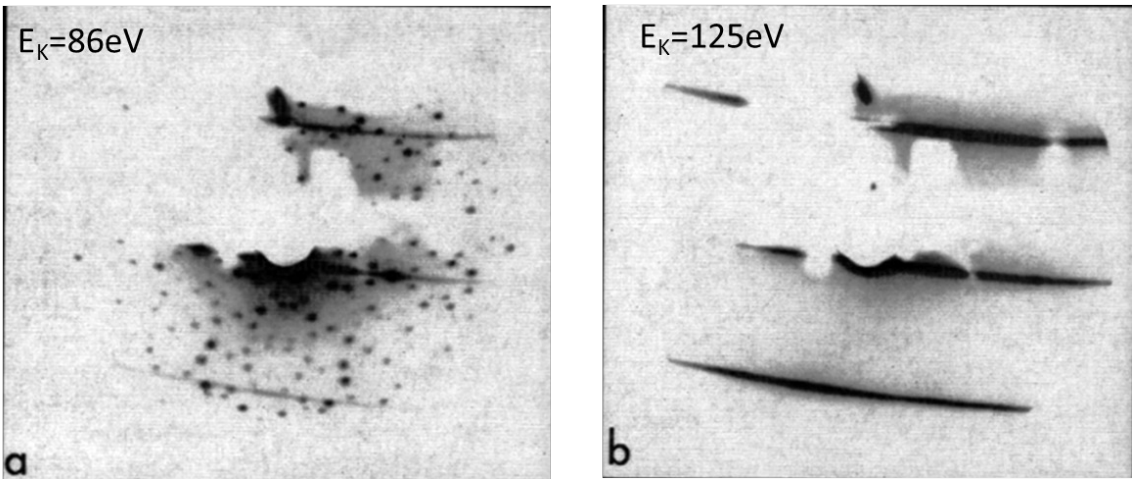

Figure 3.31: LEED patterns obtained after high temperature oxidation of $Fe_{0.53}Al_{0.47}(110)$ at 1123 K: a) oxidation with 1000 L of O_2 (E_K = 86 eV) and b) streak phase observed after exposure to 10^4 L of O_2 (E_K = 125 eV). From Ref. [16].

Only two articles [99, 137] dealt with STM measurements on oxidised $Fe_{0.53}Al_{0.47}(110)$ (Fig. 3.32). The proposed unit cell from STM measurements (18.6×19.4 Å^2 rotated by 30° with respect to $[1\bar{1}0]$ direction) is weird compared to LEED [16], all the more that, according to the authors, only one domain is present on the surface. Based on earlier theoretical model of thin alumina films [180, 220], they proposed an hypothetical structure model for alumina where Al cations are arranged in nearly the same plane as O anions with Al ions situated in octahedral and tetrahedral sites in the form of zigzag and stripe structures [137].

3.4.3.6.2 $Fe_{0.53}Al_{0.47}(100)$ High temperature oxidation of $Fe_{0.53}Al_{0.47}(100)$ (100 L of O_2 at 773-1173 K) creates an ordered alumina with a thickness of 3-5 Å; it presents (i) a $c(6 \times 6)$ (unit cell 12.2×12.2 Å^2) at 973 K and (ii) a two-domain (2×1) LEED pattern with a streaky structure along [010] and [001] directions at 1123 K [16] (Fig. 3.33-a,b). A very similar $(2 \times 1) + (1 \times 2)$ LEED pattern was also observed on $Fe_{0.85}Al_{0.15}(100)$ [93], NiAl(100) (see Sect. 3.4.3.2) and CoAl(100) (see Sect. 3.4.3.5) surfaces. In the latter case, it was assigned to the growth of a θ-Al_2O_3 film in Bain orientation [162, 163] (see Sect. 3.4.3.2, Fig. 3.21). The thickness of alumina on $Fe_{0.53}Al_{0.47}(100)$ is found around $d = 3 - 5$ Å [16, 93].

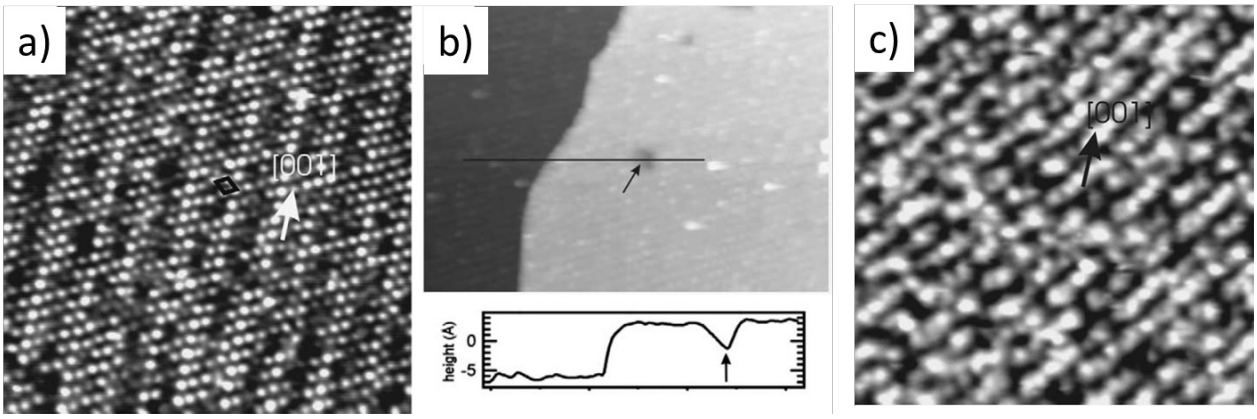

Figure 3.32: STM images of a well ordered alumina film on $Fe_{0.53}Al_{0.47}(110)$ surface (1000 L of O_2 at 1125 K). a) 70×70 nm^2, $U_b = -1.25$ V, $I_t = -0.7$ nA; a tentative unit cell (18.6×19.4 Å^2) is shown. b) 69×100 nm^2, $U_b = 1.25$ V, $I_t = 0.17$ nA; the line profile goes through a step edge and a hole in the layer. c) 50×50 nm^2, $U_t = 3.02$ V, $I_t = 1.04$ nA. A line pattern appears at positive bias. From Ref. [137].

3.4.3.6.3 $Fe_{0.53}Al_{0.47}(111)$ Since the $(\sqrt{3} \times \sqrt{3})R30°$ reconstruction of the (111) orientation is unstable above 873 K, only the disorder phase of (111) was oxidised at 973 K (250 L of O_2) leading to the formation of a complex $(6.4 \times 6.4)R30°$ incommensurate oxide superstructure (lattice parameter 26 Å) (Fig. 3.34), with a thickness of $d = 6 - 8$ Å.

3.4.3.6.4 Photoemission fingerprints of the oxide at $Fe_{0.53}Al_{0.47}$ surfaces Besides the metallic state ($E_B = 72.0$ eV), the Al 2p of amorphous oxide is characterised by a shoulder component shifted by 1.5-2.8 eV with increasing O_2 exposure up to 10^4 L. For structured oxides, it has been shown that all the surfaces of $Fe_{0.53}Al_{0.47}(110)$, (100) and (111) give rise to at least two chemically shifted Al 2p components [16, 99] (see Fig. 3.35). The major one associated with the largest binding energy ($\Delta E_B = 3 - 3.6$ eV) corresponds to the bulk of the Al_2O_3 film and the minor one with the smallest binding energy ($\Delta E_B = 0.7 - 1.6$ eV; $\Delta E_B(110) = 1.2$ eV, $\Delta E_B(100) = 1.2$ eV, $\Delta E_B(111) = 1.5$ eV) is tentatively assigned, not to defects, but to under-coordinated atoms at the interface. The width of the peak is close to experimental resolution pointing at well defined chemical environments. However, the only available Al 2p peak fitting [16] is questionable since it involves a subtraction of the metallic component prior to Shirley background subtraction and does not take into account the spin-orbit splitting of the Al 2p lineshape. Finally, as shown by band structure measurements, the oxide on $Fe_{0.53}Al_{0.47}(110)$ exhibits a highly two-dimensional electronic structure in accord with its small thickness [99].

3.4.3.6.5 $Fe_{0.75}Al_{0.25}(110)$ According to the X-ray diffraction study of Ref. [219], the clean $Fe_{0.75}Al_{0.25}(110)$ comprises a top-most atomic layer with a B_2 order on top of a bulk $D0_3$ ordered crystal. Upon oxidation at 573 K (1400 L), the crystalline order disappears over a depth of 2-3 nm; at the same time a thin smooth oxide is formed on the surface. While the

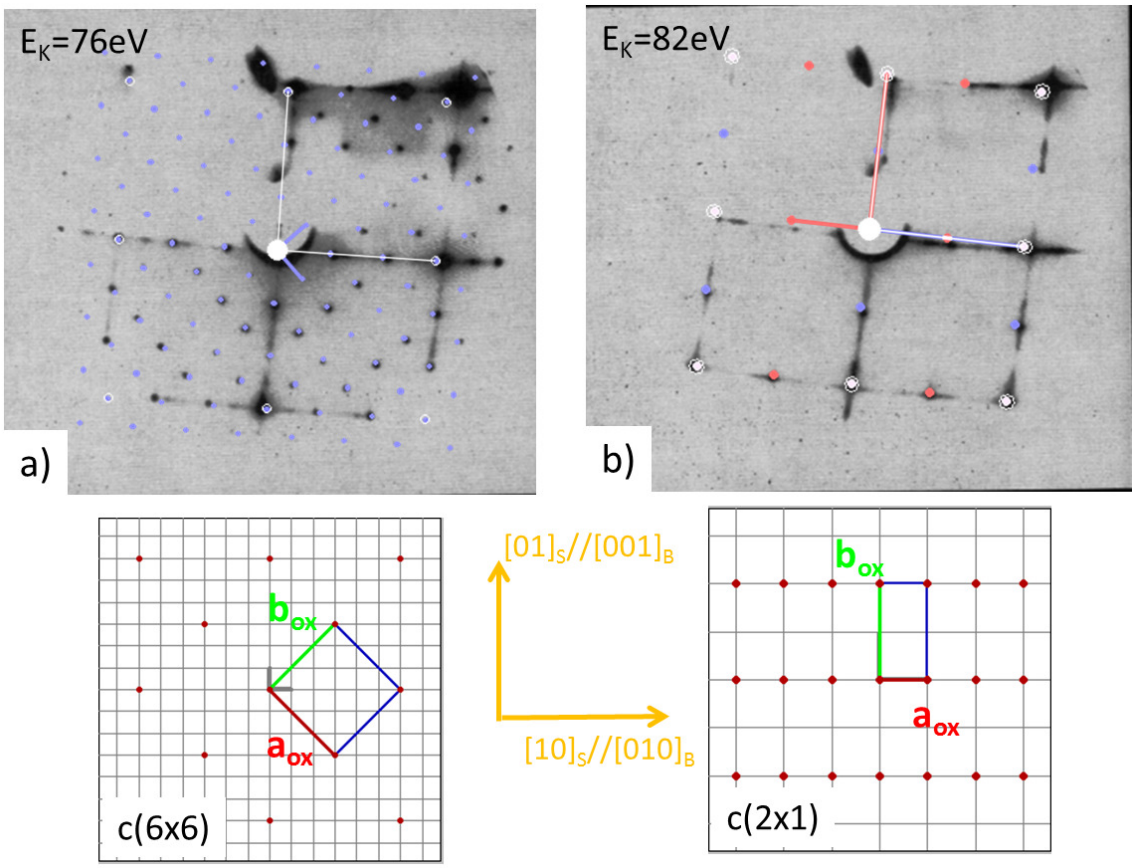

Figure 3.33: LEED patterns of the oxide layer formed by high temperature oxidation of $Fe_{0.53}Al_{0.47}(100)$ with 250 L of O_2: a) at 973 K and b) 1123 K. LEED is overlapped with a) a c(6 × 6) (matrix $\begin{bmatrix} 3 & -3 \\ 3 & 3 \end{bmatrix}$) superstructure or b) a (2 × 1) superstructure with the two equivalent domains. Corresponding direct spaces are shown below where the grey grid corresponds to surface nodes and red dots to oxide unit cell. Interpreted from Ref. [16].

clean surface is Al enriched, oxidation induces a disordered depleted subsurface region (see Fig. 3.36).

3.4.4 Common fingerprints of ultrathin oxide films formed on Al-alloys

From the above brief overview of the studies of oxidation performed on some metallic Al-alloys [12], a common set of conclusions can be drawn:

- the difference of electronic affinity between the alloying element and aluminium in the studied transition metal aluminides is enough to favour only the formation of an aluminium oxide layer; all chemical sensitive spectroscopies (photoemission or Auger spectroscopy) clearly rule out any trace of oxidation of the alloying elements when films

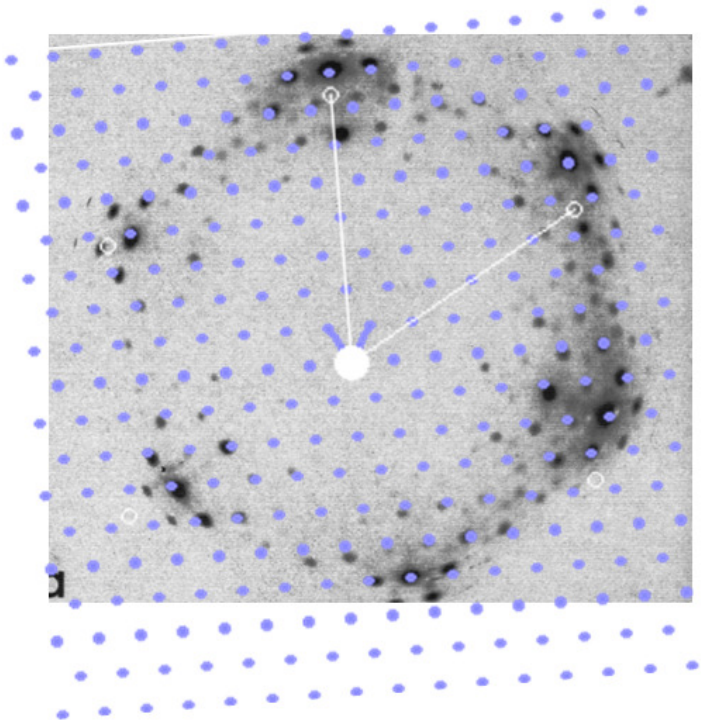

Figure 3.34: LEED pattern of the oxide layer formed by high temperature oxidation (973 K, 250 L of O_2) of FeAl(111) overlapped with the proposed $(6.4 \times 6.4)R30°$ reconstruction. From Ref. [16].

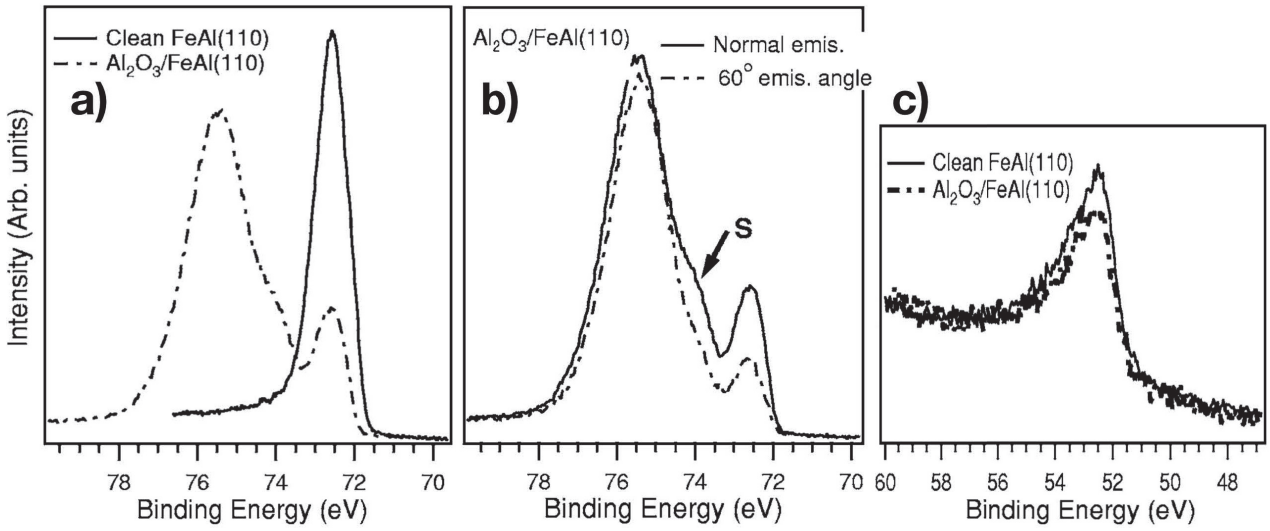

Figure 3.35: Al 2p core level spectra of $Fe_{0.53}Al_{0.47}(110)$ surface. a) Comparison of clean and oxidised surfaces at normal emission; b) Spectra of the oxidised surface at normal (0°) and grazing (60°) emission, revealing a weak shoulder assigned to the existence of interfacial Al atoms; c) Comparison of Fe 3p spectra of clean and oxidised surfaces showing the lack of chemical shift. The photon energy is 150 eV. From Ref. [99].

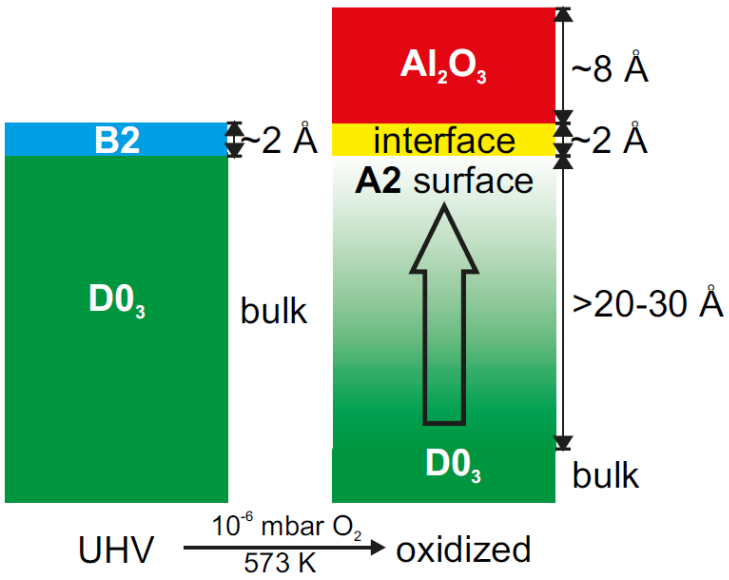

Figure 3.36: Schematic profile of composition and structure of $Fe_{0.75}Al_{0.25}(110)$ before and after oxidation. From Ref. [219].

are grown in UHV conditions *i.e.* in the Knudsen's regime at low exposure; only high exposure rates are needed to deplete the subsurface in aluminium and counterbalance its bulk diffusion rate resulting in the oxidation of the other alloying elements;

- an amorphous oxide is formed at room temperature following chemisorption on aluminium; the formation of well-ordered alumina layer requires a post-annealing step at high temperature (700-1200 K) or a direct oxidation at elevated temperature; in this respect, alloys with high melting temperature like NiAl or FeAl are ideal candidates;

- the film thickness is self-limited, typically to a few compact atomic plane of oxygen ($\sim 5-10$ Å); thickening requires much higher oxygen activity and exposure; if determined, the stoichiometry is close to Al_2O_3 and the last-plane is made out of oxygen atoms at the opposite of bulk α-$Al_2O_3(0001)$;

- phase transitions in the film have been rarely highlighted; annealing allows to recrystallise the film, the structure of which never depends on the initial reconstruction of the substrate;

- oxidation induces segregation/depletion in aluminium in the subsurface region; bulk compounds with a narrow composition windows in the bulk phase diagram seem to be more prone to maintain a fixed composition underneath the oxide by dissolving the produced defects; but these points are poorly explored in the literature due to the lack of subsurface or bulk sensitive tools (except with ion beam measurements of Ref. [216] or X-ray diffraction [219]);

- due to the structural complexity, the analysis of the LEED pattern or the interpretation of the STM images does not allow to establish a given model; but STM measurements are crucial for the determination of the topographic defects of the layer; most of the discussions on the structure of the alumina film are based on epitaxy arguments and

on the similarity with bulk alumina compounds in terms of vibrational fingerprints; but the few available structural determinations (*i.e.* atomic positions) [15, 19, 149] point at strong distortions and/or unusual occupancy of octahedral/tetrahedral sites for Al;

- despite a blurred landscape due to the complexity of multiple domains, some structures appear to be recurrent; one can quote: (i) the large $Al_{10}O_{13}$ structure with a sixton rectangular unit cell ($\sim 18\times10$ Å^2) historically studied and solved on NiAl(110) [15,149] but presents on many substrates of different crystallographic structures, symmetries or degrees of order (NiAl(110), γ-Al_4Cu_9(110), FeAl(110), Al on Ni(111), Cu-9 at.%Al(111)) or (i) the θ-distorted alumina assigned to the Bain epitaxy between the fcc stacking of oxygen at the substrate (NiAl(100), CoAl(100)).

Even if we will see that the oxide layers formed on $Fe_{0.85}Al_{0.15}$ (see Chap. 6) do not escape the last two cases, the random character of the alloy provides an extra degree of flexibility in terms of segregation that was poorly explored up to now.

CHAPTER 4

TOWARDS CLEAN $FE_{0.85}AL_{0.15}$ SURFACES: CARBON SEGREGATION AND SURFACE REACTIVITY

This thesis focuses on the aluminium segregation and oxidation processes at the surfaces of $Fe_{0.85}Al_{0.15}$ alloy. It has been chosen to study this composition as a model system for alloyed-steel (see Chap. 1) since, in the temperature range under study (300-1100 K), the alloy matrix corresponds to the ferritic solid solution which has a body centred cubic structure (labelled A_2 in Fig. 3.1) as in the case of the industrial Al-alloyed steel grades. The three low index surfaces (110), (100) and (111) have been considered herein; their schematic bulk truncation and surface unit cells are shown in Figs. 3.3-3.4-3.5. The present chapter focuses on the preparation of atomically clean and well-crystallised surfaces which is a prerequisite of any surface science analysis of their intrinsic properties. During the course of surface preparation (described in Sect. 2.2), it turned out that the $Fe_{0.85}Al_{0.15}$ surfaces were very sensitive to contamination by non metal elements, in particular carbon as any surface of pure or alloyed iron.

Carbon coverage can increase in two ways, reaction with gases from the environment [221] and segregation upon annealing [222–225]. The present concern is to study the behaviour of the Fe-Al surfaces with respect to the two phenomena, in order to find protocols to prepare clean surfaces and to keep them in this condition during specific treatments. According to litterature [221], the reactivity of surfaces of iron single crystals with alcene molecules is in the order Fe(100) > Fe(111) > Fe(110). The same hierarchy is observed for the surface oxidation of FeAl single crystal surfaces at room temperature [16]. The two observations fulfil the expectation that the denser (110) surface (see Sect. 3.2.1) is the less reactive. Therefore, it is chosen herein to describe (i) the transient carbon segregation observed during the preparation of the as-received $Fe_{0.85}Al_{0.15}$(110) in conditions in which the reaction with the residual vacuum is marginal and (ii) the reaction with UHV of the more reactive $Fe_{0.85}Al_{0.15}$(100) and (111) surfaces. Astonishingly, bulk carbon segregation was not observed on the as-received (100) and (111) crystals. All the surfaces were found free of other common contaminants of

Fe [223], such as sulphur or phosphorous but it turn out that oxygen removal after oxidation required intensive sputtering-annealing cycles.

4.1 Carbon segregation at the $Fe_{0.85}Al_{0.15}(110)$ surface

4.1.1 Graphitic films, chemisorbed carbon and carbide

To study the segregation of carbon, the as-received $Fe_{0.85}Al_{0.15}(110)$ surface was firstly degassed at ≥ 650 K and then cleaned by cycles of Ar^+ ion sputtering and annealing at increasing high temperatures in ultra-high vacuum. The transient phenomenon of carbon segregation was analysed through the analysis of C 1s, Al 2p and Fe 3p core level spectra (Fig. 4.1) upon annealing between 670 and 1070 K. The absence of a shoulder on the high binding energy of the metallic Al 2p component at 72 eV is a clear proof of the bulk origin of carbon since contamination from residual vacuum is always accompanied by oxidised Al species (see Fig. 4.10). The Al 2p peak can be decomposed into one spin-orbit split (0.4 eV) asymmetric Doniach-Sunjic line (Fig. 4.1-b and Sect. 6.2.1.2 for explanation and parameters) characteristic of the metallic state. At all temperatures but 870 K, the carbon spectra can be decomposed into two components with Gaussian shapes, one represented by a rather sharp peak at 282.7 eV (1-1.3 eV FWHM) and the other by a broad feature at 284.9 eV (3.5-3.9 eV FWHM). These binding energies correspond quite well to those of chemisorbed carbon and graphitic carbon that were found on Fe(100) at 282.6 eV and 284.6 eV, respectively, by Panzner *et al.* [224]. The labelling [224] comes from the similarity of lineshape between graphitic carbon and bulk graphite. Although aluminium carbide Al_4C_3 has a C 1s signature at 282.4 eV [226], its formation can be ruled out since the strong charge transfer to aluminium gives rise to an Al 2p component at 74 eV that is absent in our data. In the case of the 870 K annealing, the broad C 1s component peaks at 284.3 eV (Fig. 4.1). This makes possible the existence of a contribution from iron carbide Fe_3C associated to C 1s binding energies ranging from 283.4 eV to 283.7 eV [224, 225, 227, 228], although it has not been possible to evidence the Fe 3p component shifted by ~ -1.5 eV with respect to the metallic contribution, which was shown to characterise iron carbide [228].

Carbon was quantified as a function of the annealing temperature through the analysis of the ratio of $I_{C\,1s}/I_{Fe\,3p}$ and $I_{C\,1s}/I_{Al\,2p}$ integrated peak area after profile decomposition and subtraction of a Shirley background (Fig. 4.2). The ratios have been firstly corrected from ionisation cross section and analyser transmission function (see Tab. 5.1 for used parameters). Then they have been modelled in the framework of two schematic approaches. The carbon is either assumed to be evenly distributed in the bulk of the alloy (Figs. 4.2-c,d) or fully segregated as a film supported on the surface of the alloy (Figs. 4.2-a,b). Both models are detailed in Sect. 2.5.3.2 and are sketched in Fig. 5.3. In a first step, the bulk composition of the alloy required as a reference was assumed to be given by the nominal $x = 0.15$ value (Figs. 4.2-a,c). In a second step, the analysis was further refined by taking into account the actual profile of Al segregation found through the analysis of the angular dependence of Al 2p/Fe 3p ratio as developed in the next chapter 5.1 (Figs. 4.2-b,d). The question of the determination of

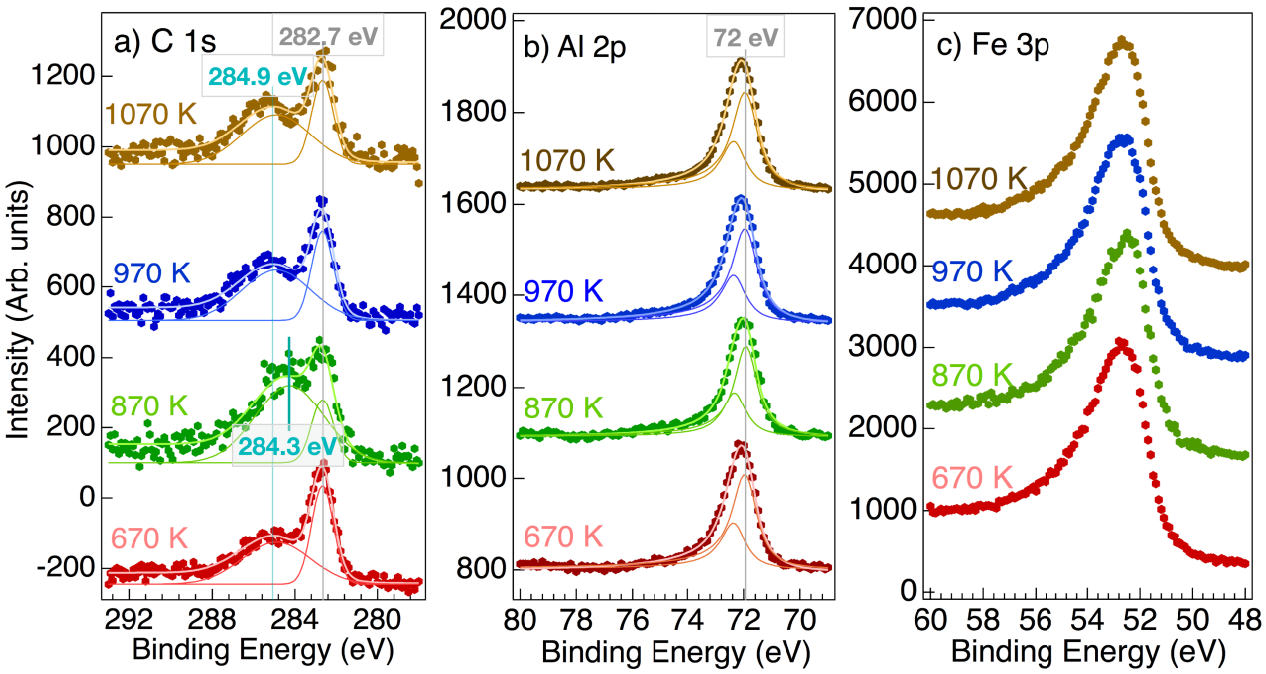

Figure 4.1: C 1s, Al 2p and Fe 3p core level photoemission spectra recorded upon annealing of the $Fe_{0.85}Al_{0.15}(110)$ surface at 670 K, 870 K, 970 K and 1070 K. XPS spectra are normalised to the maximum intensity of the main peaks. The decomposition of the lines is discussed in the text. Normal emission was used at a pass energy of $E_p = 20$ eV.

inelastic mean free paths in the alloy is postponed to Sect. 5.1.1. Regarding the damping of the photoelectron signal in the hypothetical carbon layer, values of inelastic mean free paths obtained with the TPP-2M predictive formula of Tanuma, Powell and Penn [57–66] in bulk graphite (2.26 g.cm^{-3}) at Al-Kα excitation were used: $\lambda^{graphite}_{Fe3p} = 38$ Å and $\lambda^{graphite}_{Al2p} = 37.6$ Å.

As shown in Figs. 4.2-a,c, the $I_{C\,1s}/I_{Fe\,3p}$ ratio peaks at 870 K prior to a strong decrease. The increase in C 1s intensity is mostly due to the C 1s graphitic component at > 284 eV (Figs. 4.2-a,c). Conversely, the C 1s contribution at 282.7 eV due to chemisorbed carbon is almost constant throughout the annealing process (Figs. 4.1-a,c). The model of carbon homogeneously distributed in the bulk leads to values of carbon concentration (10-25 at.%) which are expected to give rise to a sizeable content of carbides, in particular by annealing at 1070 K [229]. Such occurrence does not corresponds to the STM observations of the next section 4.1.2. In contrast, the thin carbon film model (Fig. 4.2-b) in which graphitic carbon dominates up to form 2.5 atomic layers is reminiscent of observations made for similar carbon segregation at the surface of pure iron [222, 224, 230, 231]. The known limit of solubility of carbon in iron (Fig. 4.3-a) is such that carbon tends to segregate at low temperature to give rise to surface graphite [222, 224, 230, 231], the exact temperature range depending on the carbon content of the metal [222]. At low carbon content, the $Fe_{0.85}Al_{0.15}$ alloy is expected to behave in a way similar to pure iron, which means that it involves bcc FeAl alloy (instead of bcc iron) and graphite [229]. As for the iron carbide Fe_3C which is possibly identified at

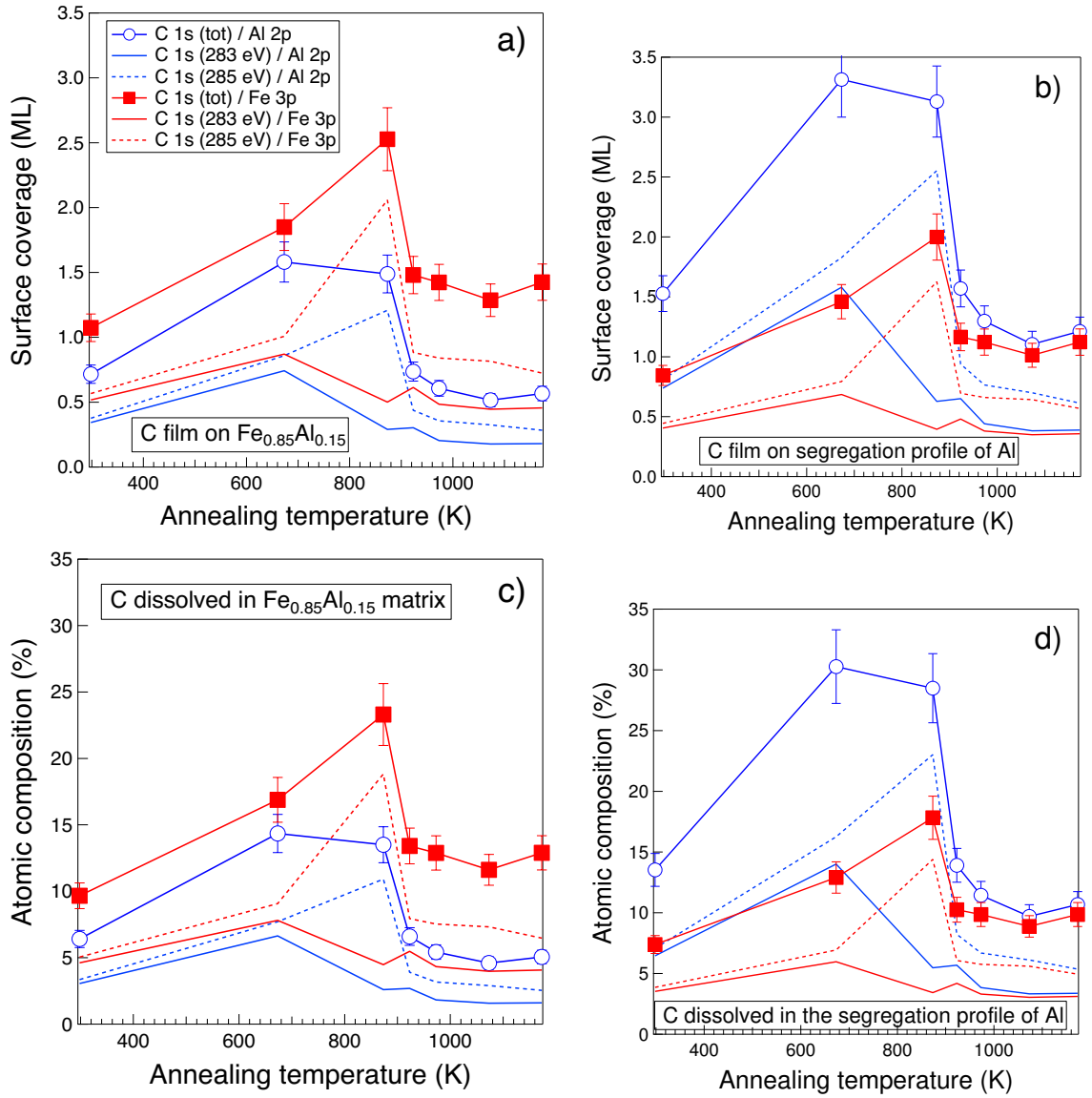

Figure 4.2: Quantification of carbon coverage from C 1s/Al 2p and C 1s/Fe 3p ratio. a)b) Model of segregated layer and c)d) model of bulk impurities starting from a)c) the $Fe_{0.85}Al_{0.15}$ bulk composition and b)d) the profile of Al segregation (see text). Coverage are given in terms of (110) monolayer. Error bars stem from uncertainties of 10 % on the ratio of intensities.

870 K (Fig. 4.1-a), it appears in bulk iron at carbon contents higher than the limit of solubility of carbon (Fig. 4.3-b) [232]. Its formation is endothermic on iron surfaces [227, 233] and it is not favoured either on Al-poor bcc FeAl alloys with low carbon content [229]. Therefore, carbide Fe_3C may be observed in the presence of graphitic carbon, but as a minority component [224, 227].

Annealing not only induced carbon segregation but also an enrichment of the surface with aluminium as testified by the increase of $I_{Al\,2p}/I_{Fe\,3p}$ ratio (Fig. 4.4). This segregation

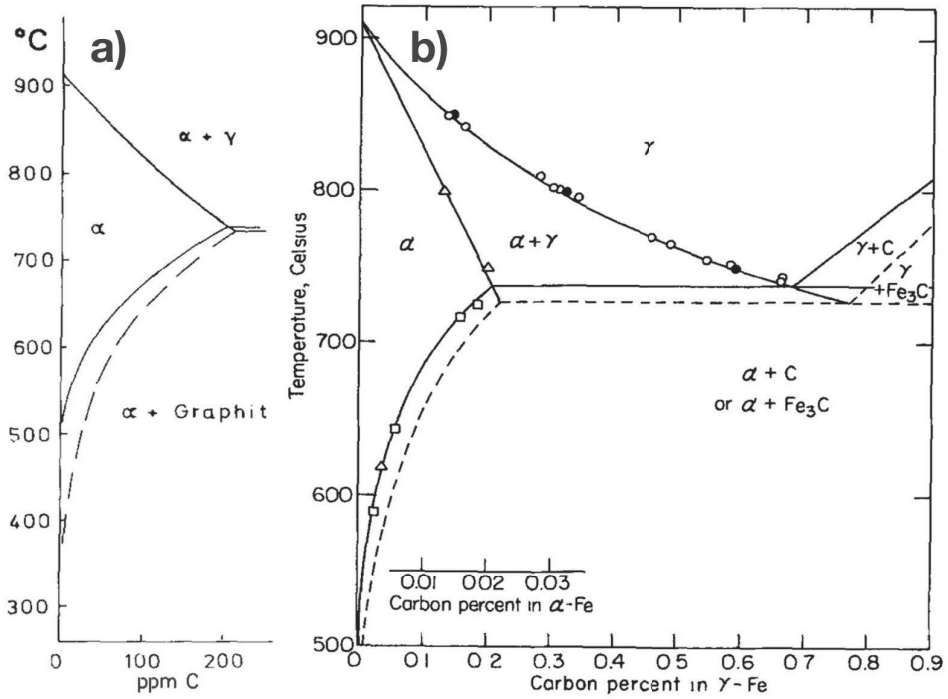

Figure 4.3: a) Carbon solubility at low-carbon concentration in the α (bcc) phase of the C-Fe binary phase diagram [222]; b) C-Fe phase diagram where the dashed lines indicates the metastable Fe-Fe_3C system [232].

phenomenon will be described in depth in the next chapter 5 for all clean surface orientations. Therefore, by using as a reference the bulk composition $Fe_{0.85}Al_{0.15}$ (Figs. 4.2-a,c), a clear discrepancy shows up between results obtained from $I_{C\,1s}/I_{Fe\,3p}$ and $I_{C\,1s}/I_{Al\,2p}$ ratios. But by using the profile of segregation found after annealing at high temperature (Sect. 5.1.2.2), the problem is cured (Figs. 4.2-b,d) at temperature above 900 K but worsens below. As shown in Sect. 5.1.2.2, this onset of temperature corresponds to development of a stationary Al profile of segregation. But below 900 K, the coupling of C and Al segregation prevents a straightforward quantitative analysis although the $Fe_{0.85}Al_{0.15}$ homogeneous alloy model is probably a faithful reference below 600 K since Al segregation is not so predominant in this temperature range.

4.1.2 Carbon-induced stripes

4.1.2.1 STM observation

As seen in large scale STM images of Fig. 4.5, the segregation of carbon at the $Fe_{0.85}Al_{0.15}(110)$ surface upon successive anneals is accompanied by the formation of self-organised equidistant stripes of tens to hundreds of nanometres long which protude over the average surface whatever the bias voltage. In parallel, a straightening of step edges as well as an enlargement of the terrace size is observed. Below 700 K (Fig. 4.5-a), the (110) surface shows terraces that are irregular in shape. Between 690 and 760 K (Fig. 4.5-b), stripes develop along the $[001]_B$

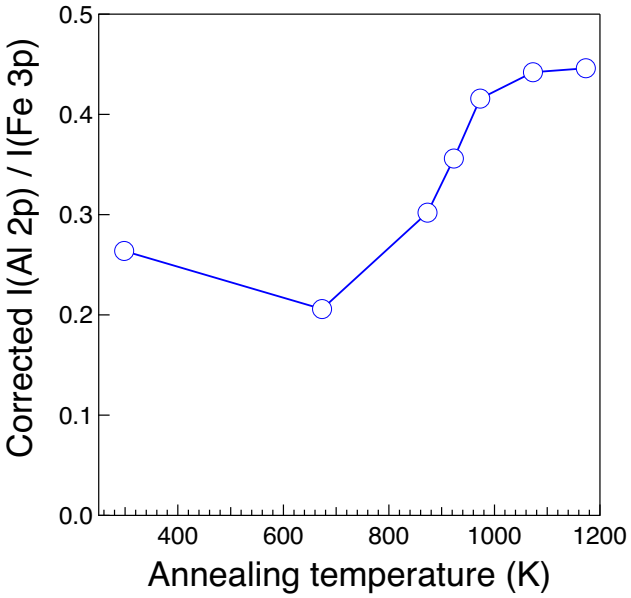

Figure 4.4: Evolution of the $I_{Al\,2p}/I_{Fe\,3p}$ ratio as function of the annealing temperature on samples showing bulk carbon segregation.

bulk direction (or $[01]_S$ surface direction) while straight steps form in the same direction. Upon annealing to higher temperatures (Fig. 4.5-c), the coverage of stripes increases while kinked steps rotated by 142° from $[001]_B$ develops. The step height is found close to 2 Å in agreement with the $a_B/\sqrt{2} = 2.04$ Å bulk $Fe_{0.85}Al_{0.15}$ expectation. Herein, the coverage of stripes is qualitatively determined by calculating the ratio between the apparent area covered by stripes and the corresponding image area. It reaches a maximum of 34 % at 950 K where the average distance between lines amounts to $\sim$ 5 nm, as measured through line profiles along the $[10]_S$ direction (Fig. 4.6-b inset). When annealing temperature rises to 1030 K, stripes fade out by decreasing in length leading to a surface coverage of 13 % and to larger stripe free domains in which the bare reconstructed FeAl surface is exposed (Fig. 4.5-c,d).

On the enlarged image shown in Fig. 4.6-a, stripes appear not to be continuous from one terrace to the other. Their apparent height varies between 0.5-2.0 Å (Fig. 4.7-b). It should be noted that the height of stripes largely depends on the location of measurement, thus the results are basically indicative of a general distribution. The distance between rows is not constant. It passes through a minimum after annealing at 950 K (Fig. 4.7-a) but shows deviation up to 2 nm. Meanwhile, annealing the $Fe_{0.85}Al_{0.15}(110)$ surface also triggers Al segregation (Fig. 4.4 and Chap. 5). The pseudo-hexagonal superstructure that is observed between stripes (Fig. 4.6-a) is attributed to a Fe-Al surface compound due to Al segregation, which will be analysed in detail afterwards (Sect. 5.2.1,5.3.1). Differences in contrast are observed when switching from positive to negative bias (Fig. 4.6-a,b).

The evolution of the stripes coverage as function of temperature parallels unambiguously that of the intensity of high-lying C 1s component observed at 284.3-284.9 eV (Fig. 4.1-a), with a maximum around 900 K (Figs. 4.2). Such a behaviour indicates that the stripes that are associated with graphitic carbon diffuse back partially into the substrate above 900 K as

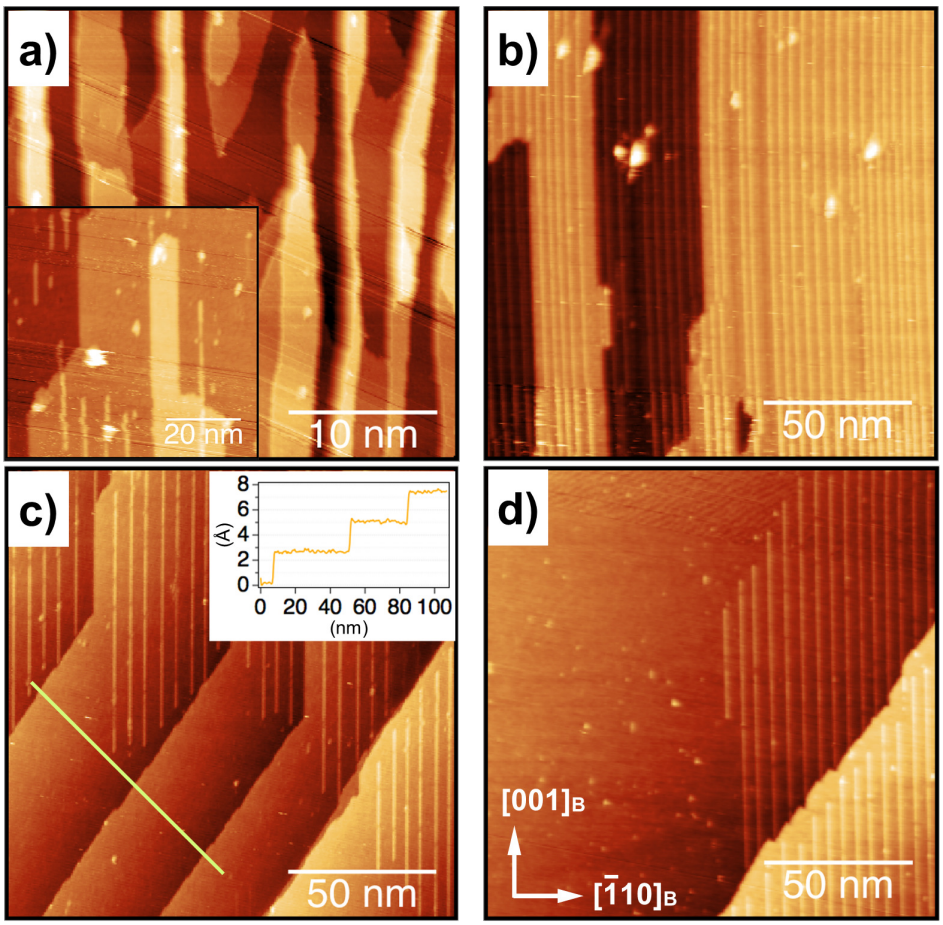

Figure 4.5: STM imaging of $Fe_{0.85}Al_{0.15}(110)$ upon annealing at increasing temperature: a) 690 K, 30×30 nm^2, $U_b = -1.0$ V, $I_t = 1.9$ nA; inset annealed at 760 K, 67×67 nm^2, $U_b = +1.7$ V, $I_t = 2$ nA; b) 950 K, 150×150 nm^2, $U_b = -1.0$ V, $I_t = 80$ pA; c) 1030 K, 150×150 nm^2, $U_b = -1.0$ V, $I_t = 80$ pA; d) 1070 K, 150×150 nm^2, $U_b = -1.0$ V, $I_t = 1.2$ nA.

observed for CO dissociated on FeAl(110) [101] [1], but not the chemisorbed carbon of which intensity is about constant throughout the annealing process. A possible explanation is the competitive segregation of bulk impurities as it was already observed on $Fe_{0.97}Al_{0.03}(100)$ in the order C, Al, S as function of temperature [234]; in our case, C 1s signal starts dropping around 900 K (Fig. 4.2) when the surface enriches in Al (Fig. 4.4) as on $Fe_{0.97}Al_{0.03}(100)$ [234]. The hierarchy of segregation is likely linked to the segregation enthalpy that are larger for C ($\Delta H_{Fe(110)} = -117$ kJ/mol [231]) than Al ($\Delta H_{Fe(110)} = -38$ kJ/mol, present *ab initio* calculations for Sect. 5.4).

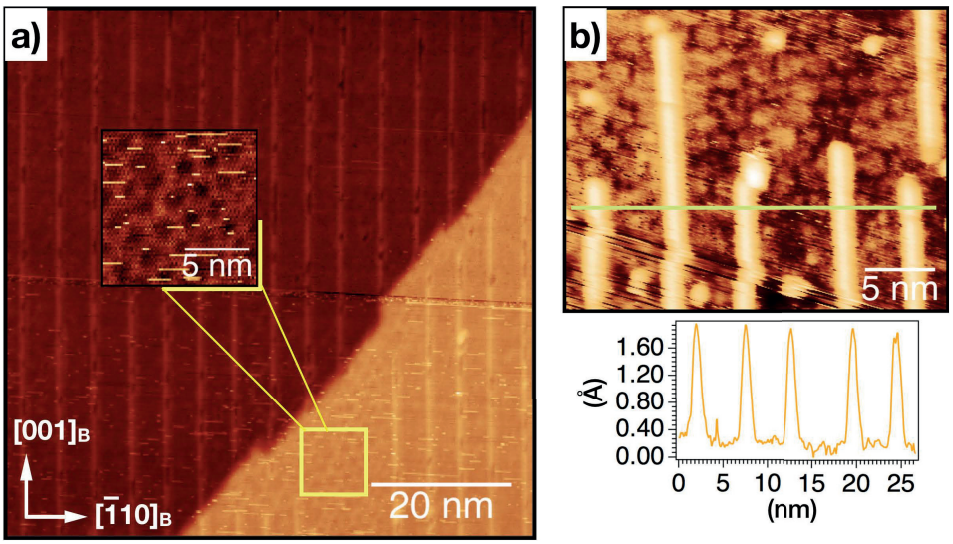

Figure 4.6: STM image of $Fe_{0.85}Al_{0.15}$(110) annealed at a) 1030 K, $U_b = -1.0$ V, $I_t = 10$ pA, 75×75 nm^2; b) 760 K, stripes develop on top of an hexagonal superstructure ($U_b = 2$ V, $I_t = 1.97$ nA, 27×21 nm^2). The inset corresponds to the line profile shown on the image.

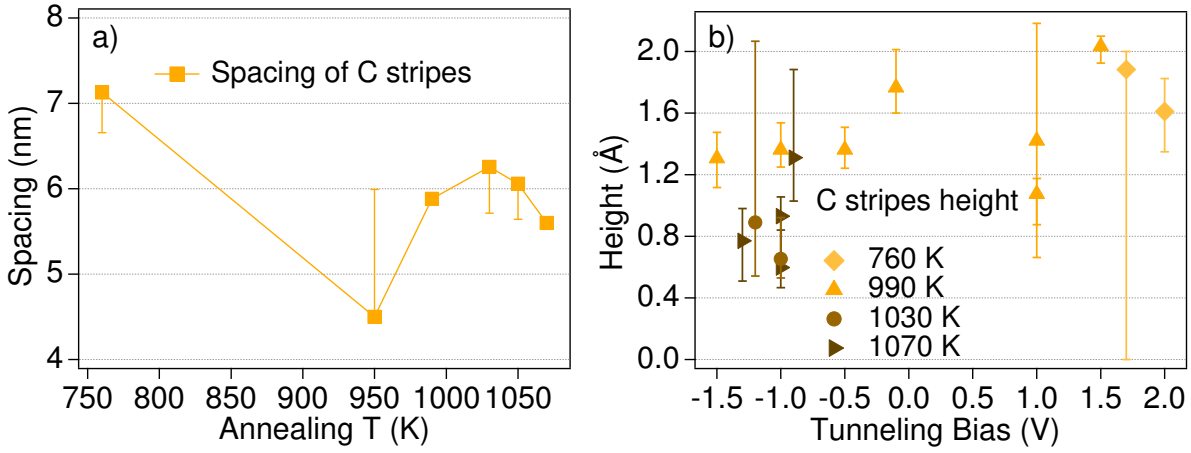

Figure 4.7: Statistic values for a) height and b) spacing of stripes derived from STM profile fits

4.1.2.2 LEED discrete diffraction spots

Sputtered (110) surfaces are characterised by a faint (1×1) LEED pattern (not shown) where only the $(11)_S$ spots are present due to the centring of the rectangular surface unit cell. Before carbon stripes apparition *i.e.* around 690 K, diffraction by a superstructure shows up only around the (1×1) $(11)_S$ spots (Fig. 4.8-a); the crystallographic analysis of this large scale reconstruction is the topic of Sect. 5.2.1. The temperature of 690 K corresponds to the

[1]Desorption is unlikely owing to the low vapor pressure of graphite and the strong Fe-C bond [2].

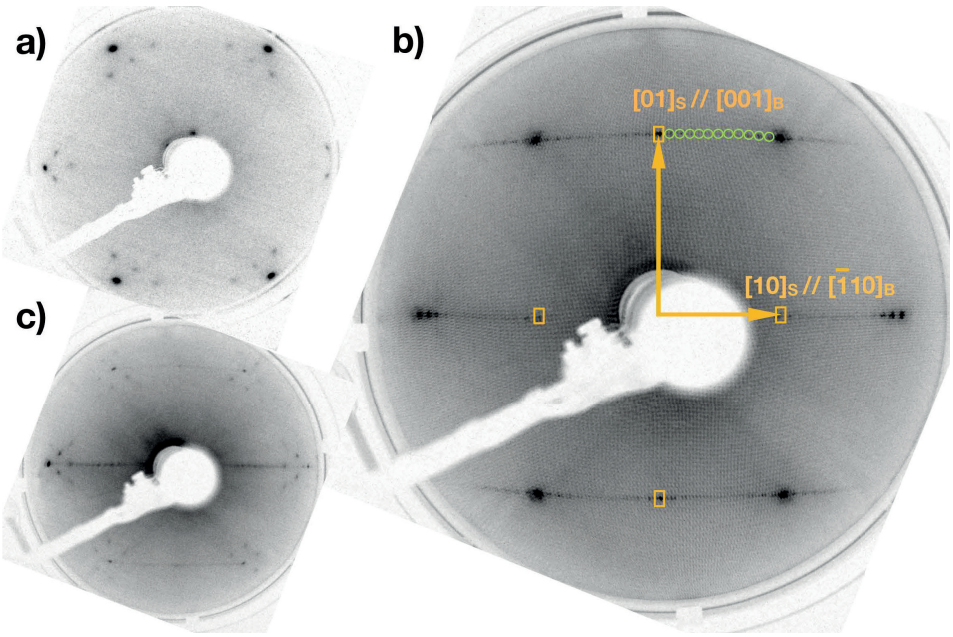

Figure 4.8: LEED pattern evolution of a C-containing $Fe_{0.85}Al_{0.15}(110)$ surface. a) After annealing at 690 K, the (1×1) is overlapped with Al-rich superstructure spots ($E_K = 110$ eV); b) at the maximum of coverage (990 K), spots related to C-stripes are regularly spaced along $[10]_S$ direction (990 K, $E_k = 174$ eV); c) at 1030 K, stripe spots start fading out and lead to a streaking along the $[10]_S$ direction while the superstructure diffraction spots reappear ($E_K = 142$ eV).

onset of segregation of aluminium as shown by photoemission analysis of the clean surface (Sect. 5.1.2.2; Fig. 5.5). Upon further annealing, these "flower"-like spots sharpen and overlap with discrete spots aligned along the $[10]_S$ direction and giving to the pattern a streaking appearance along $[10]_S$. These latter sign the occurrence of regularly spaced one-dimensional structures, namely the carbon stripes seen in STM. As already noticed in STM (Fig. 4.6), Al-rich reconstruction develop not only on C-free terraces (see Fig. 5.17-c) but also underneath C-stripes. However, at the maximum of C coverage around 990 K, the LEED is clearly dominated by stripe-related diffraction (Fig. 4.8-c) in the form discrete multiple spots with a regular spacing of around $\Delta h_S \simeq 0.1$ r.l.u (reciprocal lattice unit) along the $[10]_S$ reciprocal space direction; this correspond to a periodicity of around $a_S/\Delta h_S \simeq 4.3$ nm in good agreement with STM measurements. Finally at 1030 K (Fig. 4.8-b), the recovering of the "flower"-like spots parallels the disappearance of C-stripes seen in STM and the decay of the graphitic C 1s component. It should be stressed that, besides the mixing of C-stripes and Al-rich reconstruction, the relative contrast of the spots depends strongly on the beam energy. The streaking along the $[10]_S$ of the LEED pattern due to C-segregation resembles to that observed by Graupner *et al.* [28] between 873 and 973 K on the (110) surface of the ordered $Fe_{0.53}Al_{0.47}$ alloy (Fig. 3.13-c). Although the authors state that their sample was free of contaminants such as carbon, they did not propose any explanation of their observation.

4.1.2.3 C-induced stripes and oxidation

Some oxidation tests were performed to get rid of carbon, as in the well-known case of metallic tungsten [223]. In an astonishing way, as shown by the STM images of Fig. 4.9, oxide does form on stripe-free surface. The nature of the oxide grown on a clean surface will be detailed in depth in the last chapter 6; it appears as streaked areas in Fig. 4.9. Due to imaging difficulties and transient segregation of carbon, it is not possible to say if oxygen is adsorbed underneath the C-induced stripes. But, the contrast between areas are clearly different.

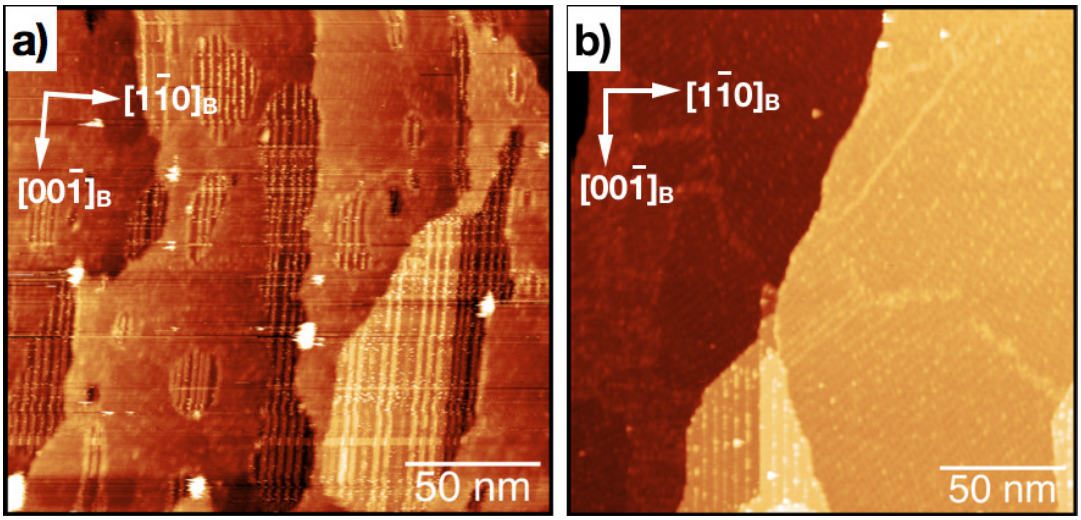

Figure 4.9: Comparison of the morphology of $Fe_{0.85}Al_{0.15}(110)$ surface after a) oxidation at room temperature (50 L of O_2) followed by annealing at 1073 K and b) oxidation (50 L of O_2) during annealing at 1073 K. a) 200×200 nm^2, $U_b = 1.5$ V, $I_t = 0.92$ nA, b) 200×200 nm^2, $U_b = 1.7$ V, $I_t = 0.1$ nA. C-induced stripes appear as white features running along the $[001]_B$ direction.

Because the self-organization of the stripes is indicative of strained structures with long-range order induced by strain effects in the metallic substrate and because stripes covered areas oxidise in a different way as bare terraces, a suggestion is that they stem from a surface compound containing carbon with an unknown Fe-C-Al composition. This hypothesis is more in agreement with the above XPS quantification (Fig. 4.2) that overcomes the apparent STM stripe coverage. In term of distances, our finding is larger by one order of magnitude than the C-chains already observed at the surface of Fe(100) upon segregation; in this case, the organisation is driven by repulsion between adsorbed C atoms at the monolayer level [235].

Although the formation of stripes remains unexplained, fortunately, intensive sputtering-annealing-oxidation cycles allowed to deplete enough the subsurface in carbon to obtain a $Fe_{0.85}Al_{0.15}(110)$ surface free of carbon, at least at the sensitivity level of XPS, LEED and STM.

4.2 Contamination from residual vacuum on $Fe_{0.85}Al_{0.15}$ (100) and (111) surfaces

As mentioned above, an other source of contamination is introduced by the reaction with residual gases of the chamber, mainly H_2O and CO. The ageing at room temperature of clean (100) and (111) surfaces prepared by sputtering and annealing at 970 K has been monitored continuously during 8 h through the evolution of the Al 2p, O 1s, C 1s and Fe 3p core levels in the XPS chamber (Fig. 4.10). During the whole measurement, although slightly spoilt by the outgasing of the X-ray gun, the vacuum level was below 5×10^{-10} mbar. After a fast transfer from the preparation to the analysis chamber, the contamination level is below the detection limit. Ageing goes with a continuous increase of C 1s and O 1s that parallels (i) the increase of a shoulder on the high binding energy side of Al 2p that is characteristic of oxidised aluminium and (ii) the damping of the metallic aluminium component. At the same time, Fe 3p lineshape poorly evolves; the signal is only damped. These evolutions are accompanied by a disappearance of the LEED pattern due to the amorphous nature of the formed film [16].

These evolutions were quantified (Fig. 4.11) through the ratios of integrated intensities $I_{C\,1s}/I_{Fe\,3p}$, $I_{O\,1s}/I_{Al\,2p}$ and $I_{O\,1s}/I_{Al\,2p}$ after Shirley background subtraction. The Al 2p line was decomposed into metallic ($E_B \simeq 72$ eV) and oxidised ($E_B \simeq 74.5$ eV) components in the form of Gaussian peaks. The same was performed for the two components of C 1s at $E_B \simeq 283$ eV and $E_B \simeq 286$ eV. After correction from photo-ionisation cross section and analyser transmission function, ratios were converted into coverage by using the model of thin film on a semi-infinite substrate (Sect. 2.5.3.2) in a way similar to the case of carbon stripes. A hypothetical graphite layer density (2.26 g.cm^{-3}) was assumed for the modelling with the following inelastic mean free paths of the photoelectrons $\lambda_{Fe3p}^{graphite} = 38$ Å, $\lambda_{Al2p}^{graphite} = 37.6$ Å, $\lambda_{O1s}^{graphite} = 27.7$ Å, $\lambda_{Al2p}^{graphite} = 33$ Å [66]. Either the bulk composition $Fe_{0.85}Al_{0.15}$ (Fig. 4.11-a,b) or the actual profile of segregation (Fig. 4.11-c,d) were used. Only the last case will be commented below.

After an initial linear increase in coverage (slope around 1.1), a saturation seems to be reached after 400 min between 3 and 5 ML. By using the total pressure of 5×10^{-10} mbar to estimate a total exposure and by adding carbon and oxygen coverage, an effective sticking coefficient of 0.65 can be determined. The oxygen and the parallel oxidised aluminium uptakes are larger on the (100) than on the (111) surface (ratio $n_{Al,O}^{111}/n_{Al,O}^{100} \sim 0.8$) following the hierarchy of compacity but the opposite is reached for carbon (ratio $n_C^{111}/n_C^{100} \sim 1.2$). The final ratio of coverage between Al 2p (oxidised) and O 1s (0.65 ± 0.05) is very close to the ideal stoichiometry Al_2O_3 showing that oxidised aluminium is most probably bounded to oxygen species.

Although ill-defined, this experiment is worth being compared to previous studies of O_2 [16], CO [101] and H_2O [91] adsorption on FeAl surfaces at low temperature, CO and H_2O being usual components of a residual vacuum. As in those cases, there is no evidence herein that iron is oxidised as the Fe 3p profile does not evolve; there is neither a shift nor a change of lineshape. Fe stays in its metallic state. Indeed $Fe^{2+,3+}$ (FeO: $E_B = 55 \pm 0.6$ eV;

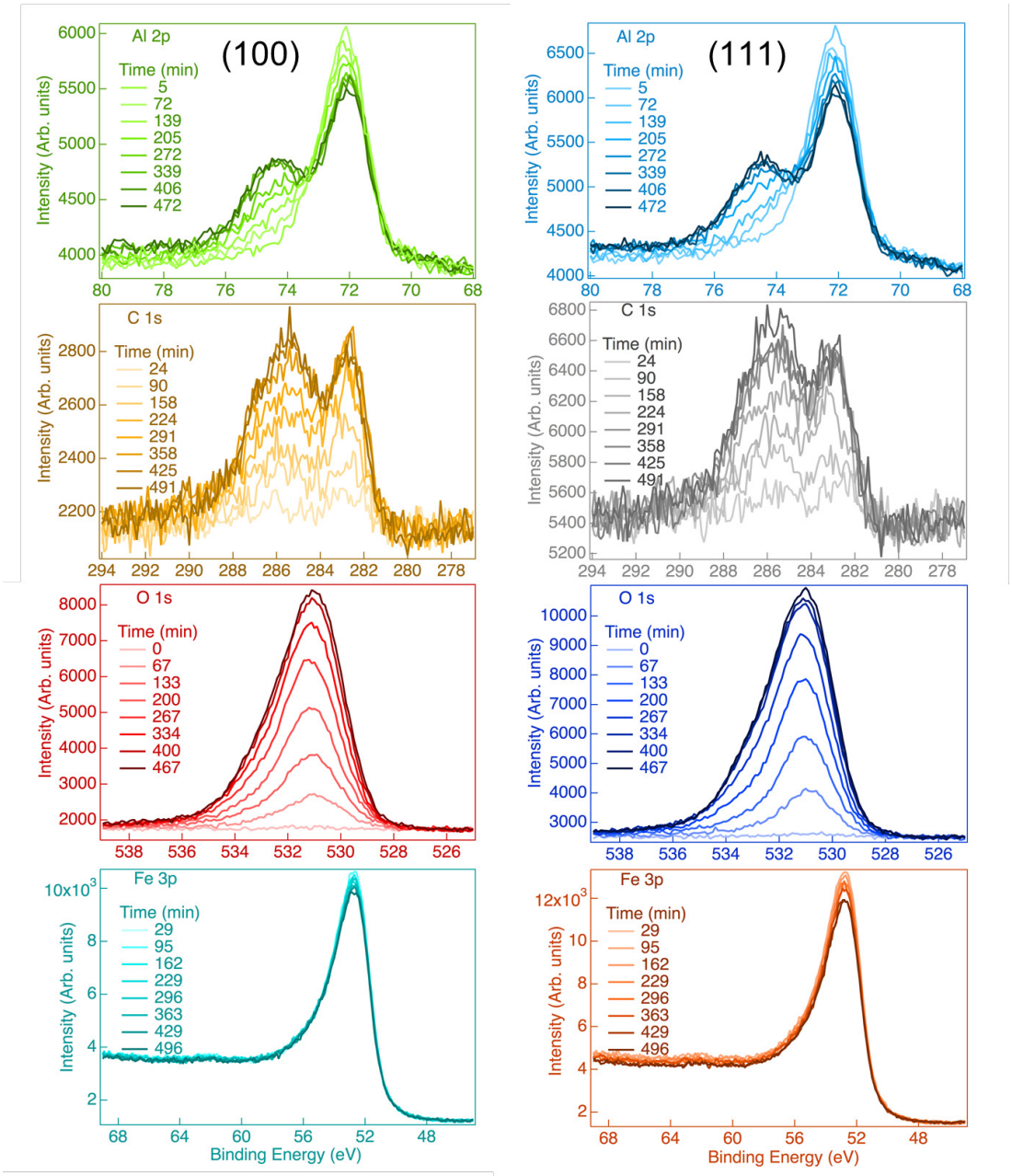

Figure 4.10: Ageing of $Fe_{0.85}Al_{0.15}$(111) and (100) surfaces (annealed at 970 K). XPS spectra of Al 2p, C 1s, O 1s and Fe 3p are recorded as a function of time at normal emission and room temperature. The chamber pressure is below 5×10^{-10} mbar. The left column corresponds the (111) surface and the right column to (100). The pass energy was set at 50 eV and the X-ray gun power kept constant for comparison.

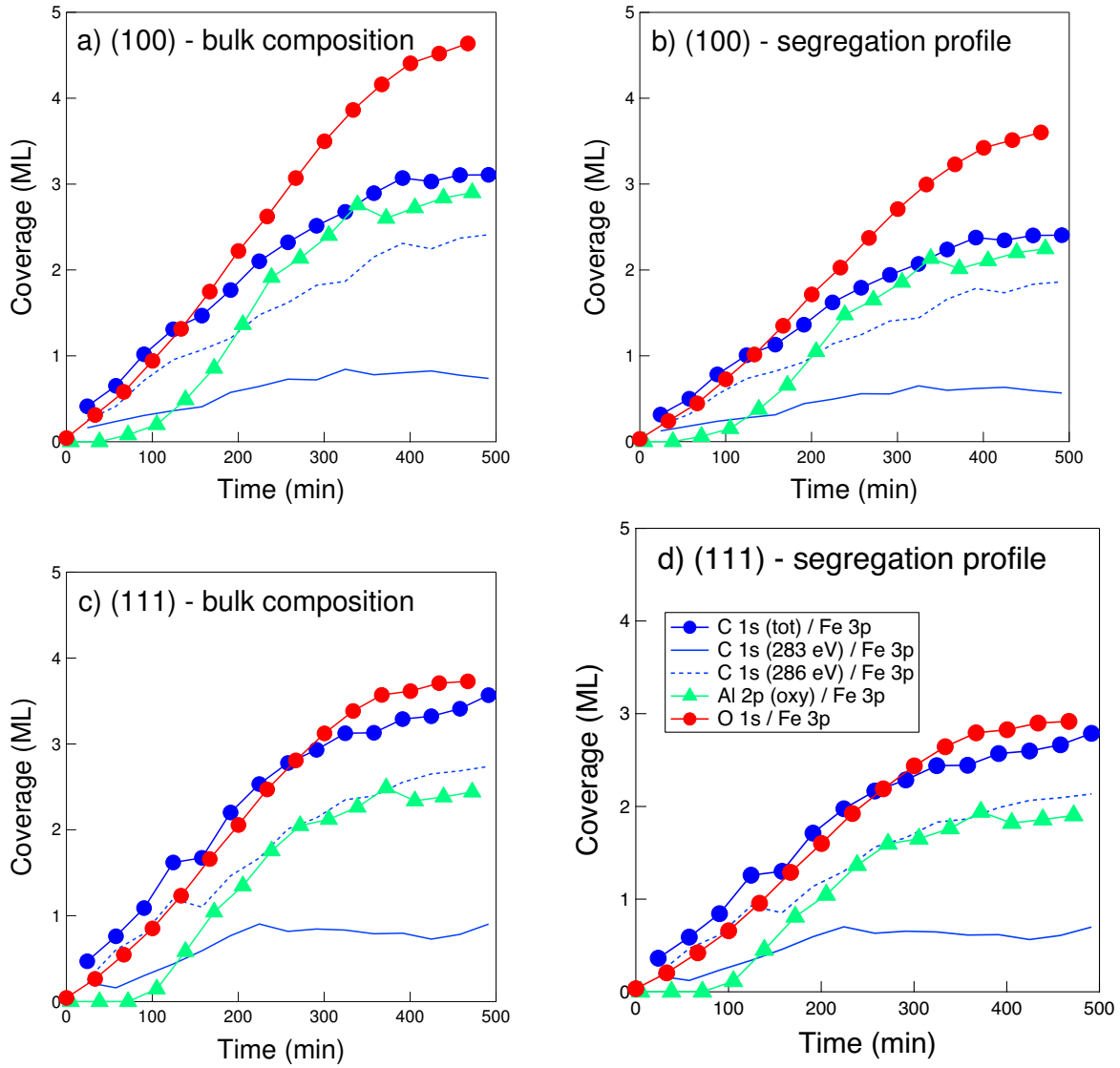

Figure 4.11: Quantification of the ageing contamination from C 1s/Fe 3p, Al 2p(oxi)/Fe 3p and O 1s/Fe 3p ratios on a)b) $Fe_{0.85}Al_{0.15}$(100) and c)d) $Fe_{0.85}Al_{0.15}$(111). The contamination layer was modelled by graphite, and either the bulk composition $Fe_{0.85}Al_{0.15}$ or the actual profile of aluminium segregation was accounted for. Coverages are given in monolayers corresponding to (100) and (111) orientations.

Fe_3O_4: $E_B = 55.1 \pm 1$; Fe_2O_3: $E_B = 55.9 \pm 0.4$ eV; FeOHO: $E_B = 56.2 \pm 1$ eV; Fe-hydrocarbon $E_B \sim 54.1$ eV) leads to a sizeable chemical shift compared to metallic iron (Fe^0: $E_B = 52.9 \pm 0.3$ eV) [50, 51, 236]. Therefore, the reactive adsorption sites involve aluminium. In the case of O_2 exposure [16], the change of growth regime was assigned to a Al diffusion limited growth through the Cabrera-Mott mechanism [197]. Previous experiments of H_2O adsorption on FeAl(110) [91] have shown a dissociative adsorption above 173 K leading to adsorbed hydroxyls (OH_{ads}) and to a desorption of molecular hydrogen above 250 K. The asymmetric O 1s core level observed in our case may reflect this mixture of chemisorbed oxygen preferentially bounded to Al (at ~ 531 eV) and of OH_{ads} shifted by ~ 1.4 eV. However, this speculative interpretation is entailed by the fact that room temperature adsorption of CO on FeAl(110) [101] results also in both molecular and dissociated species, the O binding to Al. Photoemission measurements combined with thermal desorption [101] showed that the C 1s component at ~ 285 eV is a signature of molecularly adsorbed CO while the component at lower binding energy (~ 282 eV) is assigned to chemisorbed carbon. Quite similar fingerprints are found herein on C 1s spectra.

This experiment shed light on the question of contamination related to aluminium reactivity. Although unavoidable for the time consuming STM experiments, XPS and LEED measurements on native surface were performed as fast as possible (< 30 min) [3]; in particular, segregation studies (Chap. 5) involved either a freshly prepared sample at each temperature or fast *in situ* annealing in the analysis chamber. As it will be detailed later on, oxide thin films (Chap. 6) were synthesised during the course of substrate recrystallisation annealing right after sputtering; moreover, oxide films turned out to be much less prone to contamination than bare surfaces.

[3]For instance, pass energy in XPS was increased to reduce counting time.

CHAPTER 5

ALUMINIUM SEGREGATION, ATOMIC STRUCTURE AND MORPHOLOGY OF $FE_{0.85}AL_{0.15}$(100), (110) AND (111) SURFACES

Compared to the literature dealing only with the B_2 ordered compound (see Sect. 3.3), the case of a random alloy like $Fe_{0.85}Al_{0.15}$ offers an extra degree of freedom related to the gradient of composition. Once the conditions to prepare a clean surface were identified (Chap. 4), the work focused on the orientation dependence of the interplay between segregation, atomic structure and morphology of annealed surfaces. The modelling of the angular dependence of photoemission signal is developed in Sect. 5.1 to determine the profile of segregation. The corresponding surface reconstructions are explored by LEED and GIXD (Sect. 5.2) while STM is used to unravel the associated modification of surface topography (Sect. 5.2). Although the actual behaviour of surfaces seems to be rich and complex, *ab initio* calculations are used to rationalise some observed trends (Sect. 5.4).

5.1 Angular analysis of segregation by photoemission

The angular dependence of the escape depth $\lambda\cos(\Theta)$ has been exploited to probe the profile of concentration of elements by changing the photoelectron collection angle Θ between the analyser and the surface normal from 0° up to 75°. Segregation has been quantified from the ratio of intensity of metallic Al 2p and Fe 3p core levels for two reasons:

- the proximity in kinetic energy of those two photoemission lines minimises the error due to the estimate of the transmission function of the analyser, [1]
- both lines belong only to the crystal and not to the sample plate or holder which is

[1] The maximum of error is obtained at low kinetic energy, which is not the case of the Al 2p and Fe 3p core levels.

made out of Mo, W, and Ta; this caution is particularly important at grazing emission to avoid spurious signal,

- their kinetic energies maximise the probing depth,
- the ratio is poorly sensitive to forward scattering effects along the dense crystallographic directions since, regardless of short range ordering, Al and Fe occupy the same bcc lattice sites.

After substraction of a Shirley background, Al 2p and Fe 3p peaks have been integrated and corrected from the photo-ionization cross sections $\sigma(E_K)$ [52] and the transmission function of the analyser given by $T(E_K) \sim E_K^{-1}$ [54] of our EA-125 Omicron hemispherical analyser (see Tab. 5.1). Figs. 5.4-5.7 show on all the surfaces a clear trend of enrichment in Al near the extreme surface (grazing emission conditions) after an anneal at high temperature. This trend will be analysed quantitatively hereafter.

Core level	E_B (eV)	SOS (eV) Al-Kα	E_K (eV) Al-Kα	E_K (eV) Mg-Kα	PICS (barns) Al-Kα	PICS (barns) Mg-Kα
Fe 3p	52.8	0.8	1433.8	1200.8	0.022	0.034
Al 2p	72.8 (3/2)	0.4	1413.8	1180.8	0.0072	0.012
Al 2s	118 (3/2)	-	1368.6	1135.6	0.01	0.015
C 1s	285	-	1201.6	968.6	0.013	0.022
O 1s	531	-	955.6	722.6	0.04	0.063
Fe 2p	707	13.1	779.6	546.6	0.2216	0.3529

Table 5.1: Typical core levels involed in the present study of $Fe_{0.85}Al_{0.15}$: Binding Energy (E_B) and Spin-Orbit Splitting (SOS) in the metallic state [236]; corresponding Kinetic Energy (E_K) and Photo-Ionization Cross Section (PICS) [52] for Al-Kα and Mg-Kα excitations.

5.1.1 Dependence of inelastic mean free path on composition

Assuming an in-plane homogeneous sample, the quantitative analysis of photoemission data requires the knowledge of the inelastic mean free path $\lambda(x)$ in $Fe_{1-x}Al_x$ which depends on the local composition $x(z)$ at depth z. Unfortunately, $\lambda(x)$ is not tabulated but its variation is expected to be sizeable if one compares $\lambda(x = 0)$ in bulk Fe (A_2-bcc structure) and $\lambda(x = 1)$ in bulk Al (A_1-fcc structure) that are known [58]. Whatever the kinetic energies, a difference up to 10 Å exists between the two materials which can be assigned at first sight to a change of electronic density between aluminium (0.18 e·Å^{-3}) and iron (1.35 e·Å^{-3}). To overcome this issue and to obtain $\lambda(x)$, the followed strategy has been to use the TPP-2M predictive formula of Tanuma, Powell and Penn as developed in their famous series of papers Refs [57–65]. More precisely, the QUASES-IMFP-TPP2M software [66] from S. Tougaard was employed to generate the inelastic mean free paths in $Fe_{1-x}Al_x$ from:

- its bulk density $\rho(x)$;

- its atomic mass $M(x) = (1-x)M_{Fe} + xM_{Al}$ with $M_{Fe} = 55.85$ g·mol^{-1} and $M_{Al} = 26.98$ g·mol^{-1};
- its band gap taken as zero for a metallic compound;
- the total number of valence electrons of binding energy below 30 eV as given by Tab. 5.2; basically a linear interpolation accordingly to the atomic fraction x was assumed.

			Electron spreading				
Formula	Z	Atomic structure	s+p (hbe)	s+p (lbe)	d	f	Total
Fe	26	[Ne] $3s^2$ $3p^6$ $4s^2$ $3d^6$	8	2	6	0	16
Al	13	[Ne] $3s^2$ $3p^1$	0	3	0	0	3
$Fe_{1-x}Al_x$	$-13x+26$	-	$8(1-x)$	$x+2$	$6(1-x)$	0	$-13x+16$
$Fe_{0.85}Al_{0.15}$	24.05	-	6.8	2.15	5.1	0	14.05

Table 5.2: Orbital filling used as input of QUASES-IMFP-TPP2M software to determine the inelastic mean free paths in $Fe_{1-x}Al_x$. s+p(hbe) and s+p(lbe) stand for the number of electrons per formula unit in s and p orbitals of highest and lowest binding energies. d and f correspond to electrons from d and f orbitals. Basically, a linear interpolation between Fe and Al was used for the alloy. The total number of valence electrons used in the TPP-2M formula is given in the last column.

Regarding the dependence of the bulk density on x, a careful analysis of all the Fe-Al compounds reported in the Inorganic Crystal Structure Database (ICDS [237]) was undertaken including:

- the A_2-bcc and A_1-fcc structures of pure Fe and Al,
- the most interesting data for A_2-bcc random alloy and for the high temperature quenched ordered B_2-CsCl alloys [25],
- the ordered Heussler $D0_3$ alloys (Fe_3Al),
- more exotic high temperature compounds of various symmetries in the Al rich zone of the phase diagram (see legend of Fig. 5.1).

The obtained data gathered in Fig. 5.1 showed a change from 2.7 g·cm^{-3} (Al, $x = 1$) up to 7.86 g·cm^{-3} (Fe, $x = 0$) that follows a robust linear dependence $\rho(x) = 7.94 - 5.17x$ g·cm^{-3} corresponding to a hyperbolic variation of the volume per atom $V(x) \sim \rho(x)/M(x)$ or of the atomic concentration $n(x) \sim M(x)/\rho(x)$ in $Fe_{1-x}Al_x$ compounds. This linear dependence will be assumed to hold even at segregated surfaces since it encompasses numerous local environments of Fe and Al.

The obtained TPP-2M inelastic mean free path are plotted in Fig. 5.2 for the usual Al-Kα (Fig. 5.2-a) and Mg-Kα (Fig. 5.2-b) excitations for the involved core levels (Fe 2p, Fe 3p, Al 2s, Al 2p, O 1s, C 1s). Somehow the dependency of $\lambda(x)$ is much more moderated than

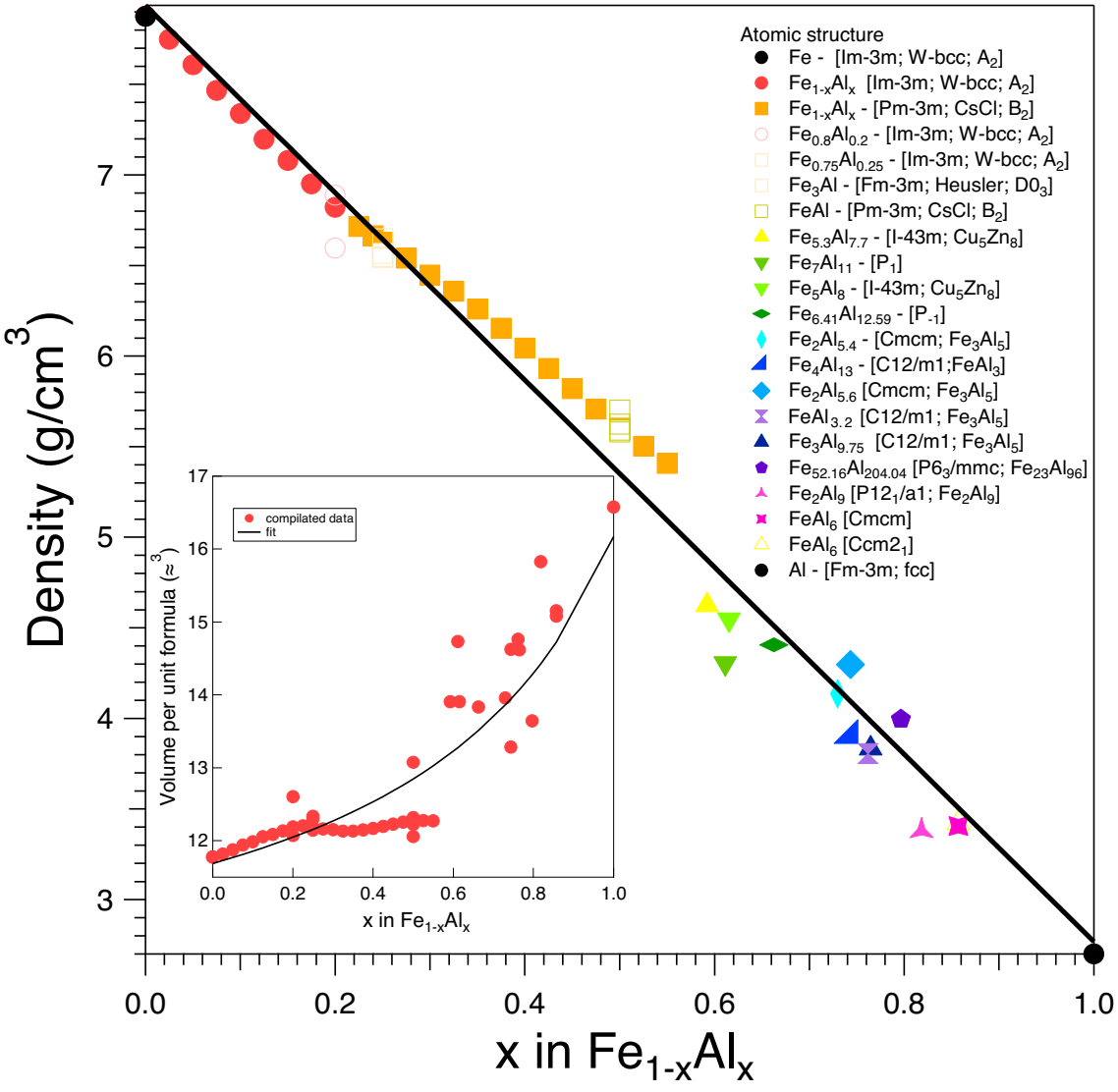

Figure 5.1: Compilation of the density $\rho(x)$ of all the Fe-Al compounds tabulated in the ICSD database overlapped with the measurements of Ref. [25] for the A_2 (red filled circles) and B_2 (orange filled squares) structures. In the legend, the corresponding compounds as well as their space groups, their parent compounds and their Strukturbericht symbol are labelled. Data are well accounted for by a linear regression (black line) corresponding to an hyperbolic variation of the atomic volume (inset).

one would expect from pure Fe and Al up to a molar fraction of $x \simeq 0.8$. Nevertheless, this variation was taken into account in the following analysis through a polynomial fit of the TPP-2M values (lines in Fig. 5.2). Finally, one should keep in mind that the accuracy of the TPP-2M formula is of the order of 20 % [57–65].

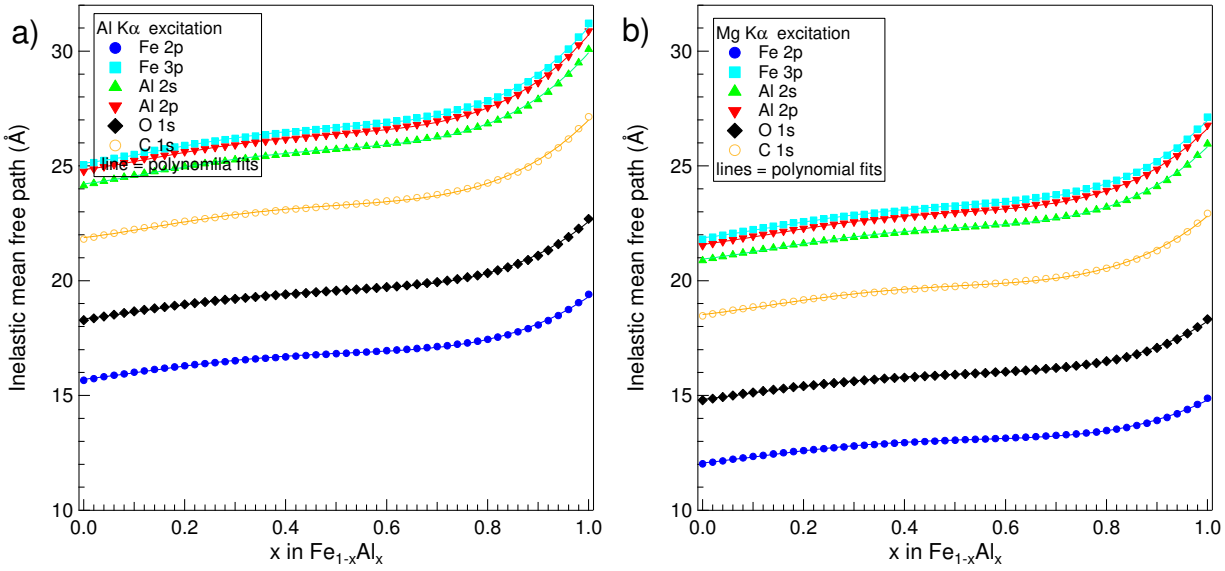

Figure 5.2: TPP-2M calculated inelastic mean free path of $Fe_{1-x}Al_x$ compounds using a linear regression of the material density (Fig. 5.1) and the orbital filling of Tab. 5.2 for a) Al-Kα ($h\nu = 1486.6$ eV) and b) Mg-Kα ($h\nu = 1253.6$ eV) photon excitations.

5.1.2 Photoemission modelling of intensities: the case of segregation at the surface of alloys

The basis of quantification in photoemission has been introduced in Sect. 2.5.3.2 where the cases of a homogeneous alloy (Fig. 5.3-a) and of an overlayer (Fig. 5.3-b) have been introduced.

5.1.2.1 Segregation at the surface of an alloy

The analysis of the segregation at the surface of an alloy is slightly more complex than the homogeneous mixture or a genuine thin film on top of a substrate. Indeed, signal in the compared core levels may come both from the bulk of the alloy or from its surface. Two models as sketched in Fig. 5.3 have been compared and are described as follows.

5.1.2.1.1 The homogeneous segregated layer on an homogeneous alloy Let us consider a segregated layer $A_{1-x_L}B_{x_L}$ on top of a semi-infinite substrate $A_{1-x_S}B_{x_S}$ (Fig. 5.3-c). If n_i^j and λ_i^j are the atomic concentration and mean free path of element $i = A, B$ in

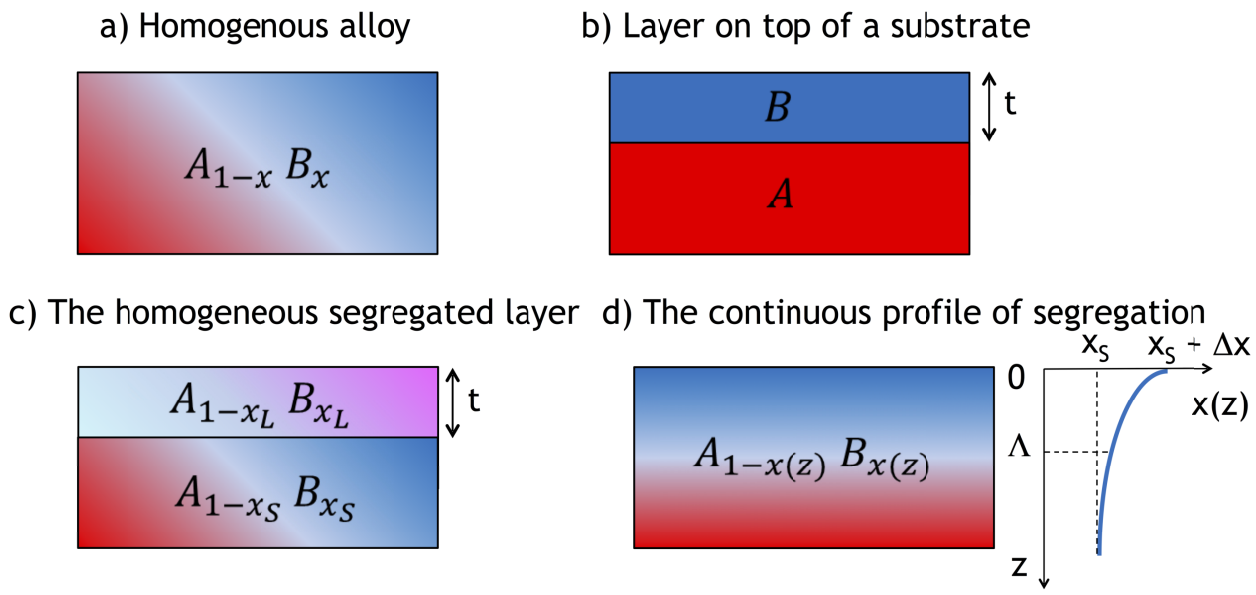

Figure 5.3: Models of profile of concentration used for photoemission analysis. a) The homogeneous semi-infinite alloy $A_{1-x}B_x$. b) The thin film on a substrate. c) The homogeneous segregated layer $A_{1-x_L}B_{x_L}$ on a semi-infinite alloy $A_{1-x_S}B_{x_S}$. d) The continuous profile of segregation $A_{1-x(z)}B_{x(z)}$.

medium $j = L, S$, the photoelectron signals from elements A, B encompass contributions from the substrate and the layer and read:

$$\begin{aligned}\frac{I_A}{T_A\sigma_A} &\sim \lambda_A^S n_A^S \exp\left(-t/\lambda_A^S \cos\Theta\right) + \lambda_A^L n_A^L \left[1 - \exp\left(-t/\lambda_A^L \cos\Theta\right)\right] \\ \frac{I_B}{T_B\sigma_B} &\sim \lambda_B^S n_B^S \exp\left(-t/\lambda_B^S \cos\Theta\right) + \lambda_B^L n_B^L \left[1 - \exp\left(-t/\lambda_B^L \cos\Theta\right)\right]. \end{aligned} \tag{5.1}$$

As reminder, Θ is the emission angle, T the analyser transmission function and σ the photoionisation cross section. If $V(x)$ is the atomic volume at atomic fraction x, $n_A^S = (1-x_S)/V(x_S)$, $n_B^S = x_S/V(x_S)$, $n_A^L = (1-x_L)/V(x_L)$, $n_B^L = x_L/V(x_L)$. If one assumes, as done in Sect. 5.1.1, that the inelastic mean free path depends on the atomic fraction x, the ratio of measured intensities reads:

$$\frac{I_B}{I_A}\frac{T_A\sigma_A}{T_B\sigma_B} = \frac{\lambda_B(x_S)x_S V(x_L)\exp\left[-t/\lambda_B(x_S)\cos\Theta\right] + \lambda_B(x_L)x_L V(x_S)\left\{1-\exp\left[-t/\lambda_B(x_L)\cos\Theta\right]\right\}}{\lambda(x_S)(1-x_S)V(x_L)\exp\left[-t/\lambda(x_S)\cos\Theta\right] + \lambda(x_L)(1-x_L)V(x_S)\left\{1-\exp\left[-t/\lambda(x_L)\cos\Theta\right]\right\}}. \tag{5.2}$$

From the knowledge of the substrate composition x_S, the previous equation can be used to fit the angular variation of the fraction $\frac{I_B}{I_A}$ to obtain film composition x_L and thickness t.

5.1.2.1.2 The continuous profile The previous model is easily generalised to any continuous profile of atomic fraction $x(z)$ (Fig. 5.3-d) by integration of the infinitesimal photo-

electron signal of layer dz of element i:

$$dI_i \propto T_i \sigma_i n_i(z) \exp\left\{\int_z^0 dz'/\lambda[x(z')]\right\} dz. \tag{5.3}$$

Using the same hypothesis as above, one obtains:

$$\begin{aligned} \frac{I_A}{T_A \sigma_A} &\propto \int_{-\infty}^0 \frac{1-x(z)}{V[x(z)]} \exp\left\{\int_z^0 dz'/\lambda_A[x(z')]\right\} dz \\ \frac{I_B}{T_B \sigma_B} &\propto \int_{-\infty}^0 \frac{x(z)}{V[x(z)]} \exp\left\{\int_z^0 dz'/\lambda_B[x(z')]\right\} dz. \end{aligned} \tag{5.4}$$

For the sake of simplicity, a diffuse profile has been chosen to analyse our data:

$$x(z) = x_S + \Delta x \exp(-z^2/\Lambda^2), \tag{5.5}$$

where $x_S = 0.15$ is the bulk value, $x_S + \Delta x$ the surface value and Λ a typical length of segregation.

5.1.2.2 Angular analysis of segregation at the surfaces of $Fe_{0.85}Al_{0.15}$

On all the surfaces, Al segregation has been quantified by photoemission through the evolution of the ratio $I_{Al\,2p}/I_{Fe\,3p}$ as a function of the annealing temperature (Fig. 5.5) after sputtering (1 keV Ar^+, 30 min, $\sim 10\,\mu A{\cdot}cm^{-2}$). The thermal cycle was kept constant with an heating/cooling rate around 500 $K{\cdot}min^{-1}$ and a plateau temperature duration of 15 min. For those so called *ex situ* data, the sample was cleaned between each measurement to avoid contamination and bias due to preferential oxidation of Al by residual pressure of the chamber (see Chap. 4). Normalisation of bare spectra to background (Fig. 5.4) points already at an increase of the raw intensity of the aluminium signal.

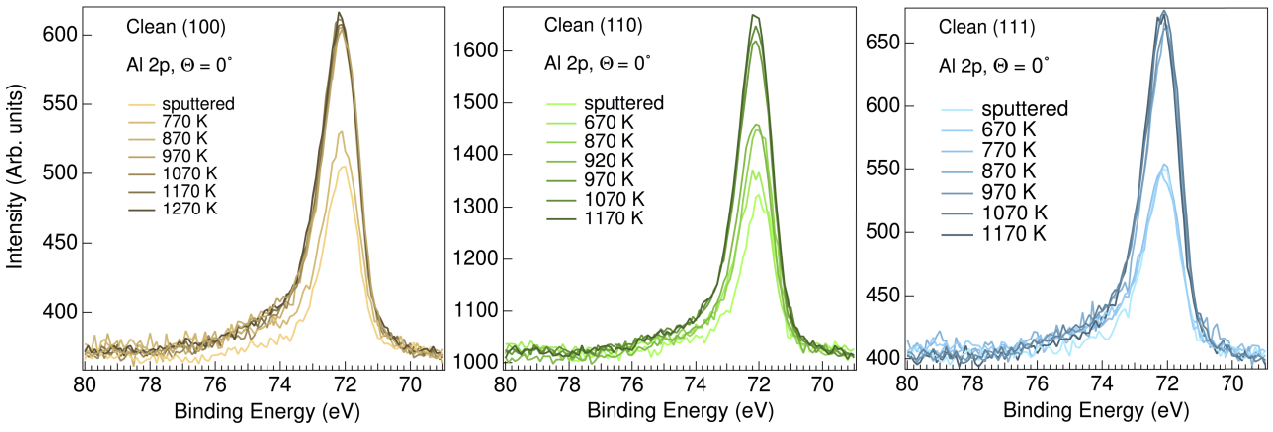

Figure 5.4: Evolution with annealing temperature of Al 2p core level (normal emission $\Theta = 0°$) of the various orientations of $Fe_{0.85}Al_{0.15}$. Spectra have been normalised to background.

Those *ex situ* data acquired at normal emission $\Theta = 0°$ have been compared to *in situ* annealing at increasing temperatures performed directly on the manipulator of the analyser

chamber at a grazing emission of $\Theta = 60°$.

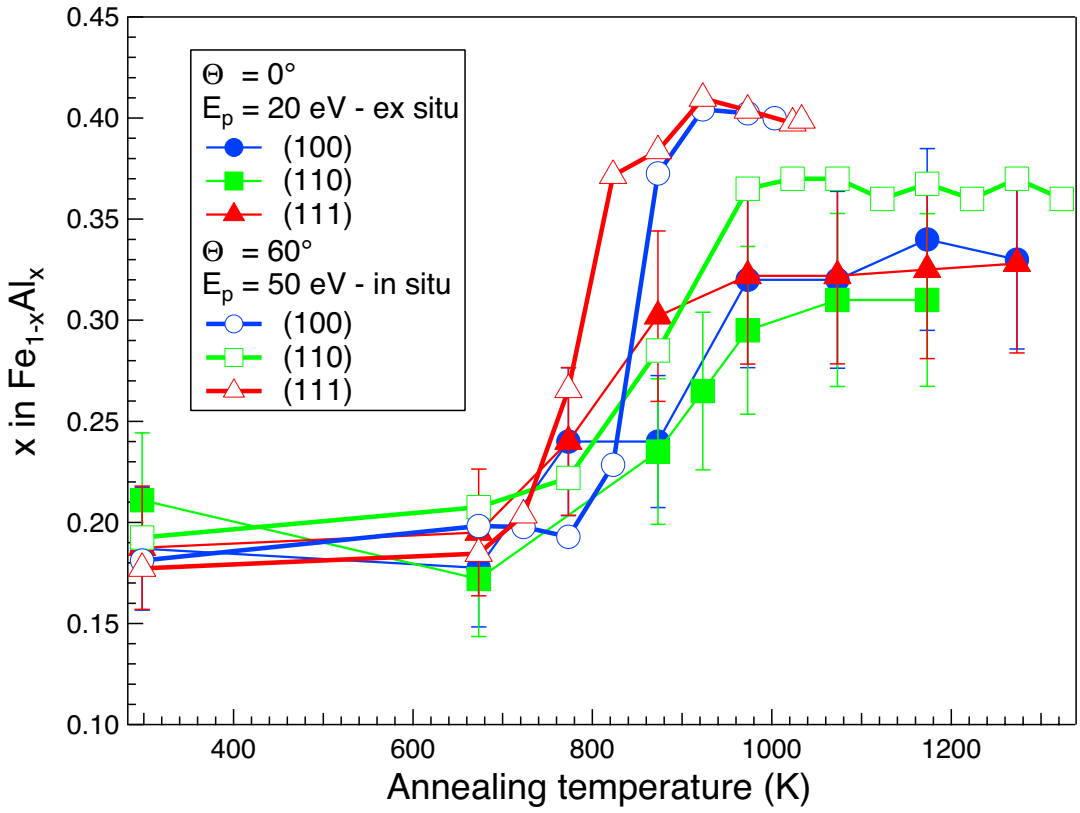

Figure 5.5: Comparison of Al segregation versus annealing temperature on $Fe_{0.85}Al_{0.15}$(100), (110) and (111). The atomic fraction corresponds to an analysis of the ratio $I_{Al\,2p}/I_{Fe\,3p}$ with an homogeneous bulk material $Fe_{1-x}Al_x$. *Ex situ* data correspond to samples annealed directly after sputtering in the preparation chamber (normal emission) and *in situ* data to a progressive annealing on the analysis chamber manipulator (grazing emission). The pass energy E_p is different for the two sets of measurements.

Data have been analysed with the model of homogeneous bulk material $Fe_{1-x}Al_x$ (Eq. 2.20) to obtain the equivalent atomic fraction x. The error bars come from a cumulative total uncertainty of 20 % on measured intensities and mean free path determination. Fig. 5.5 calls for three comments:

- strong surface enrichment due to preferential sputtering is to be excluded since normal and grazing emission data (points at T=300 K) matches within the uncertainties of measurements [2]. All our estimates on all the sputtered surfaces lead to a composition of $x = 0.19 \pm 0.05$, close to the nominal value of $x = 0.15$. Estimates of the sputtering yield with the formula of Matsumani *et al.* [27] of Fe target (1.70 atom/ion) and of Al

[2]This findings is at odd with several references [28, 30–32, 91–94] of the literature which report, or more precisely assume, a preferential sputtering of Al without any clear experimental proof !

target (1.53 atom/ion) with normal incident 1 keV Ar^+ ions [238] would slightly favour preferential Fe sputtering and the enrichment of the surface in Al as observed herein. But this conclusion should be taken with caution since our sputtering geometry (at 30° incidence) and our target ($Fe_{0.85}Al_{0.15}$) are different. Finally, the systematic come back to the same $I_{Al\,2p}/I_{Fe\,3p}$ value demonstrates that sputtering is efficient enough to remove the segregated layer [3].

- for all the orientations, an enrichment of the surface in Al starts around 750 K; since grazing measurements lead to higher values of composition than normal emission in the framework of homogeneous bulk alloy model [4], a profile of segregation should exist with an enrichment of the surface in Al compared to Fe. By comparing normal and grazing measurements, the surface enrichment seems to be larger and earlier in temperature on the (100) and (111) than on the (110) surface and equilibration of the near surface is faster than bulk.

- above $\sim$ 950 K, the profile of segregation seems to reach a steady state on a photoemission point of view since a plateau is observed.

To further confirm the Al segregation, the angular variation of the $I_{Al\,2p}/I_{Fe\,3p}$ has been measured (Fig. 5.6) between $\Theta = 0°$ and $\Theta = 75°$ after annealing at 1273 K in the steady state plateau value. The binding energy of Fe 3p is found at 53 eV in close agreement with literature ($E_B = 52.9 \pm 0.3$ eV [236]) while Al 2p is found at 72 eV shifted by -0.8 eV compared to metallic aluminium ($E_B = 72.8 \pm 0.3$ eV [236]) as it is found in the case of transition metal aluminides among which FeAl [16,101]. The clear decrease of Fe signal at grazing emission was quantitatively fitted with either an homogeneous segregated layer or a diffusive continuous profile. For both models, the substrate value was kept fixed at the nominal value $x_S = 0.15$. Fits are shown as lines in Fig. 5.7 and parameters are gathered in Tab. 5.3.

Model	Parameter	(100)	(110)	(111)
Film	Thickness t (Å)	24 ± 4	32 ± 7	23 ± 4
	Layer atomic fraction x_L	0.47 ± 0.02	0.4 ± 0.02	0.47 ± 0.03
Profile	Length Λ (Å)	26.6 ± 6	38 ± 10	25 ± 6
	Variation of atomic fraction Δx	0.35 ± 0.03	0.27 ± 0.02	0.35 ± 0.03
	Surface atomic fraction $x_s + \Delta x$	0.5 ± 0.03	0.42 ± 0.02	0.5 ± 0.03

Table 5.3: Results of the fit of the angular variation of photoemission signal: a) with a segregated layer (Eq. 5.2, Fig. 5.3-c) or b) with a continuous profile of segregation (Eq. 5.4, Fig. 5.3-d). The error bars stem from 10 % uncertainties on the corrected ration $I_{Al\,2p}/I_{Fe\,3p}$.

Error bars on the fitted parameters $t, x_L, \Lambda, \Delta x$ stem from an uncertainties of 10 % on the corrected ration $I_{Al\,2p}/I_{Fe\,3p}$. As correlations between parameters do exist, it was checked that

[3] With a sputtering yield of $\sim$ 1.5, an ion beam current of $\sim$ 10 μA·cm^{-2} allows to remove 6×10^{15} atoms·min^{-1} which corresponds to a few monolayers. Therefore, a 30 min sputtering is in principle enough to remove the 2-4 nm thick segregated layer (see below).

[4] In this model, the ratio of intensity is independent of the emission angle (Eq. 2.20).

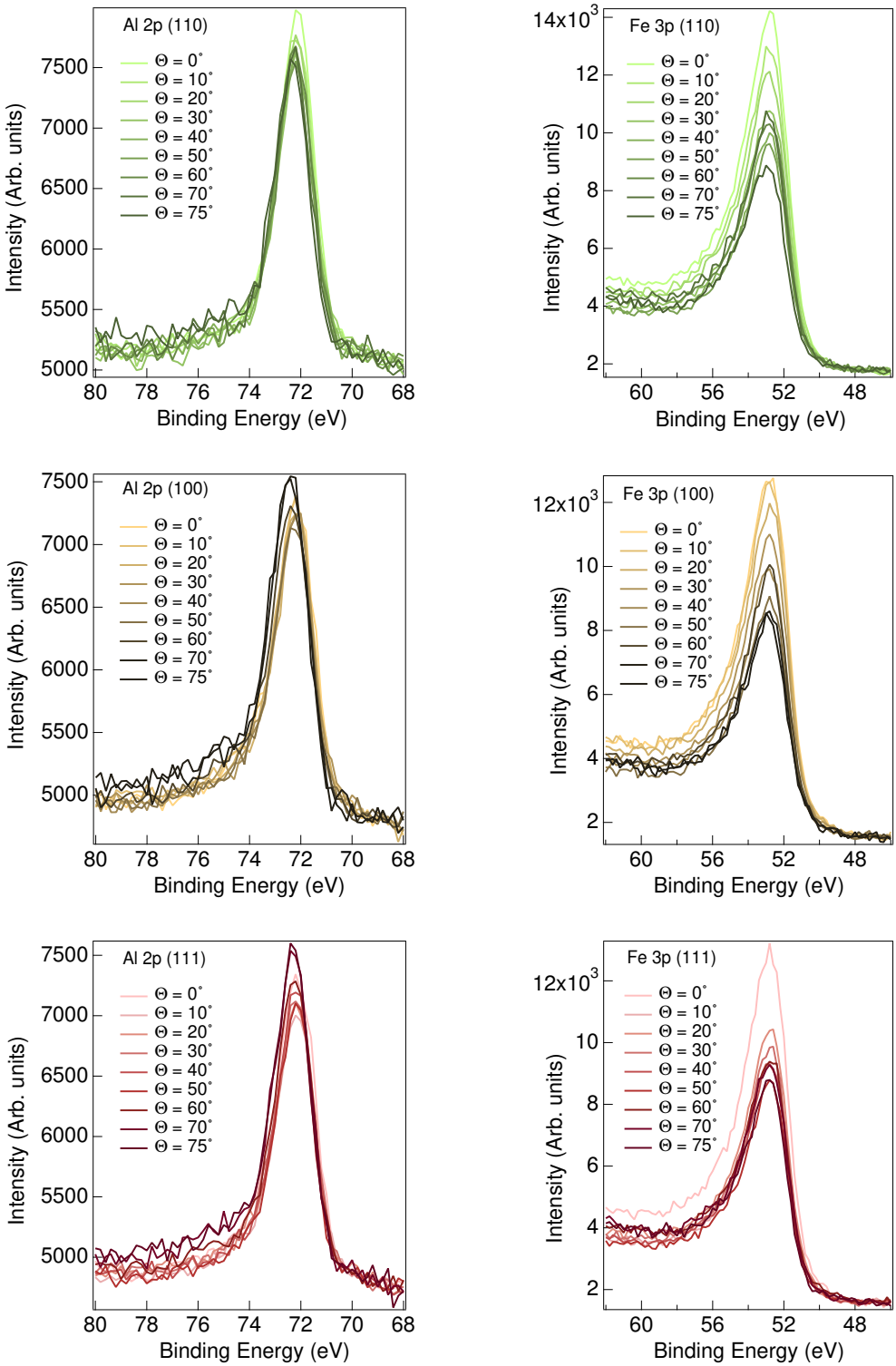

Figure 5.6: Evolution with emission angle Θ of Al 2p and Fe 3p core levels of (110), (100) and (111) surfaces of clean $Fe_{0.85}Al_{0.15}$ annealed at 1273 K. Spectra have been normalised to background.

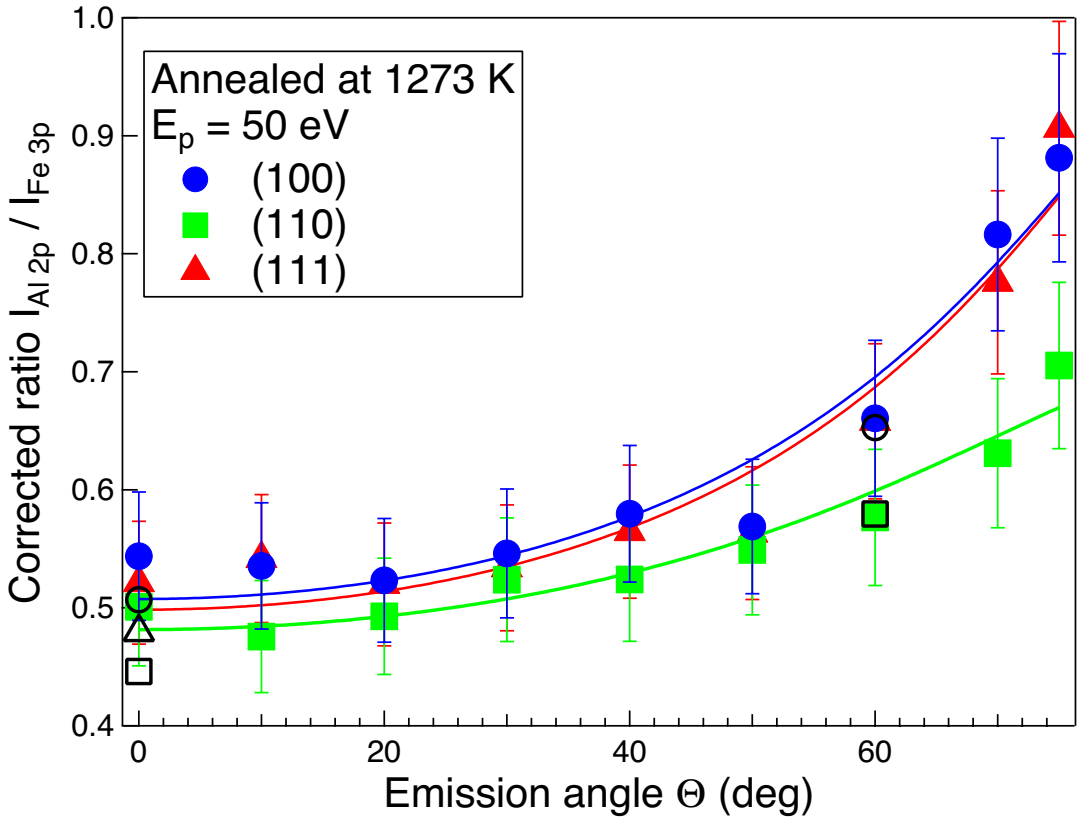

Figure 5.7: Angular modulation of the ratio $I_{Al\,2p}/I_{Fe\,3p}$ (pass energy $E_p = 50$ eV) corrected for the transmission function and photo-ionization cross sections. Samples have been annealed at the highest temperature 1273 K. Data (points) have been fitted with a model of continuous profile of segregation (lines, Eq. 5.4). A similar fit quality is obtained with the segregated layer model (Eq. 5.2). Black open symbols correspond to measurements at the highest temperature of Fig. 5.5.

systematic errors due to the determination of the inelastic mean free paths from the TPP-2M formula (up to $\delta\lambda/\lambda \sim 20$ %) lead to fitted values of t or Λ roughly within the above error bars (Tab. 5.3). In parallel, uncertainties in the determination in atomic volume $V(x)$ come into play only nearly to second order; indeed as shown by Eq. 5.2, $V(x)$ appears only as a ratio:

$$\frac{V(x_L)}{V(x_S)} = \frac{V(x_L^0)}{V(x_S^0)} \left\{ 1 + \left[\left(\frac{\partial V}{\partial x} \right)_{x_L^0} - \left(\frac{\partial V}{\partial x} \right)_{x_S^0} \right] \delta x + O(\delta x^2) \right\}, \tag{5.6}$$

in which the slopes at point x_L^0 and x_S^0 partially cancel. Basically, the same argument holds for the λ-terms and for Eq. 5.4. Therefore, x_L or Δx values are poorly influenced by systematic errors on inelastic mean free path or atomic volume.

On (110) surface, the found subsurface composition over ~ 3 nm is close to $Fe_{0.6}Al_{0.4}$; it falls into the ordered B_2 range of stability according to the bulk phase diagram (Fig. 3.1).

For (100) and (111), the composition $Fe_{0.53}Al_{0.47}$ is the Al-rich limit of CsCl B_2 phase.

5.2 Surface crystallography from LEED and GIXD

All the three surfaces of $Fe_{0.85}Al_{0.15}$ crystals show a faint (1×1) or no LEED pattern right after sputtering. Upon annealing, only on the (110) face, surface segregation was accompanied by a reproducible surface reconstruction that was analysed by LEED and GIXD. The other ones (100) and (111) displayed a (1×1) like LEED pattern without the intermediate reconstruction found in the literature (Sect. 3.3).

5.2.1 (110) orientation

5.2.1.1 LEED analysis

Due to the centring of the rectangular surface unit cell of the A_2 bcc random alloy (see Fig. 3.4), all the $h_S + k_S = 2n+1$ reflections with n integer are extinguished [5]. It is reminded that the indexes S and B stand for crystallographic quantities related to surface or bulk unit cell. Directly after sputtering and even after annealing at 673 K (not shown), the (110) surface has a faint (1×1) LEED pattern. However, on a surface free of carbon stripes (see Sect. 4.1 and Fig. 4.6), a reconstruction appears at annealing temperature above 873 K in the range of segregation of aluminium as shown by photoemission (Fig. 5.5). The corresponding LEED pattern [6] shown in Fig. 5.8 has a pseudo-hexagonal "flower"-like shape around only active (1×1) reflections.

Combining patterns taken at low energy around the $(00)_S$ reflection (Fig. 5.8-b) and the superstructure spots around $\{11\}_S$ surface reflections, the nearest commensurate superstructure unit cell could be determined with the help of the *LEEDPat* software [239] from Hermann and Van Hove (Fig. 5.9). It corresponds to a rotation matrix $\begin{bmatrix} 4 & 0 \\ 2 & 5 \end{bmatrix}$ in the rectangular centred unit cell $(\mathbf{a}_S, \mathbf{b}_S)$ of Fig. 3.4 or $\begin{bmatrix} 4 & 4 \\ -3 & 7 \end{bmatrix}$ in the primitive unit cell $(\mathbf{a}_{S,P}, \mathbf{b}_{S,P})$ unit cell of Fig. 3.4. The superstructure unit cell is close to an hexagonal one with $a_r = 16.36$ Å, $b_r = 16.61$ Å and angle of $\gamma_r = 60.5°$. Its first lattice vector $\mathbf{a}_r$ is aligned along the $\mathbf{a}_S$ direction. Being commensurate, such a reconstruction leads to only one domain.

However, despite distortions due to sample alignment, the matching between simulated and experimental LEED patterns (Fig. 5.9) is not fully satisfactory with an apparent incommensurability along the $[10]_s$. This feeling is confirmed by integrated line cuts along $[10]_S$ and $[01]_S$ direction through the $(\bar{1}1)_S$ reflection of Fig. 5.9. While commensurability is verified along the $[01]_S$ direction ($\Delta h_S = 0.2$, $\times 5$ periodicity), peaks appear at $h_S = \pm 0.12, \pm 0.56$ along the $[10]_S$ direction that is to say at a distance of $\Delta h_S = 0.44$ from the surface Bragg

[5] An $A_2(110)$ surface as determined from photoemission should lift these extinctions. But this seems to be blurred by the complex surface superstructure described hereafter.

[6] The (110) LEED pattern of native surface decays upon ageing under vacuum (see Sect. 4.2)

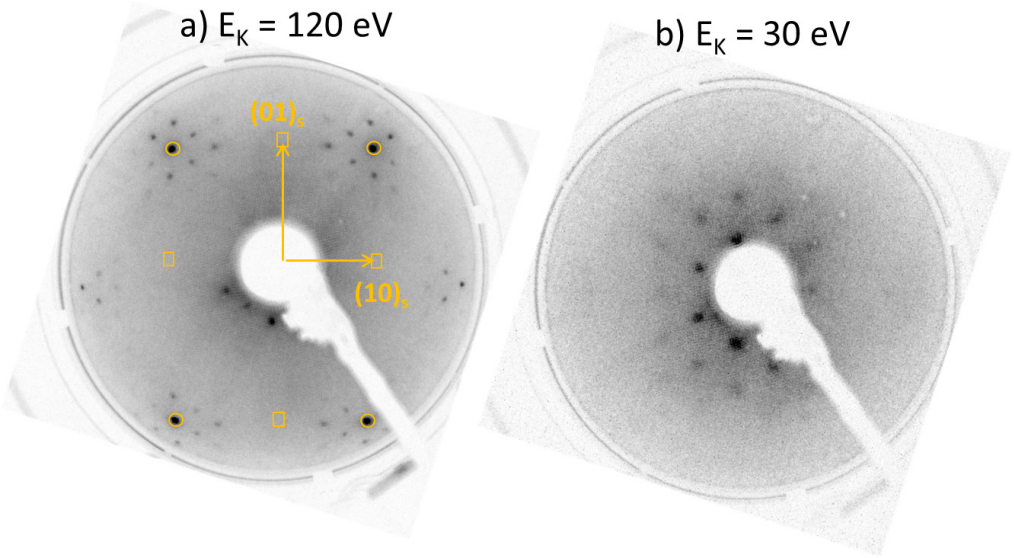

Figure 5.8: LEED patterns of a clean $Fe_{0.85}Al_{0.15}$(110) surface annealed at 1123 K. Beam energies are indicated in figure. The active and extinguished bulk spots are shown as orange circles and squares, respectively.

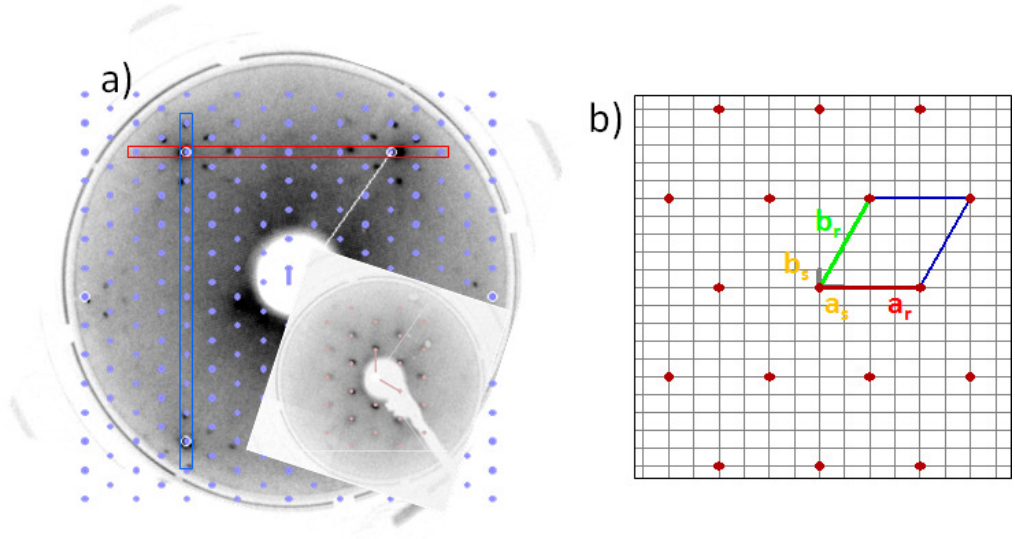

Figure 5.9: a) Overlap between LEED pattern of Fig. 5.8 with the proposed commensurate superstructure. The inset shows the overlap close to the origin of the reciprocal space. Red and blue boxes correspond to line cuts shown in Fig. 5.10. Notice the discrepancy along $[10]_S$. b) Corresponding direct space. The grey grid stand for the nodes of the (1×1) rectangular unit cell $(\mathbf{a}_S, \mathbf{b}_S)$. The red dots are the nodes of the superstructure with basis vectors $\mathbf{a}_r$ (red) and $\mathbf{b}_r$ (green).

peaks. Indeed, whatever the beam energy, the superstructure spots are found only around Bragg spots. This convolution of reciprocal space nodes by superstructure ones (that verifies also the surface extinctions of $\{10\}_S$ and $\{01\}_S$) corresponds typically to an incommensurate modulation in direct space along $[h_S 0]$ of the atomic positions and/or of the composition of the unit cell. This is not a simple incommensurate overlayer on-top of the substrate leading to a Moiré pattern. By introducing the corresponding expansion along $[10]_S$ in the commensurate unit cell matrix, the modulation itself can be described by the matrix $\begin{bmatrix} 4.55 & 0 \\ 2.27 & 5 \end{bmatrix}$ in the rectangular centred unit cell $(\mathbf{a}_S, \mathbf{b}_S)$. The "unit cell" corresponding to this modulation ($a_{r,m} = 18.57$ Å, $b_{r,m} = 17.19$ Å and angle of $\gamma_{r,m} = 57.27°$) is a hexagon squeezed along the $[01]_S$. Now, by convoluting all the substrate nodes of reciprocal space by the LEED pattern corresponding to this matrix, the matching with the LEED pattern is perfect (Fig. 5.10-c).

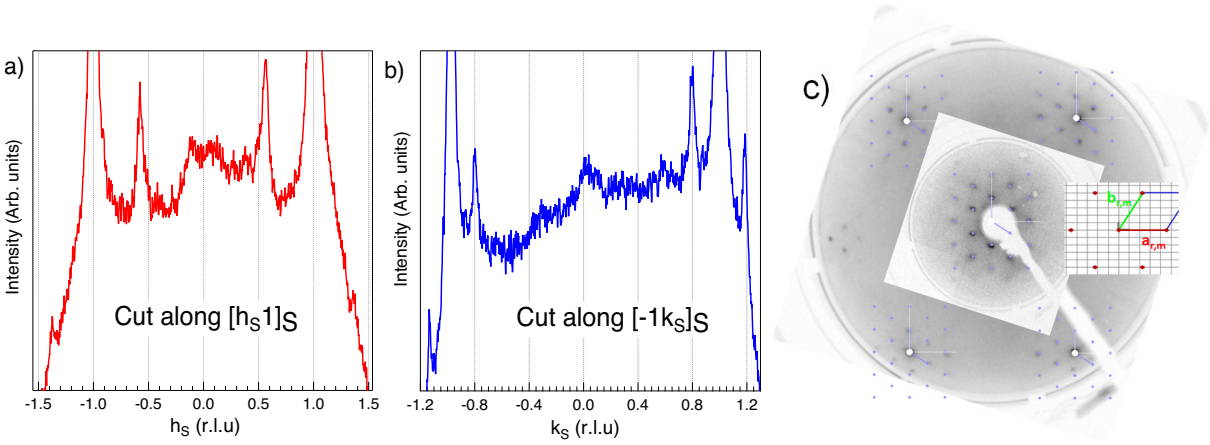

Figure 5.10: Line cuts of the LEED pattern of Fig. 5.9 along a) $[10]_S$ (red box) and b) $[01]_S$ (blue box). c) Convolution of the nodes of substrate reciprocal space with a modulation of unit cell shown as inset (see text).

5.2.1.2 GIXD analysis

The LEED findings have been further confirmed by GIXD. The three main directions $(h_S, 0)$, $(0, k_S)$ and (h_S, h_S) of reciprocal space have been scanned in GIXD at $l_s = 0.075$ on a clean surface annealed at 1050 K (Fig. 5.11 black lines). The main reconstruction peaks (grey lines) appear at $(h_S = 1.56 - 3.56 - 5.56)$ and $(0, k_S = 1.10 - 1.8 - 2.2 - 3.8 - 4.2)$ showing that the superstructure due to the aluminium segregation is commensurate along the $[01]_S$ but incommensurate along the $[10]_S$. Analysis of peak width of the reconstruction peaks around integer positions both in radial and angular scans points at a nearly constant reciprocal broadening of $\Delta q_A \simeq 0.05 - 0.06$ Å^{-1} for $(h_S \pm 0.44, k_S)$ and of $\Delta q_B \simeq 0.03 - 0.04$ Å^{-1} for $(h_S \pm 0.22, k_S \pm 0.2)$. The corresponding coherence length of $1/\Delta q_A \simeq 16 - 20$ Å and $1/\Delta q_B \simeq 24 - 33$ Å is of the order of the modulation showing its disordered character as seen in STM (Sect. 5.3.1).

Besides those peaks that are similar to those of LEED, broad bumps of FWHM $\Delta k_S \simeq 0.3$ are visible at $(0, k_s = 2.76, 4.76, 6.76)$ (Fig. 5.11-b) and also along the more complex (h_S, h_S) direction (Fig. 5.11-c). Those are reminiscent of a complex modulation of the unit cell content, position and/or composition over a length $a_S/\Delta k_S \simeq 14$ Å.

Out-of-plane scan at the position of the most intense superstructure peak ($h_S = 0, k_S = 2.2$) (Fig. 5.12) has a strong modulation with an increasing broadening with l_S. An approximative analysis of peak FWHM Δl_S in terms of size ($\Delta l_{S,s}$) and strain ($\frac{\Delta c_r}{c_r}$) effects of Williamson-Hall type $\Delta l_S^2 = \Delta l_{S,s}^2 + \left(\frac{\Delta c_r}{c_r}\right)^2 l^2$ (inset of Fig. 5.12) leads to a variation of lattice parameter of $\frac{\Delta c_r}{c_r} \simeq 0.2$ and a domain size of $c_S/\Delta l_{S,s} \simeq 8$ Å *i.e.* around 6 atomic layers.

Finally, the extended reflectivity or the $(0, 0, l_S)$ rod was measured at room temperature after sputtering and along the annealing up to 1053 K. The poor evolution of the rod up to 873 K parallels the temperature dependence of segregation of aluminium observed with photoemission (Fig. 5.5) and the smoothing of the surface seen with microscopy (Sect. 5.3.1). The shape of the rod (red curve of Fig. 5.13) points at surface relaxations and/or modulation of composition. Further analysis is needed to model the atomic profile of segregation.

5.2.2 (100) orientation

Starting from an annealing temperature of 673 K up to 1123 K, the LEED pattern is sharp and (1×1) (see Fig. 5.2.2) without any traces of reconstruction. Spot sharpen with temperature and $(n \times n)$ reconstruction can be ruled out from the Bragg angle estimated from screen-sample distance and screen size.

5.2.3 (111) orientation

From an annealing temperature of 773 K to 1273 K, the $Fe_{0.85}Al_{0.15}(111)$ orientation has a (1×1) surface structure as shown in Fig. 5.15. No superstructure peak has ever been found. The marked evolution of the peak intensity with beam energy with an apparent 3-fold symmetry is due the open structure of the (111) surface of body-centred metal (see Fig. 3.5) and the reminiscence of the bulk extinctions. Indeed, the surface unit cell $(\mathbf{a}_S, \mathbf{b}_S, \mathbf{c}_S)$ (of parameter $a_s = b_s = a\sqrt{2}, c_s = a\sqrt{3}/2$) is occupied by three atoms at coordinates $(0, 0, 0)$, $(1/3, 2/3, 1/3)$ and $(2/3, 1/3, 2/3)$ leading to a structure factor with bulk extinctions when $h_S + 2k_S + l_S = 3n + 1$ and $h_S + 2k_S + l_S = 3n + 2$ with n integer (or $h_S + 2k_S + l_S = 3n + 2$ and $h_S + 2k_S + l_S = 3n + 1$). Therefore, for bulk diffraction, one over three Bragg peaks will be active along the $(10l_S)$ and $(11l_S)$ rod but with an offset of $\Delta l_S = 1$ between the two types of rods. Since atoms are not coplanar on the (111) surface, this conclusion partially applies to electron diffraction despite the poor penetration depth of electrons.

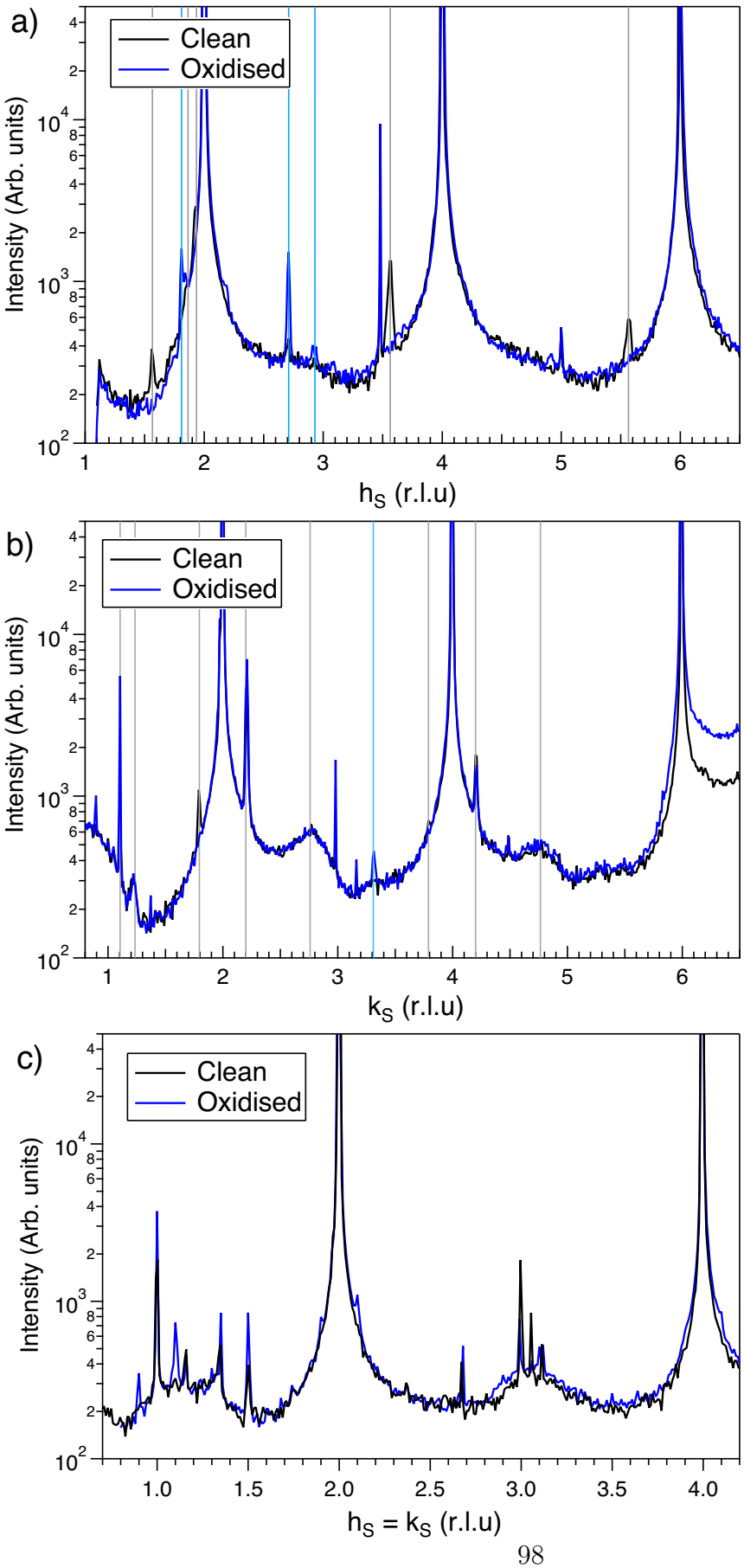

Figure 5.11: In-plane radial diffraction scans ($l = 0.075$) of a clean $Fe_{0.85}Al_{0.15}(110)$ surface annealed at 1050 K (black line) and after oxidation at the same temperature with 500 L of O_2. a) $(h_S, 0, 0.075)$, b) $(0, k_S, 0.075)$, c) $(h_S, h_S, 0.075)$. Grey lines points at peaks due the clean surface reconstruction and light blue ones to new peaks due to the oxide layer.

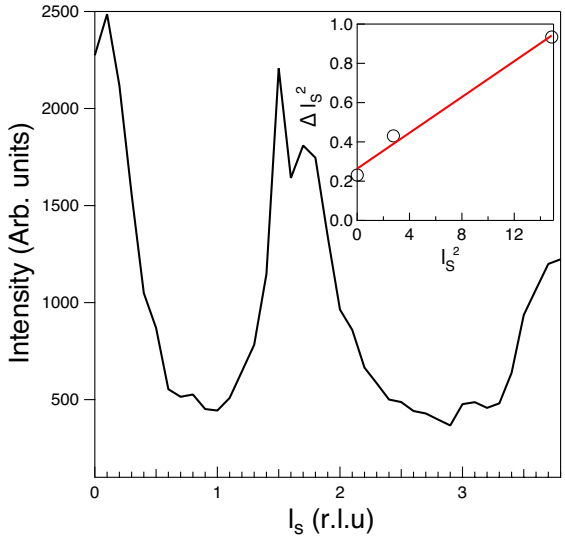

Figure 5.12: Out-of-plane l_S scan on the reconstruction peak ($h_S = 0, k_S = 2.2$) of the clean $Fe_{0.85}Al_{0.15}(110)$ surface. The inset shows a Williamson-Hall plot of peak width.

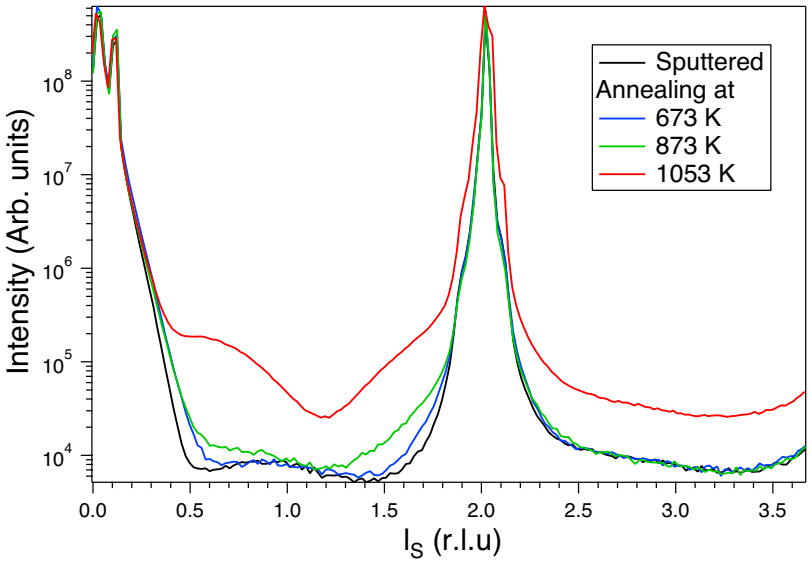

Figure 5.13: $(0, 0, l_S)$ rod evolution of a sputtered $Fe_{0.85}Al_{0.15}(110)$ surface during annealing at increasing temperature.

5.3 Morphology of the $Fe_{0.85}Al_{0.15}$(110), (100) and (111) surfaces

5.3.1 $Fe_{0.85}Al_{0.15}$(110)

As seen in Sect. 4.1.2 and in particular in Fig. 4.5, annealing the (110) surface after sputtering induces a sizeable smoothing, a straightening of the step edges and an increase of average size of terraces which become separated mostly by monoatomic height steps (as seen for instance in Fig. 4.5 and in the height distribution of Fig. 5.17-d).

As already partially evoked in Sect. 4.1.2 about carbon segregation, zooms at higher resolution let appear a long-range ordered hexagonal-like superstructure in between the carbon

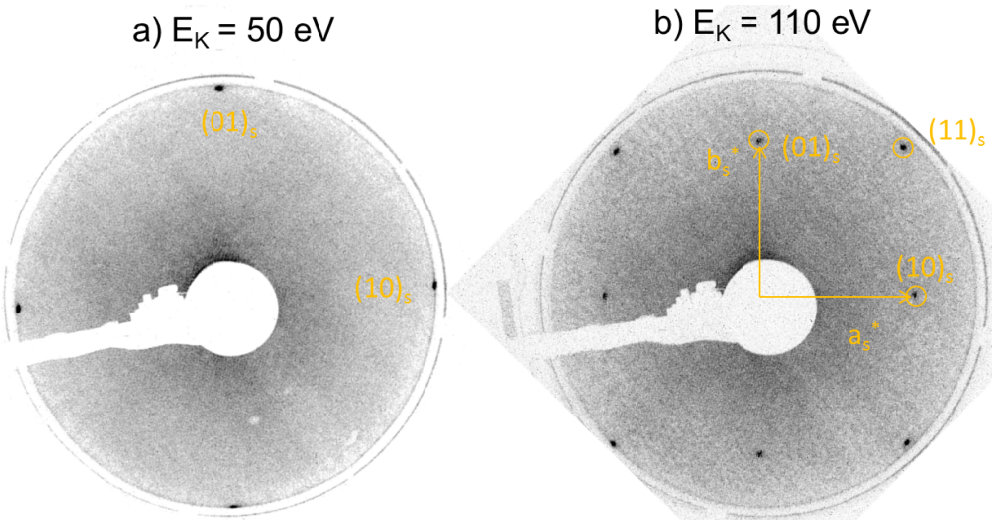

Figure 5.14: LEED patterns of a $Fe_{0.85}Al_{0.15}$(100) surface annealed at 973 K. The surface is (1×1) as indicated by spot indexes.

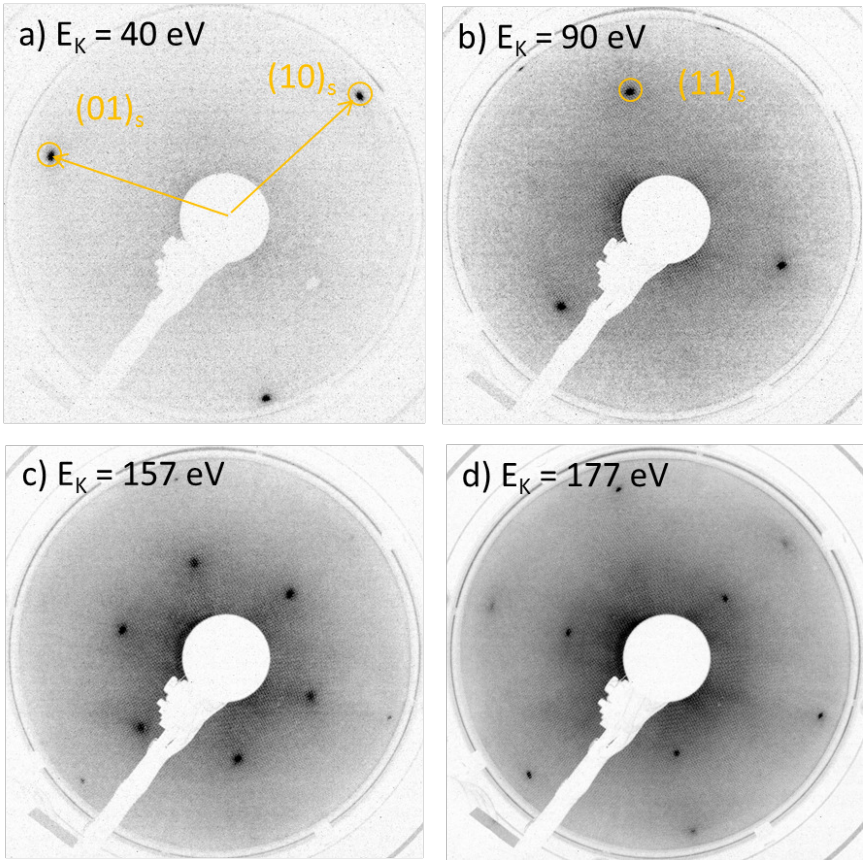

Figure 5.15: Evolution with beam energy of the LEED pattern of $Fe_{0.85}Al_{0.15}$(111) after annealing at 973 K.

stripes (Fig. 5.16-a) and also on flat terraces (Fig. 5.17-a). Because of the very complicated intensity modulations, the determination of periodicities is difficult from simple line profile (Fig. 5.16-a, Fig. 5.17-a). Fortunately, the autocorrelation function [204] is a well-established tool for determining periodicities in complex images. It is defined as:

$$C(\xi,\eta) \propto \frac{1}{2X}\frac{1}{2Y}\int_{-X}^{+X}\int_{-Y}^{+Y}[z(x,y)-\overline{z}][z(x+\xi,y+\eta)-\overline{z}]dxdy, \tag{5.7}$$

where $\overline{z}$ is the mean height. After drift correction, the average periodicity measured on the autocorrelation images (Fig. 5.16-d; Fig. 5.17-b) along the three "equivalent hexagonal" directions is 2.1 ± 0.2 nm which matches the lattice parameters of 18.6×17.2 Å^2 of the "pseudo" hexagonal supercell found with LEED. The superstructure occupies the whole surface from one terrace to the other as seen in Fig. 5.17-c,d and does not appear as different domains which confirms the description with only one supercell as obtained from LEED and GIXD. It is worth noticing the strong fluctuations of the "hexagon" sizes and shapes but with a low apparent surface corrugation of 0.05-0.1 Å (see line profiles Fig. 5.16-b, Fig. 5.17-e). Amazingly, the contrast is inverted between images taken at different polarities (Figs. 5.16-a,c) demonstrating, beyond topographic contribution, also the role of density of states, the nature of atoms and the hybridisation between Fe and Al [240]. Indeed, in a naive picture, Fe 3d electronic states are expected to be more localised and to lie more below the Fermi level than the Al sp ones which are more delocalised. But *ab initio* calculations of $Fe_{1-x}Al_x$ [241] pointed at a strong hybridisation between Fe 3d and Al sp levels with a strong local character between nearest neighbours; the density of states at the Fermi level is in fact dominated by Fe 3d levels with some contributions from Al 3p. Therefore, the perimeter of "hexagons" is probably more iron rich (Fig. 5.16-c).

Some bright protrusions are also apparent and are probably related to contamination due to the reactivity of the surface (see Chap. 4). The hexagonal superstructure seems to appear already from the lowest annealing temperature (not shown) at the onset of aluminium segregation.

5.3.2 $Fe_{0.85}Al_{0.15}$(100)

Large scale STM images of a (100) surface (Fig. 5.18) annealed at increasing temperatures exhibit a clear improvement of the roughness and a straightening of the step edges along approximatively the $[10]_S = [001]_B$ direction. But the step edges are not perfectly straight along the most compact $[10]_S$ direction; they are clearly kinked. Anyway, the step height agrees perfectly with the distance between atomic planes on the (100) surface. It can be estimated through a line profile perpendicular to the step (inset of Fig. 5.18-d) or more accurately by plotting a height histogram of a given STM image as depicted in Fig. 5.19 where four terraces are clearly observed with a separation of 1.45 ± 0.07 Å (the distance between (100) atomic planes being 1.445 Å).

At higher magnification, the terraces appear flat at the atomic scale (Figs. 5.20-5.21). Indeed, the roughness calculated on each image from $R_a = \frac{1}{N}\sum_{j=1}^{N} \mid z_j - \bar{z} \mid$ where z_j is the

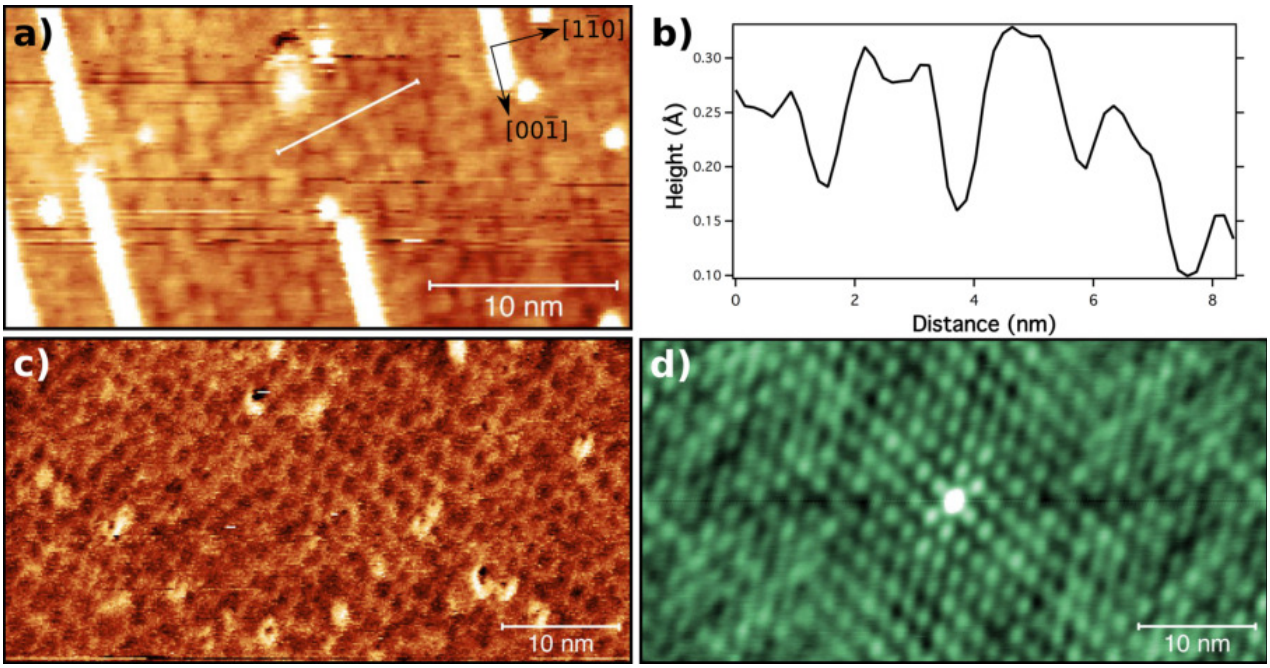

Figure 5.16: High resolution STM images of the $Fe_{0.85}Al_{0.15}$(110) surface annealed a) at 823 K (33×17 nm^2, $U_b = 2.0$ V, $I_t = 1.77$ nA; notice the presence of residual carbon stripes which appear as white lines) and b) line profile shown in Fig. a, c) at 1073 K (53×28 nm^2, $U_b = -1.3$ V $I_t = 0.23$ nA). c) 2D autocorrelation of image c.

pixel height and $\bar{z}$ the average pixel heigh amounts to 0.34 ± 0.05 Å and 0.12 ± 0.02 Å respectively; it is due to an actual electronic contrast *i.e.* a variation of the local density of state and not to topographic contrast. However, some line profiles exhibit holes, like the 1 Å deep one on Fig. 5.21-b,c that may be due to a missing atom. Image 5.20-b is reminiscent of the only STM observation of the literature on the (1×1) terminated $Fe_{0.85}Al_{0.15}$(100) showing disordered patches of protruding atoms (see Fig. 3.11 [32]). Protrusions, like on Fig. 5.20, are likely due to adsorbate and/or atoms on the surface since they can be moved by the tip between successive scans (Fig. 5.22).

5.3.3 $Fe_{0.85}Al_{0.15}$(111)

The smoothing of the (111) surface with increasing temperatures is even more apparent than on the two other orientations (Fig. 5.23). On large scale images, sputtering induces long range undulations with an amplitude of several nanometres and a correlation length of the order of several hundreds nanometres. Upon annealing, the roughness parameter R_a drops by an order of magnitude (from 1 nm to 0.1 nm) between 785 K and 1186 K where it reaches an atomic amplitude (see Fig. 5.23-bottom). Only some residual deep pits remain on large images.

However, upon increasing the magnification, the surface appears to be covered by nanometre-sized pits forming mainly triangular-shaped features aligned along the $[10]_S = [1\bar{1}0]_B$ and the

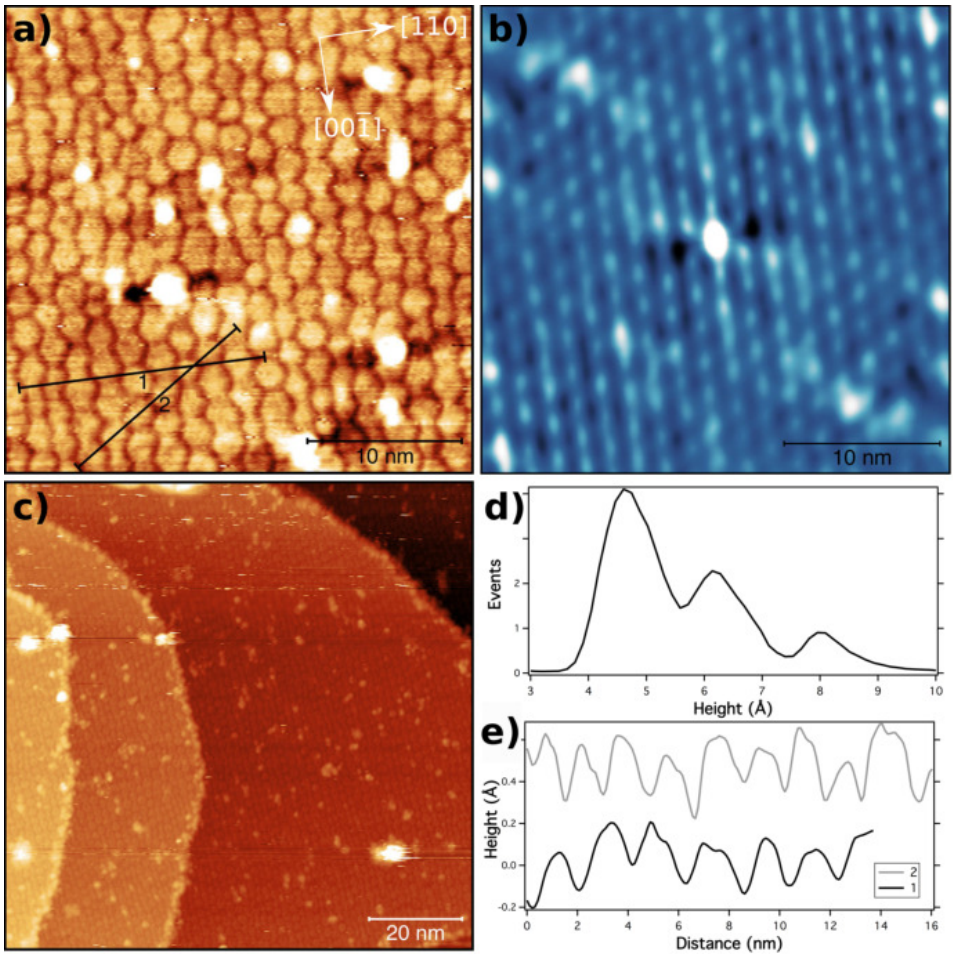

Figure 5.17: a) High resolution STM images of the $Fe_{0.85}Al_{0.15}$(110) surface annealed at 1150 K (30×30 nm^2, $U_b = 2.3$ V, $I_t = 0.2$ nA). b) 2D autocorrelation of the image-b. c) Large scale image (100×100 nm^2, $U_b = 2.1$ V, $I_t = 0.2$ nA). d) Height histogram of image-c. e) Line profiles shown in image a.

other two equivalent directions (Fig. 5.24). Pits have a size of around 1-2 nm and are organised as pyramidal protrusions (black and yellow triangles), holes with an internal periodicity (blue and green triangles) or even chains (green ellipses). This topographic appearance can be understood if one remembers that the (111) surface of body-centred metal is already open at the atomic scale (see Fig. 3.5); it exhibits three different levels separated by $a_B/2\sqrt{3} = 0.83$ Å (a_B being the bulk lattice parameter). Indeed, as shown on a small scale (20×18 nm^2) image (Fig. 5.25), height distribution histogram can be decomposed into gaussian peaks corresponding to different atomic planes; their constant spacing of 0.72 Å agrees with the bulk spacing and the number of peaks corresponds to nearly two unit cells along the $[111]_B$ direction.

A further analysis of the local slopes τ of pits of highest height demonstrate that they are nanopyramids with (111) vicinal side facets. As shown in Fig. 5.26, line cuts along three equivalent $[21]_S = [1\bar{2}1]_B$ directions at 120° that is to say normal to the $[10\bar{1}]_B$ pyramid edge give

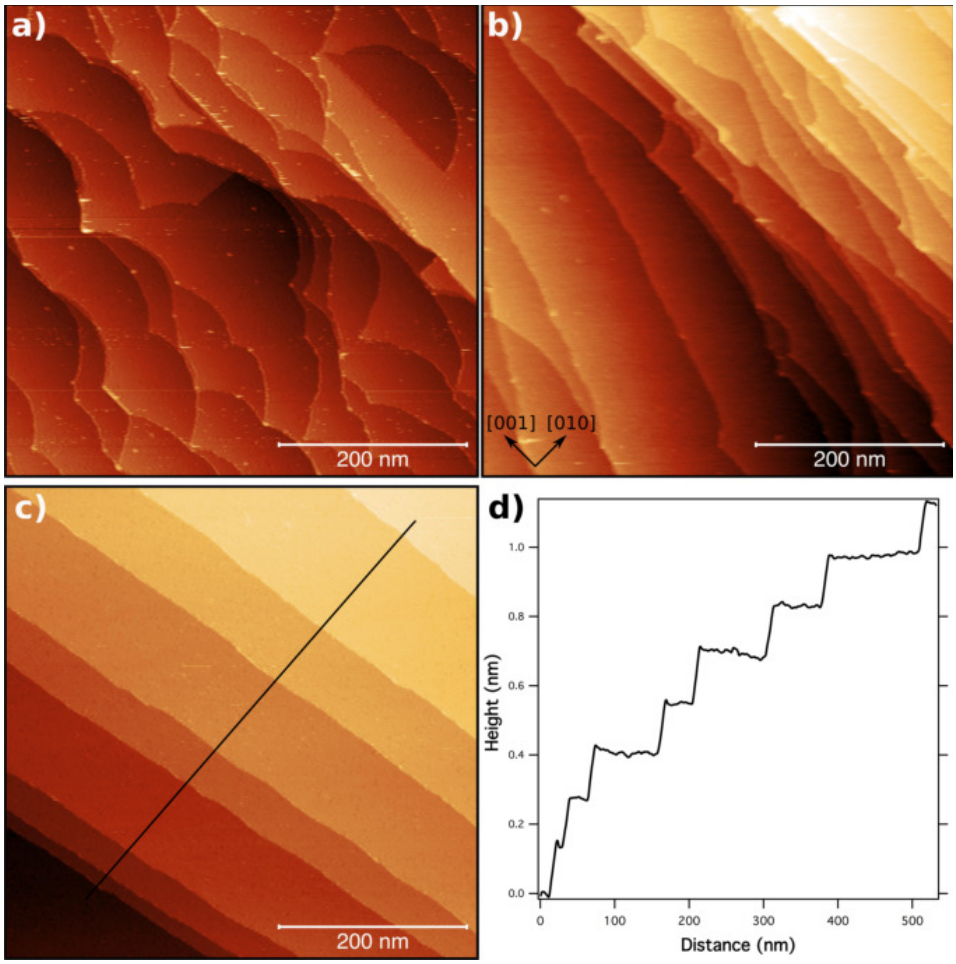

Figure 5.18: Large scale STM images (500×500 nm^2) of the $Fe_{0.85}Al_{0.15}(100)$ surface after annealing at three different temperatures: a) 1051 K ($U_b = 1.5$ V, $I_t = 0.4$ nA), b) 1078 K ($U_b = 0.9$ V, $I_t = 0.1$ nA), c) 1178 K ($U_b = -0.9$ V, $I_t = 0.3$ nA). d) Line profile drawn on the image c.

a local slope of 8.5° very close to the $\tau = 8.05°$ of (433) vicinal orientation. This conclusion is further confirmed by a global analysis of local slope angles τ on image 5.24-a. The distribution with a three-fold symmetry (not shown) is dominated by small τ values around $6 - 7°$ with a very poor contribution from flat areas at the opposite of (100) and (110) faces. A comparison with the expected angles for vicinal (111) surfaces of type $(hkk), h > k$, *i.e.* including the $[01\bar{1}]_B$ direction is given as grey lines in Fig. 5.24 [7]. The slope density peaks around (655), (544), (977) and (433) orientations. The three equivalent $(hkk), (khk), (kkh)$ form nanopyramids with downhill edges along the $[11\bar{3}]_B, [1\bar{3}1]_B, [\bar{3}11]_B$. But the symmetric orientations [8]

[7] The angle between (hkk) is given by $\cos\tau = \frac{h+2k}{\sqrt{3}\sqrt{h^2+2k^2}}$.

[8] The vicinal surface symmetric to $(hkk), h > k$ still including the $[01\bar{1}]_B$ bulk direction has an opposite slope. Their indexes $(h_s k_s k_s), h_s < k_s$ are given by the solution of the equation $\cos\tau = \frac{h+2k}{\sqrt{3}\sqrt{h^2+2k^2}} = \frac{h_s+2k_s}{\sqrt{3}\sqrt{h_s^2+2k_s^2}}$. A straightforward algebra give $\frac{h_s}{k_s} = \frac{4k-h}{2h+k}$. For instance, the symmetric vici-

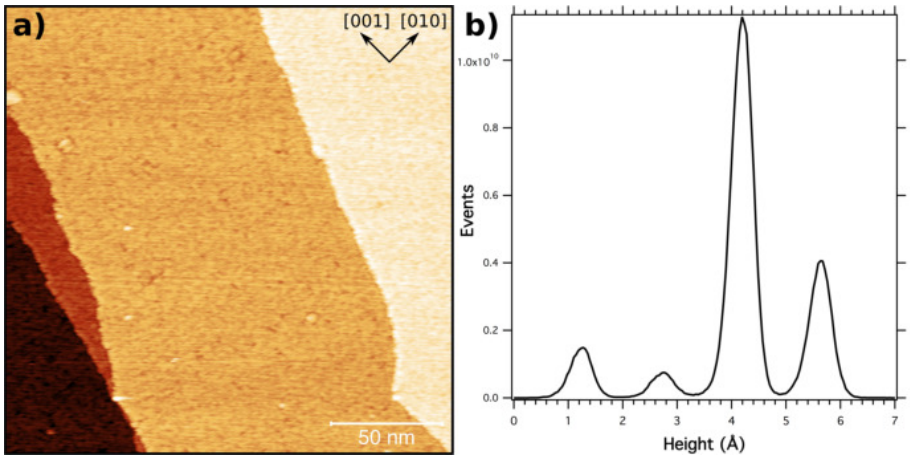

Figure 5.19: a) STM image of the $Fe_{0.85}Al_{0.15}$(100) surface after annealing at 1078 K (200 × 200 nm^2, $U_b = 0.9$ V, $I_t = 0.1$ nA. b) Corresponding histogram of the height of each pixel throughout the entire STM image.

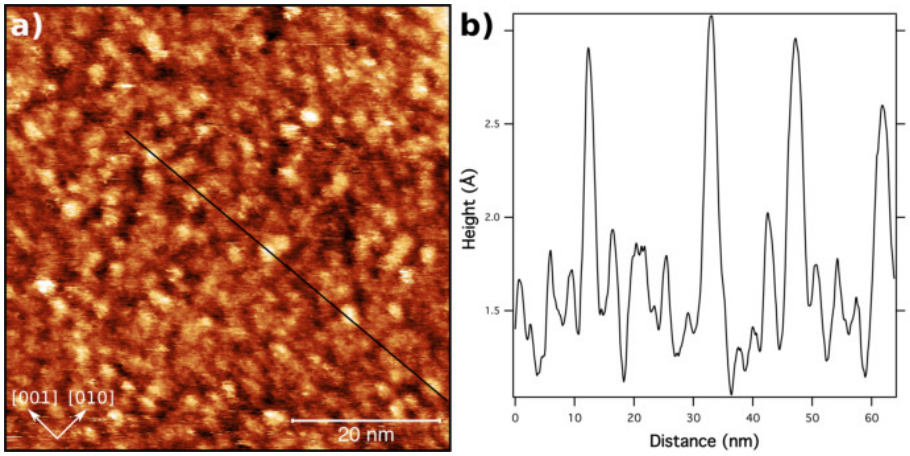

Figure 5.20: a) STM image (60 × 60 nm^2) of the $Fe_{0.85}Al_{0.15}$(100) surface after annealing at 913 K ($U_b = 0.2$ V, $I_t = 0.8$ nA). b) Line profile corresponding to the black line in the STM image.

corresponding to pyramids rotated by 180° do not appear, may be because of the miscut of the sample. At the opposite of face centred cubic lattice (111) vicinal surfaces which are staircases of compact (111) planes of decreasing lengths with τ and separated by single steps $a_B/\sqrt{3}$ (see Fig. 5.28), the (111) vicinal of body centred material are more complex (Fig. 5.27). They are made out of (211) local facets [9] separated by single steps $a_B/\sqrt{3}$ aligned along $[01\bar{1}]_B$ directions. The (211) facet (Fig. 5.29) includes protruding three-fold coordinated atom row along the "downhill" $[1\bar{1}\bar{1}]_B$ direction leading to open step edges with two-fold coordinated

nal of $(322), (755), (977)$ are $(588), (13, 19, 19), (19, 25, 25)$ planes.

[9] This holds true for angles higher and lower than that of (211) face.

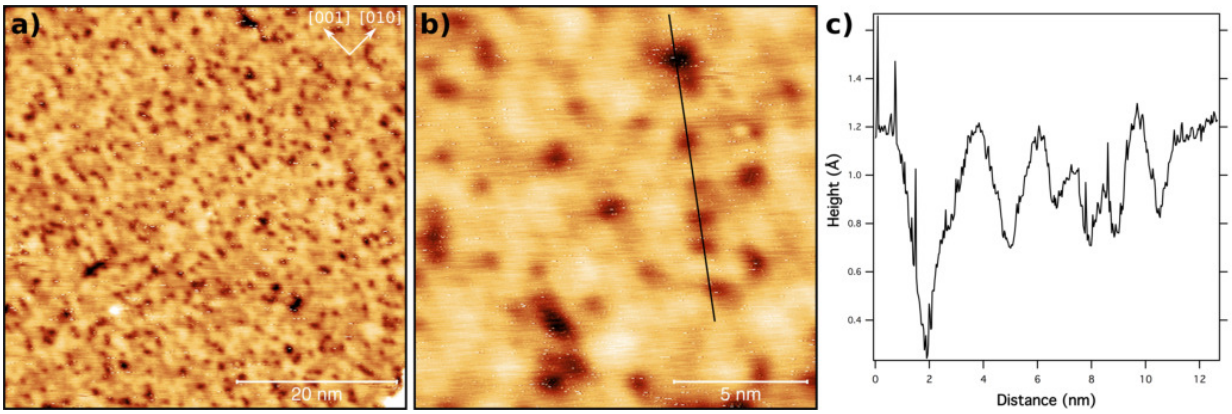

Figure 5.21: STM images a) 50×50 nm^2 and b) 15×15 nm^2 of the $Fe_{0.85}Al_{0.15}(100)$ surface after annealing at 1051 K ($U_b = 1.6$ V, $I_t = 0.4$ nA). c) Line profile corresponding to the black line in the STM image.

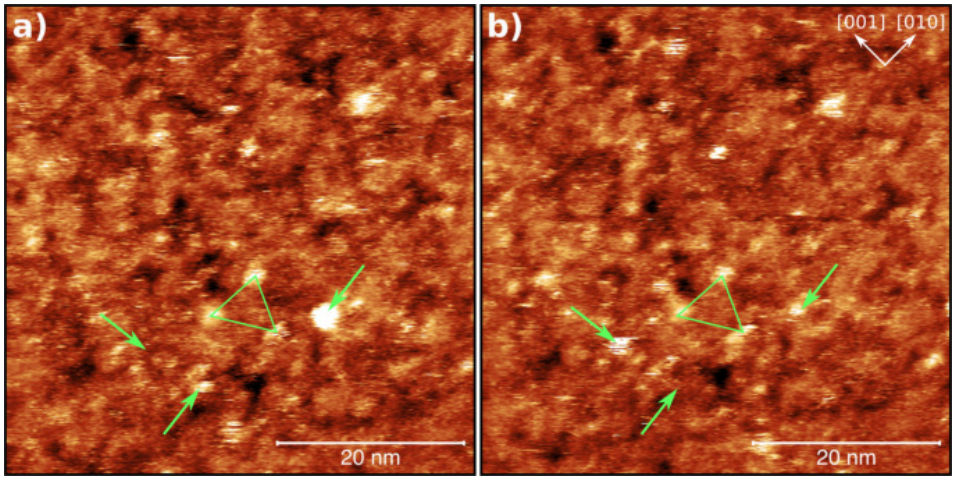

Figure 5.22: Successive STM images on a "clean" $Fe_{0.85}Al_{0.15}(100)$ (50×50 nm^2, $U_b = 0.6$ V, $I_t = 0.3$ nA). The arrows indicate the feature changing from one image to the other. The triangle is used as a reference.

and isolated atoms. Finally, the existence of only a few (111) atomic planes in the height distribution histogram (Fig. 5.25) is not really incompatible with nanometric size nanopyramids.

Aluminium segregation may favour this nanofacetting trend as it is known for other atomically rough and non-close-packed surfaces with high surface free energy when covered with a foreign element [242, 243]. For instance, when covered with oxygen or other metals, body-centred W(111)/Mo(111), face centred cubic Ir(210)/Pt(210) and hexagonal compact Re($12\bar{3}1$) spontaneously rearrange above 700 K to minimise their total surface energy by developping facets even if it involves an increase in surface area and step/kink energy contribution. Faceting on W(111) develops (211) facets upon O, Pt, Pd, etc... adsorption [242–244].

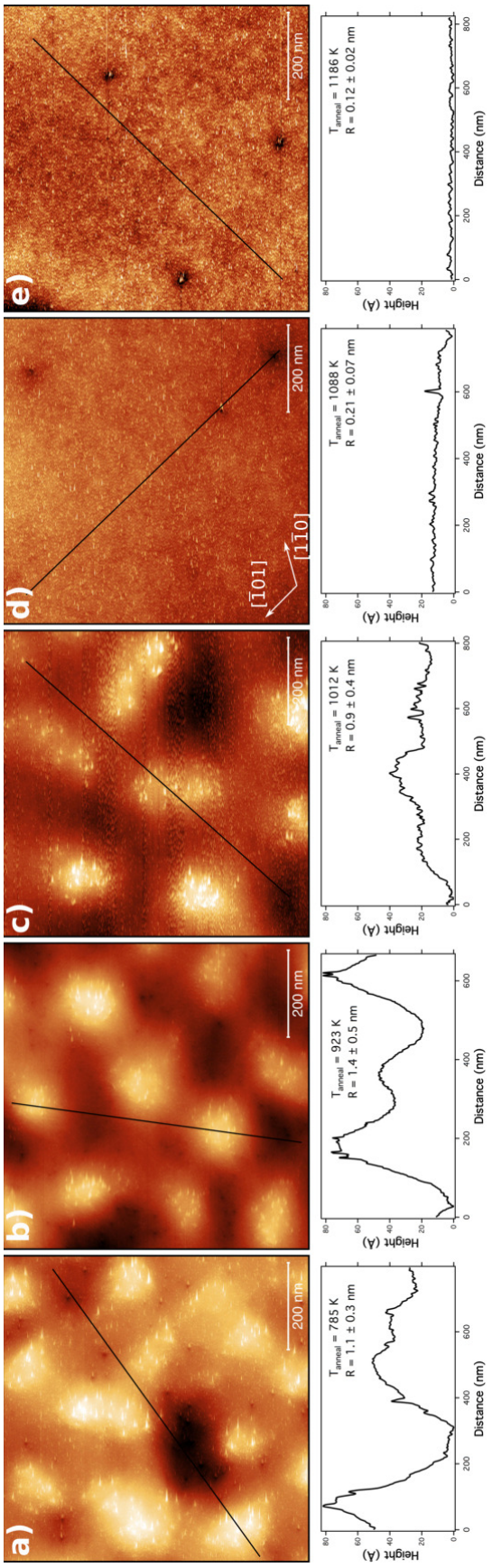

Figure 5.23: STM images (700×700 nm^2) of the $Fe_{0.85}Al_{0.15}(111)$ surface for different annealing temperatures as indicated in the figure. A typical line profile is drawn under each image and the roughness parameter R_a is also indicated. a) $U_b = -1.6$ V, $I_t = 0.4$ nA, b) $U_b = 1.5$ V, $I_t = 0.4$ nA, c) $U_b = -1.5$ V, $I_t = 0.4$ nA, d) $U_b = 1.6$ V, $I_t = 0.4$ nA, e) $U_b = 1.6$ V, $I_t = 0.4$ nA.

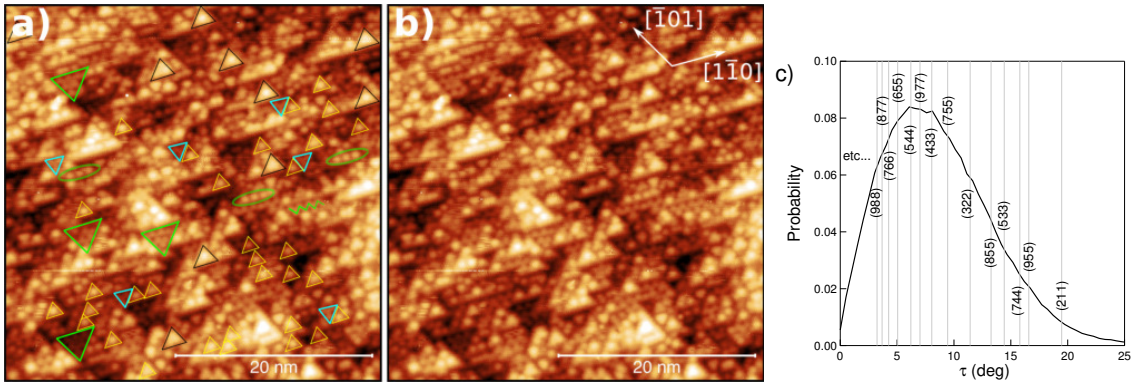

Figure 5.24: a) STM image (38×38 nm^2, $U_b = -1.5$ V, $I_t = 0.4$ nA) of the $Fe_{0.85}Al_{0.15}$(111) surface annealed at 973 K representing various topographical features regularly reproduced. c) Local slope τ distribution of image a. The values for (111) vicinal surfaces of type (hkk) with $h \leq 9$ and $k < h$ are pointed.

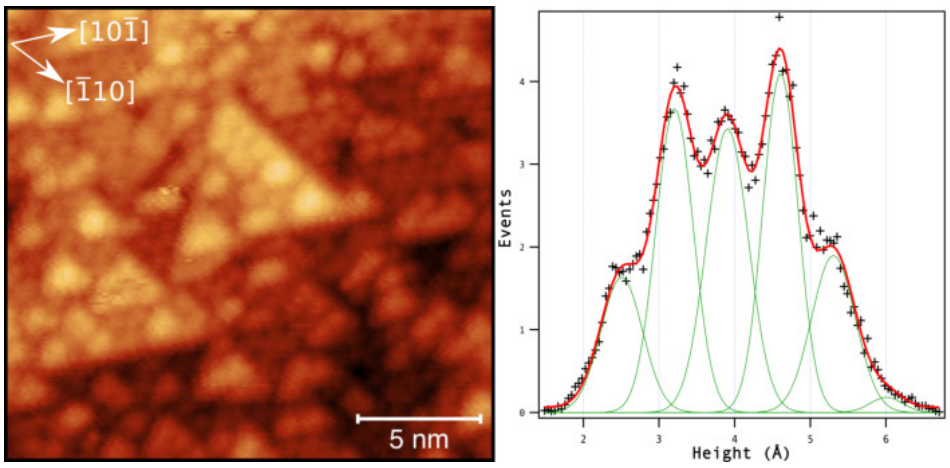

Figure 5.25: a) STM image (20×18 nm^2, $U_b = -1.6$ V, $I_t = 0.5$ nA) of the $Fe_{0.85}Al_{0.15}$(111) surface annealed at 1173 K. b) Corresponding height histogram with its fit with several equidistant peaks.

In those cases, the driving force for faceting is thermodynamics, since it leads to a reduced surface energy of the covered vicinal surface with respect to the flat surface. According to calculations [90], this is already verified in the case of bare iron; an extended (211) surface has a lower energy that the open (111) surface ($E_{Fe}^{111} = 2.73$ J·m^{-2}; $E_{Fe}^{211} = 2.59$ J·m^{-2}). But faceting is controlled by kinetics and mass transport. On body-centred (111) surfaces, one physical monolayer is required; it corresponds to three atomic (111) planes; more material leads to islanding or alloying. Most of the time the formed facets are more close-packed than the initial one and facetting keeps the symmetry of the initial surface (C_{3v} in the case of $Fe_{0.85}Al_{0.15}$(111)). In our case, nano-facetting is observed upon aluminium segregation like in the case of sulphur on Fe(111) [245] and seems homogeneous since nano-pyramids do not

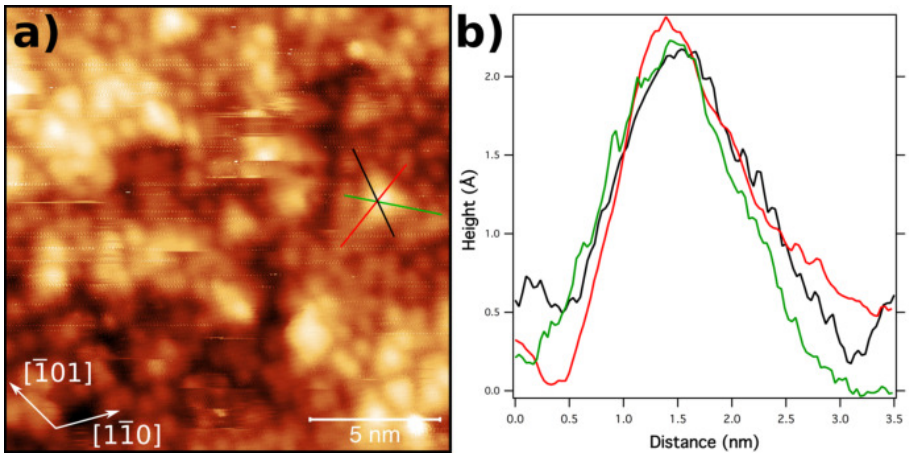

Figure 5.26: STM images of the $Fe_{0.85}Al_{0.15}$(111) surface (17×17 nm^2, $U_b = -1.2$ V, $I_t = 0.4$ nA) annealed at 785 K. The line profiles are represented on the right with the same colour code.

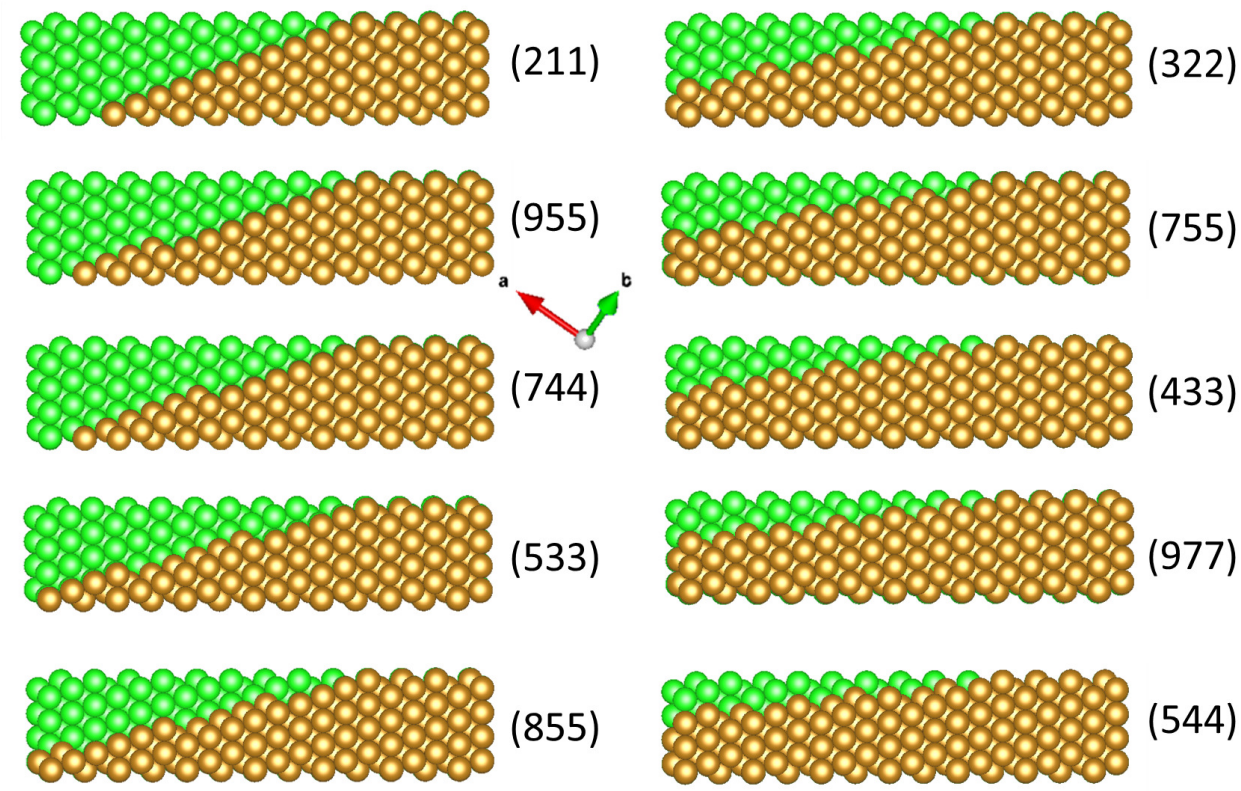

Figure 5.27: Ball model (brown spheres) of body-centred (111) vicinal surfaces normal to the [01$\bar{1}$] direction. Green balls stand for missing atoms of full (111) surface.

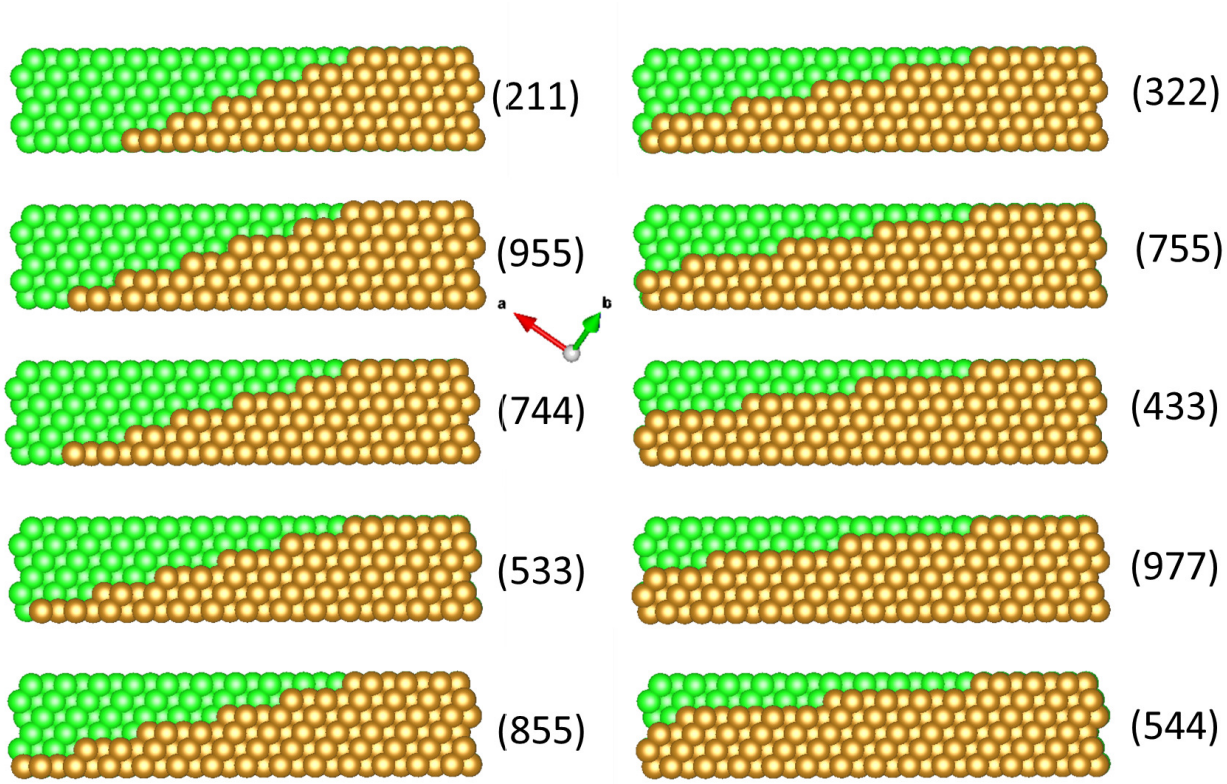

Figure 5.28: Same as Fig. 5.27 but for face-centred cubic material.

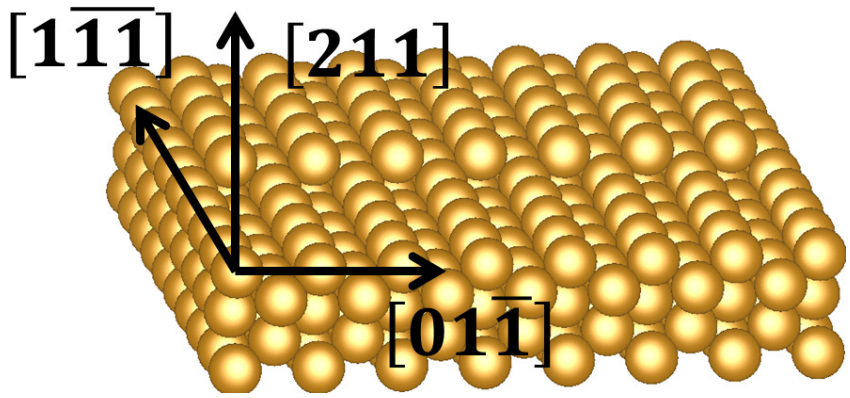

Figure 5.29: View in perspective of the (211) body-centred surface showing a step edge and protruding atom rows.

coexist with planar surface. Usually, faceting by an adsorbate is limited to a given temperature window before the onset of desorption of the foreign element; above the surface flattens again. But in the present case, segregation of aluminium provides an infinite reservoir; despite the increase of temperature (Fig. 5.23), the $Fe_{0.85}Al_{0.15}(111)$ smoothens but never flattens. Finally, at the opposite of metal covered W(111), not only (211) facets are observed on $Fe_{0.85}Al_{0.15}(111)$) but vicinal of (111) maybe because of the complex interplay between segregation, formation of a surface alloy and faceting.

At last, few areas appear locally flat at the atomic scale with an hexagonal periodicity along bulk directions of ~ 8 Å which is the double of the surface lattice parameter ($a_S = 4.01$ Å). A likely hypothesis is local ordering of the segregated aluminium atoms in a B_2-CsCl structure in agreement with the $Fe_{0.5}Al_{0.5}$ surface composition found in XPS. Indeed on the FeAl(111), the lattice spacing is 7.35 Å.

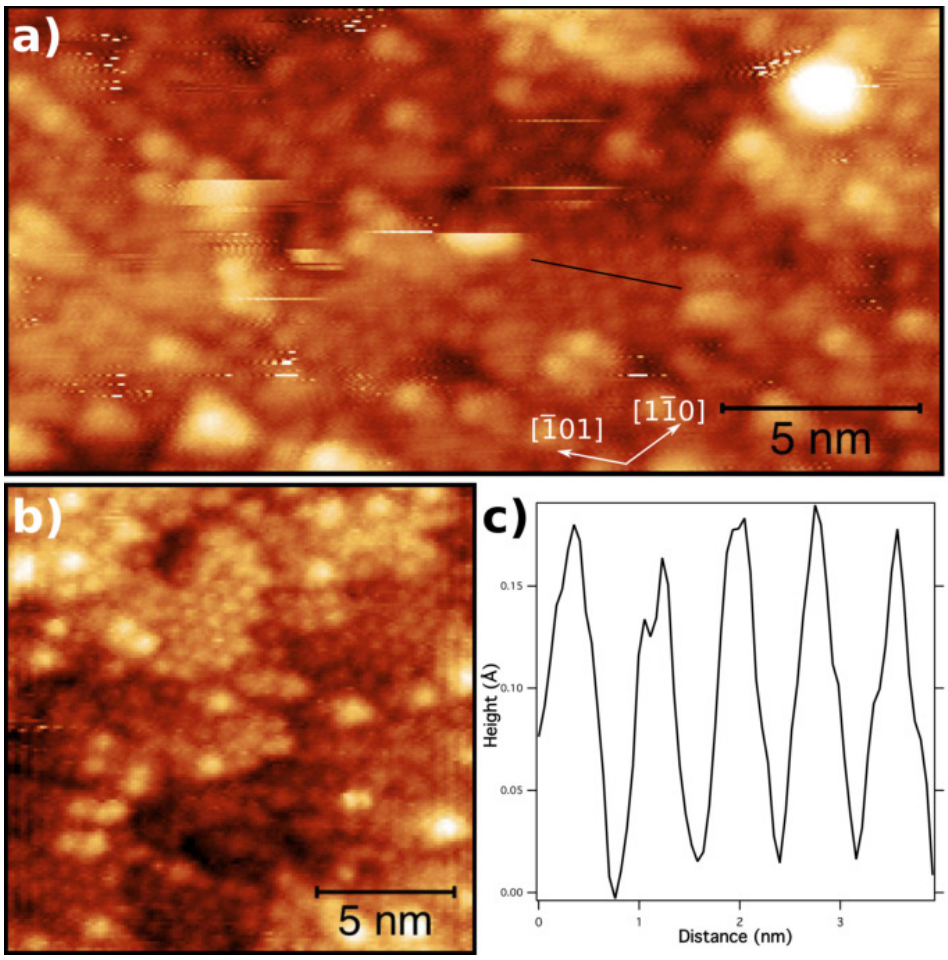

Figure 5.30: High resolution STM images of the $Fe_{0.85}Al_{0.15}(111)$ surface annealed at 785 K. a) 23.5×11.5 nm^2, $U_b = -1.6$ V, $I_t = 0.4$ nA, b) 17×17 nm^2, $U_b = -1.6$ V, $I_t = 0.5$ nA, c) Line profile corresponding to the black line of figure-a.

5.4 *Ab initio* calculations of Al segregation trend

To rationalise the segregation trend found mainly by photoemission (Sect. 5.1), *ab initio* calculations of mixing and segregation energies of aluminium in iron have been undertaken (J. Goniakowski, Institut des NanoSciences de Paris).

5.4.1 Computational methods and settings

All the calculations were performed within the Density Functional Theory (DFT) implemented in VASP (Vienna Ab Initio Simulation Package) [246, 247]. The interaction of valence electrons with ionic cores was described within the Projector Augmented Wave (PAW) method [248,249], and the Kohn-Sham orbitals were developed on a plane-wave basis set with a cutoff energy of 300 eV. Semi-core Fe 3p electrons were treated explicitly. All the calculations were spin-polarised with a ferromagnetic ordering of iron spins. Gradient-corrected PW91 [250] exchange-correlation functional was used.

Results summarised in Tab. 5.4 show a satisfactory agreement between computational and experimental results for bulk Fe and Al. We have checked that a Γ-centred (10×10×10) Monkhorst-Pack grid for k-point sampling of the Brillouin zone of the primitive unit cell of bulk iron (a_B = 2.84 Å) insures a convergence of the calculated lattice parameters (a_B) to within 0.005 Å and of cohesion energy (E_{coh}) to within 0.005 eV/Fe. A very similar degree of convergence is obtained with an equivalent ($7 \times 7 \times 7$) k-point sampling of the Brillouin zone of bulk aluminium (a_B = 4.05 Å) unit cell. We note that the overestimation of the bulk cohesion energy of Fe is principally due to a less accurate estimation of the total energy of an isolated Fe atom, and will thus not impact directly the calculated mixing, substitution, and segregation energies.

Fe (bcc)	a_B (Å)	E (eV)	B (GPa)	Al(fcc)	a_B (Å)	E (eV)	B (GPa)
calc.	2.836	5.06	186	calc.	4.052	3.43	72
exp.	2.867	4.29	170	exp.	4.050	3.34	76

Table 5.4: Calculated and experimental characteristics of bulk iron and aluminium: lattice parameter a_B (Å), cohesion energy E_{coh} (eV), and bulk modulus B (GPa).

Calculations on bulk $Fe_{1-x}Al_x$ ($x < 0.5$) phases were performed in a cubic ($2 \times 2 \times 2$) iron supercell containing 16 atoms. All the configurations were thoroughly optimised, including cell lattice parameters and all the atomic positions (residual forces smaller than 0.01 eV/Å).

Calculations of Al segregation energies at Fe surfaces of different orientations were performed in slab geometry. In all the cases, a single Al substitution per unit cell has been considered and its energy has been evaluated as: $E_{sub} = (E(\text{FeAl}) - (E(\text{Fe}) + E(\text{Al}))$, where E(FeAl) and E(Fe) are the total energies of Fe slab with and without an Al substitution and E(Al) is the total energy of an Al atom in bulk aluminium.

Different surface orientations required different computation settings to achieve an equivalent degree of convergence. Slabs composed of 7-9, 9-11, and 13-15 atomic layers have been used to represent (110), (100) and (111) surfaces, respectively. With these settings the surface energies (2.45 J/m^2, 2.53 J/m^2, and 2.67 J/m^2, respectively) are converged to within 0.01 J/m^2. Differences of E_{sub} for an Al substitution in the slab center between the thinner and the thicker slab are less than 0.01, 0.04, and 0.02 eV/atom, respectively.

5.4.2 Results

5.4.2.1 Calculated properties of bulk FeAl phases

We have considered the two known ordered bulk phases of $Fe_{1-x}Al_x$ ($x < 0.5$), namely $Fe_{0.5}Al_{0.5}$ (B_2) and $Fe_{0.75}Al_{0.25}$ ($D0_3$) and an additional low-concentration ($Fe_{0.9375}Al_{0.0625}$) cubic structure with a single Al atom in the (2×2×2) cell of bulk iron ($Fe_{15}Al_1 = Fe_{0.9375}Al_{0.0625}$). Tab. 5.5 summarises the essential structural and energetic characteristics of these systems.

	a_B (Å)	d_{Al-Al} (Å)	E_{mix} (eV/atom)	E'_{sub} (eV/atom)
Fe (bcc)	2.836 (+0.00%)	-	0.000	0.000
$Fe_{0.9375}Al_{0.0625}$ (bcc)	2.849 (+0.42%)	5.698	-0.045	-0.044
$Fe_{0.75}Al_{0.25}$ ($D0_3$)	2.870 (+1.16%)	4.059	-0.197	-0.190
$Fe_{0.5}Al_{0.5}$ (B_2)	2.877 (+1.45%)	2.877	-0.343	-0.332

Table 5.5: Calculated characteristics of bulk $Fe_{1-x}Al_x$ ($x < 0.5$) phases: lattice parameter a_B (Å), distance between Al atoms in the ($2 \times 2 \times 2$) unit cell : d_{Al-Al}, mixing energies: E_{mix} (eV/atom) and E'_{mix} (eV/atom). See text for details.

The mixing energy was evaluated with respect to pure bulk aluminium and iron reference $E_{mix}(Fe_{1-x}Al_x) = \{E(Fe_{1-x}Al_x) - [(1-x)E(Fe) + xE(Al)]\}/n$, where $E(Fe_{1-x}Al_x)$, $E(Fe)$, and $E(Al)$ are the total energies of bulk $Fe_{1-x}Al_x$ alloy, bulk iron and bulk aluminium, respectively and n is the number of sites in the units cell ($n = 16$ in the present case).

We find relatively large negative mixing energies, fully consistent with the existence of the ordered B_2 and $D0_3$ $Fe_{1-x}Al_x$ phases and in agreement with the large enthalpies of formations found in the literature [79, 83, 241]. Interestingly, since the Al-induced expansion of Fe lattice parameters is relatively small (< 1.5 %) for the considered Al concentrations ($x < 0.5$), we find that the mixing energies E'_{mix}, calculated without accounting for this expansion (lattice parameters fixed to bulk Fe values), are only little underestimated with respect to the fully optimised result (E_{mix} and E'_{mix} differ by less than 4%).

As a reference, a calculation in the more diluted case ($Fe_{0.981}Al_{0.019}$), performed in a cubic ($3 \times 3 \times 3$) unit cell (54 Fe atoms), predicts the lattice parameter of 2.839 Å (+0.001 % with respect to bulk Fe) and the mixing energy E_{mix} = -0.014 eV/atom.

5.4.2.2 Trends in Al segregation to the surface

(1×1) and (2×2) surface unit cells (see Sect. 3.2.1) have been systematically used for (100) and (111) oriented surfaces, while (1×1) and (2×3) surface cells were used for the (110) orientation. As it can be seen in Tab. 5.6, in case of (110) and (100) orientations, the (1×1) unit cells produce short nearest neighbour Al-Al distances, typical for these in $Fe_{0.5}Al_{0.5}$ (B_2) alloy. The larger surface cells [(2×2) and (2×3)] enable an accommodation of Al-Al distances equal to or larger than these in the diluted bulk case $Fe_{0.9375}Al_{0.0625}$ (bcc), where the Al substitutions are spaced by $d_{Al-Al} = 5.70$ Å.

	(110)	(100)	(111)
(1×1)	2.84, 4.01	2.84, 2.84	4.01, 4.01
(2×2)	-	5.67, 5.67	8.02, 8.02
(2×3)	8.51, 8.02	-	-

Table 5.6: Distances between Al substitutions d_{Al-Al} (Å) in the different surface unit cells used in the calculations.

Despite this fact, with the larger cells, we find that the calculated E_{sub} for Al substitution in the slab center (-0.83, -0.80, and -0.89 eV/atom, for (110), (100), and (111) orientations, respectively) are systematically more negative compared to the estimation obtained for the bulk $Fe_{0.9375}Al_{0.0625}$ phase, E_{sub} = -0.68 eV/Al. Results obtained for Al substitutions in the slab center of the (1×1) unit cells (-0.69, -0.61, and -0.83 eV/Al, respectively) represent a less favourable substitution with respect to the large cells. Aside a small contribution due to a possible lack of a full convergence with respect to the slab thickness and to fine differences in the sampling of the Brillouin zone of differently oriented slabs, these results reveal a many-body character of the iron-mediated Al-Al interaction, which likely depends on the precise configuration of the Al substitutions in the subsequent coordination shells. This trend to ordering was already pointed in Sect. 3.1.

In the following, we will analyse the variation of E_{sub} as a function of position of the Al substitutions within the slabs of different orientations. For this purpose, for each subsequent atomic layer i ($i = 1$ corresponds to the surface atomic layer), we define the segregation energy as $E^i_{seg} = E^i_{sub} - E^c_{sub}$, where E^i_{sub} and E^c_{sub} are substitution energies in i-th atomic layer and in the slab center, respectively. Fig. 5.4.2.2 summarises the results obtained with differently oriented slabs for both (1×1) and for the larger surface unit cells.

We note that, despite significantly different Al densities in calculations with the small and with the large surface unit cells, the obtained segregation profiles are qualitatively similar and that the main quantitative differences concern the surface layers only. This validates the present computational settings and shows the robustness of the calculated behaviours and trends.

For the three surfaces, we find a general oscillatory behaviour of E^i_{seg} which consists of an increase of tendency for segregation at the surface (negative E^i_{seg}), followed by a decrease

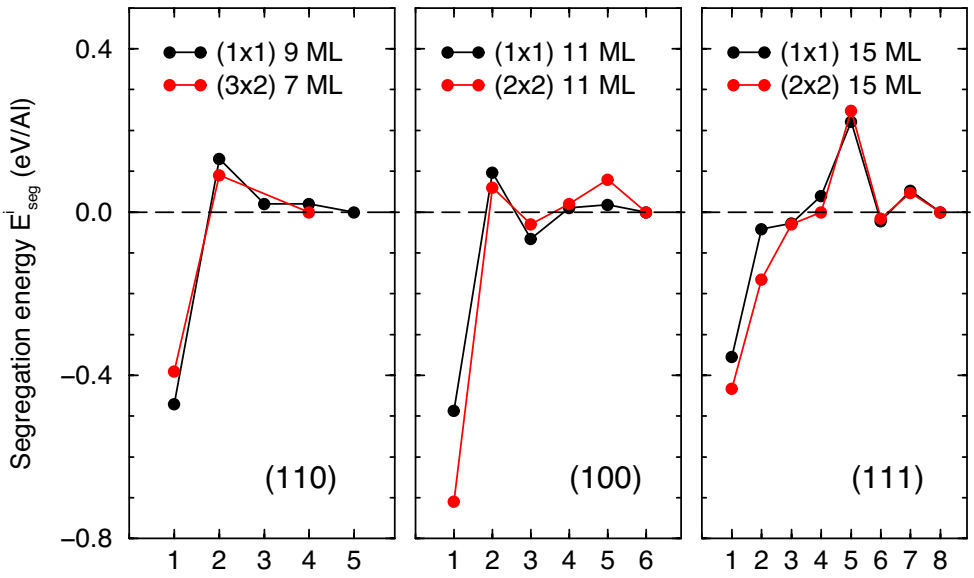

Figure 5.31: Layer-resolved profiles of segregation energies of Al substitutions in Fe slabs of different orientations.

(positive E^i_{seg}) in a sub-surface region. Underneath the sub-surface region the variations of E^i_{seg} become relatively small. In the case of (110) and (100) surfaces, both the surface and the subsurface regions consist essentially of a single atomic layer ($i = 1$ for the surface and $i = 2$ for the sub-surface region), and variations of segregation profile are strongly attenuated already for $i > 3$. Conversely, in case of the (111) surface, the surface region with negative E^i_{seg} extends over three surface atomic layers ($i = 1 - 3$) and is followed by a sub-surface region composed of layers $i = 4$ and 5, the 5th one being particularly strongly unfavourable for Al segregation. In this case variations of segregation profile are attenuated only below the 6th atomic layer. The very different thickness of the surface region of the (111) surface can be directly linked to the very open character of this surface. Indeed, under-coordinated atoms (atoms with missing nearest neighbours (NN)) at this surface can be found down to the 3rd surface layer (4 NN, 7 NN, and 7 NN in the 1st, 2nd and 3rd surface layers, compared to 8 NN for bulk atoms). Conversely, at the (110) and (100) surfaces, the under-coordinated atoms are present in the 1st surface layer only (6 NN and 4 NN, respectively). Calculated E^1_{seg} which describe the thermodynamic bias for surface segregation show that the results obtained with small and with large surface unit cells are essentially very similar except for the (100) surface, where the segregation effect is visibly stronger at low Al coverage. This is to be assigned to the high density of surface Al in the (1×1)-(100) unit cell.

In the following, we focus on the results obtained in the limit of low Al concentrations (large unit cells). We find that surface segregation is the most favoured at the (100) surface ($E^1_{seg} \sim$ -0.7 eV) and that the (110) and (111) oriented surfaces are characterised by a similar E^1_{seg} of about -0.4 eV. The principal force responsible for the strong segregation at (100) surfaces is the low coordination of its surface atoms (4 NN, compared to 6 NN on the (110) surface). Interestingly, an equally low coordination of surface atoms on the (111) surface (4 NN) does not produce an equally strong segregation. It is to be assigned to a much stronger surface relaxation at the (111) surface, induced by under-coordinated atoms in the 2nd and 3rd surface layers. This strong relaxation results in particularly short surface inter-atomic

distances which partially compensate the effect of lost neighbours.

5.4.2.3 Trends in Al surface adsorption energies

The adsorption energy of Al adatoms at iron surfaces of different orientations was defined as $E_{ads} = -(E(\text{Fe+Al}) - (E(\text{Fe}) + E(\text{Al}))$, where E(Fe+Al) and E(Fe) are the total energies of Fe slab with and without Al adsorbates and E(Al) is the total energy of an isolated Al atom. Tab. 5.7 summarises the computed adsorption characteristics of Al at the three iron surfaces.

	(110)	(100)	(111)
(1×1)	4.04	4.54	4.69
(2×2)	-	3.90	4.78
(2×3)	3.86	-	-

Table 5.7: Adsorption energies (eV) of Al adatoms at differently oriented Fe surfaces obtained with different surface unit cells.

In all the considered cases, surface adsorption of Al atoms is thermodynamically favoured (positive adsorption energies). Moreover, since adsorption energies are larger than Al cohesive energy (Tab. 5.4), adsorption on the Fe surface is favoured over formation of 3D Al clusters. Regarding the (110) and (100) surfaces, we find that E_{ads} increases at a higher density of surface Al, what reveals an attractive interaction between Al ad-atoms. The increase is particularly well pronounced in the case of (100) surface, where the (1×1)-(100) unit cell configuration corresponds to a dense surface Al ad-layer. Conversely, the effect is small and opposite at the (111) surface, where however the distances between Al adatoms in the (1×1) unit cell are much larger (Tab. 5.6).

Focusing on the energetically favoured case of adsorption in dense configurations [(1×1) unit cells], the progressive increase of E_{ads} along the series is to be linked to the increase of the number of first Fe and Al neighbours of the adsorbed atom [(110): 2 NN Fe and 2 NN Al, (100): 4 NN Fe and 4 NN Al, (111): 4 NN Fe and 0 NN Al). In the case of (111) surface E_{ads} is likely influenced by the strong surface relaxation. Most likely it will be additionally enhanced if the surface Al layer is made more dense.

5.5 Discussion and conclusion

The composition of the sputtered $Fe_{0.85}Al_{0.15}$ surface was found close to the nominal one with a slight enrichment in Al. Upon annealing of all the studied low index surfaces, photoemission evidenced a strong aluminium segregation with a similar onset of temperature around 700 K probably dictated by bulk diffusion [96]. Whatever the orientation, both models of photoemission analysis (segregated film or profile) agree with a near surface composition close to $Fe_{0.5}Al_{0.5}$ with a typical affected depth of around 25 Å except on the (110) surface for which those figures are slightly different ($Fe_{0.6}Al_{0.4}$; $\sim$ 40 Å; Tab. 5.3). Although in agreement on the phenomenon with the existing literature obtained mainly on FeAl (Sect. 3.3) and with the

above calculations in terms of segregation and adsorption trends (Sect. 5.4), the thickness impacted by segregation is much larger than that determined previously by Auger spectroscpy or dynamic LEED measurements on FeAl [28,29,29–34,92,93,96] [10]. According to the bulk phase diagram (Fig. 3.1), the profile of composition should cross all the transitions $A_2 \leftrightarrow D0_3 \leftrightarrow B_2$ from the bulk to the surface. This gradient of composition was never really evidenced up to now in the $Fe_{1-x}Al_x$ system, probably because studies focused on ordered alloys; anyway, it was suspected in the diffraction study of Kotcke *et al.* [92] on FeAl(100). This segregation is accompanied:

- by the appearance of a non commensurate complex long-range structural/chemical superstructure with a pseudo-hexagonal unit cell of ~ 20 Å on the (110) surface,
- by a (1×1) termination on the (100) surface,
- by an intense faceting in the form of triangular pits having vicinal (111) side facets for the (111) orientation.

The slightly lower surface composition on the (110) surface found by photoemission ($Fe_{0.6}Al_{0.4}$ compared to $Fe_{0.5}Al_{0.5}$ on (100) and (111) surfaces) can be assigned according to *ab initio* calculations to a denser surface. A difference appears on the core levels. At grazing emission, Fe 3p peaks of all the surfaces overlap while, despite the poor resolution, fits conclude at a Al 2p (110) component narrower and more symmetric than on the other orientations pointing at a better defined chemical environment (Gaussian FWHM (110) 0.76 eV; (111) 0.84 eV; (100) 0.90 eV). Finally, theoretical work is on going to rationalise the observed faceting on the (111) surface.

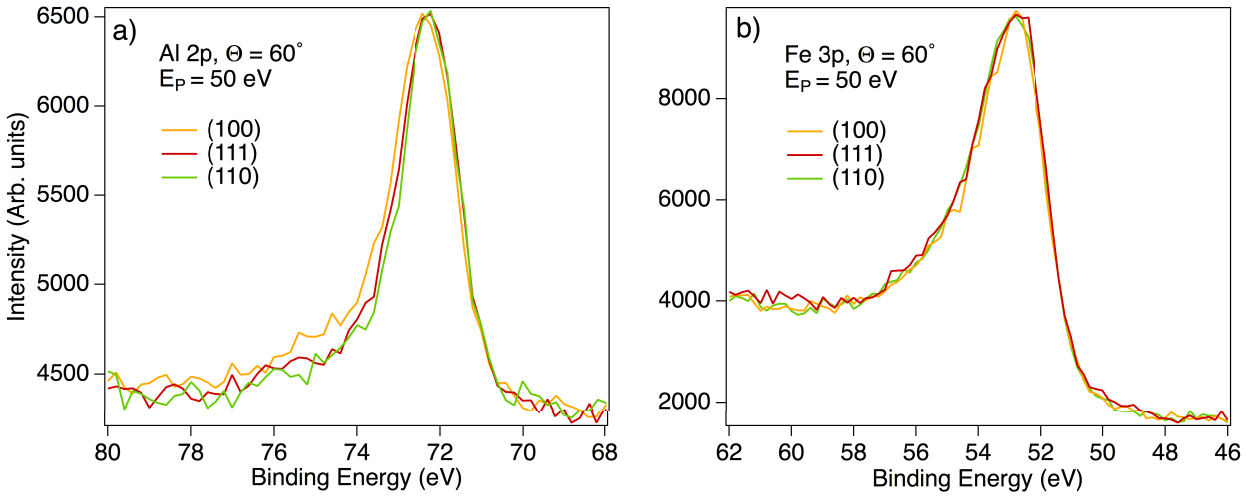

Figure 5.32: Comparison at grazing emission of the profile of the a) Al 2p and b) Fe 3p core level of the three orientations after annealing in the regime of Al segregration. Despite a slight oxidation, the (100) Al 2p is shifted and broader.

[10] Grasping oscillatory behaviour of composition found in the first layers of FeAl (see Sect. 3.3) and predicted by the present calculations (Sect. 5.4) is well beyond the sensitivity of our measurements.

CHAPTER 6

OXIDES ON THE $FE_{0.85}AL_{0.15}$(110), (100) AND (111) SURFACES

6.1 Film synthesis

Oxide films have been synthesised following the same protocol on all surfaces. Oxygen is introduced at a pressure in the range of $p = 10^{-7} - 10^{-6}$ mbar during the recrystallisation annealing plateau (15-20 mins) after sputtering. Duration was adapted to achieve a given exposure (1-1000 L) and the temperature was selected in the range 973-1173 K corresponding to the steady state regime of segregation on the bare surface (Fig. 5.5) but below the temperature at which oxide film decay is usually observed [16]. On the (110) surface, the oxide film characteristics are apparently poorly dependent on the moment of oxygen introduction in the annealing plateau (not shown). Despite the high temperature that imparts the residence time of oxygen, the reactivity of aluminium is such that a full layer (on the LEED and/or STM points of view) is always reached above 100 L whatever the surface. A few tests of two-step oxidation (room temperature exposure followed by high temperature annealing) have been performed on the (110) surface giving similar results like on NiAl(110) [152, 200].

6.2 Oxide on $Fe_{0.85}Al_{0.15}$(110)

6.2.1 Photoemission analysis

6.2.1.1 Angular dependence of core levels

Fig. 6.1 shows an angular analysis of the main three core levels after oxidation: Fe 3p, Al 2p and O 1s. The presence of O 1s and the strong enhancement of the Al 2p shoulder at grazing emission compared to the metallic component at $E_B = 72$ eV points at the formation of an aluminium oxide layer on top of the substrate. In parallel, as shown by the perfect overlap of Fe 3p profile before and after oxidation (Fig. 6.31), there is no visible evolution of the chemical state of iron even at grazing emission *i.e.* at the interface between the oxide and the substrate.

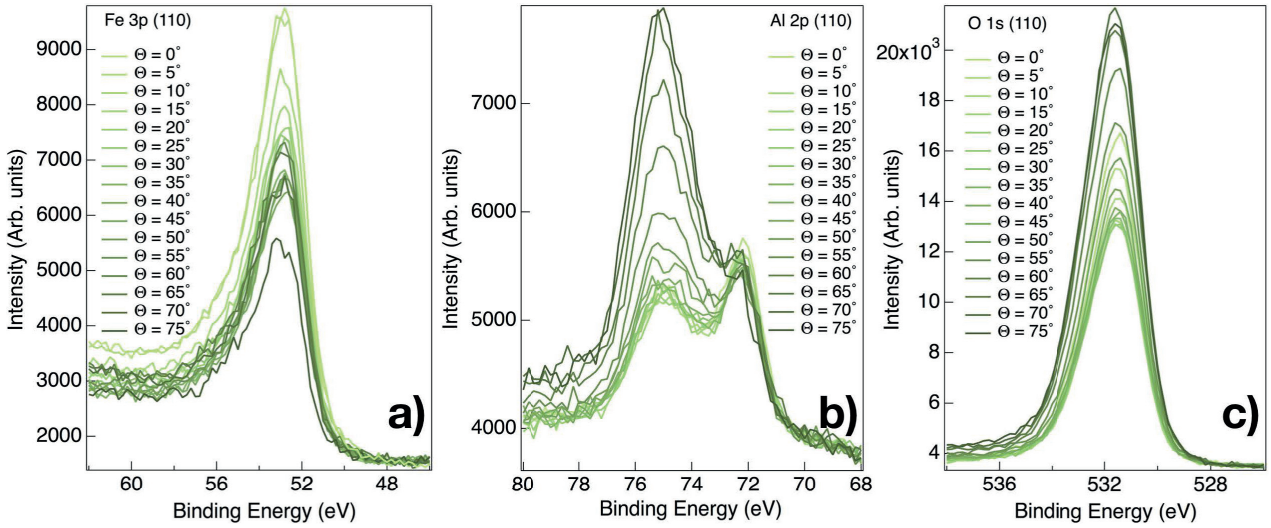

Figure 6.1: Evolution of the a) Fe 3p, b) Al 2p and c) O 1s core levels as a function of the emission angle for a (110) oxidised surface (500 L of O_2, 1123 K). Data have been normalised to the same background at low binding energy. High pass energy $E_p = 50$ eV was used for a faster acquisition.

Indeed, according to binding energy databases [50,51,236], iron oxides (FeO: $E_B = 55 \pm 0.6$ eV; Fe_3O_4: $E_B = 55.1 \pm 1$; Fe_2O_3: $E_B = 55.9 \pm 0.4$ eV; FeOHO: $E_B = 56.2 \pm 1$ eV [1]) or compounds with iron in different oxidation states (2+ or 3+) have a Fe 3p binding energy higher than that of metallic iron (Fe^0: $E_B = 52.9 \pm 0.3$ eV). But the corresponding shoulder on the high binding energy side of Fe 3p has never been observed in our experiments. This is in line with the difference of electronegativity of the two elements ($I_{Fe} = 1.83$; $I_{Al} = 1.61$; Pauling's scale [251]) which favours the preferential oxidation of aluminium.

6.2.1.2 Lineshape fitting

In the absence of iron oxidation, the profile of Al 2p (Fig. 6.2) core levels has been decomposed as explained in Sect. 2.5.3.1. As in the case of the oxide on NiAl(110) [13, 150, 151], three doublets are needed to describe Al 2p, one of which corresponds obviously to the metallic substrate. The spin orbit splitting of all components was kept at 0.4 eV as reported in databases [236] both for Al^0 and Al^{n+}. Metallic Al^0 component was accounted for by a Doniach-Sunjic profile (Eq. 2.18) while a Voigt function (Eq. 2.15) was used for the two extra oxide components. Similar values of the asymmetry parameter of the metal peak (Eq. 2.18) were found on the clean and oxidised surfaces. Shirley background subtraction and fit were done outside the range of X-ray source satellites (see Sect. 2.5.2). As in the following, the Lorentzian broadening (Eq. 2.17) of peaks was found very close to the emission width of Al-Kα (0.85 eV; see Sect. 2.5.2). Instrumental contribution to the peaks broadening as well as sample-related ones were included through the convolution with a Gaussian (Eq. 2.16). The obtained parameters are gathered in Tab. 6.1.

[1] Error bars stems from various references of [236].

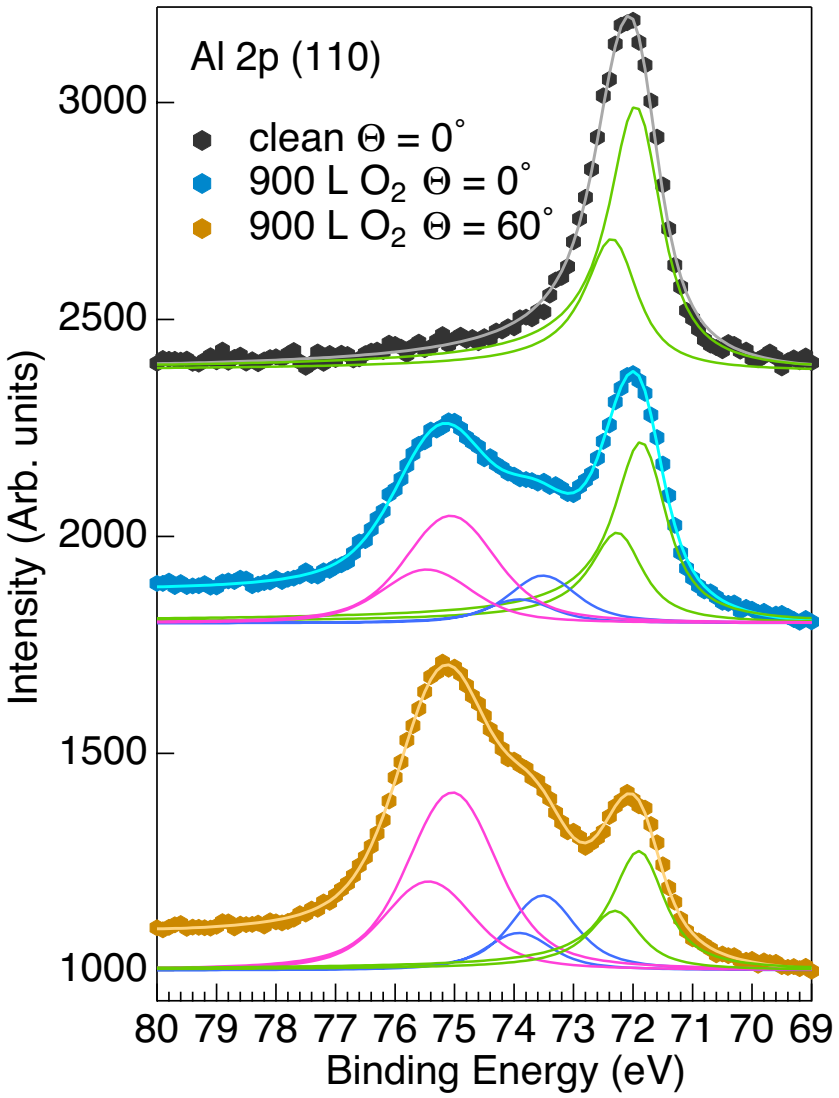

Figure 6.2: Line shape decomposition of the Al 2p core level for the (110) orientation. (Top panel) Clean surface annealed at 1123 K (normal emission); (Bottom and middle panels) Surface oxidised at the same temperature with 900 L of O_2 (normal and grazing emission). Three spin orbit split components are needed to fit accurately the data (points) for the oxide layer (see text). Only one is required for the clean surface. Fit parameters are given in Tab. 6.1. Spectra have been collected at a pass energy $E_p = 20$ eV providing the best resolution. Spin-orbit splitting was fixed at 0.4 eV for all components.

The good fit of the Al 2p core level of the clean surface with an unique Doniach-Sunjic profile, both in normal and grazing emission, evidences the lack of oxidation of the native surface (see Chap. 4). The binding energy $E_B = 71.9$ eV is smaller than the metallic Al^0 in databases [236] ($E_B = 72.6 \pm 0.3$ eV) by $\Delta E_B = -0.7$ eV, a phenomenon already known in the transition metal aluminides and assigned to the bonding between the transition metal and aluminium [101]. Comparison to values found for Al_2O_3 ($E_B = 74.1 \pm 1$ eV [236]) or film of aluminium oxide on Al ($E_B = 74.4 \pm 1.5$ eV [236]) favours an oxidation Al^{3+} state.

Finally, the assignment of the two oxide components to the surface and the interface atoms is based only on the comparison with conclusion drawn in terms of chemical environments on NiAl(110) [144, 151] and on FeAl(110) [16]. Indeed, at the opposite to synchrotron photoemission [144, 151], our measurements show no relative differences between the two oxide component intensities by switching from normal to grazing emissions (Tab. 6.1). The dis-

	Type	Shape	Relative area	E_B (eV)	L-FWHM (eV)	G-FWHM (eV)	Asymmetry
Clean-NE $\Theta = 0°$	Bulk	DS	1.0	71.90	0.85	0.35	0.09
Oxi NE-$\Theta = 0°$	Bulk	DS	0.45	71.85	0.85	0.35	0.10
	Interface	V	0.14	73.50	0.85	0.80	-
	Surface	V	0.41	75.10	0.85	1.30	-
Oxi GE-$\Theta = 60°$	Bulk	DS	0.25	71.90	0.85	0.35	0.08
	Interface	V	0.19	73.50	0.85	0.75	-
	Surface	V	0.56	75.00	0.85	1.30	-

Table 6.1: Fit parameters of the Al $2p_{3/2}$ core level decomposition for (110) surface (Fig. 6.2). Clean (1273 K) and oxidised (1123 K, 500 L of O_2) surfaces are compared either at normal emission ($\Theta = 0°$) or at grazing emission ($\Theta = 60°$). DS and V stand for Doniach-Sunjic and Voigt profiles. Binding energy (E_B) and Lorentzian and Gaussian FWHMs of the corresponding components are given. The DS asymmetry is given for the metallic component. Error bars are of the order of the step size, *i.e.* 0.05 eV.

tributions of environments for the surface aluminium oxide atoms may explain the larger broadening compared to the interface atoms.

6.2.1.3 Segregation under the oxide from angular analysis

From the previous core level decomposition, the aluminium enrichment underneath the oxide formed at the (110) surface was obtained from the angular evolution (Fig. 6.1) of the ratio of areas of metallic Al 2p and Fe 3p components. The case of an oxide film synthesised with a high exposure (1123 K, 500 L of O_2) was selected to ensure a covering layer. The template found at low pass energy $E_p = 20$ eV (Tab. 6.1) was kept fixed to analyse angular data at lower resolution ($E_p = 50$ eV). Compared to the bare surface (Fig. 6.3), a flat profile and a nearly constant composition are found over the typical probing depth of laboratory photoemission. To further quantify it, an approach similar to that developed for bare surface (Sect. 5.1.2.1) was employed by fitting the experimental results of Fig. 6.3 (open circles) with the models of (i) an homogeneous segregated layer (Eq. 5.2, Fig. 5.3-c) or of (ii) a continuous diffusive profile (Eq. 5.4, Fig. 5.3-d; line). The bulk atomic fraction *i.e.* far from the oxide/metal interface was kept at $x_S = 0.15$. In principle, any signal of the substrate should be further damped in the oxide overlayer through a term that accounts for the partial coverage of the oxide, if any, and for its thickness. Fortunately, since Al 2p and Fe 3p core levels are very close in binding energies (Tab. 5.1), their inelastic mean free paths in the alumina layer are the same (Tab. 6.3); both signals are damped in a similar way, an effect which is cancelled through their ratio of intensities.

Not surprisingly, the typical length of the segregated layer (Tab. 6.2) which is obtained is much larger than the probing depth of photoemission with a large uncertainty. Nevertheless, the composition of the subsurface of the substrate under the oxide is enriched in aluminium $x_L \simeq x_S + \Delta x \simeq 0.31$ but at a lower level than in the case of a bare surface $x_L \simeq x_S + \Delta x \simeq 0.42$

(Tab. 5.3).

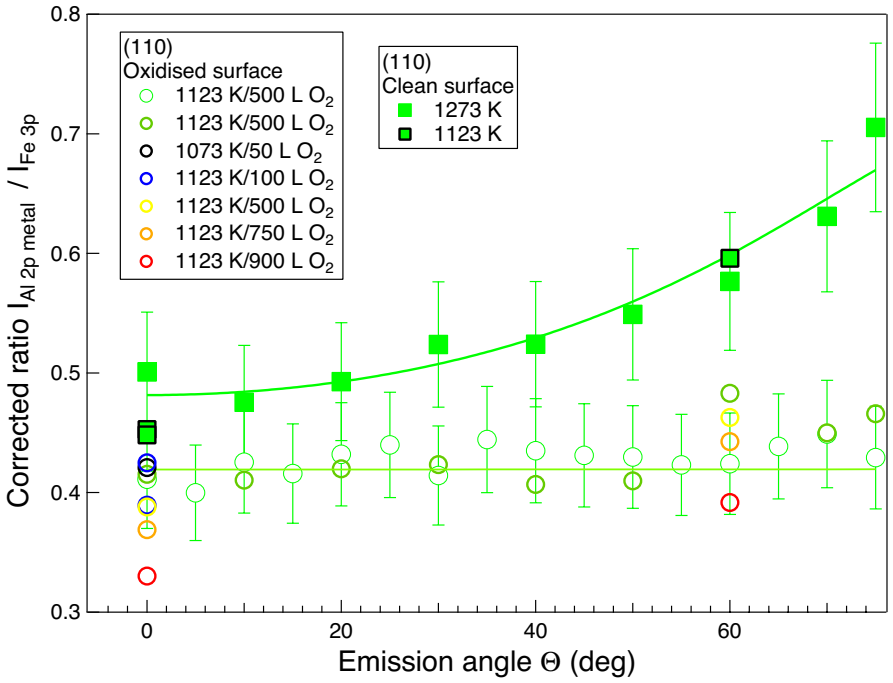

Figure 6.3: Comparison of angular variation of the corrected ratio $I_{Al\,2p\,metal}/I_{Fe\,3p}$ (pass energy $E_p = 50$ eV) for the metallic components in the as-prepared (110) surface (filled squares) and after oxidation as indicated in figure (open circles). Dedicated angular measurements are compared to more punctual normal/grazing measurements; the chosen error bars of 10 % on the experimental ratio matches with data dispersion. At the opposite to the clean surface, no apparent segregation is found underneath the oxide layer over the probing depth of photoemission as confirmed by a fit with a continuous profile (line, Eq. 5.4).

6.2.1.4 Oxide film thickness and stoichiometry

Assuming a continuous oxide film, the oxide thickness can be obtained from ratios of areas of photoemission peaks coming from the substrate and the film. Compared to the case of a semi-infinite homogeneous substrate covered by a thin film as treated in Eq. 5.1, the segregation of aluminium underneath the oxide slightly complicates the situation. Actually, this is not really the case for (110) surface for which the profile of segregation corresponds nearly to a semi-infinite substrate on the photoemission point of view. But the formalism will be developed here for the case of oxides on (100) and (111) surfaces that will be treated later on in this chapter. Using the notations of Sect. 5.1.2, if the photoemission signal I_L of the oxide layer L of thickness t is given by:

$$\frac{I_L}{T_L \sigma_L} \sim n_L \lambda_L^L \cos\Theta \left[1 - \exp\left(-t/\lambda_L^L \cos\Theta\right)\right], \tag{6.1}$$

the normalization to the substrate signal I_S has to take into account the profile of segregation and its damping in the oxide layer. If the segregation is described as a continuous profile of

Model	Parameter	(100)	(110)	(111)
Film	Thickness t (Å)	26 ± 3	75 ± 41	46 ± 12
	Layer atomic fraction x_L	0.51 ± 0.02	0.31 ± 0.01	0.34 ± 0.01
Profile	Length Λ (Å)	29 ± 5	> 130	62 ± 22
	Variation of atomic fraction Δx	0.39 ± 0.03	0.16 ± 0.01	0.20 ± 0.01
	Surface atomic fraction $x_s + \Delta x$	0.54 ± 0.03	0.31 ± 0.01	0.35 ± 0.01

Table 6.2: Results of the fit of the angular variation of Al 2p (metal)/Fe 3p area ratio for surfaces oxidised with the highest amount of oxygen (pass energy $E_p = 50$ eV with a) a segregated layer (Eq. 5.2, Fig. 5.3-c) or with b) a continuous profile of segregation (Eq. 5.4, Fig. 5.3-d). The error bars stem from 10 % uncertainties on the corrected ration $I_{Al\,2p}/I_{Fe\,3p}$.

composition $x(z)$ in $Fe_{1-x}Al_x$ (see Sect. 5.1.2.1) and when the Al signal for the substrate S is used:

$$\frac{I_S}{T_S \sigma_S} \sim \int_{-\infty}^{0} \frac{x(z)}{V[x(z)]} \exp\left\{\int_z^0 dz'/\lambda_S[x(z')]\right\} dz \times \exp\left(-t/\lambda_S^L \cos\Theta\right) \tag{6.2}$$

where λ_S^L is the electron mean free path of the substrate photoelectron in the oxide layer. The generalization of Eq. 6.2 to the case of Fe (term in $1 - x(z)$ for the concentration) and to a homogeneous segregated layer underneath the oxide is straightforward from Eqs. 5.1-5.2. Notice that the damping term in Eq. 6.2 is valid only for a continuous oxide layer. The treatment of fractional coverage is beyond the scope of our measurements and clearly does not correspond to the case of the highest (>500 L) O_2 exposure (see below).

For all the substrate orientations, the profile of segregation found from the ratio $I_{Al2p(metal)}/I_{Fe3p}$ (Tab. 6.2) was kept fixed and the oxide thickness was obtained by comparing the ratio $\frac{I_L}{T_L \sigma_L} \frac{T_S \sigma_S}{I_S}$ calculated from the above formula and experimental values for various combinations of core levels, namely $I_{Al2p(oxide)}/I_{Fe3p}$, $I_{Al2p(oxide)}/I_{Al2p(metal)}$, I_{O1s}/I_{Fe3p}, $I_{O1s}/I_{Al2p(metal)}$. The search was performed by dichotomy and the error bar on thickness obtained by assuming 10 % of standard deviation on the experimental value of corrected ratio. The used oxide-related electron mean free paths and density are given in Tab. 6.3. Compared to the alloy, a special care should be paid to the stoichiometry n_{sto} in the calculation of the atomic concentration of the oxide $n_L \propto n_{sto}\rho_L/M_L$ from its density ρ_L and its molar mass M_L. Assuming insulating behavior, the TPP-2M predictive formula [57–66] was used to calculate λ_L^L, λ_S^L for bulk alumina Al_2O_3 (corindon structure) and a fictitious material $Al_{10}O_{13}$ equivalent to the oxide thin film found on NiAl(110) [15, 19, 121] in terms of composition, molar mass and density.

Fig. 6.4 shows the calculated oxide thickness on the (110) surface for various models and all the combination of core levels. Assuming a substrate with a constant atomic fraction fixed at $x_S = 0.15$ that is to say $Fe_{0.85}Al_{0.15}$, a striking discrepancy up to a factor two appears between the thicknesses obtained by normalizing to Al 2p (metal) or to Fe 3p. It is obviously linked to the effect of aluminium segregation which is further confirmed by simulations performed with the profile found on the clean surface or on the oxidised one (nearly equivalent to $x_S = 0.31$).

Material		Al_2O_3		$Al_{10}O_{13}$	
Core level	E_B (eV)	λ Mg-Kα (Å)	λ Al-Kα (Å)	λ Mg-Kα (Å)	λ Al-Kα (Å)
Fe 3p	52.8	28.9	33.2	25.0	28.57
Al 2p	72.8 (3/2)	28.5	32.8	24.6	28.3
Al 2s	118 (3/2)	27.7	32.0	23.9	27.6
C 1s	285	24.5	28.9	21.2	25.0
O 1s	531	19.8	24.3	17.0	21.0
Fe 2p	707	16.2	20.9	13.9	18

Table 6.3: Inelastic mean free paths calculated from the TPP-2M formula for photoelectrons [66] of various core levels at Al-Kα and Mg-Kα excitation in: a) bulk alumina Al_2O_3 (molar mass $M_L = 101.95$ g·cm^{-3}, density $\rho_L = 3.99$, number of valence electrons $n_V = 24$), and in b) the oxide found on NiAl(110) namely $Al_{10}O_{13}$ (molar mass $M_L = 95.56$ g·cm^{-3}, density $\rho_L = 4$, number of valence electrons $n_V = 21.6$).

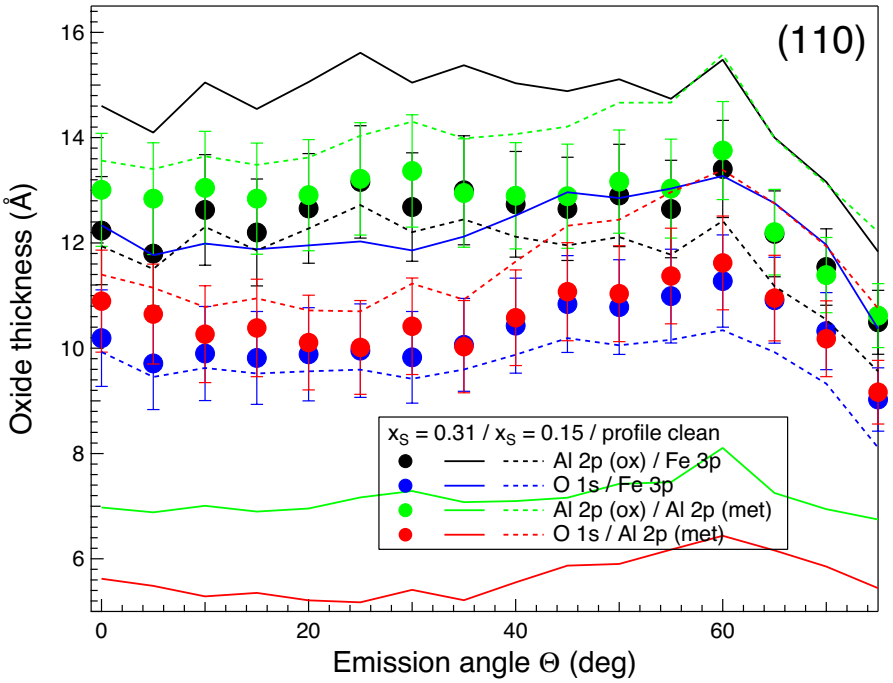

Figure 6.4: Thickness of the oxide layer (1123 K, 500 L of O_2) on the (110) surface calculated from ratios of core level areas as indicated in the figure. The atomic fraction of Al of the substrate is fixed at that of the bulk $x_S = 0.15$ (full lines) or to the segregation found under the oxide $x_s = 0.31$ (markers, Tab. 6.2) or to the profile of segregation found on the clean surface (dotted lines). The film composition is fixed at Al_2O_3 (see text).

In the last case, curves overlap two by two at given oxide core level showing that the problem comes from the photoemission modelling of the oxide itself and not of the profile of segregation. Various trials with different x_S values showed the robustness of this findings (not shown).

Since the film is found thinner from O 1s core levels than from Al 2p (oxide), an understoichiometry in oxygen compared to the nominal composition Al_2O_3 is expected; the ratio of thicknesses ($t \simeq 12.5$ Å black/green versus $t \simeq 10.5$ Å blue/red points in Fig. 6.4) points at a stoichiometry of $Al_2O_{2.5}$. This qualitative description is confirmed by the better agreement of all curves if calculations are made for an oxide composition close to that found on NiAl(110) *i.e.* $Al_{10}O_{13}$ =$Al_2O_{2.6}$ (lines in Fig. 6.5).

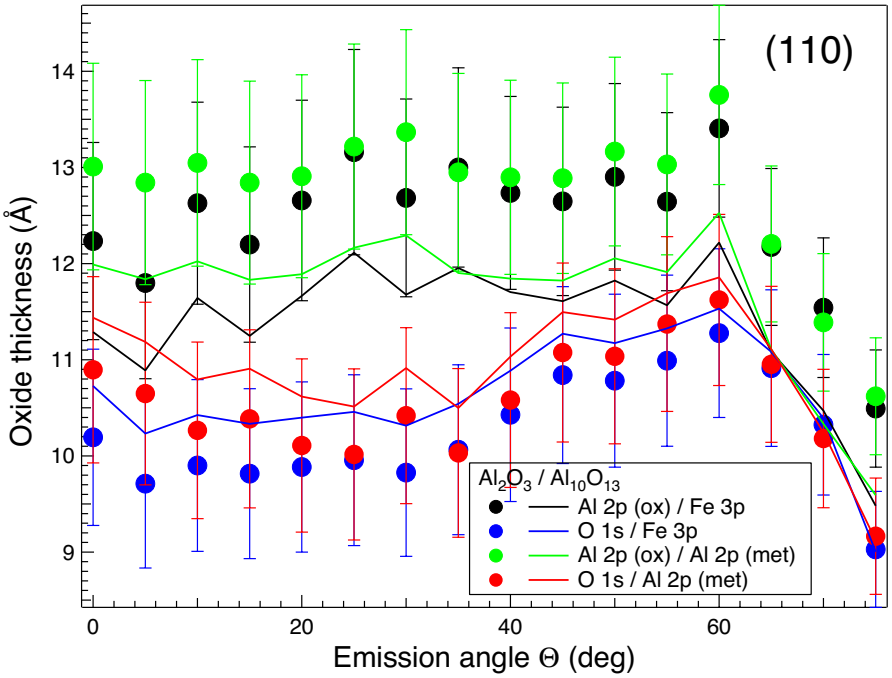

Figure 6.5: Calculated oxide thickness on the (110) surface for various film stoichiometry (Al_2O_3 (points) and $Al_{13}O_{10}$ (lines)) at fixed substrate composition of $x_S = 0.31$ corresponding to the found segregation underneath the oxide.

The absolute value of the film thickness (around 11.5 Å) should be taken with caution because of the uncertainties on mean free paths. Anyway, the consistency of the found thicknesses with emission angle rule out a partial coverage that would severely impacts the thickness trend. This finding validates *a posteriori* the treatment with the model of a continuous film and is in line with the STM observations.

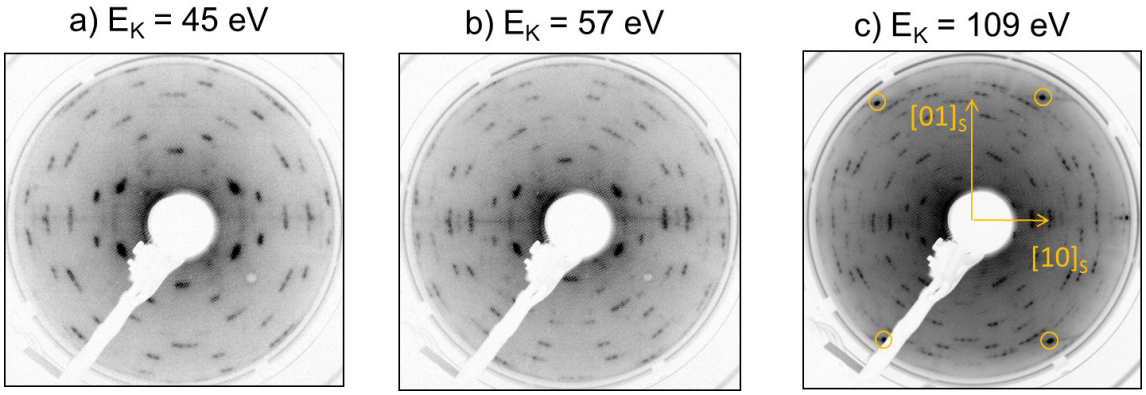

Figure 6.6: LEED patterns of the oxide film on $Fe_{0.85}Al_{0.15}$(110) (oxidation at 1123 K with 50 L of O_2): Beam energy a) 45 eV, b) 57 eV, c) 109 eV. The substrate surface $\{11\}_S$ reflections are circled in orange; the $\{10\}_S$ ones are missing due to the centring of the rectangular surface unit cell of random A_2 alloy. The reciprocal surface direction $[10]_S \parallel [1\bar{1}0]_B$ and $[01]_S \parallel [001]_B$ are shown. Faint traces of C stripes appear also on patterns along the $[10]_S$ direction.

6.2.2 The unit cell from diffraction

6.2.2.1 LEED pattern analysis

The LEED pattern of the oxide layer (Fig. 6.6) is quite complex and does not show the $\{11\}_S$ substrate reflections except at the lowest exposures (such as in Fig. 6.6-c, with 50 L of O_2) where an overlap with the pseudo hexagonal superstructure due to segregation is also visible (not shown, with 10 L of O_2). This agrees with a film progressively covering the whole surface. The diffraction pattern has two mirror planes crossing at the center of reciprocal space. This is compatible with a *pmm* symmetry which is a subgroup of the *cmm* rectangular centred surface unit cell. Owing to the number of spots in the reciprocal surface unit cell of the substrate (Fig. 6.6-c), the lattice parameters of the oxide should be much larger than those of the surface (a_S, b_S). Fortunately, a close inspection of the LEED pattern shows that it shares some similarities with that obtained on NiAl(110) and FeAl(110) (Figs. 3.31,3.17). On those substrates, the LEED could be indexed with a rotated quasi-rectangular unit cell with two domains due to the *cmm* symmetry of the substrate unit cell (see Fig. 6.7). As shown in Fig. 3.17, Graupner *et al.* proposed to index the reflections of the oxide on FeAl(110) within a matrix $\begin{bmatrix} 4 & 2.53 \\ -1 & 3.37 \end{bmatrix}$ [2] similar to that obtained on NiAl(110) [14]. Already, a direct comparison with our pattern (Fig. 6.8) shows a good qualitative overlap with the main central spots.

Based on this observation, the strategy to obtain the actual unit cell was to combine LEED and GIXD starting with the search of potential coincidences between a slightly distorted rectangular unit cell with parameters close to literature values (Tab. 6.4) and multiples of

[2] Although the agreement is not really demonstrated in the article (see Fig. 3.17-c) !

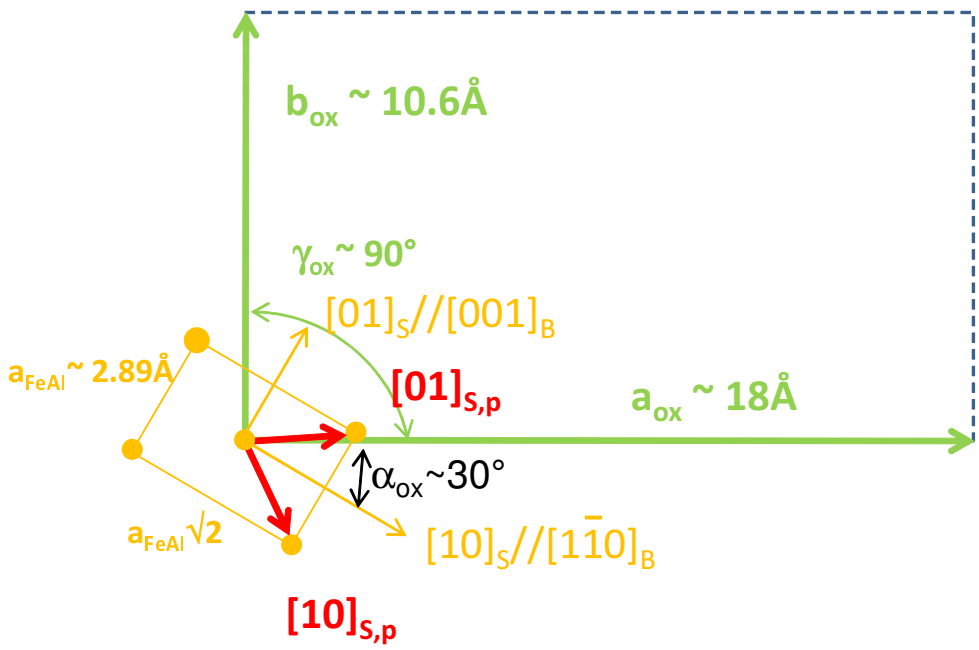

Figure 6.7: Scheme of the direct space unit cells used in the analysis of the LEED pattern of the oxide film on $Fe_{0.85}Al_{0.15}$(110). The oxide unit cell is quasi-rectangular with lattice parameters a_{ox}, b_{ox} and angle γ_{ox}; it is rotated by angle α_{ox} from the $[10]_S \parallel [1\bar{1}0]_B$ direction. The surface unit cell of the random alloy can be defined as rectangular centred (orange, vectors $\mathbf{a}_S = [10]_S, \mathbf{b}_S = [01]_S$) or as primitive (red, $\mathbf{a}_{S,P} = [10]_{S,P}, \mathbf{b}_{S,P} = [01]_{S,P}$). The angle between $[10]_{S,P}, [01]_{S,P}$ is 35.26° and $\mathbf{a}_S = \mathbf{a}_{S,P} + \mathbf{b}_{S,P}, \mathbf{b}_S = \mathbf{a}_{S,P} - \mathbf{b}_{S,P}$.

the surface unit cell of $Fe_{0.85}Al_{0.15}$(110). Compared to NiAl(110) and FeAl(110) (B_2/CsCl structure), the random alloy (A_2/bcc structure) offers in terms of symmetry an extra degree of matching due to the centring of the surface unit cell (Fig. 6.7). In other words, the matching was sought with multiples of the primitive surface unit cell (Fig. 6.7, vectors $[10]_{S,P}, [01]_{S,P}$) both along the oxide lattice parameter $\mathbf{a}_{ox}$ and $\mathbf{b}_{ox}$. Coincidence of $(1\times1), (1\times2), (2\times1), (3\times1), (1\times3)$ oxide unit cells were numerically found within reasonable limits:

$$a_{ox} = 18.5 \pm 13\ \%; b_{ox} = 10.5 \pm 13\ \%; \gamma_{ox} = 91 \pm 3°; \alpha_{ox} = 26 \pm 6°. \tag{6.3}$$

The corresponding LEED patterns were simulated with the *LEEDPat* software [239] from Hermann and Van Hove including the two symmetric domains. Tab. 6.5 and Fig. 6.9 show the summary of the coincidences that give the best qualitative agreement between experimental and simulated LEED patterns up to ×2. Good matching (not shown) was found also for numerous $(1\times3), (3\times1)$. Unfortunately, distortion on the outside of the LEED screen due to sample mispositioning and tilt did not allow to check among the found solutions the agreement on the $\{11\}_S$ substrate spots (Fig. 6.6-c) and therefore on the lattice parameters. This is all the more difficult than the substrate spots are often not visible. So, the unit cell was determined from GIXD measurements which is much more precise and sensitive to the substrate.

Work	Substrate	$a_B, (a_S \times b_S)$ (Å)	a_{ox} (Å)	b_{ox} (Å)	$\gamma_{ox}(deg)$	α_{ox} (deg)	M_S	Commensurate
SPA-LEED- [14]	NiAl(110)	2.887	17.89	10.55	88.67	24.1	$\begin{bmatrix} 4 & 2.53 \\ -1 & 3.37 \end{bmatrix}$	$[11]_S$
	B_2-CsCl	4.083×2.887						
GIXD- [121]	NiAl(110)	2.887	18.01	10.59	91.15	24.01	$\begin{bmatrix} 4.03 & 2.54 \\ -1.10 & 3.32 \end{bmatrix}$	$[11]_S$
	B_2-CsCl	4.083×2.887						
DFT- [15]	NiAl(110)	2.895	17.9	10.93	91.84	-	-	$[11]_S$
	B_2-CsCl	4.094×2.895						
GIXD- [19]	Al/Ni(111)	3.524	18.23	10.53	90	-	-	sixton rectangle
	A_1-fcc	2.491×2.491						
LEED- [16]	FeAl(110)	2.906	18.01	10.62	88.66	24.1	$\begin{bmatrix} 4 & 2.53 \\ -1 & 3.37 \end{bmatrix}$	-
	B_2-CsCl	4.110×2.9064						
GIXD-This work	$Fe_{0.85}Al_{0.15}$(110)	2.888	18.8	10.68	91.2	27.5	$\begin{bmatrix} 4.08 & 3.01 \\ -1.25 & 3.24 \end{bmatrix}$	(1×2)
	A_2-bcc	4.091×2.888	± 0.2	± 0.08	± 0.8	± 0.4		

Table 6.4: Aluminium oxide unit cell parameters at the surface of metallic substrate as determined in the literature.

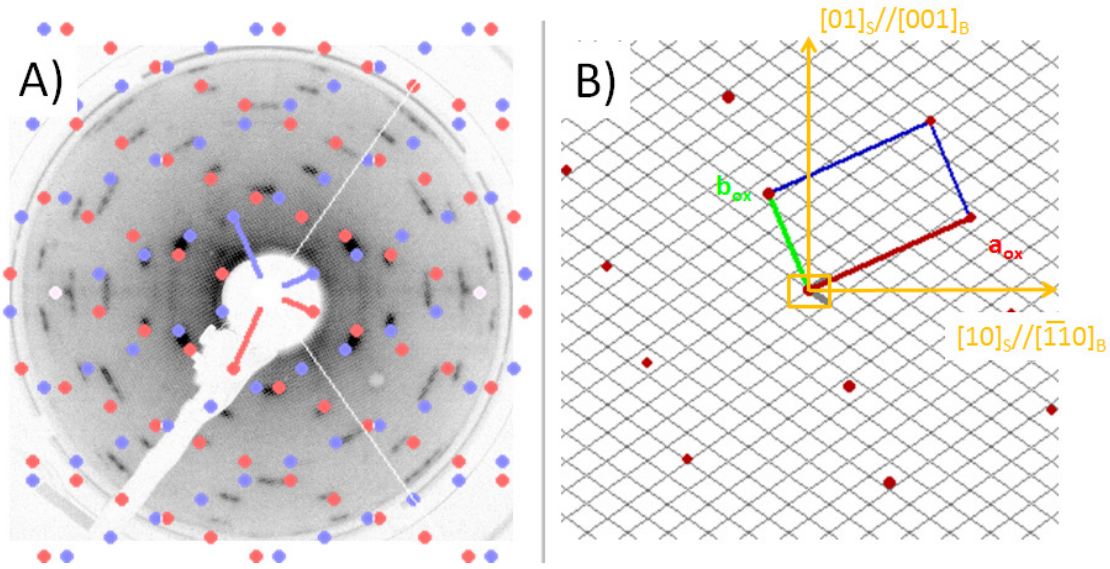

Figure 6.8: a) Comparison between experimental LEED pattern of the oxide on $Fe_{0.85}Al_{0.15}$(110) and the simulated one with Graupner's rotation matrix $\begin{bmatrix} 4 & 2.53 \\ -1 & 3.37 \end{bmatrix}$ [16]. b) Corresponding real space. The grey grid corresponds to the primitive unit cell; the centred rectangular unit cell is in orange.

6.2.2.2 GIXD analysis

Fig. 5.11 compares in-plane reciprocal scans along the main axis ($(h_S, 0, 0.075)$ in Fig. 5.11-a; $(0, k_S, 0.075)$ in Fig. 5.11-b; $(h_S, h_S, 0.075)$ in Fig. 5.11-c) before and after high temperature oxidation. If, accordingly to STM, XPS and LEED, the chosen exposure of 500 L of O_2 give rise to an oxide layer covering the whole surface, radial scans before and after oxidation overlaps along the $(0, k_S, 0.075)$ direction while the superstructure peaks along $(h_S, 0, 0.075)$ at $(1.56 - 3.56 - 5.56, 0, 0.075)$ are lifted by oxidation. Therefore, oxidation does not only change the profile of segregation underneath the oxide film as demonstrated by photoemission (see Sect. 6.3.1.2) but also impacts the nature of the superstructure underneath by releasing the "incommensurate" direction. Of course, new peaks appear (blue lines in Fig. 5.11) that are characteristic of the oxide layer itself.

To isolate them, a limited portion of in-plane reciprocal space at $l_S = 0.075$ of both the clean surface (Fig. 6.10) and of the oxide layer (Fig. 6.11) has been mapped in grazing incidence diffraction through angular ω-scans. By scrutinizing Fig. 6.10-6.11, (i) obvious powder-like spurious spots due to crystal imperfection and (ii) reflections belonging to reconstructed clean surface could be excluded from the oxide reciprocal map (grey open squares in Fig. 6.10-6.11). A set of potential oxide reflections (green circles and black squares) could be identified among which three aligned intense spots (but non-colinear with the substrate directions) are undoubtedly in-plane Bragg reflection of the oxide (double circles in Fig. 6.11; reflection 1,2,3 in Tab. 6.6). From these three, the most likely oxide unit cell parameters

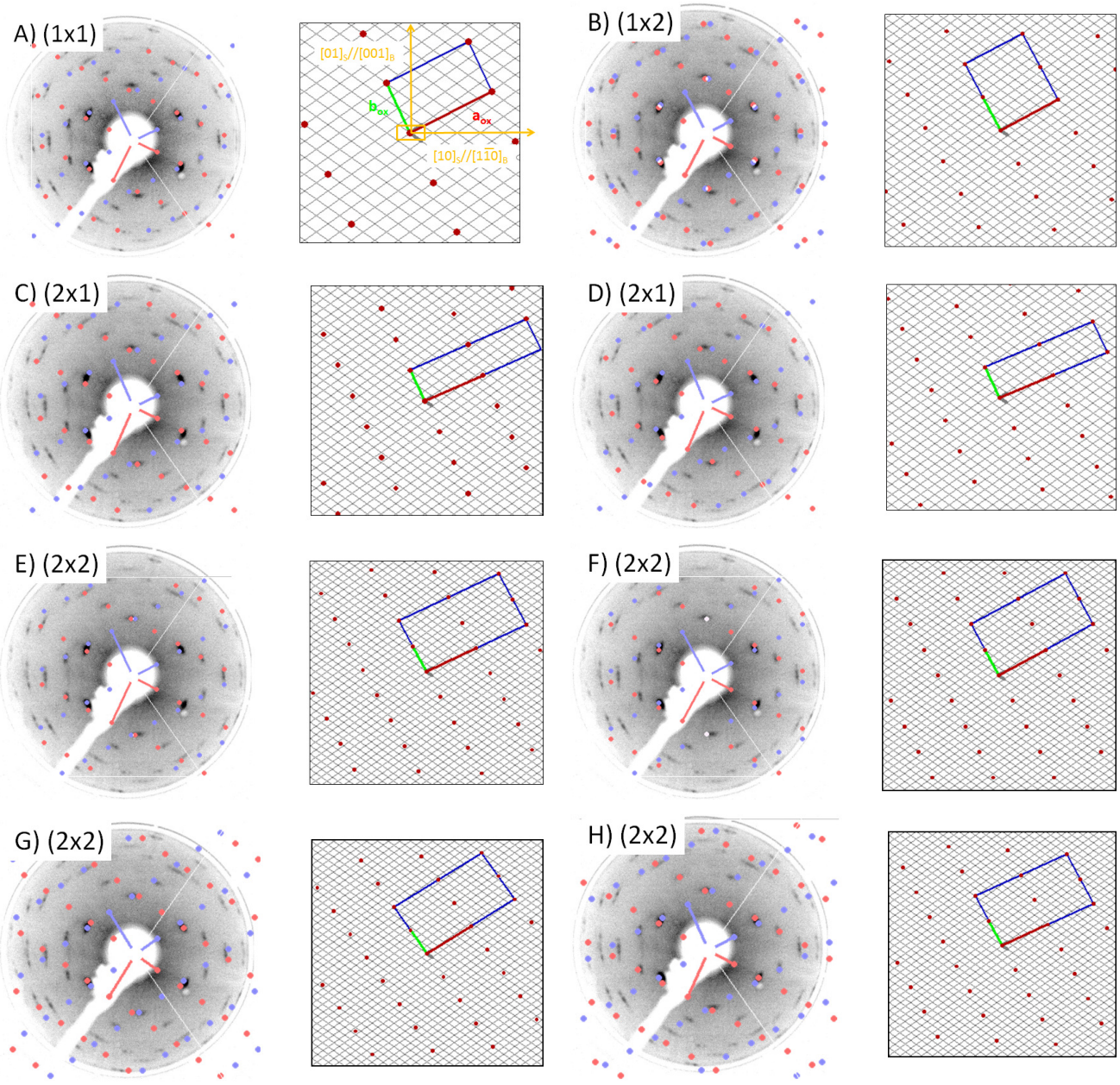

Figure 6.9: Comparison between experimental and simulated LEED patterns (left) for the superstructures of Tab. 6.5. Blue and red points correspond to the two domains. Red and green vectors correspond to $\mathbf{a}_{ox}$ and $\mathbf{b}_{ox}$. The right pictures show the direct space overlap between the grey grid which corresponds to the primitive unit cell and the $(n \times m)$ oxide supercell (red points). The substrate rectangular centred unit cell is shown in orange in Fig. a.

Superstructure	a_{ox} (Å)	b_{ox} (Å)	γ_{ox} (Å)	α_{ox} (deg)	Coincidence Superlattice Matrix $M_P = A_P^{-1}B_P$
A-(1×1)	16.03	9.59	88.44	26.80	$\begin{bmatrix} 1.0 & 6.0 \\ -4.0 & 2.0 \end{bmatrix} = \begin{bmatrix} 1 & 0 \\ 0 & 1 \end{bmatrix}^{-1} \begin{bmatrix} 1 & 6 \\ -4 & 2 \end{bmatrix}$
B-(1×2)	18.51	10.69	90.6	27.94	$\begin{bmatrix} 1.0 & 7.0 \\ -4.5 & 2.0 \end{bmatrix} = \begin{bmatrix} 1 & 0 \\ 0 & 2 \end{bmatrix}^{-1} \begin{bmatrix} 1 & 7 \\ -9 & 4 \end{bmatrix}$
C-(2×1)	17.88	9.59	91.39	23.85	$\begin{bmatrix} 1.5 & 6.5 \\ -4.0 & 2.0 \end{bmatrix} = \begin{bmatrix} 2 & 0 \\ 0 & 1 \end{bmatrix}^{-1} \begin{bmatrix} 3 & 13 \\ -4 & 2 \end{bmatrix}$
D-(2×1)	16.65	9.59	92.25	22.97	$\begin{bmatrix} 1.5 & 6.0 \\ -4.0 & 2.0 \end{bmatrix} = \begin{bmatrix} 2 & 0 \\ 0 & 1 \end{bmatrix}^{-1} \begin{bmatrix} 3 & 12 \\ -4 & 2 \end{bmatrix}$
E-(2×2)	20.34	10.70	93.31	25.24	$\begin{bmatrix} 1.5 & 7.5 \\ -4.5 & 2.0 \end{bmatrix} = \begin{bmatrix} 2 & 0 \\ 0 & 2 \end{bmatrix}^{-1} \begin{bmatrix} 3 & 15 \\ -9 & 4 \end{bmatrix}$
F-(2×2)	19.75	10.69	90.14	28.38	$\begin{bmatrix} 1.0 & 7.5 \\ -4.5 & 2.0 \end{bmatrix} = \begin{bmatrix} 2 & 0 \\ 0 & 2 \end{bmatrix}^{-1} \begin{bmatrix} 2 & 15 \\ -9 & 4 \end{bmatrix}$
G-(2×2)	19.22	10.62	93.51	31.76	$\begin{bmatrix} 0.5 & 7.5 \\ -4.5 & 1.5 \end{bmatrix} = \begin{bmatrix} 2 & 0 \\ 0 & 2 \end{bmatrix}^{-1} \begin{bmatrix} 1 & 15 \\ -9 & 4 \end{bmatrix}$
H-(2×2)	19.11	10.70	93.96	24.59	$\begin{bmatrix} 1.5 & 7.0 \\ -4.5 & 2.0 \end{bmatrix} = \begin{bmatrix} 2 & 0 \\ 0 & 2 \end{bmatrix}^{-1} \begin{bmatrix} 3 & 14 \\ -9 & 4 \end{bmatrix}$

Table 6.5: Best $(1\times 1), (1\times 2), (2\times 1), (2\times 2)$ oxide unit cells in coincidence with the primitive substrate unit cell that qualitatively fit the experimental LEED patterns. Parameters of the quasi-rectangular oxide unit cell $(a_{ox}, b_{ox}, \gamma_{ox}, \alpha_{ox})$ are defined in Fig. 6.7 with $a_S = 4.089$ Å and $b_S = 2.891$ Å. The rotation matrix M_P between the oxide and the primitive unit cell is decomposed into a product of matrices $A_P^{-1}B_P$ which characterise the common coincidence supercell in the basis of the overlayer (A_P) and of the substrate (B_P). The labelling of the proposed superstructures correspond to the A_P matrix.

$(a_{ox}, b_{ox}, \gamma_{ox}, \alpha_{ox})$ and reflection indexing $[(h^i_{ox}, k^i_{ox}), i = 1\ldots 3]$ were sought as follows.

For a given set $(a_{ox}, b_{ox}, \gamma_{ox}, \alpha_{ox})$, the oxide superlattice matrix in the rectangular surface unit cell (a_S, b_S) is given by (see Fig. 6.7):

$$M_S = \begin{bmatrix} m_{11} & m_{12} \\ m_{21} & m_{22} \end{bmatrix} = \begin{bmatrix} a_{ox}\cos(\alpha_{ox})/a_S & a_{ox}\sin(\alpha_{ox})/b_S \\ b_{ox}\cos(\alpha_{ox}+\gamma_{ox})/a_S & b_{ox}\sin(\alpha_{ox}+\gamma_{ox})/b_S \end{bmatrix}. \tag{6.4}$$

A straightforward algebra shows that a (h_{ox}, k_{ox}) reflection in the oxide reciprocal unit cell corresponds to (h_S, k_S) indexes in the reciprocal unit cell of the substrate through:

$$\begin{bmatrix} h_S \\ k_S \end{bmatrix} = \frac{a_S b_S}{a_{ox} b_{ox}\sin\gamma_{ox}} \begin{bmatrix} m_{22} & -m_{12} \\ -m_{21} & m_{11} \end{bmatrix} \begin{bmatrix} h_{ox} \\ k_{ox} \end{bmatrix}, \tag{6.5}$$

where the prefactor comes from the ratio of the surfaces of the unit cells. Therefore, for a given set of measured reflections $[(h^i_S, k^i_S), i = 1\ldots N]$ defined in the rectangular centred substrate unit cell and indexed as $[(h^i_{ox}, k^i_{ox}), i = 1\ldots N]$ in the oxide cell, the best $(a_{ox}, b_{ox}, \gamma_{ox}, \alpha_{ox})$ oxide unit cell can be found by minimizing:

$$\chi^2 = \frac{1}{2N}\sum_{i=1}^{N}\left\{\left[\frac{h_S(h^i_{ox}, k^i_{ox}) - h^i_S}{\Delta h_S}\right]^2 + \left[\frac{k_S(h^i_{ox}, k^i_{ox}) - k^i_S}{\Delta k_S}\right]^2\right\} \tag{6.6}$$

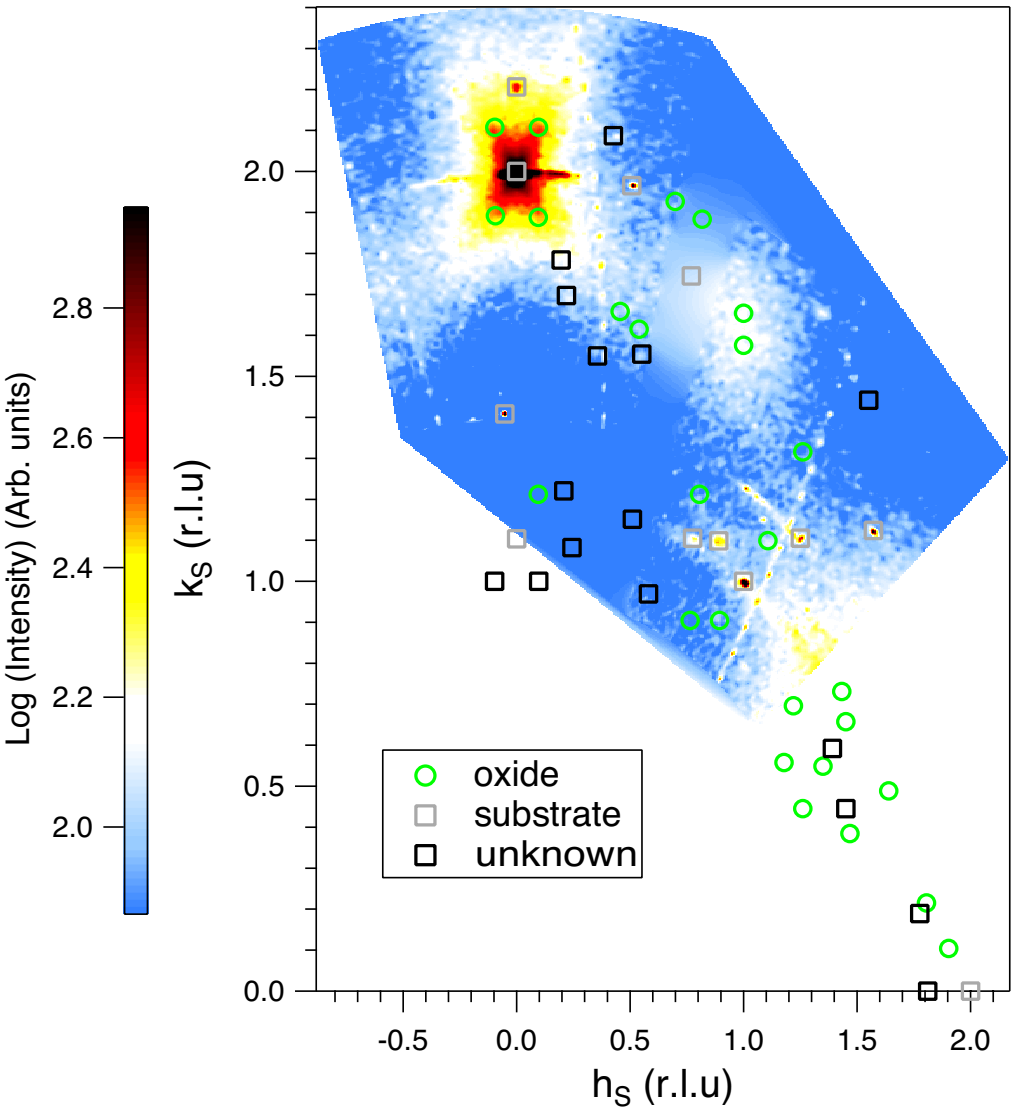

Figure 6.10: In-plane map ($l_S = 0.075$) of the reciprocal space of the clean $Fe_{0.85}Al_{0.15}$(110) surface. Only a small fraction of reciprocal space has been scanned around $(20)_S$ and $(11)_S$ surface reflections. The continuous blue colour region is just an artefact of the data interpolation and does not correspond to actual measurements. Main peaks have been circled (see text).

where $h_S(h^i_{ox}, k^i_{ox}), k_S(h^i_{ox}, k^i_{ox})$ are given by Eqs. 6.4-6.5 and $\Delta h_S, \Delta k_S = 0.02$ stand for typical error bars in the determination of the reflection position of our maps.

The search of the unit cell relies on a proper indexing $[(h^i_{ox}, k^i_{ox}), i = 1 \dots N]$ of the actual reflections. In this respect, the work performed with coincidence cells on LEED patterns is helpful but within small distortions of the unit cell, an uncertainty about the belonging of the observed reflections to a given domain remains.

To solve this, in the first step, a brute force search of minimal χ^2 for the three most obvious reflections 1-3 of Tab. 6.6 was performed (i) at fixed $a_{ox} = 18.5$ Å, $b_{ox} = 10.5$ Å, $\gamma_{ox} = 91°$ close to value of the literature and for $\alpha_{ox} = 26 \pm 6°$ down to 0.5° and (ii) for indexes of $-12 \leq h^i_{ox}, k^i_{ox} \leq 12, i = 1 \dots 3$ being blind on the belonging of the reflection to a given domain. To do so, all the combinations $[(h^i_S, \pm k^i_S), i = 1 \dots 3]$ related by the domain symmetry

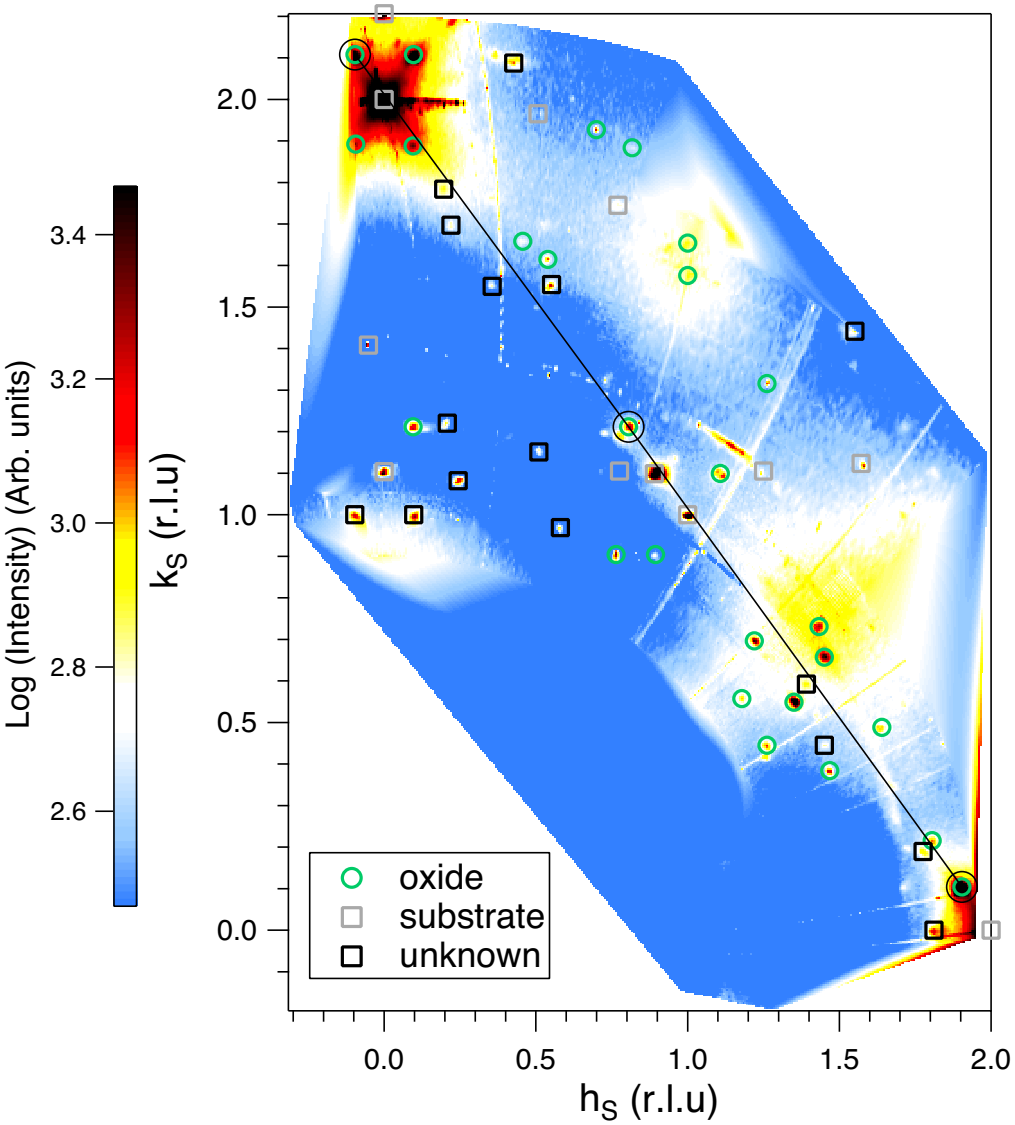

Figure 6.11: The same as Fig. 6.10 but for the oxide on $Fe_{0.85}Al_{0.15}$(110). The double circled spots have been used for unit cell indexing; they are perfectly aligned (see text).

have been systematically tested. It turned out that a satisfactory indexing ($\chi^2 = 1.9$ with (h^i_{ox}, k^i_{ox}) values of Tab. 6.6) could be obtained for these three reflections within the same domain. This finding is not astonishing since it is unlikely that the three spots would be perfectly aligned without belonging to the same domain.

To confirm this, in the second step, the same brute force minimization of χ^2 was performed (i) within the boundaries of Eq. 6.3 for $(a_{ox}, b_{ox}, \gamma_{ox}, \alpha_{ox})$ down to 0.25 Å for the lattice parameters and 0.25° for the angles and (ii) for $(\Delta h_{ox} = \pm 4, \Delta k_{ox} = \pm 4)$ around the previous found values. The obtained $\chi^2 = 0.18$ confirmed the already found solution since the next ones are much worst in $\chi^2 = 1.13, 1.60$ and with a much poorer agreement in terms of LEED pattern (not shown).

In the third step, based on this unit cell, all the potential reflections of Fig. 6.11 have

Domain	h^i_{ox}	k^i_{ox}	$h^{i,exp}_S(h^{i,calc}_S)$	$k^{i,exp}_S(k^{i,calc}_S)$
1-A	6	7	-0.1 (-0.10)	2.11 (2.12)
2-A	8	-2	1.90 (1.88)	0.10 (0.11)
3-A	7	3	0.81 (0.80)	1.21 (1.24)
4-B	-6	-7	0.10 (0.10)	-2.11 (-2.12)
5-A	7	0	1.35 (1.33)	0.55 (0.52)
6-B	4	-4	1.45 (1.47)	-0.66 (-0.66)
7-B	-3	-4	0.10 (0.14)	-1.21 (-1.18)
8-B	5	-3	1.47 (1.49)	-0.38 (-0.35)
9-B	4	-3	1.26 (1.30)	-0.44 (-0.42)
10-A	6	2	0.76 (0.79)	0.90 (0.92)
11-B	1	-5	1.11 (1.08)	-1.10 (-1.13)
12-A	6	6	0.10 (0.08)	1.89 (1.88)
13-B	-6	-6	-0.10 (-0.08)	-1.90 (-1.88)
14-B	1	-6	1.26 (1.25)	-1.32 (-1.37)
15-B	1	-4	0.90 (0.90)	-0.90 (-0.89)
16-B	-3	-7	0.70 (0.67)	-1.93 (-1.90)
17-A	9	5	0.82 (0.83)	1.88 (1.86)

Table 6.6: Set of oxide film reflections indexed with the (1×2) oxide unit cell (see text). $h^{i,exp}_S(h^{i,calc}_S)$ correspond to experimental (and calculated) positions in the substrate surface unit cell which was set at $a_S = 4.091$ Å and $b_S = 2.888$ Å from (020) and (200) bulk Bragg reflections. A, B stand for the two domains.

been indexed one by one excluding on purpose those for which the intensity is too weak or the overlap between the two domains does not allow a clear assignment. On the remaining 17 reflections $[(h^i_{ox}, k^i_{ox}), i = 1 \dots 17]$ (Tab. 6.6), the oxide unit cell parameters have been searched by looking for the minimum of χ^2 down to 0.01 Å and 0.02° for parameters and angles. From the Hessian matrix of χ^2 $\mathcal{H}_{i,j} = \frac{1}{2}\frac{\partial^2\chi^2}{\partial x_i \partial x_j}$, error bars on each fitting parameter x_i could be determined as $\sqrt{\mathcal{H}^{-1}_{ii}}$ as well as the correlation matrix between $\frac{\mathcal{H}^{-1}_{i,j}}{\sqrt{\mathcal{H}^{-1}_{i,i}\mathcal{H}^{-1}_{i,j}}}$. The found solution ($\chi^2 = 1.2$; Tab. 6.4) was:

$$a_{ox} = 18.8 \pm 0.2 \ \mathring{A}; b_{ox} = 10.68 \pm 0.08 \mathring{A}; \gamma_{ox} = 91.2 \pm 0.8°; \alpha_{ox} = 27.5 \pm 0.4°, \tag{6.7}$$

with the following correlation matrix:

$$\begin{bmatrix} 1.00 & -0.12 & -0.02 & -0.45 \\ -0.12 & 1.00 & 0.30 & 0.26 \\ -0.02 & 0.30 & 1.00 & -0.40 \\ -0.45 & 0.26 & -0.40 & 1.00 \end{bmatrix}. \tag{6.8}$$

The agreement with the experimental LEED pattern (Fig. 6.12) within expected distortions further confirms the found solution. However, some LEED spots are not indexed and are assigned to double diffraction as in the case of NiAl(110) [14] (see Fig. 3.17).

The solution corresponds to a rotation matrix from the primitive unit cell M_S:

$$M_S = \begin{bmatrix} 1.07 & 7.09 \\ -4.50 & 1.99 \end{bmatrix} = \begin{bmatrix} 1 & 0 \\ 0 & 2 \end{bmatrix}^{-1} \begin{bmatrix} 1.07 & 7.09 \\ -9.00 & 3.98 \end{bmatrix} \simeq \begin{bmatrix} 1 & 0 \\ 0 & 2 \end{bmatrix}^{-1} \begin{bmatrix} 1 & 7 \\ -9 & 4 \end{bmatrix} \tag{6.9}$$

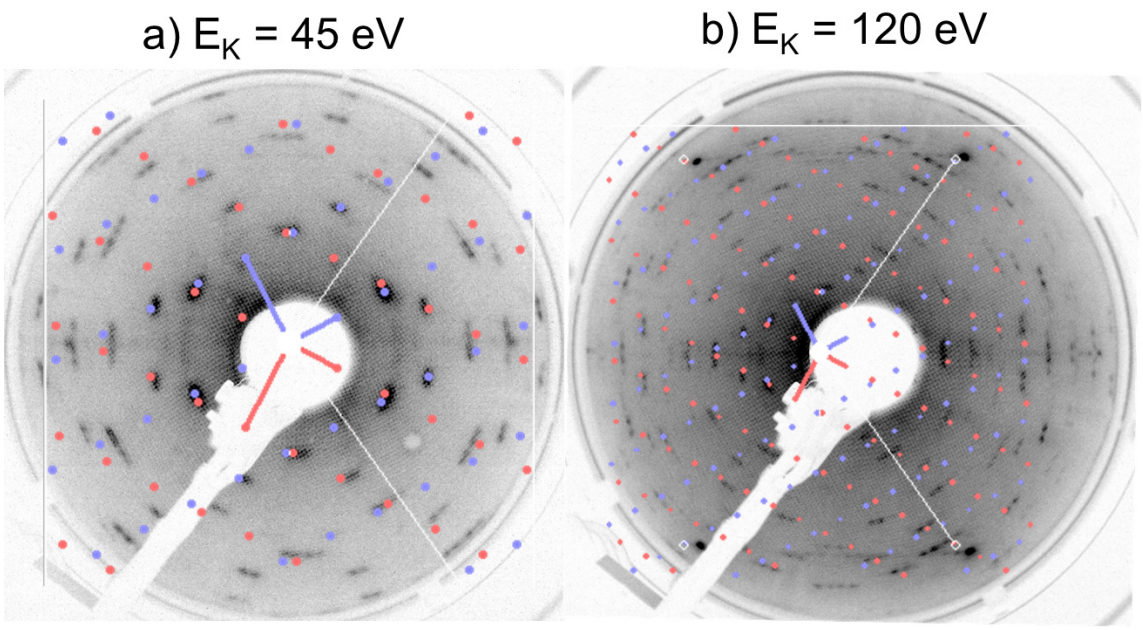

Figure 6.12: Overlap of the simulated LEED pattern obtained from the GIXD oxide unit cell. a) $E_K = 45$ eV, b) $E_K = 120$ eV. Discrepancies are due to distorsion and sample tilt.

which correspond to an oxide cell commensurate along $2\mathbf{b}_{ox}$ (within 0.2 %) and nearly commensurate along $\mathbf{a}_{ox}$ (within 2 %). Calculations shows that the perfect coincidence supercell (1×2) is within the error bars of Eq. 6.7. This matching was already found from LEED analysis (B-(1×2) structure, Tab. 6.5 and Fig. 6.9).

Finally, the rocking width $\Delta\omega(q)$ of a given oxide reflection (h_S, k_S) of reciprocal space vector modulus $q = \sqrt{(h_S a_S^*)^2 + (k_S b_S^*)^2}$ may originate from either a limited size of the oxide coherent domain $\Delta q_o = 2\pi/d_o$ leading to a constant $q\Delta\omega(q)$ broadening in reciprocal space or from in-plane mosaic spread M. Assuming uncorrelated effects, the peak broadening in reciprocal space should follows : $q^2\Delta\omega(q)^2 = \Delta q_o^2 + q^2M^2$. As show in Fig. 6.13, the analysis of all the identified experimental in-plane oxide reflection widths $\Delta\omega(q)$ yield a low mosaic spread and a coherent domain size of $d_o \simeq 20$ nm.

6.2.3 Oxide surface morphology from STM

Large scale STM images of $Fe_{0.85}Al_{0.15}$(110) oxidised at 1073 K with 90 L of O_2 are presented in Fig. 6.14. Besides domains occupied by carbon stripes (see Chap. 4), the whole surface seems to be fully covered by an oxide layer with two domains showing straight line patterns (Fig. 6.15) separated by irregular boundaries [14, 252]. As determined at several locations, the average angle between the lines and the $[1\bar{1}0]_B$ direction of the substrate is $30 \pm 3°$. The angle between lines of two domains is close to 60°. If present, the carbon stripes serves as accurate marker of the crystallographic directions since, as shown by room temperature oxygen adsorption, C-covered area are not oxidised and the C-stripes are aligned along the $[001]_B$

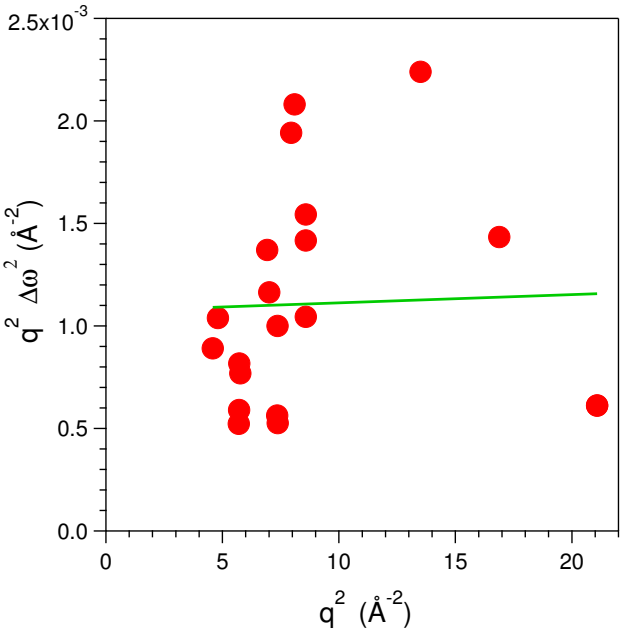

Figure 6.13: In-plane analysis of the oxide reflection widths $\Delta\omega(q)$. The linear regression (green line) of $q^2\Delta\omega(q)^2$ versus q^2 allows to unfold size and mosaic spread effects.

direction (see Sect. 4.1.2). Both angles agrees with the rotated rectangular unit cell found with diffraction within the drift effects due to room temperature STM measurements. Substrate and oxide step heights can be distinguished with a line profile through areas covered with C-stripes; the apparent height between oxide and the bottom between stripes is 2.7 ± 0.2 Å in close agreement with expected spacing between compact oxygen planes in alumina structures. On the other hand, step heigths of FeAl are close to 2 Å (see Fig. 6.14-c); double steps of iron aluminide have never been seen like on NiAl [14, 205].

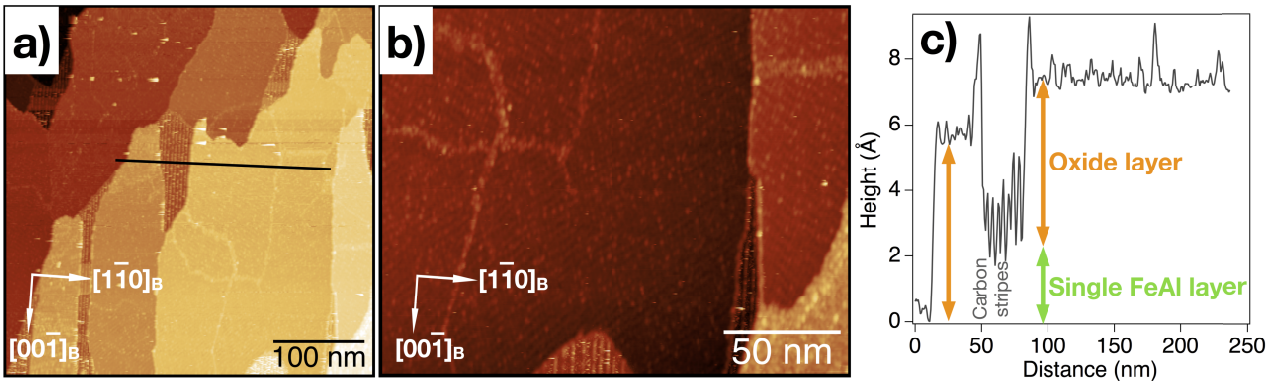

Figure 6.14: STM images of the $Fe_{0.85}Al_{0.15}$(110) surface after annealing at 1073 K in 2×10^{-7} mbar O_2 for 10 min (90 L): a) 400×400 nm^2, $U_b = 2.0$ V, $I_t = 0.4$ nA. b) 200×145 nm^2, $U_b = 2.0$ V, $I_t = 0.4$ nA. c) Line profile from image-a.

All theses findings are in line with the existence of two domains related by the mirror plane

symmetry of the substrate with a rotated unit cell as found by diffraction. Lower scale images displayed in Fig. 6.15 exhibit a periodic arrangement, but because of the very complicated intensity modulations, the determination of the constituting unit cell is difficult and requires image autocorrelation as already used for the oxide on NiAl(110) [204]. A clear distorted rectangular mesh appears on the autocorrelation images (Figs. 6.15-b,e). Unfortunately drift prevents an accurate determination of the angle between the basis vectors as well as the vertical periodicity; on the other hand, the distance found along the scan axis of 2.2 ± 0.2 nm is close to the $a_{ox} = 18.5$ Å (Sect. 6.2.2.2).

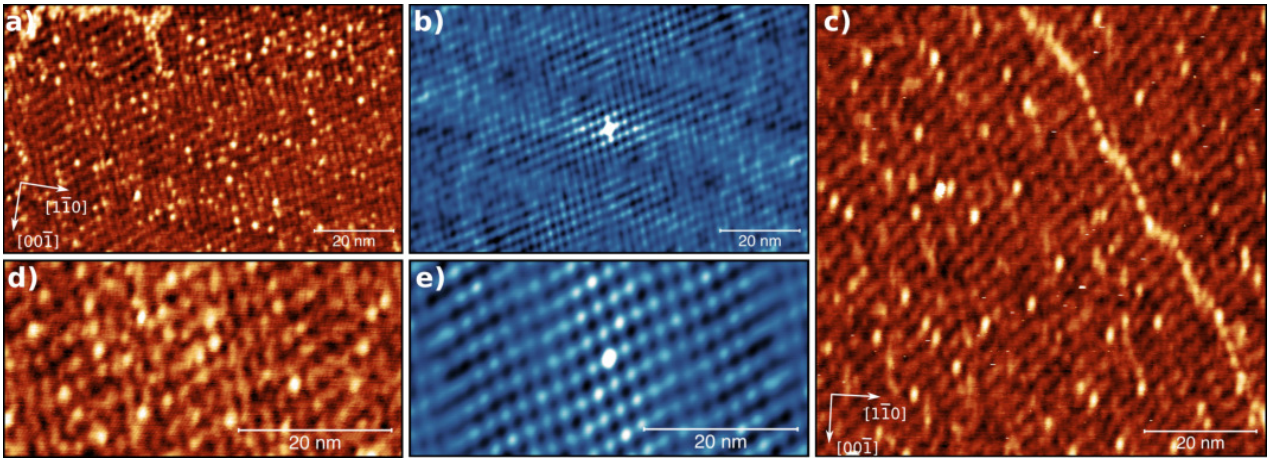

Figure 6.15: STM images of the $Fe_{0.85}Al_{0.15}$(110) surface after annealing at 1073 K for 10 min in 2×10^{-7} mbar O_2 for 10 min (90 L) for (a) and (b) and for 5 min (50 L) for (c), (d) and (e). a) 100×62 nm^2, $U_b = 2.0$ V, $I_t = 0.04$ nA and b) corresponding 2D autocorrelation image. c) 80×80 nm^2, $U_b = 2.0$ V, $I_t = 0.02$ nA. d) 52×25 nm^2, $U_b = 1.7$ V, $I_t = 0.01$ nA. e) Corresponding 2D autocorrelation image.

Anti-phase domain boundaries are typical defects of the oxide on NiAl(110); they result from the insertion of an oxygen deficient line of atoms that releases the strain energy in the layer through a shift of ~ 3 Å and appears in the form of straight lines along $\mathbf{b}_{ox}$ or zigzag lines along the diagonal of the oxide unit cell in STM [14, 153, 158, 207] or in Low Energy Electron Microscopy [202]. At the opposite to rotation domains related by substrate-layer symmetries, these translation related domains do not result from impinging islands with displaced lattice but from misfit dislocation [158, 202]; they spontaneously nucleate and grow within individual islands. They have a peculiar electronic structure in the band gap of the oxide [207] and act as favourable nucleation sites for metallic atoms or molecule adsorption [158]. While reflection domain boundaries are quite clear in STM images of the oxide on $Fe_{0.85}Al_{0.15}$(110) (Fig. 6.14) and run in arbitrary directions [207], anti-phase domain boundaries are much less apparent and dense than on NiAl(110). One is visible in Fig. 6.15-c. On NiAl(110), they appear as bright lines in topographic images above a bias of 1.5 V with a contrast that peaks at 2.5 V [207]. For those running along the short axis of the oxide unit cell and they are introduced every 8-10 nm to release strain due to the lattice mismatch along the $[1\bar{1}0]_B$ direction

(the film is incommensurate along the other $[001]_B$ direction which inhibits the development of lattice strain). The previous diffraction analysis (Sect. 6.2.2.2) concluded at a lack of lattice mismatch along $2\mathbf{b}_{ox}$ (0.2 %) and mismatch of 2 % along the $\mathbf{a}_{ox}$. A likely explanation for the lack of clear anti-phase domain boundary along this mismatched direction at the opposite of NiAl(110) is the extra-degree of structural (lattice parameter) freedom provided by the composition of the $Fe_{0.85}Al_{0.15}$ alloy in the subsurface region. A similar lack but associated with an imbalance between the two rotational domains was observed on the vicinal NiAl(110) surface [131] and assigned to the introduction of step edge and given oxide terrace size to release the oxide stress.

With respect to image 6.15-c, no difference show up after an overnight ageing (Fig. 6.15-d) demonstrating the lack of reactivity of the oxide surface at the opposite of the clean FeAl substrate. In the case of NiAl(110), the inertness was assigned to an oxygen termination of the oxide film. Finally, very similar topographies (not shown) were found after 50 L of O_2 exposure at room temperature followed by annealing at 1073 K.

6.3 Oxide on $Fe_{0.85}Al_{0.15}$(100)

6.3.1 Photoemission analysis

6.3.1.1 Angular analysis and lineshape fitting

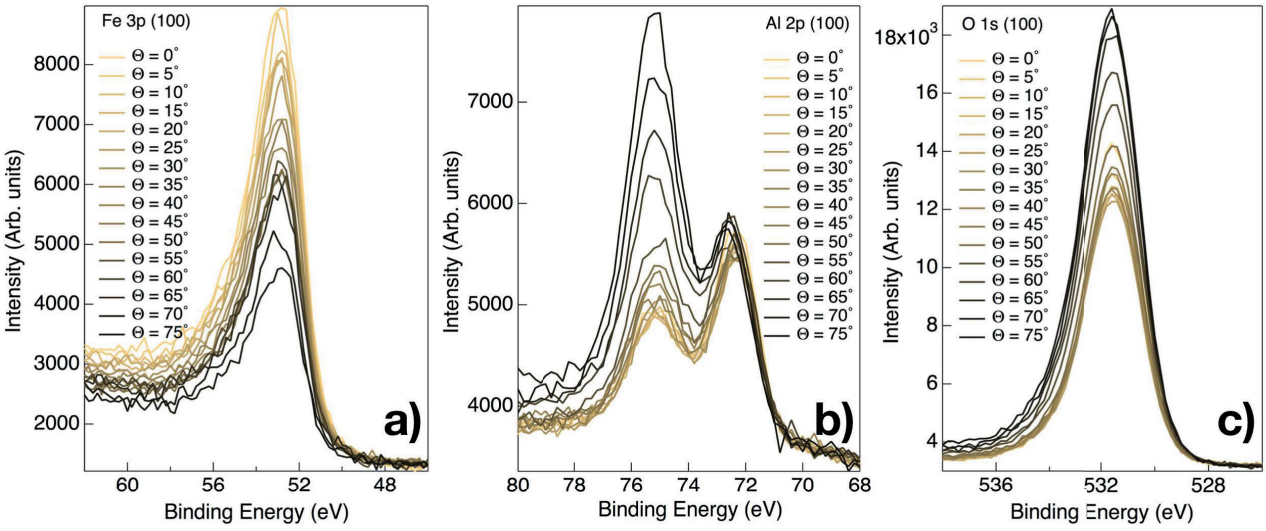

Figure 6.16: Evolution of the a) Fe 3p, b) Al 2p and c) O 1s core levels as a function of emission angle for a (100) oxidised surface (100 L of O_2, 973 K). Data have been normalised to the same background. Pass energy is $E_p = 50$ eV.

After oxidation (100 L of O_2, 973 K), an angular analysis of the three main core levels Fe 3p, Al 2p and O 1s similar to that performed on (110) surface was undertaken to study segregation (Fig. 6.16). As for (110), there is no trace of iron oxidation (see Fig. 6.31); the

uptake of oxygen is only accompanied by aluminium oxidation as seen by the appearance of a shoulder on the high binding energy side of the Al 2p peak.

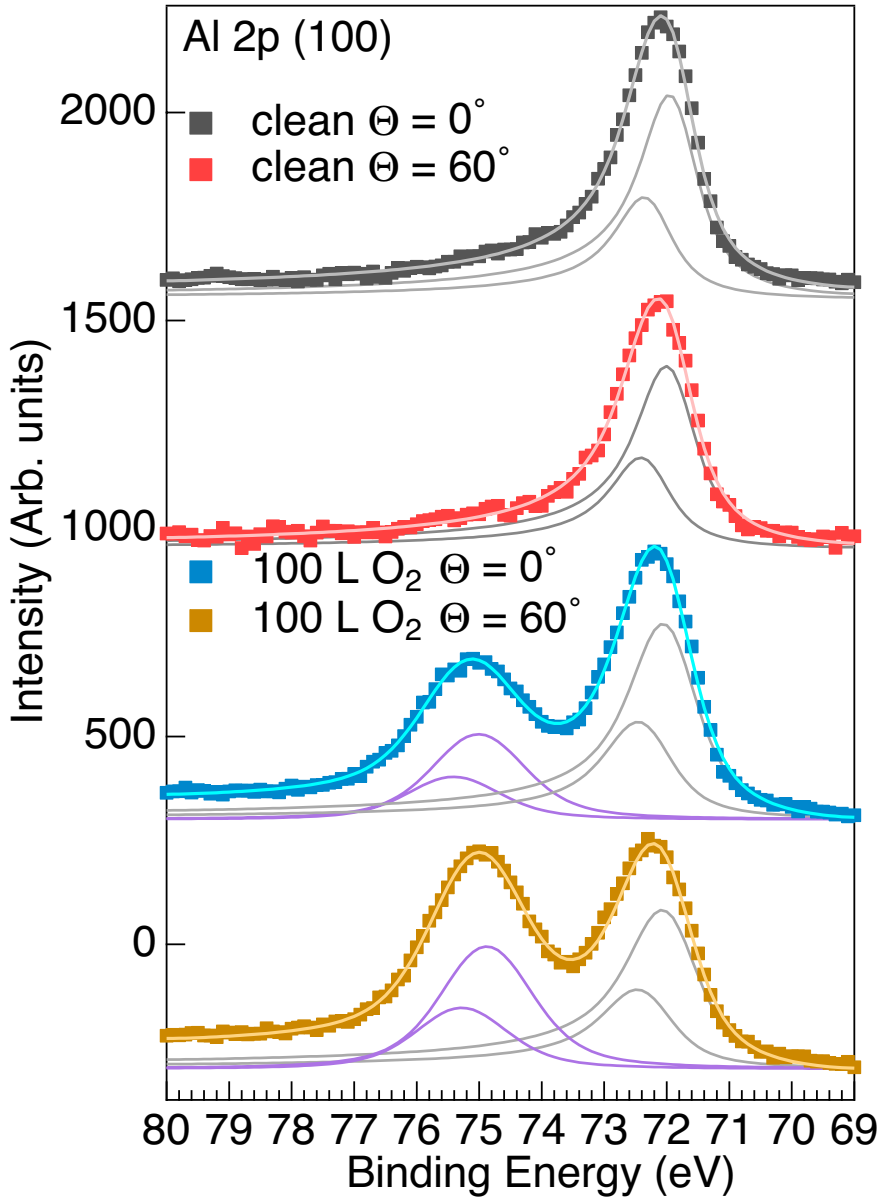

Figure 6.17: Line shape decomposition of the Al 2p core level for the (100) orientation. (Top panel) Clean surface annealed at 973 K (normal emission); (Bottom panels) Surface oxidised at the same temperature with 100 L of O_2. Two spin orbit split components are needed to fit accurately the data (points) for the oxide layer (see text). Fit parameters are given in Tab. 6.7. Spectra have been collected at a pass energy $E_p = 20$ eV providing the best resolution.

Fit strategy similar to that developed for (110) orientation (see Sect. 6.2.1.2) was applied to (100) surface. At the opposite to (110) face, it turned out that, besides the substrate contribution, only one component was needed to account for the experimental Al 2p profile both for normal and grazing emissions (Fig. 6.17) as in Ref. [133, 165, 212] for NiAl(100). On the other hand, two components were found on FeAl(100) [16] and on NiAl(100) [253] but without taking into account the spin-orbit splitting of Al 2p in the decomposition. Fit parameters are given in Tab. 6.7. Again, the existence of only one asymmetric Al 2p component on the clean surface testifies for the cleanliness of the sample.

	Type	Shape	Relative area	E_B (eV)	L-FWHM (eV)	G-FWHM coeff.	Asymmetry (eV)
Clean NE-$\Theta = 0°$	Bulk	DS	1	71.90	0.85	0.40	0.15
Clean GE-$\Theta = 60°$	Bulk	DS	1	71.95	0.85	0.45	0.15
Oxi NE-$\Theta = 0°$	Bulk	DS	0.63	72.00	0.85	0.65	0.14
	Surface	V	0.37	75.00	0.85	1.30	-
Oxi GE-$\Theta = 60°$	Bulk	DS	0.5	72.00	0.85	0.70	0.19
	Surface	V	0.5	75.00	0.85	1.25	-

Table 6.7: Fit parameters for Al $2p_{3/2}$ of $Fe_{0.85}Al_{0.15}$(100) surfaces. Clean (973 K) and oxidised (973 L, 100 L of O_2) surfaces are compared. Photoemission spectra are recorded at 0° and 60° emissions. Fit function types DS, V are short for Doniach-Sunijch, Voigt respectively. Error bars are of the order of the step size, *i.e.* 0.05 eV.

6.3.1.2 Segregation under the oxide from angular analysis

In a similar way to the (110) orientation, by using the previous decomposition of peaks, the aluminium segregation under the oxide was probed through the angular variation of the metallic components $I_{Al\,2p\,metal}/I_{Fe\,3p}$ (Fig. 6.18). At the opposite to the (110) orientation (Fig. 6.3), the strong increase of corrected ratio $I_{Al\,2p\,metal}/I_{Fe\,3p}$ at grazing emission parallels the findings on the clean surface (Fig. 6.18 open versus filled points). A quantitative analysis with the model of an homogeneous segregated layer under the oxide or with the case of a damped profile (see Sect. 6.2.1.3 and Sect. 5.1.2.1 for explanations) pointed at segregation parameters $(x_L, \Lambda, \Delta x)$ quite similar to those found on the clean surface (Tab. 6.2 versus 5.3). The composition at the interface with the oxide is still very close to $Fe_{0.5}Al_{0.5}$.

6.3.1.3 Oxide film thickness and stoichiometry

The strategy used to determine the oxide thickness from ratio of different photoemission core levels follows exactly that developed for the (110) orientation (see Sect. 6.2.1.4). But in contrast to the (110) orientation for which the profile of segregation was found to be flat but different from bulk composition, the thickness quantification on the (100) requires to account for the actual profile of segregation. Indeed without it, *i.e.* with fixed bulk composition ($x_S = 0.15$), an enormous discrepancy by a factor 3 appears between values obtained by normalizing to Fe 3p or Al 2p (metal). This difference is wiped out if segregation is accounted for (markers versus line in Fig. 6.19). Surprisingly, all determinations of thicknesses agree around a value around $t = 8.5$ Å if the stoichiometry of the films is taken as Al_2O_3. In other words, the small mismatch found in the case of (110) (Fig. 6.4) [3] and assigned to a composition $Al_{10}O_{13}$ is not found. Finally, the lack of variation of thickness with angle corroborate the modelling with a thin continuous film.

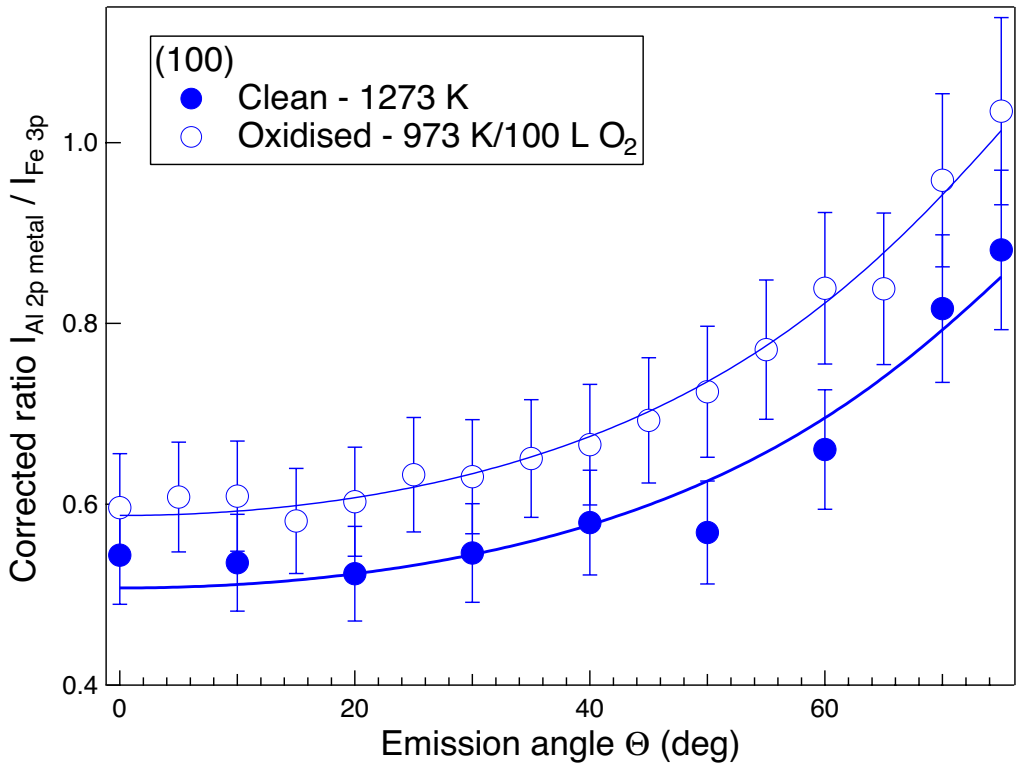

Figure 6.18: Comparison of angular variation of the corrected ratio $I_{Al\,2p\,metal}/I_{Fe\,3p}$ (pass energy $E_p = 50$ eV) for the metallic Al component of the as-prepared (100) surface (1273 K; filled circles) and after oxidation (973 K, 100 L of O_2; open circles). Data (points) have been fitted with a model of continuous profile of segregation (lines, Eq. 5.4) which values are given in Tab. 5.3 and 6.2. Similar fit quality is obtained with the segregated layer model (Eq. 5.2).

6.3.2 Oxide superstructure from LEED

A typical LEED pattern of the oxide formed at the (100) surface of $Fe_{0.85}Al_{0.15}$ is shown in Fig. 6.20. It corresponds to that observed on FeAl(100) [16] (see Fig. 3.33-b), on NiAl(100) [162, 164, 212] and on $Fe_{0.85}Al_{0.15}$(100) [93] with an intense streaking along the main $[10]_S \parallel [010]_B$ and $[01]_S \parallel [001]_B$ directions around main spots but also around half order ones. At a first sight, this matches with a two-domain (1×2) superstructure (see Fig. 3.33-b) that was interpreted on NiAl(100) as due to the formation of θ-alumina in Bain epitaxy [147, 162–168]. However, by reducing the beam energy, this streaking transforms into spot splitting, particularly visible around half integer. As already shown with much better resolution in the spot profile analysis of Ref. [164] on NiAl(100), this splitting matches with a (1×9) shape convolution (Fig. 6.21) corresponding to the formation of high aspect ratio oxide stripes regularly spaced by $9a_S \sim 5$ nm. This will be confirmed by STM later on.

It is worth noticing that, at the opposite to the oxide on (110), the substrate spots

[3]That will appear on (111) films also!

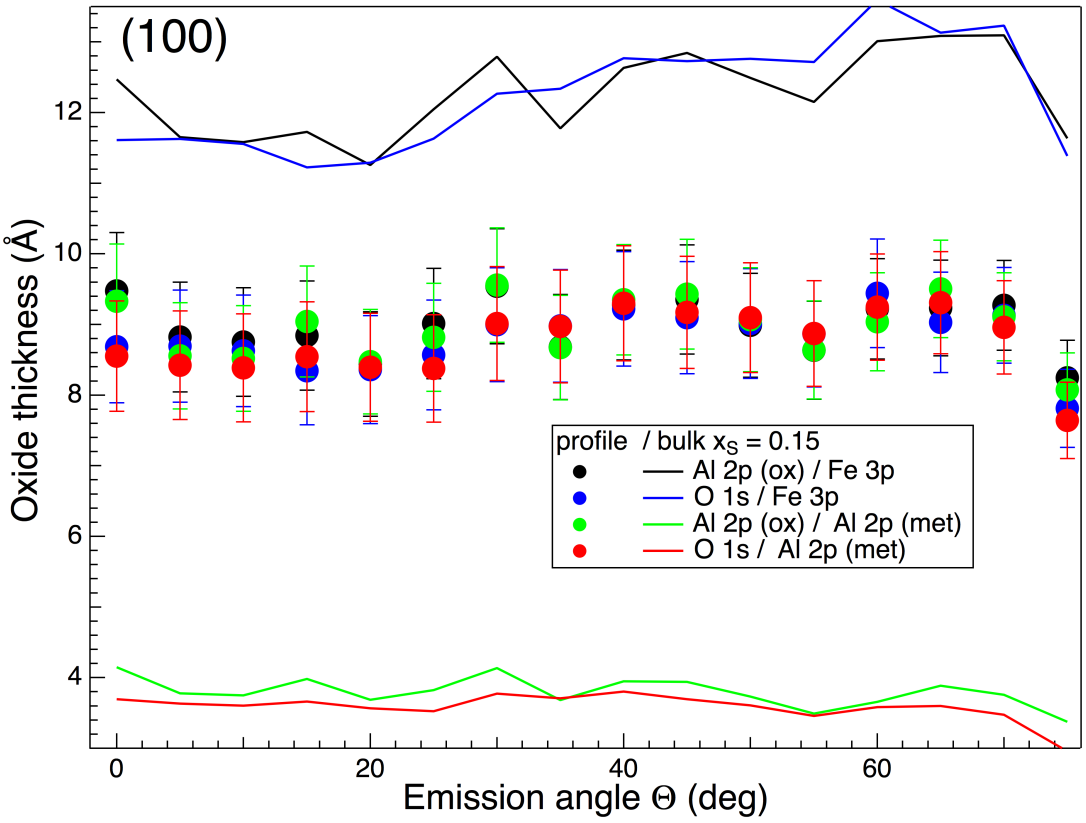

Figure 6.19: Thickness of the oxide layer (973 K, 100 L of O_2) on the (100) surface calculated from ratios of core levels as indicated in figure. Calculations assume a bulk like homogeneous substrate ($x_S = 0.15$, lines) or take into account the actual profile of segregation (markers). The layer stoichiometry is Al_2O_3.

(Fig. 6.20; orange circles) are visible even though in STM the film apparently covers the whole surface; this is in line with a thinner film than on (110) as shown by the photoemission analysis. Finally, although the temperature of synthesis is the same of the study of Graupner *et al.* [16] on FeAl(100), the oxide never adopts the c(6 × 6) superstructure.

6.3.3 Surface morphology from STM

As shown in the STM images of Figs. 6.22-a,b,c, the oxidation at high temperature gives rise to an oxide layer that covers the whole surface with small domains of which borders follow the square symmetry of the substrate. A statistical analysis of apparent height distribution shows the existence of terraces separated by a distance of 1.6 Å pointing at single step. This value is in between the distance between atomic planes along the $[001]_B$ direction in $Fe_{0.85}Al_{0.15}$ ($a_B/2 = 1.45$ Å) and the spacing between the closed-pack oxygen plane in the θ-Al_2O_3 structure proposed in the case of NiAl(100) ($d_{Oplane} = 1.91$ Å).

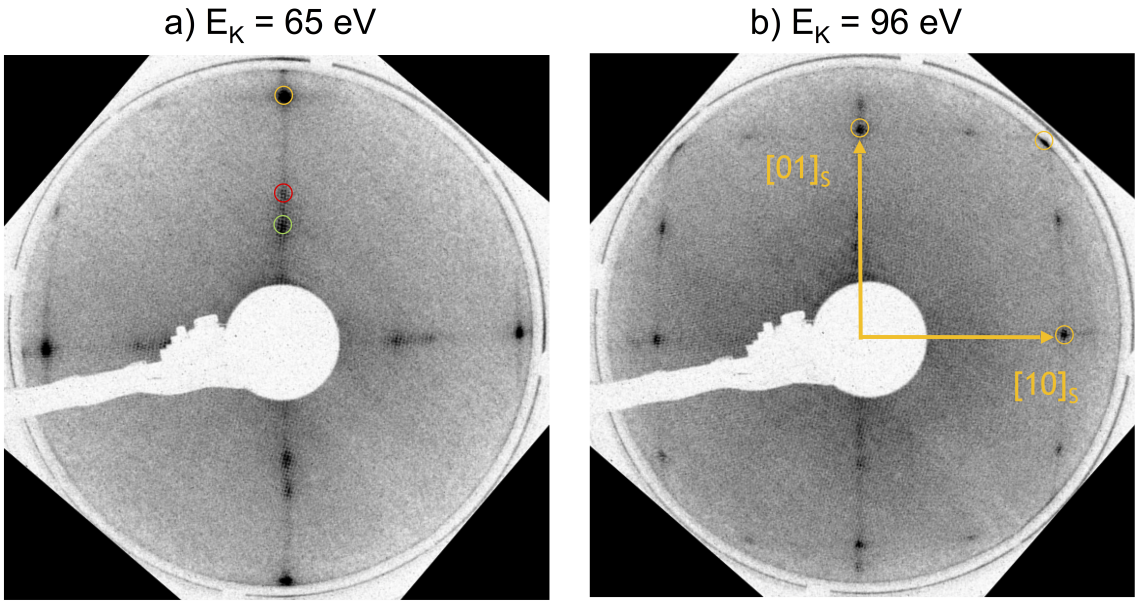

Figure 6.20: LEED patterns of the oxide film on $Fe_{0.85}Al_{0.15}$(100) (oxidation at 973 K with 100 L of O_2): Beam energy a) 65 eV, b) 96 eV. The substrate surface $\{10\}_S$ reflections are circled in orange.

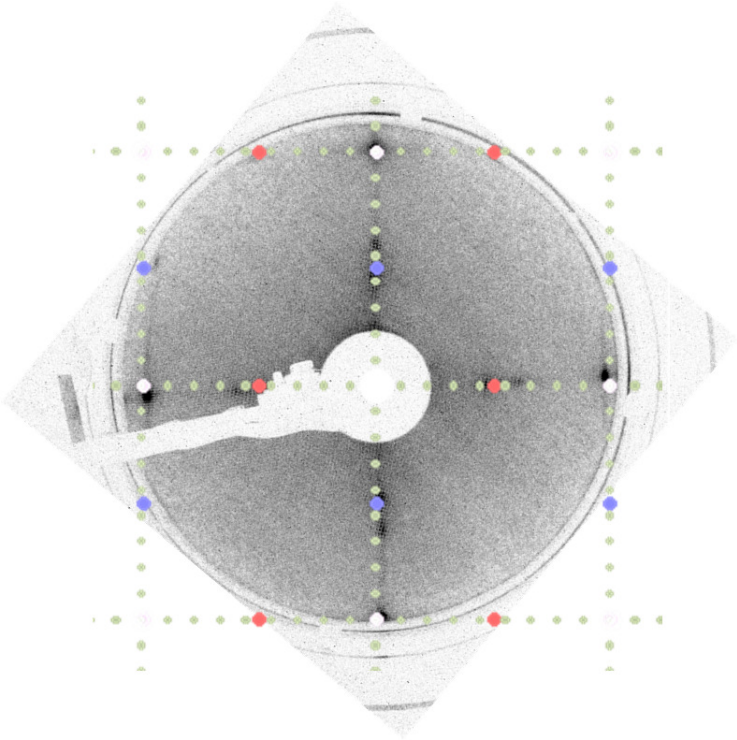

Figure 6.21: Overlap between (1×2) and (1×9) superstructures including the two domains with the experimental LEED pattern of Fig. 6.20-a.

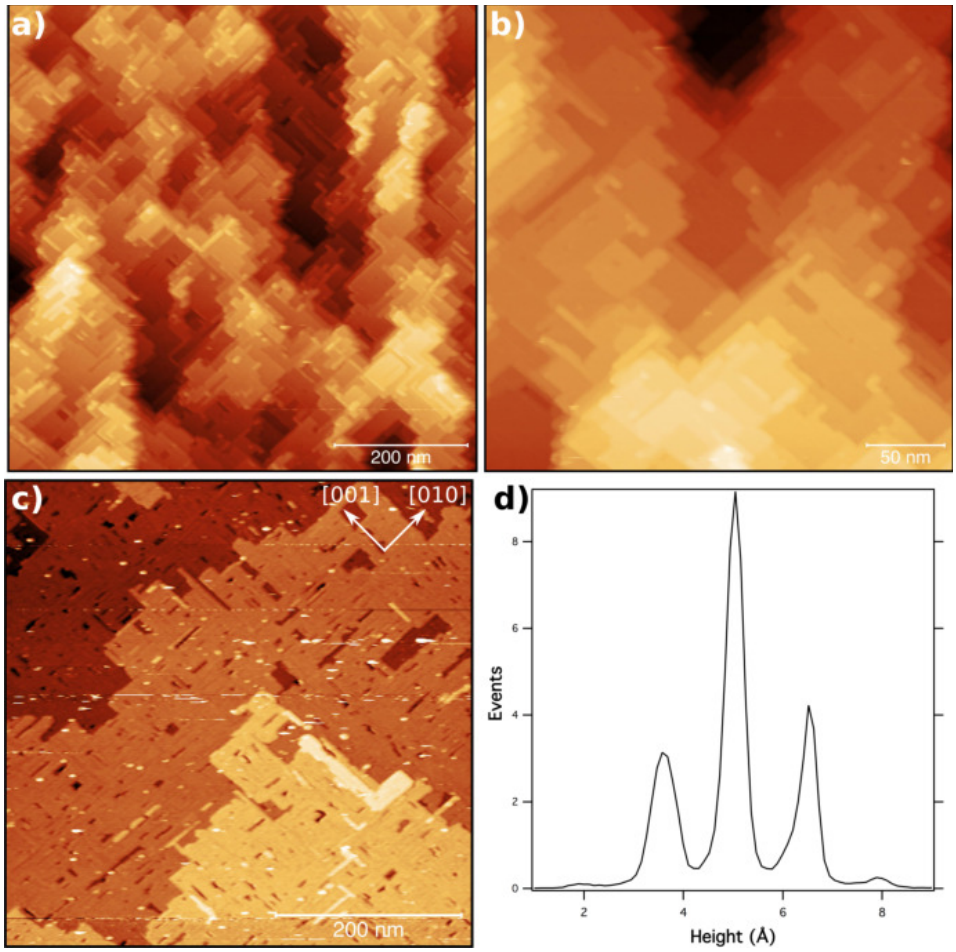

Figure 6.22: STM images of the $Fe_{0.85}Al_{0.15}$(100) surface after exposure to 10 L of O_2 at 973 K. a) 700×700 nm^2, $U_b = -1.1$ V, $I_t = 0.2$ nA, b) 300×300 nm^2, $U_b = -1.1$ V, $I_t = 0.2$ nA, c) after exposure to 100 L of O_2 at 973 K, 500×500 nm ^{2}, $U_b = -1.0$ V, $I_t = 0.3$ nA. d) Corresponding height histogram of image c).

At higher magnification (Fig. 6.23), the domains appear clearly as compact stripes with very high aspect ratio running along the $[010]_B$ and $[001]_B$ directions. Those stripes which are always limited in length by a orthogonal ones are regularly spaced by 6.9 ± 0.2 Å (Fig. 6.23-b,c) and packed in bunches separated by trenches with a periodicity of 5 ± 2 nm. The corrugation of the modulation due to stripes is 0.3 ± 0.1 Å. Numerous topographic defects are presented among which holes with an apparent depth of 1.6 ± 0.2 Å similar to the distance between terraces observed at large scale (Fig. 6.22-d). This distance is therefore more in line with a physical hole in the terrace of the oxide, since the substrate step height amounts to $a_B/2 = 1.45$ Å.

Quite similar topographies have been observed on NiAl(100) [164, 167] (see Sect. 3.4.3.2) or CoAl(100) [124, 125, 165, 166, 212] (see Sect. 3.4.3.5) with a stripe period of ~ 54 Å and a size/height of $\sim 26/11$ Å [164,167] for isolated ones grown at very low oxygen coverage. Stripes do not cross or coalesce as in our case. This morphology was assigned to the growth of a θ-

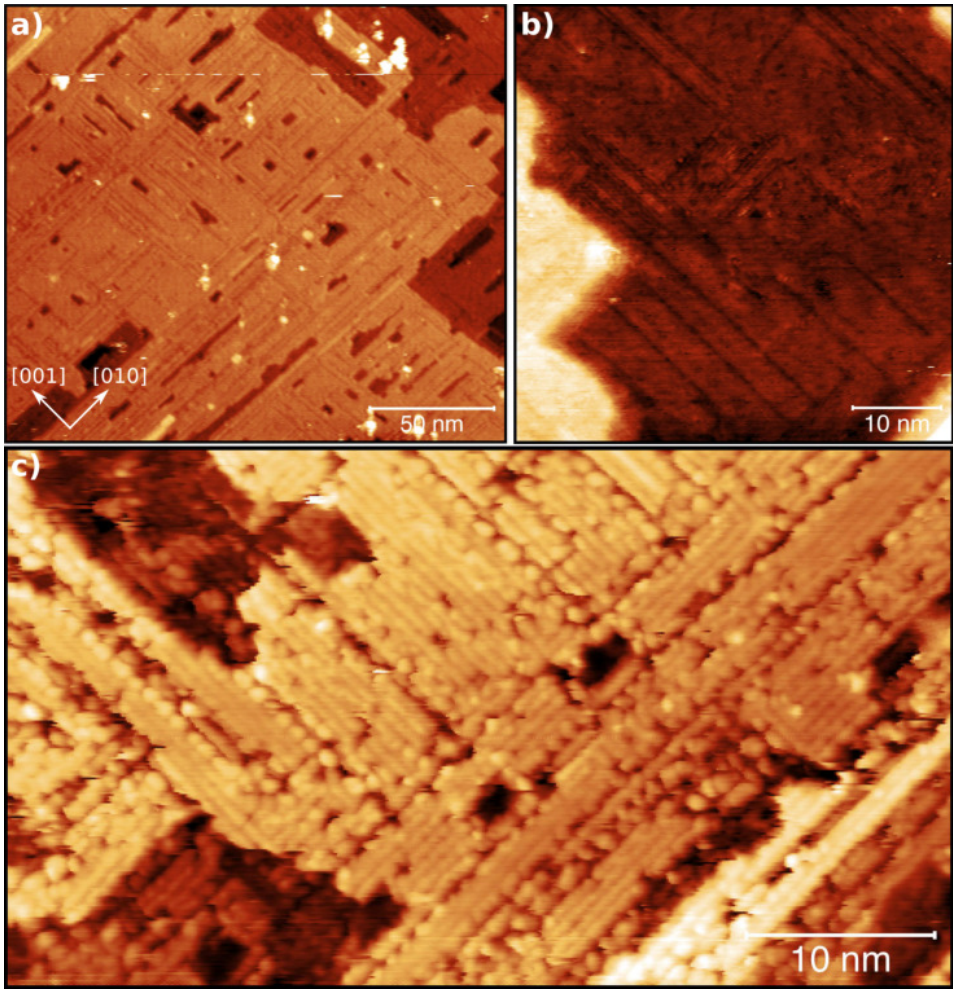

Figure 6.23: STM images of the $Fe_{0.85}Al_{0.15}$(100) surface after exposure to O_2 at 973 K. a) 100 L, 200 × 174 nm^2, $U_b = -1.0$ V, $I_t = 0.3$ nA, b) 10 L, 60 × 60 nm^2, $U_b = -1.2$ V, $I_t = 0.2$ nA, c) 100 L, 50 × 27 nm^2, $U_b = -0.8$ V, $I_t = 0.1$ nA.

Al_2O_3 layer [147,166] in Bain's epitaxy (see Sect. 3.4.3.2) $(001)[001]_{Fe_{0.85}Al_{0.15}} \parallel (001)[1\bar{1}0]_{\text{O-fcc}} \parallel (001)[010]_{\theta-Al_2O_3}$. This leads to a $(2 \times 1), (1 \times 2)$ superstructure with a lattice mismatch of -2.5 % along $a_{\theta-Al_2O_3}$ and 1 % along $b_{\theta-Al_2O_3}$ ($a_{Fe_{0.85}Al_{0.15}} = 2.8914$ Å, $a_{\theta-Al_2O_3} = 5.64$ Å, $b_{\theta-Al_2O_3} = 2.92$ Å, $c_{\theta-Al_2O_3} = 11.83$ Å). While the other alumina polymorphs (δ- and γ-Al_2O_3) have an identical fcc oxygen stacking, only the monoclinic θ-Al_2O_3 can explain a multidomain anisotropic structure [166]. In principle four equivalent domains rotated by 90° should be present due to the monoclinic structure of θ-Al_2O_3; but the domains rotated by 180° can not be differentiated in LEED and are seen only in GIXD [147]. The origin of the limited stripe width was assigned to the stress build-up along the high lattice mismatch direction. Since the lattice parameter of $Fe_{0.85}Al_{0.15}$ is very close to that of NiAl, the same interpretation is likely in our case. But at the opposite to exposure of NiAl(100) [166, 212] at 1025 K (∼ 1000 L), the growth of alumina on iron aluminium does not seem to be accompanied with amorphous oxide domains that require prolonged annealing (and cycle of exposure) to enlarge the surface

covered by stripes.

6.4 Oxide on $Fe_{0.85}Al_{0.15}$(111)

6.4.1 Photoemission analysis

6.4.1.1 Angular analysis and lineshape fitting

Like for the other orientations, photoemission results favour preferential oxidation of aluminium and inertness of iron towards oxygen. Using the same procedure of decomposition than for the two other orientations (110) (Sect. 6.2.1.2) and (100) (Sect. 6.3.1.1), reasonable fits (Fig. 6.24) were obtained with two oxide components for Al 2p. From their angular dependence (Fig. 6.25, Tab. 6.8), one is assigned to oxidised aluminium close to the interface (E_B = 75.3 eV) and the other to atoms closer to the interface with the substrate (E_B = 73.3 eV). Fits parameters are gathered in Tab. 6.8.

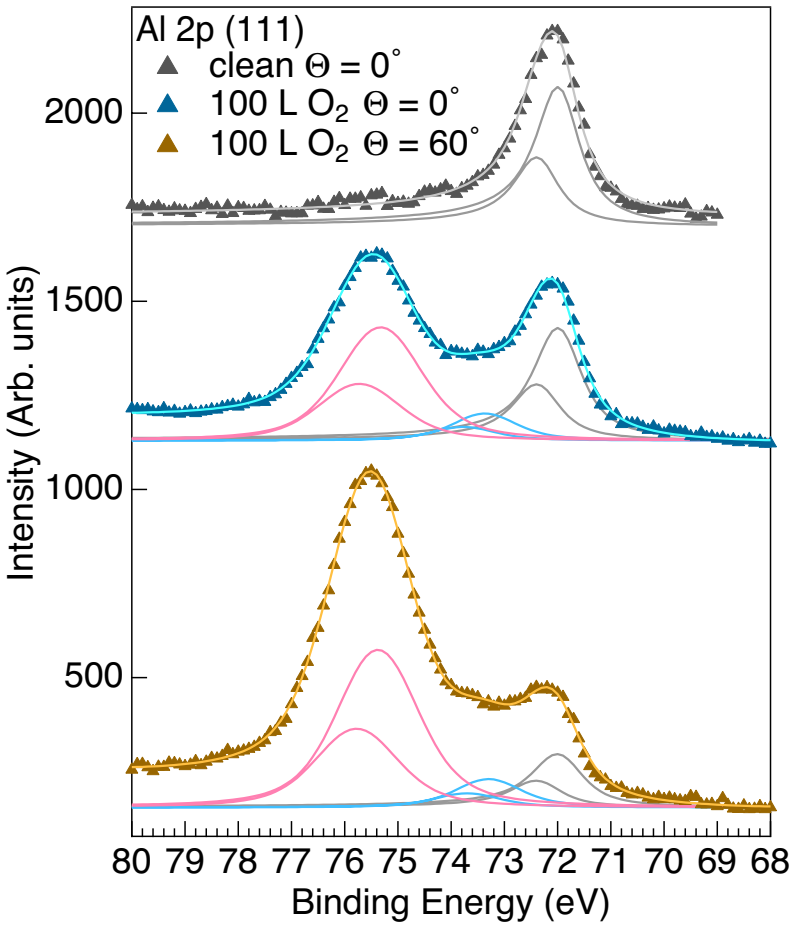

Figure 6.24: Line shape decomposition of the Al 2p core level for the (111) orientation. (Top panel) Clean surface annealed at 973 K (normal emission); (Bottom panels) Surface oxidised at the same temperature with 100 L of O_2 (normal and grazing emission). Three spin orbit split components are needed to fit accurately the data (points) for the oxide layer (see text). Fit parameters are given in Tab. 6.8. Spectra have been collected at a pass energy E_P = 20 eV providing the best resolution.

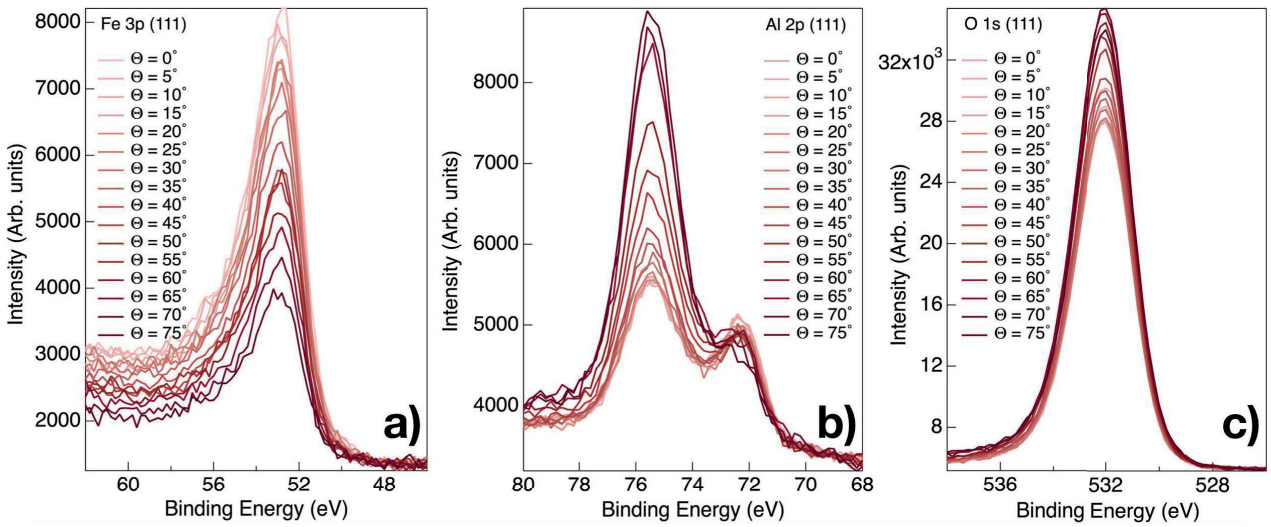

Figure 6.25: Evolution of the a) Fe 3p, b) Al 2p and c) O 1s core levels as a function of emission angle for a (111) oxidised surface (100 L of O_2, 973 K). Data have been normalised to the same background. Pass energy is $E_p = 50$ eV.

	Type	Shape	Relative area	E_B (eV)	L-FWHM (eV)	G-FWHM (eV)	Asymmetry (eV)
Clean NE-$\Theta = 0°$	Bulk	DS	1	72.00	0.85	0.30	0.09
Oxi NE-$\Theta = 0°$	Bulk	DS	0.35	72.00	0.90	0.40	0.08
	Interface	V	0.11	73.35	0.85	0.90	-
	Surface	V	0.54	75.35	0.85	1.35	-
Oxi GE-$\Theta = 60°$	Bulk	DS	0.17	72.00	0.85	0.50	0.090
	Interface	V	0.11	73.30	0.90	0.90	-
	Surface	V	0.72	75.40	0.85	1.30	-

Table 6.8: Fit parameters for Al $2p_{3/2}$ core level of $Fe_{0.85}Al_{0.15}$(111) surfaces. Clean (973 K) and oxidised (973 K, 100 L of O_2) are compared at normal ($\Theta = 0°$) and grazing ($\Theta = 60°$) emissions. DS, V are shorthands for Doniach-Sunjich, Voigt function. Error bars are of the order of the step size, *i.e.* 0.05 eV.

6.4.1.2 Segregation under the oxide from angular analysis

Like for the two other orientations (110) (Sect. 6.2.1.3) and (100) (Sect. 6.3.1.2), the profile of segregation was obtained from the modelling of the angular profile of the $I_{Al\,2p\,metal}/I_{Fe\,3p}$ intensity ratio (Fig. 6.25). As shown in Fig. 6.26, the profile of segregation is flatter under the oxide than on the clean surface. Indeed, the thickness of the segregated layer is larger than on the bare surface and with an interfacial composition still enriched in aluminium but equal to $x_S + \Delta x \simeq x_L \sim 0.31$.

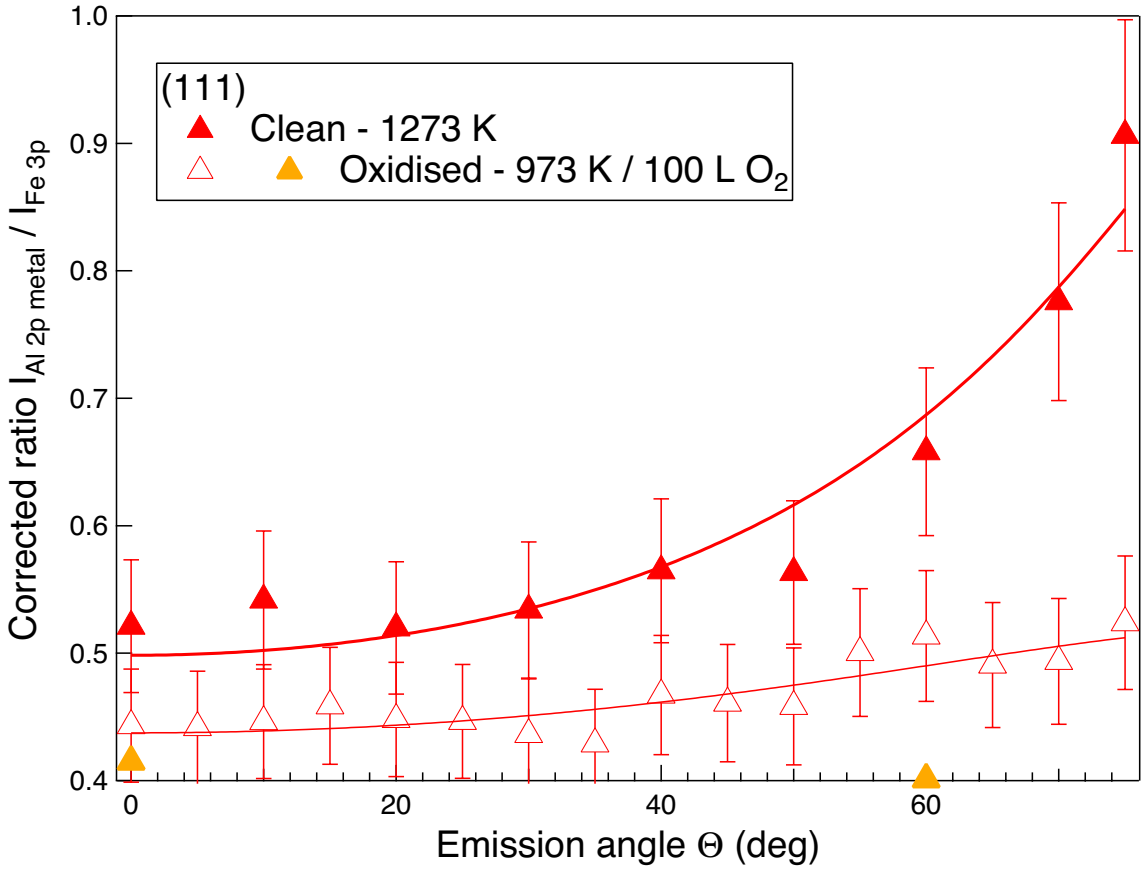

Figure 6.26: Segregation under the oxide at the (111) surface from the angular variation of the corrected ratio $I_{Al\,2p\,metal}/I_{Fe\,3p}$ (pass energy E_p = 50 eV) in the as-prepared (111) surface (1273 K; filled triangles) and after oxidation (973 K, 100 L of O_2; open triangles). Data (points) have been fitted with a model of continuous profile of segregation (lines, Eq. 5.4) which values are given in Tab. 5.3, 6.2. The orange points correspond to another measurement.

6.4.1.3 Oxide film thickness and stoichiometry

As on (110) (Sect. 6.2.1.4) and (100) (Sect. 6.3.1.3) surfaces, the modelling of the various ratios of core level intensities in terms of film thickness led to the imperious need of accounting for the profile of segregation under the oxide (lines vs symbol in Fig. 6.27). Once the analysis is corrected from this bias, a matching by pair, *i.e.* for a given substrate core level, is achieved. But, at the opposite of (100) orientation, thicknesses predicted for O 1s intensity are larger than those obtained from Al 2p(metal) pointing at a problem of stoichiometry of the oxide in the quantification. The effect was reversed for (110) orientation and was assigned to an under-stoichiometry in oxygen with an average composition of $Al_2O_{2.5}$. The present ratio of thicknesses of ~ 1.25 obtained from O 1s, Al 2p(oxi)/Fe 3p, Al 2p(metal) points at a stoichiometry of $Al_2O_{3.5}$ as confirmed by simulations (not shown [4]) with a thickness around

[4]In the simulations, only the stoichiometry and molar mass were changed at fixed density and mean free paths since the structure of the oxide is unknown. But the latter parameter impacts much more the actual

19 Å. Finally, the decrease of the film thickness at high emission angles (Fig. 6.27) highlights a weakness of the continuous thin film interpretation which is due to the roughness of the film as it will be apparent in STM.

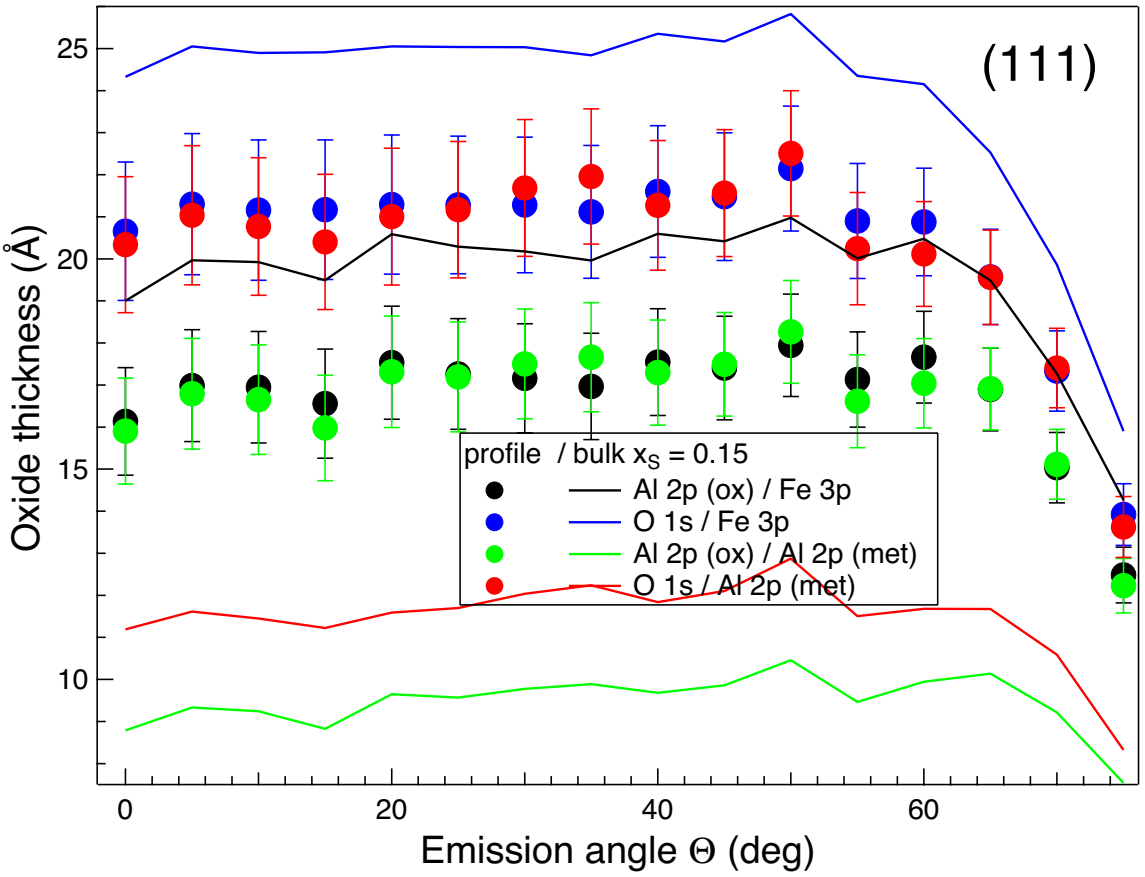

Figure 6.27: Thickness of the oxide layer (973 K, 100 L of O_2) on the (111) surface calculated from ratio of core levels as indicated in the figure. Calculations assume a bulk-like homogeneous substrate ($x_S = 0.15$, lines) or take into account the actual profile of segregation (markers). The layer stoichiometry is fixed at Al_2O_3.

6.4.2 Oxide crystallography from LEED

Whatever the oxidation route, an ordered LEED pattern has never been observed after oxidation of the (111) surface. High temperature oxidation (973 K) with different amounts of oxygen (1, 10, 20, 100 L of O_2) but also room temperature oxidation followed by high temperature annealing up to 1123 K never led to any clear ordering. While covering oxide give rise to only diffuse background pointing at the lack of epitaxial oxide, small exposures led to a faint (1×1) pattern. Amazingly, surfaces slighly contaminated with oxygen and annealed leads to a spot splitting of $\{10\}_S$ and $\{11\}_S$ reflections that evolves with beam energy. This

thickness than the overlap between the values obtained from the different core level ratios.

is typical for a facetting of the surface along a direction $\langle 12 \rangle_S$ which is known to occur when adsorbates are present on an open (111) of body-centred metal (like W(111) [242, 243]). The driving force is the lower surface energy of the covered vicinal surface over the clean open (111) one. But the reproducibility of such LEED pattern and the lack of local analysis does not allow to further comment this observation.

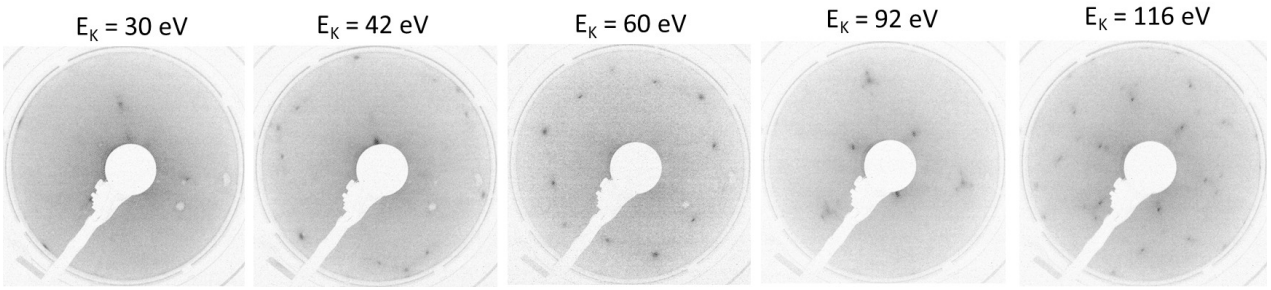

Figure 6.28: Traces of surface faceting observed after high temperature annealing of a $Fe_{0.85}Al_{0.15}$(111) surface slightly contaminated with oxygen.

The absence of an ordered oxide compared to NiAl(111), Ni_3Al(111) or Al/Ni(111) (see Sect. 3.4.3) can be assigned to the intense roughening and faceting observed on the clean surface (Sect. 5.3.3). Graupner *et al.* found a complex ordered $(6.4\times6.4)R30°$ incommensurate oxide on FeAl(111) [16]; the difference lies probably in the use of a defined compound in their study.

6.4.3 Surface morphology from STM

STM imaging supports the LEED conclusions of the lack of growth of any ordered oxide layer. Whatever the route of oxidation, the surface is rough and difficult to image. Fig. 6.29 shows a typical large scale topography where appear large three-dimensional features with a typical size in the range of several tens of nanometres and height of 7 ± 2 nm. These islands present facets inclined by $10 - 15°$ with respect to the surface plane and are surrounded by small features with a corrugation of 0.5 ± 0.2 nm. This surface roughness explains the lack of LEED pattern, the deviation from the thin film model for photoemission angular measurements points at a three dimensional growth of alumina.

6.5 Influence of oxygen exposure and growth mode

The thickness analysis was also performed for films grown on (110) surface at O_2 exposures ranging from 1 to 1000 L at fixed temperature (1123 K) (Fig. 6.30). In most cases, only the available normal and grazing ($\Theta = 60°$) measurements were analysed at a fixed bulk composition enriched in aluminium as found above ($x_S = 0.31$ at 500 L) and at a fixed Al_2O_3 stoichiometry. Despite these simplifying assumptions, a clear saturation of thickness appears above 100 L while below 50 L partial coverage is suspected. Indeed, below 50 L, substrate

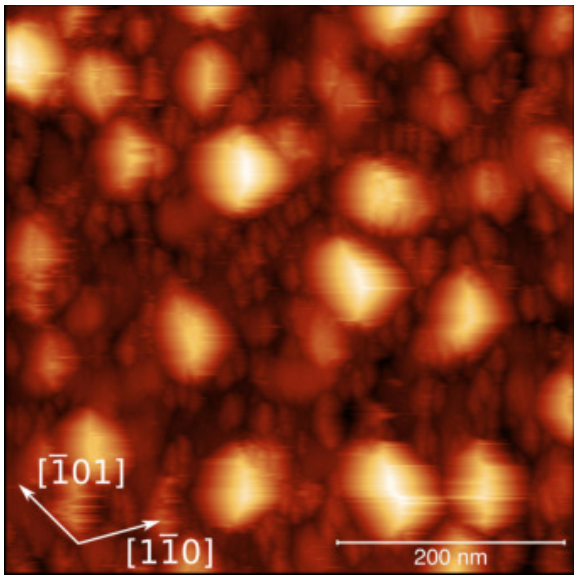

Figure 6.29: STM image of the $Fe_{0.85}Al_{0.15}$(111) surface after oxidation at 973 K and 100 L of O_2 (500×500 nm^2, $U_b = -1.7$ V, $I_t = 1.7$ nA).

LEED spots are still visible (see Sect. 6.2.2.1) as well as some reconstructed domains in STM (not shown).

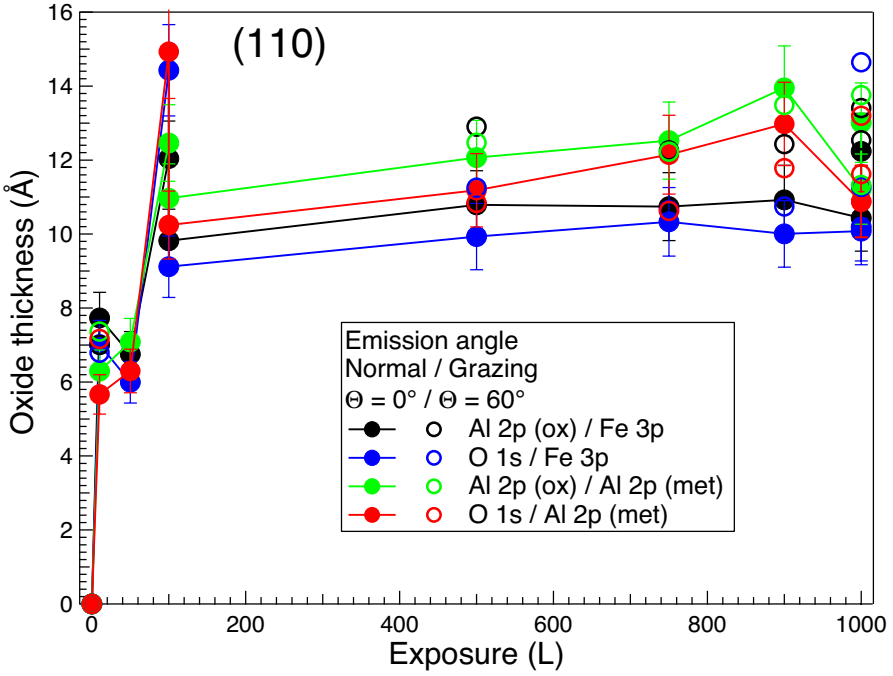

Figure 6.30: Evolution of film thickness with O_2 exposure for film synthesised at high temperature (1123 K) on (110) surface. Normal and grazing measurements are compared for all the combinations of core levels for different experiments. Film composition and photoemission parameters have been fixed at those of Al_2O_3 with a fixed substrate bulk composition of $x_S = 0.31$.

To further assess the interplay between oxide film thickening, stoichiometry and segregation, a more systematic angular analysis as described above was undertaken on all the orientations for 1,10,100 (500) L of O_2 at a given annealing temperature. The characteristic length Λ of the fitted exponential segregation profile, the surface composition $x(0) = x_S + \Delta x$, the oxide thickness t and its stoichiometry are gathered in Tab. 6.9. Of course, the use of a continuous film model on top of an in-plane homogeneous profile of segregation is questionable in the case of a partial coverage. But again the (100) orientation distinguishes from the two others. While the film thickens continuously on (110) and (111), it seems to stabilise quickly with exposure on (100) without changing at all the profile of segregation underneath. 1 L of O_2 is enough to grow a 6.2 Å thick film very close to the final thickness of ~ 9 Å. Assuming a θ-alumina structure as found on NiAl(100), this corresponds to roughly 4 oxygen planes and a surface density of oxygen of 4×10^{15} O atoms·cm^{-2} which is even higher than the oxygen exposure of 1 L. If stoichiometry poorly change on (100) and (111) surfaces leading to a continuous 2D films, it changes on (111) which further oxide thickening should be tested above 100 L.

(110)@1123 K		Exposure (L)			
	Parameter	0	1	10	500
Subsurface	Λ (Å)	38 ± 10	26 ± 6	15.5 ± 4	> 130
	$x(0) = x_S + \Delta x$	0.42 ± 0.03	0.45 ± 0.03	0.5 ± 0.03	0.31 ± 0.01
Oxide	Thickness t (Å)	0	1.7 ± 0.4	3.8 ± 0.4	11.4 ± 1.6
	Stoichiometry	–	$Al_2O_{2.8\pm0.2}$	$Al_2O_{2.6\pm0.2}$	$Al_2O_{2.5\pm0.2}$

(100)@973 K		Exposure (L)			
	Parameter	0	1	10	100
Subsurface	Λ (Å)	26.5 ± 6	30 ± 6	26 ± 5	29 ± 5
	$x(0) = x_S + \Delta x$	0.5 ± 0.03	0.51 ± 0.03	0.55 ± 0.03	0.54 ± 0.03
Oxide	Thickness t (Å)	0	6.2 ± 0.7	8.2 ± 0.8	8.9 ± 0.8
	Stoichiometry	–	$Al_2O_{2.5\pm0.2}$	$Al_2O_{2.9\pm0.2}$	$Al_2O_{3\pm0.2}$

(111)@973 K		Exposure (L)			
	Parameter	0	1	10	100
Subsurface	Λ (Å)	25.5 ± 6	30 ± 8	> 60	62 ± 22
	$x(0) = x_S + \Delta x$	0.5 ± 0.03	0.41 ± 0.03	0.27 ± 0.03	0.35 ± 0.03
Oxide	Thickness t (Å)	0	3.9 ± 0.5	12.5 ± 2	17.5 ± 2
	Stoichiometry	–	$Al_2O_{2.8\pm0.2}$	$Al_2O_{2.8\pm0.2}$	$Al_2O_{3.5\pm0.2}$

Table 6.9: Results of angular analysis of photoemission performed on oxide films grown at various exposures. Error bars stem from cumulative uncertainties of 10 % on measured ratios and on average of thickness over emission angle.

6.6 Discussion

6.6.1 Comparison of the oxide on the various orientations of $Fe_{0.85}Al_{0.15}$

Oxidation was performed on all three faces following a common protocol (see Sect. 2.1). While oxidation of iron can be excluded in all cases (see Fig. 6.31) pointing at a preferential oxidation of aluminium, the formed oxide layers have different intrinsic characteristics that are summarised in Tab. 6.10.

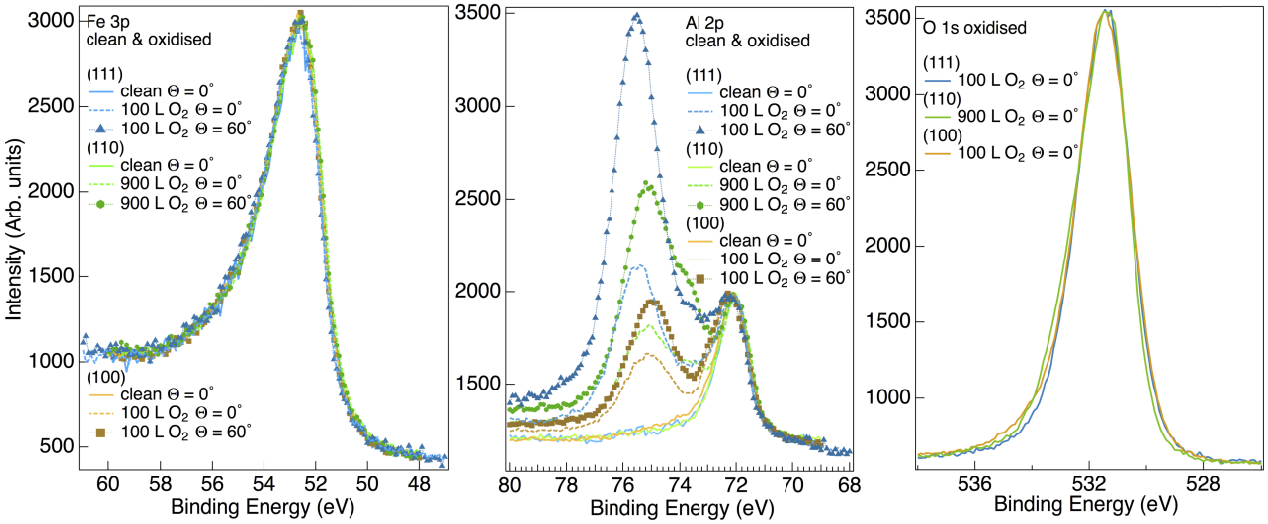

Figure 6.31: (Left) Overlap of Fe 3p core levels for all clean and oxidised surfaces as indicated in figure. Even for surface sensitive geometry (grazing emission $\Theta = 60°$), no oxidation of iron is observed. Spectra have been normalised to the same background and peak intensity. (Middle) Same for Al 2p but after normalization on the metallic component. (Right) Overlap of O 1s core levels after normalization.

While the self-limited growth could be clearly explored only on the (110) orientation up to 1000 L (Fig. 6.30), STM, LEED and angular analysis of photoemission demonstrated the formation of a covering oxide of nanometre thickness on all surfaces in the range of 100 L of exposure. While a three dimensional growth happens on (111) probably due to the already complex nano-faceting found on the clean surface, flat and covering film grow on (110) and (100) with a thickness in the range of a few O-O interlayer spacings ($\sim$ 2.2 Å) as found in all the alumina polymorphs (see Sect. 3.4.1) [5]. However, similar values deduced from photoemission were obtained in the literature for instance on NiAl(110) [152, 200, 254] or on FeAl(110) [16] after oxidation at high temperature; lower values are found in the case of two-steps oxidation process.

[5] Absolute values should be taken with caution due to uncertainties on inelastic mean free path and on the use of a continuous models of analysis. Nevertheless, the accuracy of profile of segregation and of stoichiometry are much better since they result from ratio.

Orientation	(110)	(100)	(111)
Thickness (Å)	~ 11	~ 9	~ 18.5
Stoichiometry	$Al_2O_{2.5}$	Al_2O_3	$Al_2O_{3.5}$
E_B Al 2p oxide (eV)	73.5 / 75	75	73.4 / 75.3
Unit cell	Rotated rectangular with 2 domains	(1×2)-like with 2 domains	no LEED -
Λ (Å)	$38 \rightarrow \infty$	$26.5 \rightarrow 29$	$25.4 \rightarrow 62$
$x(0) = x_S + \Delta x$	$0.42 \rightarrow 0.31$	$0.5 \rightarrow 0.54$	$0.5 \rightarrow 0.35$
Fe-Al structure	$B_2 \rightarrow D0_3$	$B_2 \rightarrow B_2$	$B_2 \rightarrow D0_3$
Morphology	Flat film with two domains	Elongated stripes	Rough

Table 6.10: Comparison of the characteristics of the oxide films obtained at $Fe_{0.85}Al_{0.15}$ surfaces. $x(0) = x_S + \Delta x$ is the average surface composition; the corresponding bulk structure is indicated below; the arrow stands for the change from clean to oxidised surface.

The (100) face behaves differently from the two other ones. Oxidation gives rise to a thinner oxide, which diffraction spots are still present in the LEED pattern, without any strong change of the segregation profile underneath. The subsurface composition is close to $Fe_{0.5}Al_{0.5}$ *i.e.* to the B_2 ordered alloy accordingly to phase diagram (Fig. 3.1) over a depth of 3 nm. Meanwhile, on (110) and (111) surfaces, oxidation depletes the subsurface in aluminium compared to the bare surface and pumps out aluminium from the bulk leading to a flatter but deeper profile of segregation. For those orientations, the subsurface composition gets closer to $Fe_{0.66}Al_{0.33}$ in the range of stability of the ordered $D0_3$ alloy (Fig. 3.1); relying only on bulk stability, this would imply a transition of phase induced by the growth of the oxide. A possible explanation is a subtle minimisation of the interfacial stress between the oxide film and the subsurface of the alloy. Indeed, as shown in Tab. 3.1 and the inset of Fig. 5.1 [25], the variation of the lattice parameter between $x = 0$ and $x = 0.5$ in A_2-B_2 structures is only 1.4 % and, on a symmetry point of view, the bulk (110) truncation of A_2, $D0_3$ and B_2 have quite close lattice parameters. Poorly studied in surface science, such kind of oxide-induced depletion was partly evidenced on Fe_3Al(110) [219] (Fig. 3.36).

While two chemical environments can be identified for aluminium, on (110) and (111), one closer to the surface one to the interface, only one Al 2p oxide core level is found on (100). Their interpretation in terms of tetrahedral (low binding energy) and octahedral (high binding energy) coordinated aluminium and the labelling of the film based on the closest bulk alumina parent polymorph was often used in the first photoemission studies on NiAl [13, 144, 150] on FeAl [16]. Although useful for very thick films, such comparisons are hazardous for few monolayers thick oxide films where coordination of atoms are strongly distorted and chemical states are influenced by the underlying substrate. This was clearly shown by the high resolution photoemission study of the oxide on NiAl(110) [151] compared to the Kresse's model [15]. Poorly discussed up to now in our study, the O 1s core level of all our oxide films (Fig. 6.31) is strongly asymmetric and can always be decomposed into two components

which high binding energy one corresponds to surface species as it is always slightly enhanced at grazing emission. Finally, the stoichiometry of our films estimated from photoemission changes from sub- to over- stoichiometry in oxygen from (110) to (111), with an stoichiometry Al_2O_3 composition for (100). On a LEED point of view, only the oxide on (111) surface is "amorphous".

6.6.2 Comparison to the existing literature

Already addressed all along this chapter, strong similarities appeared between existing literature and our present findings on (110) and (100) surfaces.

6.6.2.1 Oxide at (110) surface

The unit cell found by GIXD for the oxide film on $Fe_{0.85}Al_{0.15}$ is very close to the only two accurate determinations on NiAl(110) [14, 121] and Al/Ni(111) [19] (see Tab. 6.4); the film LEED pattern shares also some symmetry similarities with the other substrates such as FeAl(110) [16], Cu-9 at.% Al(111) [18] and γ-Al_4Cu_9(110) [217]. According to photoemission, its stoichiometry is close to $Al_2O_{2.6}$, the $Al_{10}O_{13}$ one found in the theoretical study of Kresse *et al.* [15] and detailed in Sect. 3.4.3.2.1. However, a discrepancy remains on its thickness which is found larger than a O-bilayer film. Modulo a few distortions, this structure seems to be found on support of different symmetries and structures. The actual role of the substrate in its formation is still puzzling. While Prevot *et al.* argue that its an archetype of free-standing oxide [19] since, according to their diffraction study, it poorly affects the atomic positions of Ni(111), but the substrate-induced strain is present on NiAl(110) and manifests through dense anti-phase domain boundaries. On $Fe_{0.85}Al_{0.15}$, the freedom of composition of the subsurface leads to a nearly perfect matching with a (1×2) oxide unit cell giving rise to a very low density of such linear defects in STM.

In their high resolution photoemission analysis of the oxide on NiAl(110) based on density functional calculations, Martin *et al.* [151] isolated two sizeable core level shifts for oxidised Al 2p compared to metallic Al (Tab. 3.4) that were assigned to interface and surface aluminiums. Moreover, if similar oxidised Al 2p species are probably present in our study (Tab. 6.1), their chemical shift are much larger (ΔE_B(NiAl) = 1; 2.27 eV versus $\Delta E_B(Fe_{0.85}Al_{0.15}) = 1.68; 3.23$). If a part of the shift is due to a different metallic reference ($E_B(Al^0_{2p}, \text{NiAl}) = 72.5$ eV; $E_B(Al^0_{2p}, Fe_{0.85}Al_{0.15}) = 72$ eV) [101, 151], leading to similar value for the interface component, the surface one is still different, demonstrating the role of the interaction with the substrate and/or a different environnement. According to *ab initio* calculations and experiment on NiAl(110) [151], a broader distribution of core level shifts is expected for surface aluminium atoms than for interface ones due to numerous slightly different environments; this is in close agreement with the present results on the Gaussian FWHM of the peaks (Tab. 6.1, FWHM(Al_s) = 1.3 vs FWHM(Al_i) = 0.8). Finally, our O 1s component can be fitted perfectly with two Voigt components shifted by 1.23 eV as for NiAl(110) [144, 151] with a somehow larger ratio 0.33 compared to 0.19 in Ref. [151]. It is reminded that the high binding energy O 1s component was assigned to specific O atoms of

the O-surface planes, the remaining atoms contributing to the other component.

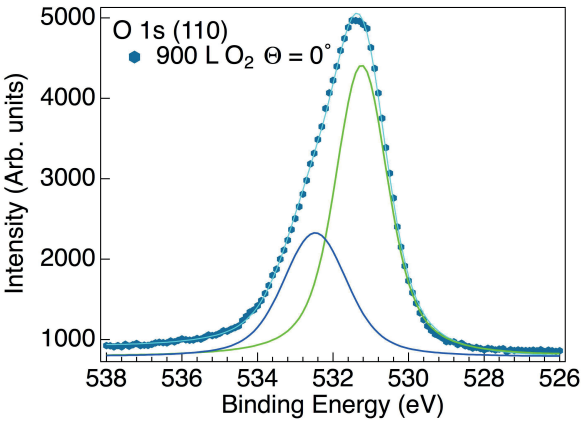

Figure 6.32: Fit of the O 1s core level of the oxide film at $Fe_{0.85}Al_{0.15}$(110) surface (1123 K, 500 L of O_2).

All these findings let suppose that the structure of the oxide film formed at the surface of $Fe_{0.85}Al_{0.15}$(110) is close to that found on NiAl(110). Only its thickness is larger than a simple bilayer film.

6.6.2.2 Oxide at (100) surface

On (100) surface, both the (1×2) LEED pattern and the formation of 5 nm periodic stripes are strongly similar to all the literature results on NiAl(100) (Sect. 3.4.3.2.1), CoAl(110) (Sect. 3.4.3.5) and FeAl(100) (Sect. 3.4.3.6) which atomic structures are the same (B_2 CsCl) and lattice parameters very close. In the present case, the subsurface composition of the clean and oxidised $Fe_{0.85}Al_{0.15}$ is close to $Fe_{0.5}Al_{0.5}$ the bulk structure of which is again B_2 CsCl. The common explanation is given through the already evoked Bain's epitaxy between the fcc oxygen stacking in θ-alumina and the substrate (Fig. 3.21). Diffraction data of Stierle *et al.* concluded at 7.5 Å thick θ-alumina with strong distorsion with a preference of tetrahedral coordinated sites at the interface and octahedral at the surface. But, if our photoemission analysis indeed resulted in the expected Al_2O_3 stoichiometry and a similar thickness (9 Å), the only one chemical state for Al 2p and probably two for O 1s were put forward. This finding is in accord with previous works on NiAl(100) [133, 165, 212] but questions the proposed θ-alumina structure which involves a mixture of tetrahedral and octahedral aluminium sites.

6.6.2.3 Oxide at (111) surface

The lack of clear crystallised thin film, the sub-stoichiometry in Al and the three dimensional growth prevents any relevant comparison to known literature.

CHAPTER 7

CONCLUSION

This work aimed at exploring the orientation dependence of aluminium segregation and oxidation at surfaces of $Fe_{0.85}Al_{0.15}$ single crystals. This random bcc alloy was selected to mimic those effects at the more complex alloyed-steel surfaces. This thesis developed a surface science approach under ultra-high vacuum of the questions at hand. By using core-level photoemission, not only the chemistry of the oxide films but also the profile of segregation and film thicknesses were determined thank to the in-depth sensitivity of the technique. The atomic structure of the surfaces, and more precisely the unit cells, were explored with Low-Energy Electron Diffraction. Synchrotron Grazing Incidence X-Ray Diffraction was also used to refine the large oxide unit cell at (110) surface. Theses studies were supplemented by Scanning Tunnelling Microscopy to explore the topography of the surfaces. At last, *ab initio* calculations helped to rationalise the effects of orientation on the trend of segregation.

In the first step, a common protocol of preparation of clean surfaces was established. Bulk impurities as well as contamination from residual vacuum were two major difficulties to overcome. The former requires intensive cycles of surface preparation by sputtering-annealing to get rid of carbon. Although unavoidable for time consuming measurements such as STM and GIXD, vacuum contamination was avoided through fast XPS/LEED measurements. Coupled to that of aluminium, an intense carbon impurity segregation was observed only on (110) orientation in the form of self-organised stripes separated by ~ 6 nm as found by STM and LEED. Upon annealing, two types of C 1s photoemission fingerprints were evidenced, one assigned to graphitic-like carbon and another one to chemisorbed carbon. Bulk carbide formation could not be excluded. Quantification of the graphitic component in photoemission paralleled the optimum of apparent coverage of stripes at ~ 850 K. The latter started decaying at the onset of aluminium segregation and prevented the formation of fully covered oxide layer.

Upon annealing, all surfaces of $Fe_{0.85}Al_{0.15}$ *i.e.* (110), (100) and (111) were prone to intense segregation of aluminium that is accompanied by step straightening, terraces widening and surface smoothing. Although segregation is presented on B_2-FeAl surfaces according to the literature, the A_2 random alloy provides one more degree of freedom linked to potential

phase transitions and ordering from the bulk to the surface. A special emphasis was put on the quantification of the segregation profile via photoemission. Dedicated models were developed including the variation of electron inelastic mean free paths with composition, although this turned out to be important only for the case of large aluminium atomic fraction. At the opposite of literature, sputtering seemed to slightly enrich the surface with aluminium. Segregation happened between 700 and 1000 K but the onset was much earlier at the surface than in the bulk; *i.e.* the surface equilibrates first. After 1000 K, a steady state regime and therefore a constant composition was reached at least on the photoemission point of view. In this regime, the impacted depth is around 2-3 nm with an atomic fraction corresponding to the ordered B_2 structure at the surface, is in agreement with the tendency of short-range order known in Fe-Al alloys. But, on a structural point of view, the three surfaces behaved drastically in different ways. Only the (110) face developed a large scale pseudo-hexagonal reconstruction, never disclosed up to now. Its unit cell of $\sim$ 2 nm is squeezed along one direction. According to LEED and GIXD, it is not a simple incommensurate reconstruction but in fact, it corresponds to a in-plane modulation of lattice parameter that extends up to 6 atomic planes below the surface. This yielded a strong apparent irregularity of hexagon rings in STM. On the other hand, whatever the temperature, the (100) surface was always (1×1) terminated with a marbled-like appearance assigned to an electronic contrast, probably due to a chemical one. At last, despite a smoothing at large distances, the (111) surface was always locally rough with the development of triangular pits involving several atomic levels with a distribution of local slopes peaking around $\sim 6°$. Assigned to the formation of vicinal (111) orientations which are dominated by (211) terraces, this faceting seems to be a characteristic of the atomically rough bcc (111) orientation. But at the opposite of the literature where it is observed upon adsorption of an element that lowers the surface energy of covered (211) surface compared to bare (111), the present faceting happened upon segregation. The gain in energy should counterbalance the cost of formation of numerous under-coordinated kinks and steps. If simulations predicted a favourable Al segregation energy in the first layer of Fe with a slight oscillatory behaviour, the experimental situation on the three low index orientations appeared to be richer and more complex than expected. Theoretical work in still on-going to understand the relative stability of Al-covered Fe(211) surface and bare Fe(111) surfaces.

The surfaces of $Fe_{0.85}Al_{0.15}$ crystals have then been oxidised at a temperature corresponding to the steady-state regime of segregation. The used ultra-high vacuum conditions (1-1000 L) led to a selective oxidation of aluminium and to the growth of alumina films with a self-limited thickness of 1-2 nm. Iron always stayed in its metallic state. Ultrathin oxide was observed on (110) and (100) orientations while a three-dimensional growth happened on (111) surface. Through a decomposition of Al 2p core level into metallic and oxide states, an analysis of the profile of segregation was undertaken showing quite distinct behaviours. Subsurface of (110) and (111) orientations were found to be depleted in aluminium, but still richer than bulk; they adopt a composition close to the $D0_3$ phase up to the probing depth of photoemission. On the other hand, the segregation profile at the (100) surface was insensitive to oxidation and the subsurface kept its B_2 structure.

All the STM, LEED and XPS fingerprints of the oxide at (110) and (100) surfaces were

very close to previous observations of the literature on NiAl, showing the recurrence of the corresponding structures and questioning the actual role of the substrate in their formation and stability. At (110) surface, a two-domain alumina film grew with a (18.5×10.5) Å^2 nearly-rectangular rotated unit cell as determined by GIXD having a nearly perfect (2×1) matching with the substrate. The existence of two core level shifts for Al 2p, a stoichiometry of $Al_2O_{2.6}$ and the symmetry of the unit cell let suppose that its structure is identical to the quite complex one identified at the surface of NiAl(110) [15] and for Al-deposit on Ni(111) [19]. But its XPS thickness is larger than a simple bilayer remains unexplained. However, fewer anti-phase domain boundaries have been observed at $Fe_{0.85}Al_{0.15}$(110) than at NiAl(110). While the former is a way to adapt the lattice mismatch along one direction of NiAl, the capability of the random alloy to change its subsurface structure could be a way to reach this lattice matching. According to preliminary *ab initio* calculations, the model of Kresse is stable on $Fe_{0.85}Al_{0.15}$(110) with minor distortions. On (100) surface, $(2 \times 1) + (1 \times 2)$ film was observed in the form of orthogonal stripes; a likely explanation is the formation of a distorted θ-Al_2O_3 structure in Bain's epitaxy. This epitaxy is related to the stacking of oxygen anions that is common to all alumina polymorphs. But the existence of only one chemical shift for aluminium remains puzzling in light of the complexity of the proposed structural model on NiAl(100) [147] and the existence of mixture of tetrahedral and octahedral sites for aluminium in θ-Al_2O_3. Calculations are still on-going to see if this structure is actually stable. Finally, the lack of clear structure and the oxide film roughness observed on (111) orientation may be related to the strong tendency of this surface to nano-facet.

From the above findings, it is apparent that there is a coupling between the oxide structure, the orientation and the profile composition of the subsurface; therefore the creation and/or annihilation of point defects (antisite or vacancies) below the film is an essential part of the process of oxide growth. Tackling the problem on a theoretical point of view is already tough on NiAl(110) [112]. Finally, whether the found profile is kinetically or thermodynamically driven is however still open.

Compared to the upstream context of formation of oxides at the surface of Al-alloyed steel, this study is only a first fundamental step on model single crystals. The role of oxygen activity, the nature of the oxidising agent and the switch from external to internal oxidation have been put aside by restricting to the Knudsen's regime, to O_2 and to single crystals. Indeed, not speaking about polycristalline samples and the role of grain boundaries, many studies point at a thickening of the film on single crystals at much higher oxygen activity as well as a potential oxidation of the transition metal and/or formation of mixed compounds, depending upon the kinetics [16]. For instance, the growth of 80 nm thick epitaxial γ-Al_2O_3(111) films has been observed on NiAl(110) single crystal after oxidation in dry air [210, 211]; in their study of multistep selective oxidation of NiAl(110) under ultra-high vacuum, Krukowski and coworkers [209] claimed to have grown α-alumina on NiAl(110). Since bulk alumina has a rich phase diagram with differences between polymorphs being just due to small variation in the relative octahedral/tetrahedral cation occupation, quite complex scenario of phase transitions upon annealing have been reported on Fe-Al polycrystalline alloys in the order γ, δ, θ up to the formation of the most stable α-Al_2O_3 [20]. Mirroring the bulk behaviour in

the case of these "thick" films can be quite useful but with the caveat that ultrathin films can develop atomic and electronic structures with aluminium environments without any bulk counterpart [255, 256]. For those peculiar ultrathin 2D oxides, some open surface science questions remains for $Fe_{0.85}Al_{0.15}$:

- is segregation coupled to the growth of the oxide? Is the profile thermodynamically or kinetically driven?
- why the observed oxide structures are recurrent on so many substrates? What is the actual role of the substrate in terms of stress and/or symmetry?
- what are the first steps of oxidation, the type of defects induced in the substrate and how does the structure progressively build-up depending on orientation?
- why is the film thickness self-limited? What is the rate limiting step? How does the transition to films with a "bulk-like" phase (thickening) proceed?

REFERENCES

[1] http://www.worldautosteel.org/.

[2] L. Davis. Weight reduction, materials challenges and impact on paint process. In *PSA Peugeot Citroën, SurCar conference*, June 2011.

[3] R. Cavallotti. *Effets de la terminaison de l'α-alumine sur le comportement au mouillage du zinc*. PhD thesis, Université Pierre et Marie Curie, 2014.

[4] P. Drillet, Z. Zermout, D. Bouleau, J. Mataigne, and S. Claessens. Selective oxidation of high Si, Mn and Al steel grades during recrystallization annealing and steel/Zn reactivity. *La Revue de Métallurgie-CIT*, 101(10):831–837, 2004.

[5] A. Ollivier-Leduc, M.-L. Giorgi, D. Balloy, and J.-B. Guillot. Nucleation and growth of selective oxide particles on ferritic steel. *Corros. Sci.*, 52(7):2498–2504, 2010.

[6] M.-L. Giorgi, J. Diawara, S. Chen, A. Koltsov, and J.-M. Mataigne. Influence of annealing treatment on wetting of steels by zinc alloys. *J. Mater. Sci.*, 47(24):8483–8495, 2012.

[7] R. Cavallotti, J. Goniakowski, R. Lazzari, J. Jupille, A. Koltsov, and D. Loison. Role of surface hydroxyl groups on zinc adsorption characteristics on $\alpha-Al_2O_3(0001)$ surfaces: first-principles study. *J. Phys. Chem. C*, 118:13578–13589, 2014.

[8] H.T. Le, J. Goniakowski, C. Noguera, A. Koltsov, and J.-M. Mataigne. First-principles study on the effect of pure and oxidized transition-metal buffers on adhesion at the alumina/zinc interface. *J. Phys. Chem. C*, 120(18):9836–9844, 2016.

[9] R. Cavallotti, H.T. Le, J. Goniakowski, R. Lazzari, J. Jupille, A. Koltsov, and D. Loison. New routes for improving adhesion at the metal/α-Al_2O_3 (0001) interface. *Phys. Chem. Chem. Phys.*, 18(4):3032–3039, 2016.

[10] H.T. Le, R. Lazzari, J. Goniakowski, S. Cavallotti, R. Chenot, C. Noguera, J. Jupille, A. Koltsov, and J.-M. Mataigne. Tuning adhesion at metal/oxide interfaces by surface hydroxylation. *J. Phys. Chem. C*, 121(21):11464–11471, 2017.

[11] S.C. Deevi and V.K. Sikka. Nickel and iron aluminides: An overview on properties, processing, and applications. *Intermetallics*, 4(5):357–375, 1996.

[12] Q.H. Wu, A. Fortunelli, and G. Granozzi. Preparation, characterisation and structure of Ti and Al ultrathin oxide films on metals. *Int. Rev. Phys. Chem.*, 28(4):517–576, 2009.

[13] R.M. Jaeger, H. Kuhlenbeck, H.-J. Freund, M. Wuttig, W. Hoffmann, R. Franchy, and H. Ibach. Formation of a well-ordered aluminium oxide overlayer by oxidation of NiAl(110). *Surf. Sci.*, 259(3):235–252, 1991.

[14] J. Libuda, F. Winkelmann, M. Bäumer, H.-J. Freund, Th. Bertrams, H. Neddermeyer, and K. Müller. Structure and defects of an ordered alumina film on NiAl (110). *Surf. Sci.*, 318(1-2):61–73, 1994.

[15] G. Kresse, M. Schmid, E. Napetschnig, M. Shishkin, L. Köhler, and P. Varga. Structure of the ultrathin aluminum oxide film on NiAl (110). *Science*, 308(5727):1440–1442, 2005.

[16] H. Graupner, L. Hammer, K. Heinz, and D.M. Zehner. Oxidation of low-index FeAl surfaces. *Surf. Sci.*, 380(2-3):335–351, 1997.

[17] A. Yamauchi, M. Tsunekane, K. Kurokawa, S. Hanada, and K. Yoshimi. Influence of vacuum annealing conditions on the surface oxidation and vacancy condensation in the surface of an FeAl single crystal. *Intermetallics*, 18:412–416, 2010.

[18] E. Napetschnig, M. Schmid, and P. Varga. Ultrathin alumina film on Cu-9 at% Al (111). *Surf. Sci.*, 602(10):1750–1756, 2008.

[19] G. Prévot, S. Le Moal, R. Bernard, B. Croset, R. Lazzari, and D. Schmaus. Archetypal structure of ultrathin alumina films: Grazing-incidence X-ray diffraction on Ni (111). *Phys. Rev. B*, 85(20):205450, 2012.

[20] H.J. Grabke. Oxidation of NiAl and FeAl. *Intermetallics*, 7(10):1153–1158, 1999.

[21] C. Wagner. Reaktionstypen bei der oxydation von legierungen. *Zeitschrift für Elektrochemie, Berichte der Bunsengesellschaft für physikalische Chemie*, 63(7):772–782, 1959.

[22] D.R. Lide. *CRC handbook of chemistry and physics*, volume 85. CRC press, 2004.

[23] H. Lüth. *Surface and Interfaces of Solids*, volume 15 of *Surface Science*. Springer Verlag, 1992.

[24] H. Ibach and D.L. Mills. *Electron Energy Loss Spectroscopy and Surface Vibrations*. Academic Press, New York, 1982.

[25] M. Ellner and I. Park. On the partial atomic volume of aluminum in solid solutions based on the 3d transition metals and copper. *Metall. Mater. Trans. A*, 33(12):3591–3595, 2002.

[26] http://www.physik.de/mateck.

[27] N. Matsunami, Y. Yamamura, Y. Itikawa, N. Itoh, Y. Kazumata, S. Miyagawa, K. Morita, R. Shimizu, and H. Tawara. Energy dependence of the ion-induced sputtering yields of monatomic solids. *Atomic Data and Nuclear Data Tables*, 31(1):1–80, 1984.

[28] H. Graupner, L. Hammer, K. Müller, and D.M. Zehner. Composition and structure of the (100) and (110) surfaces of FeAl. *Surf. Sci.*, 322(1):103–115, 1995.

[29] W. Meier, V. Blum, L. Hammer, and K. Heinz. Equilibration of stoichiometrically distorted $Fe_{1-x}Al_x$ (100) surfaces. *J. Phys.: Condens. Matter*, 13(9):1781–1791, 2001.

[30] L. Hammer, H. Graupner, V. Blum, K. Heinz, G.W. Ownby, and D.M. Zehner. Segregation phenomena on surfaces of the ordered bimetallic alloy FeAl. *Surf. Sci.*, 412-413:69–81, 1998.

[31] K. Heinz and L. Hammer. Surface structure and segregation of bimetallic bcc-type alloys. *J. Phys.: Condens. Matter*, 11(43):8377, 1999.

[32] V. Blum, L. Hammer, W. Meier, K. Heinz, M. Schmid, E. Lundgren, and P. Varga. Segregation and ordering at $Fe_{1-x}Al_x$ (100) surfaces-a model case for binary alloys. *Surf. Sci.*, 474(1):81–97, 2001.

[33] V. Blum, L. Hammer, W. Meier, and K. Heinz. Quantification of substitutional disorder and atomic vibrations by LEED-the role of parameter correlations. *Surf. Sci.*, 488(1):219–232, 2001.

[34] L. Hammer, W. Meier, V. Blum, and K. Heinz. Equilibration processes in surfaces of the binary alloy Fe-Al. *J. Phys: Condens. Matter*, 14(16):4145–4164, 2002.

[35] C.J. Chen. *Introduction to scanning tunneling microscopy*, volume 2. Oxford University Press New York, 1993.

[36] Ø. Fischer, M. Kugler, I. Maggio-Aprile, C. Berthod, and C. Renner. Scanning tunneling spectroscopy of high-temperature superconductors. *Rev. Mod. Phys.*, 79(1):353, 2007.

[37] E. Stoll. Resolution of the scanning tunnel microscope. *Surf. Sci.*, 143(2):411–416, 1984.

[38] J. Tersoff and D.R. Hamann. Theory and application for the scanning tunneling microscope. *Phys. Rev. Lett.*, 50(25):1998, 1983.

[39] J. Tersoff and D.R. Hamann. *Theory of the scanning tunneling microscope*. Springer, 1985.

[40] H.B. Michaelson. The work function of the elements and its periodicity. *J. Appl. Phys.*, 48(11):4729–4733, 1977.

[41] J. Bardeen. Tunnelling from a many-particle point of view. *Phys. Rev. Lett.*, 6(2):57, 1961.

[42] I. Giaever. Energy gap in superconductors measured by electron tunneling. *Phys. Rev. Lett.*, 5(4):147, 1960.

[43] J.P. Ibe, P.P. Bey Jr, S.L. Brandow, R.A. Brizzolara, N.A. Burnham, D.P. DiLella, K.P. Lee, C.R.K. Marrian, and R.J. Colton. On the electrochemical etching of tips for scanning tunneling microscopy. *J. Vac. Sci. Technol. A*, 8(4):3570–3575, 1990.

[44] V.V. Dremov, V.A. Makarenko, S.Y. Shapoval, V.G. Beshenkov, O.V. Trofimov, and I.I. Khodos. Sharp and clean tungsten tip for STM investigations. *Nanobiology*, 3:83–88, 1994.

[45] Gwyddion software, http://gwyddion.net/.

[46] S. Hüfner. *Photoelectron spectroscopy: principles and applications*. Springer Science & Business Media, 2013.

[47] S. Hofmann. *Auger-and X-ray photoelectron spectroscopy in materials science: a user-oriented guide*, volume 49. Springer Science & Business Media, 2012.

[48] D.J. O'Connor, B.A. Sexton, and R.St.C. Smart. *Surface analysis methods in materials science*, volume 23. Springer Science & Business Media, 2013.

[49] K. Oura, V.G. Lifshits, A. Saranin, A.V. Zotov, and M. Katayama. *Surface science: an introduction*. Springer Science & Business Media, 2013.

[50] J.F. Moulder, W.F. Stickle, P.E. Sobol, and K.D. Bomben. *Handbook of X-ray photoelectron spectroscopy*. Physical Electronics, Inc., 1995.

[51] C.D. Wagner and G.E. Muilenberg. *Handbook of X-ray photoelectron spectroscopy*. Perkin-Elmer, 1979.

[52] J.J. Yeh and I. Lindau. Atomic subshell photoionization cross sections and asymmetry parameters: $1 \leqslant Z \leqslant 103$. *At. Data Nucl. Data Tables*, 32(1):1–155, 1985.

[53] D.J. Kennedy and S.T. Manson. Photoionization of the noble gases: Cross sections and angular distributions. *Phys. Rev. A*, 5(1):227–247, 1972.

[54] P. Ruffieux, P. Schwaller, O. Gröning, L. Schlapbach, P. Gröning, Q.C. Herd, D. Funnemann, and J. Westermann. Experimental determination of the transmission factor for the Omicron EA125 electron analyzer. *Rev. Sci. Instrum.*, 71(10):3634–3639, 2000.

[55] S. Doniach and M. Sunjic. Many-electron singularity in X-ray photoemission and X-ray line spectra from metals. *J. Phys. C*, 3(2):285, 1970.

[56] D.A. Shirley. High-resolution X-ray photoemission spectrum of valence bands of gold. *Phys. Rev. B*, 5(12):4709, 1972.

[57] S. Tanuma, C.J. Powell, and D.R. Penn. Calculations of electron inelastic mean free paths for 31 materials. *Surf. Interface Anal.*, 11(11):577–589, 1988.

[58] S. Tanuma, C.J. Powell, and D.R. Penn. Calculations of electorn inelastic mean free paths. II. Data for 27 elements over the 50-2000 eV range. *Surf. Interface Anal.*, 17(13):911–926, 1991.

[59] S. Tanuma, C.J. Powell, and D.R. Penn. Calculations of electron inelastic mean free paths: III Data for 15 inorganic compounds over the 50-2000 eV range. *Surf. Interface Anal.*, 17(13):927–939, 1991.

[60] S. Tanuma, C.J. Powell, and D.R. Penn. Calculations of electron inelastic mean free paths (IMFPS). IV. Evaluation of calculated IMFPs and of the predictive IMFP formula TPP-2 for electron energies between 50 and 2000 eV. *Surf. Interface Anal.*, 20(1):77–89, 1993.

[61] S. Tanuma, C.J. Powell, and D.R. Penn. Calculations of electron inelastic mean free paths. V. Data for 14 organic compounds over the 50-2000 eV range. *Surf. Interface Anal.*, 21(3):165–176, 1994.

[62] S. Tanuma, C.J. Powell, and D.R. Penn. Calculations of electron inelastic mean free paths (IMFPs) VI. Analysis of the Gries inelastic scattering model and predictive IMFP equation. *Surf. Interface Anal.*, 25(1):25–35, 1997.

[63] S. Tanuma, C.J. Powell, and D.R. Penn. Calculation of electron inelastic mean free paths (IMFPs) VII. reliability of the TPP-2M IMFP predictive equation. *Surf. Interface Anal.*, 35(3):268–275, 2003.

[64] S. Tanuma, C.J. Powell, and D.R. Penn. Calculations of electron inelastic mean free paths. *Surf. Interface Anal.*, 37(1):1–14, 2005.

[65] H. Shinotsuka, S. Tanuma, C.J. Powell, and D.R. Penn. Calculations of electron inelastic mean free paths. X. data for 41 elemental solids over the 50 ev to 200 kev range with the relativistic full penn algorithm. *Surf. Interface Anal.*, 47(9):871–888, 2015. SIA-15-0197.

[66] S. Tougaard. QUASES-IMFP-TPP2M Software. http://www.quases.com/products/quases-imfp-tpp2m/.

[67] J. Als-Nielsen and D. McMorrow. *Elements of modern X-ray physics*. John Wiley & Sons, New York, 2001.

[68] V. Holý, U. Pietsch, and T. Baumbach. *High-resolution X-ray scattering from thin films and multilayers*, volume 149 of *Springer Tracts in Modern Physics*. Spinger, 1998.

[69] R. Feidenhans. Surface structure determination by X-ray diffraction. *Surf. Sci. Rep.*, 10(3):105–188, 1989.

[70] G. Renaud. Oxide surfaces and metal/oxide interfaces studied by Grazing Incidence X-Ray Scattering. *Surf. Sci. Rep.*, 32(1-2):5–90, 1998.

[71] G. Renaud, R. Lazzari, and F. Leroy. Probing surface and interface morphology with grazing incidence small angle X-ray scattering. *Surf. Sci. Rep.*, 64(8):255–380, 2009.

[72] http://www.esrf.eu/UsersAndScience/Experiments/CRG/BM32.

[73] Lawrence Berkeley National Laboratory. Center for X-ray optics. http://www.cxro.lbl.gov/.

[74] O. Kubaschewski. *Iron-Binary phase diagrams*. Springer Science & Business Media, 2013.

[75] J.M. Sanchez, V. Pierron-Bohnes, and F. Mejía-Lira. Reciprocal-space analysis of short-range-order intensities by the cluster-variation method. *Phys. Rev. B*, 51(6):3429, 1995.

[76] J.B. Staunton, M.F. Ling, and D.D. Johnson. A theoretical treatment of atomic short-range order and magnetism in iron-rich bcc alloys. *J. Phys.: Condens. Matter*, 9(6):1281, 1997.

[77] X.L. Li, A. Scherf, M. Heilmaier, and F. Stein. The Al-rich part of the Fe-Al phase diagram. *J. Phase Equilibria Diffus.*, 37(2):162–173, 2016.

[78] B. Predel. Al-Fe (Aluminum-Iron). In *Ac-Ag ... Au-Zr: Supplement to Subvolume IV/5A*, Landolt-Börnstein-Group IV Physical Chemistry 12A: Physical Chemistry, pages 1–2. Springer-Verlag Berlin Heidelberg, 2006.

[79] V. Blum. *On the interplay of surface segregation and bulk order in binary alloys*. PhD thesis, Friedrich-Alexander University Erlangen-Nürnberg, 2002.

[80] Z.K. Liu and Y.A. Chang. Thermodynamic assessment of the Al-Fe-Si system. *Metall. Mater. Trans. A*, 30(4):1081–1095, 1999.

[81] M. Fähnle, J. Mayer, and B. Meyer. Theory of atomic defects and diffusion in ordered compounds, and application to B_2-FeAl. *Intermetallics*, 7(3):315–323, 1999.

[82] G. Bester, B. Meyer, and M. Fähnle. Atomic defects in the ordered compound B_2-CoAl: A combination of *ab initio* electron theory and statistical mechanics. *Phys. Rev. B*, 60(21):14492, 1999.

[83] R. Hultgren, P.D. Desai, D.T. Hawkins, M. Gleiser, and K.K. Kelley. Selected values of the thermodynamic properties of binary alloys. Technical report, National Standard Reference Data System, 1973.

[84] M.-C. Desjonqueres and D. Spanjaard. *Concepts in surface physics*. Springer Science & Business Media, 2012.

[85] U. Bardi. The atomic structure of alloy surfaces and surface alloys. *Rep. Prog. Phys.*, 57(10):939–987, 1994.

[86] M.A. Vasiliev. Surface effects of ordering in binary alloys. *J. Phys. D*, 30(22):3037, 1997.

[87] M. Polak and L. Rubinovich. The interplay of surface segregation and atomic order in alloys. *Surf. Sci. Rep.*, 38(4):127–194, 2000.

[88] W.R. Tyson and W.A. Miller. Surface free energies of solid metals: Estimation from liquid surface tension measurements. *Surf. Sci.*, 62(1):267–276, 1977.

[89] H.L. Skriver and N.M. Rosengaard. Surface energy and work function of elemental metals. *Phys. Rev. B*, 46(11):7157, 1992.

[90] L. Vitos, A.V. Ruban, H.L. Skriver, and J. Kollár. The surface energy of metals. *Surf. Sci.*, 411(1):186–202, 1998.

[91] N.R. Gleason and D.R. Strongin. Water adsorption and thermal decomposition on FeAl (110). *J. Phys. Chem.*, 100(48):18829–18838, 1996.

[92] M. Kottcke, H. Graupner, D.M. Zehner, L. Hammer, and K. Heinz. Segregation-induced subsurface restructuring of FeAl (100). *Phys. Rev. B*, 54(8):R5275, 1996.

[93] B. Eltester, C. Uebing, H. Viefhaus, and H.J. Grabke. AES and LEED investigation of Al segregation and oxidation of the (100) face of $Fe_{85}Al_{15}$ single crystals. *Fresen. J. Anal. Chem.*, 358(1-2):196–199, 1997.

[94] O. Kizilkaya, D.A. Hite, D.M. Zehner, and P.T. Sprunger. Surface reconstruction of FeAl (110) studied by scanning tunnelling microscopy and angle-resolved photoemission spectroscopy. *J. Phys.: Condens. Matter*, 16(30):5395–5406, 2004.

[95] M.P. Seah. A quantitative framework for the analysis of surfaces by AES and XPS. *Analusis*, 9(5):171–180, 1981.

[96] M. Gemmaz, M. Afyouni, and A. Mosser. Determination of the diffusion coefficient of Al in an Fe-Al alloy by Auger spectrometry. *Surf. Sci.*, 227(1-2):L109–L111, 1990.

[97] C.P. Wang, F. Jona, N.R. Gleason, D.R. Strongin, and P.M. Marcus. Atomic structure of FeAl {001}. *Surf. Sci.*, 298(1):114–120, 1993.

[98] A.P. Baddorf and S.S. Chandavarkar. Identification of an incommensurate $FeAl_2$ overlayer on FeAl (110) using X-ray diffraction and reflectivity. *Physica B*, 221(1-4):141–144, 1996.

[99] O. Kizilkaya, I.C. Senevirathne, and P.T. Sprunger. The electronic structure of ultrathin aluminum oxide film grown on FeAl (110): A photoemission spectroscopy. *J. Appl. Phys.*, 101(6):063706, 2007.

[100] J.L. Pan, J. Ni, and B. Yang. Stability of FeAl (110) alloy surface structures: a first principle study. *Eur. Phys. J. B*, 73(3):367–373, 2010.

[101] N.R. Gleason and D.R. Strongin. A photoelectron spectroscopy and thermal desorption study of CO on FeAl (110) and polycrystalline TiAl and NiAl. *Surf. Sci.*, 295(3):306–318, 1993.

[102] W.H. Gitzen. *Alumina as a ceramic material*. American ceramic society edition, 1970.

[103] E. Dörre and H. Hübner. *Alumina: processing, properties, and applications*, volume 3. Not Avail, 1984.

[104] I. Levin and D. Brandon. Metastable alumina polymorphs: crystal structures and transition sequences. *J. Am. Ceram. Soc.*, 81(8):1995–2012, 1998.

[105] J. Kelber. Alumina surfaces and interfaces under non-ultrahigh vacuum conditions. *Surf. Sci. Rep.*, 62(7):271–303, Jul 2007.

[106] D.P. Woodruff. Quantitative structural studies of corundum and rocksalt oxide surfaces. *Chem. Rev.*, 113(6):3863–3886, 2013.

[107] J. Goniakowski, F. Finocchi, and C. Noguera. Polarity of oxide surfaces and nanostructures. *Rep. Prog. Phys.*, 71(1):016501, 2008.

[108] P. Guénard, G. Renaud, A. Barbier, and M. Gautier-Soyer. Determination of the α-Al_2O_3(0001) surface relaxation by measurements of crystal truncation rods. *Surf. Rev. Lett.*, 5(1):321–324, 1998.

[109] P.J. Eng, T.P. Trainor, G.E. Brown Jr, G.A. Waychunas, M. Newville, S.R. Sutton, and M.L. Rivers. Structure of the hydrated α-Al_2O_3 (0001) surface. *Science*, 288(5468):1029–1033, 2000.

[110] T.M. French and G.A. Somorjai. Composition and surface structure of the (0001) face of α-alumina by low energy electron diffraction. *J. Phys. Chem.*, 74(12):2489–2495, 1970.

[111] G. Renaud, B. Villette, I. Vilfan, and A. Bourret. Atomic structure of the α-Al_2O_3 (0001) $(\sqrt{31}\times\sqrt{31})$ R $\pm$ 9 $^\circ$ reconstruction. *Phys. Rev. Lett.*, 73(13):1825–1828, 1994.

[112] M.W. Finnis, A.Y. Lozovoi, and A. Alavi. The oxidation of NiAl: What can we learn from *ab initio* calculations? *Surf. Sci.*, 35:167–207, 2005.

[113] S. Swaminathan and M. Spiegel. Thermodynamic and kinetic aspects on the selective surface oxidation of binary, ternary and quarternary model alloys. *Appl. Surf. Sci.*, 253(10):4607–4619, 2007.

[114] J. Zimmermann and L. Colombi Ciacchi. Origin of the selective Cr oxidation in CoCr alloy surfaces. *J. Phys. Chem. Lett.*, 1(15):2343–2348, 2010.

[115] B.G. Demczyk. Oxidation behavior of annealed CoCr thin films. *J. Vac. Sci. Technol. A*, 11(4):1458–1463, 1993.

[116] G.C. Wood. High-temperature oxidation of alloys. *Oxid. Met.*, 2(1):11–57, 1970.

[117] L. Latu-Romain, S. Mathieu, M. Vilasi, G. Renou, S. Coindeau, A. Galerie, and Y. Wouters. The role of oxygen partial pressure on the nature of the oxide scale on a NiCr model alloy. *Oxid. Met.*, pages 1–13, 2016.

[118] T. Nakayama and K. Kaneko. Selective oxide films of a 5 % aluminum-iron alloy in a low oxygen potential atmosphere. *Corrosion*, 26(7):187–188, 1970.

[119] R. Prescott and M.J. Graham. The oxidation of iron-aluminum alloys. *Oxid. Met.*, 38(1):73–87, 1992.

[120] R.E. Grace and A.U. Seybolt. Selective oxidation of Al from an Al-Fe alloy. *J. Electrochem. Soc.*, 105(10):582–585, 1958.

[121] A. Stierle, F. Renner, R. Streitel, H. Dosch, W. Drube, and B.C. Cowie. X-ray diffraction study of the ultrathin Al_2O_3 layer on NiAl (110). *Science*, 303(5664):1652–1656, 2004.

[122] A. Rosenhahn, J. Schneider, C. Becker, and K. Wandelt. Oxidation of Ni_3Al (111) at 600, 800, and 1050 K investigated by scanning tunneling microscopy. *J. Vac. Sci. Technol. A*, 18(4):1923–1927, 2000.

[123] M. Yoshitake, W.J. Song, J. Libra, K. Mašek, F. Šutara, V. Matolín, and K.C. Prince. Interface termination and band alignment of epitaxially grown alumina films on Cu-Al alloy. *J. Appl. Phys.*, 103(3):033707, 2008.

[124] V. Rose, V. Podgursky, I. Costina, and R. Franchy. Growth of ultra-thin amorphous Al_2O_3 films on CoAl (100). *Surf. Sci.*, 541(1):128–136, 2003.

[125] V. Rose, V. Podgursky, I. Costina, R. Franchy, and H. Ibach. High temperature oxidation of CoAl (100). *Surf. Sci.*, 577(2):139–150, 2005.

[126] A.H. Heuer, D.B. Hovis, J.L. Smialek, and B. Gleeson. Alumina scale formation: a new perspective. *J. Am. Ceram. Soc.*, 94(s1), 2011.

[127] J.E. Crowell, J.G. Chen, and J.T. Yates. Surface sensitive spectroscopic study of the interaction of oxygen with Al (111)-low temperature chemisorption and oxidation. *Surf. Sci.*, 165(1):37–64, 1986.

[128] N. Cai, G.W. Zhou, K. Müller, and D.E. Starr. Effect of oxygen gas pressure on the kinetics of alumina film growth during the oxidation of Al (111) at room temperature. *Phys. Rev. B*, 84(12):125445, 2011.

[129] N. Cai, G.W. Zhou, K. Müller, and D.E. Starr. Tuning the limiting thickness of a thin oxide layer on Al (111) with oxygen gas pressure. *Phys. Rev. Lett.*, 107(3):035502, 2011.

[130] I. Popova, V. Zhukov, and J.T. Yates Jr. Comparative study of Al (111) oxidation with O_3 and O_2. *Surf. Sci.*, 518(1):39–48, 2002.

[131] S. Ulrich, N. Nilius, and H.-J. Freund. Growth of thin alumina films on a vicinal NiAl surface. *Surf. Sci.*, 601(19):4603–4607, 2007.

[132] R. Franchy, J. Masuch, and P. Gassmann. The oxidation of the NiAl (111) surface. *Appl. Surf. Sci.*, 93(4):317–327, 1996.

[133] N. Cai, H.L. Qin, X. Tong, and G.W. Zhou. Growth of ultrathin amorphous alumina films during the oxidation of NiAl (100). *Surf. Sci.*, 618:20–26, 2013.

[134] G. Hamm, C. Barth, C. Becker, K. Wandelt, and C.R. Henry. Surface structure of an ultrathin alumina film on Ni_3Al (111): a dynamic scanning force microscopy study. *Phys. Rev. Lett.*, 97(12):126106, 2006.

[135] O. Kurnosikov, L. Jurczyszyn, B. Pieczyrak, and A. Krupski. Atomic structure and electronic properties of Ni_3Al (001) surface. *Surf. Sci.*, 602(18):2994–2999, 2008.

[136] A. Rosenhahn, J. Schneider, C. Becker, and K. Wandelt. The formation of Al_2O_3-layers on Ni_3Al (111). *Appl. Surf. Sci.*, 142(1):169–173, 1999.

[137] O. Kizilkaya, D.A. Hite, D.M. Zehner, and P.T. Sprunger. Formation of aluminum oxide thin films on FeAl (110) studied by STM. *Surf. Sci.*, 529(1-2):223–230, Apr 2003.

[138] C.H. Xu, W. Gao, and Y.D. He. High temperature oxidation behaviour of FeAl intermetallics-oxide scales formed in ambient atmosphere. *Scripta Mater.*, 42(10):975–980, 2000.

[139] M. Yoshitake, S. Bera, and Y. Yamauchi. AES and LEED study of well-ordered oxide film grown on Cu-9 at.% Al (111). *Surf. Interface Anal.*, 35(10):824–828, 2003.

[140] G. Prévot, A. Naitabdi, R. Bernard, and Y. Borensztein. Sixton rectangles in the structure of alumina ultrathin films on metals. *Phys. Rev. B*, 81(8):085405, 2010.

[141] S. Nemšák, T. Skála, M. Yoshitake, N. Tsud, T. Kim, S. Yagyu, and V. Matolin. Growth of thin epitaxial alumina films onto Ni (111): an electron spectroscopy and diffraction study. *Surf. Interface Anal.*, 42(10-11):1581–1584, 2010.

[142] S. Nemšák, T. Skála, M. Yoshitake, K.C. Prince, and V. Matolín. Depth profiling of ultra-thin alumina layers grown on Co (0001). *J. Phys.: Condens. Matter*, 25(9):095004, 2013.

[143] A. Kiejna and B.I. Lundqvist. Stability of oxygen adsorption sites and ultrathin aluminum oxide films on Al (111). *Surf. Sci.*, 504:1–10, 2002.

[144] J. Libuda, M. Frank, A. Sandell, S. Andersson, P.A. Brühwiler, M. Bäumer, N. Mårtensson, and H.-J. Freund. Interaction of rhodium with hydroxylated model substrates. *Surf. Sci.*, 384(1-3):106–119, 1997.

[145] A.Y. Lozovoi, A. Alavi, and M.W. Finnis. Surface energy and the early stages of oxidation of NiAl (110). *Comput. Phys. Commun.*, 137(1):174–194, 2001.

[146] A.Y. Lozovoi, A. Alavi, and M.W. Finnis. Surface stoichiometry and the initial oxidation of NiAl (110). *Phys. Lev. Lett.*, 85(3):610, 2000.

[147] A. Stierle, V. Formoso, F. Comin, and R. Franchy. Surface X-ray diffraction study on the initial oxidation of NiAl (100). *Surf. Sci.*, 467(1):85–97, 2000.

[148] A. Stierle, F. Renner, R. Streitel, and H. Dosch. Observation of bulk forbidden defects during the oxidation of NiAl (110). *Phys. Rev. B*, 64(16):165413, 2001.

[149] A. Stierle, C. Tieg, H. Dosch, V. Formoso, E. Lundgren, J.N. Andersen, L. Köhler, and G. Kresse. Surface core level shift observed on NiAl (110). *Surf. Sci.*, 529(3):L263–L268, 2003.

[150] A. Mulligan, V. Dhanak, and M. Kadodwala. A high-resolution photoemission study of nanoscale aluminum oxide films on NiAl (110). *Langmuir*, 21(18):8312–8318, 2005.

[151] N.M. Martin, J. Knudsen, S. Blomberg, J. Gustafson, J.N. Andersen, E. Lundgren, H.H. Ingelsten, P.-A. Carlsson, M. Skoglundh, A. Stierle, et al. High-resolution core-level spectroscopy study of the ultrathin aluminum oxide film on NiAl (110). *Phys. Rev. B*, 83(12):125417, 2011.

[152] T.T. Lay, M. Yoshitake, and W.J. Song. Epitaxial growth of well-ordered ultra-thin Al_2O_3 film on NiAl (110) by a single-step oxidation. *Appl. Surf. Sci.*, 239(3):451–457, 2005.

[153] M. Kulawik, N. Nilius, H.-P. Rust, and H.-J. Freund. Atomic structure of antiphase domain boundaries of a thin Al_2O_3 film on NiAl (110). *Phys. Rev. Lett.*, 91(25):256101, 2003.

[154] G.H. Simon, T. König, M. Nilius, H.-P. Rust, M. Heyde, and H.-J. Freund. Atomically resolved force microscopy images of complex surface unit cells: Ultrathin alumina film on NiAl (110). *Phys. Rev. B*, 78(11):113401, 2008.

[155] Y.J. Li, J. Brndiar, Y. Naitoh, Y. Sugawara, and I. Štich. Atomic force microscopy identification of Al-sites on ultrathin aluminum oxide film on NiAl (110). *Nanotechnology*, 26(50):505704, 2015.

[156] G.H. Simon, T. König, H.-P. Rust, M. Heyde, and H.-J. Freund. Atomic structure of the ultrathin alumina on NiAl (110) and its antiphase domain boundaries as seen by frequency modulation dynamic force microscopy. *New J. Phys.*, 11(9):093009, 2009.

[157] G.H. Simon, T. König, L. Heinke, L. Lichtenstein, M. Heyde, and H.-J. Freund. Atomic structure of surface defects in alumina studied by dynamic force microscopy: strain-relief-, translation-and reflection-related boundaries, including their junctions. *New J. Phys.*, 13(12):123028, 2011.

[158] M. Schmid, M. Shishkin, G. Kresse, E. Napetschnig, P. Varga, M. Kulawik, N. Nilius, H.-P. Rust, and H.-J. Freund. Oxygen-deficient line defects in an ultrathin aluminum oxide film. *Phys. Rev. Lett.*, 97(4):046101, 2006.

[159] K.H. Hansen, T. Worren, S. Stempel, E. Lægsgaard, M. Bäumer, H.-J. Freund, F. Besenbacher, and I. Stensgaard. Palladium nanocrystals on Al_2O_3: structure and adhesion energy. *Phys. Rev. Lett.*, 83(20):4120, 1999.

[160] D.R. Mullins and S.H. Overbury. The structure and composition of the NiAl (110) and NiAl (100) surfaces. *Surf. Sci.*, 199(1-2):141–153, 1988.

[161] R.-P. Blum, D. Ahlbehrendt, and H. Niehus. Preparation-dependent surface composition and structure of NiAl (001): SPA-LEED and NICISS study. *Surf. Sci.*, 366(1):107–120, 1996.

[162] P. Gassmann, R. Franchy, and H. Ibach. Preparation of a well ordered aluminum oxide layer on NiAl (001). *J. Electron. Spectrosc. Relat. Phenom.*, 64:315–320, 1993.

[163] P. Gassmann, R. Franchy, and H. Ibach. Investigations on phase transitions within thin Al_2O_3 layers on NiAl (001)-HREELS on aluminum oxide films. *Surf. Sci.*, 319(1-2):95–109, 1994.

[164] R.-P. Blum and H. Niehus. Initial growth of Al_2O_3 on NiAl (001). *Appl. Phys. A*, 66(1):S529–S533, 1998.

[165] N. Frémy, V. Maurice, and P. Marcus. X-ray photoelectron spectroscopy study of thin oxide layers formed on (001)-oriented β-NiAl single-crystal surfaces. *Surf. Interface Anal.*, 34(1):519–523, 2002.

[166] N. Frémy, V. Maurice, and P. Marcus. Initial stages of growth of alumina on NiAl (001) at 1025 K. *J. Am. Ceram. Soc.*, 86(4):669–75, 2003.

[167] R.-P. Blum, D. Ahlbehrendt, and H. Niehus. Growth of Al_2O_3 stripes in NiAl (001). *Surf. Sci.*, 396(1-3):176–188, 1998.

[168] C.T. Wang, C.W. Lin, C.L. Hsia, B.W. Chang, and M.F. Luo. Under-surface observation of thin-film alumina on NiAl (100) with scanning tunneling microscopy. *Thin Solid Films*, 520(11):3952–3959, 2012.

[169] H. Niehus, W. Raunau, K. Besocke, R. Spitzl, and G. Comsa. Surface structure of NiAl (111) determined by ion scattering and scanning tunneling microscopy. *Surf. Sci.*, 225(1-2):L8–L14, 1990.

[170] D.M. Lipkin, H. Schaffer, F. Adar, and D.R. Clarke. Lateral growth kinetics of α-alumina accompanying the formation of a protective scale on (111) NiAl during oxidation at 1100 °C. *Appl. Phys. Lett.*, 70(19):2550–2552, 1997.

[171] E. Loginova, F. Cosandey, and T.E. Madey. Nanoscopic nickel aluminate spinel ($NiAl_2O_4$) formation during NiAl (111) oxidation. *Surf. Sci.*, 601(3):L11–L14, 2007.

[172] D. Sondericker, F. Jona, and P.M. Marcus. Atomic structure of alloy surfaces. II. Ni_3Al {111}. *Phys. Rev. B*, 34(10):6770, 1986.

[173] C. Wang and C.-Y. Wang. Density functional theory study of Ni/Ni_3Al interface alloying with Re and Ru. *Surf. Sci.*, 602(14):2604–2609, 2008.

[174] L. Jurczyszyn, A. Krupski, S. Degen, B. Pieczyrak, M. Kralj, C. Becker, and K. Wandelt. Atomic structure and electronic properties of Ni_3Al (111) and (011) surfaces. *Phys. Rev. B*, 76(4):045101, 2007.

[175] E. Vesselli, L. Bianchettin, A. Baraldi, A. Sala, G. Comelli, S. Lizzit, L. Petaccia, and S. de Gironcoli. The Ni_3Al (111) surface structure: experiment and theory. *J. Phys.: Condens. Matter*, 20(19):195223, 2008.

[176] Y.G. Shen, D.J. O'Connor, and R.J. MacDonald. Studies of surface composition, structure and oxygen adsorption of Ni_3Al (110) by Li^+ and He^+ ion scattering. *Surf. Interface Anal.*, 18(10):729–739, 1992.

[177] M. Garza, N.P. Magtoto, and J.A. Kelber. Characterization of oxidized Ni_3Al (110) and interaction of the oxide film with water vapor. *Surf. Sci.*, 519(3):259–268, 2002.

[178] F. Qin, N.P. Magtoto, and J.A. Kelber. H_2O-induced instability of Al_2O_3/Ni_3Al (110) and Al_2O_3/Ni_3Al (111) thin films under non-UHV conditions. *Surf. Sci.*, 565(2):L277–L282, 2004.

[179] F. Qin, N.P. Magtoto, J.A. Kelber, and D.R. Jennison. Theory and experiments on the structure of 7 Å alumina films grown on Ni_3Al. *J. Mol. Catal. A: Chem.*, 228(1):83–87, 2005.

[180] D.R. Jennison, C. Verdozzi, P.A. Schultz, and M.P. Sears. *Ab initio* structural predictions for ultrathin aluminum oxide films on metallic substrates. *Phys. Rev. B*, 59(24):R15605, 1999.

[181] V. Podgursky, I. Costina, and R. Franchy. Ultra thin Al_2O_3 films grown on Ni_3Al (100). *Appl. Surf. Sci.*, 206(1):29–36, 2003.

[182] U. Bardi, A. Atrei, and G. Rovida. Initial stages of oxidation of the Ni_3Al alloy: structure and composition of the aluminum oxide overlayer studied by XPS, LEIS and LEED. *Surf. Sci.*, 268(1-3):87–97, 1992.

[183] C. Becker, J. Kandler, H. Raaf, R. Linke, T. Pelster, M. Dräger, M. Tanemura, and K. Wandelt. Oxygen adsorption and oxide formation on Ni_3Al (111). *J. Vac. Sci. Technol. A*, 16(3):1000–1005, 1998.

[184] M. Hansen and K. Anderko. *Constitution of binary alloys*. Number 1. McGraw-Hill, 1965.

[185] S.G. Addepalli, B. Ekstrom, N.P. Magtoto, J.-S. Lin, and J.A. Kelber. STM atomic-scale characterization of the γ-Al_2O_3 film on Ni_3Al (111). *Surf. Sci.*, 442(3):385–399, 1999.

[186] T. Maroutian, S. Degen, C. Becker, K. Wandelt, and R. Berndt. Superstructures and coincidences of a thin oxide film on a metallic substrate: A STM study. *Phys. Rev. B*, 68(15):155414, 2003.

[187] S. Degen, A. Krupski, M. Kralj, A. Langner, C. Becker, M. Sokolowski, and K. Wandelt. Determination of the coincidence lattice of an ultra thin Al_2O_3 film on Ni_3Al (111). *Surf. Sci.*, 576(1):L57–L64, 2005.

[188] S. Gritschneder, C. Becker, K. Wandelt, and M. Reichling. Disorder or complexity? Understanding a nanoscale template structure on alumina. *J. Am. Chem. Soc.*, 129(16):4925–4928, 2007.

[189] J. Ferrante. An Auger electron spectroscopy and LEED study of equilibrium surface segregation in copper-aluminum alloys. *Acta Metall.*, 19(8):743–748, 1971.

[190] Y. Yu, K. Sagisaka, and D. Fujita. Surface segregation of aluminum atoms on Cu-9 at.% Al (111) studied by Auger electron spectroscopy and low energy electron diffraction. *Surf. Sci.*, 603(4):723–726, 2009.

[191] S. Nemšák, M. Yoshitake, and K. Mašek. Ultra-thin oxide layer formation on Cu-9 % Al (111) surface and Pd growth studied using reflection high energy electron diffraction and Auger electron spectroscopy. *Surf. Sci.*, 600(18):4357–4360, 2006.

[192] S. Andersson, P.A. Brühwiler, A. Sandell, M. Frank, J. Libuda, A. Giertz, B. Brena, A.J. Maxwell, M. Bäumer, H.-J. Freund, et al. Metal-oxide interaction for metal clusters on a metal-supported thin alumina film. *Surf. Sci.*, 442(1):L964–L970, 1999.

[193] M.J. Mehl, J.E. Osburn, D.A. Papaconstantopoulos, and B.M. Klein. Structural properties of ordered high-melting-temperature intermetallic alloys from first-principles total-energy calculations. *Phys. Rev. B*, 41(15):10311, 1990.

[194] V. Rose and R. Franchy. The band gap of ultrathin amorphous and well-ordered Al_2O_3 films on CoAl (100) measured by scanning tunneling spectroscopy. *J. Appl. Phys.*, 105(7):07C902, 2009.

[195] V. Podgursky, V. Rose, J. Costina, and R. Franchy. The coexistence of γ ($\gamma\prime$) and θ alumina observed by STM and LEED on top of oxide layer grown on CoAl (100). *Appl. Surf. Sci.*, 252(24):8394–8398, 2006.

[196] V. Podgursky, V. Rose, J. Costina, and R. Franchy. Study of phase transitions within alumina grown on top of CoAl (100) surface. *Surf. Sci.*, 601(16):3315–3323, 2007.

[197] N.F.M.N. Cabrera and N.F. Mott. Theory of the oxidation of metals. *Rep. Prog. Phys.*, 12(1):163, 1949.

[198] M. Bäumer and H.-J. Freund. Metal deposits on well-ordered oxide films. *Prog. Surf. Sci.*, 61(7):127–198, 1999.

[199] H.-J. Freund and G. Pacchioni. Oxide ultra-thin films on metals: new materials for the design of supported metal catalysts. *Chem. Soc. Rev.*, 37(10):2224–2242, 2008.

[200] W.J. Song and M. Yoshitake. X-ray photoelectron spectroscopy and low-energy electron diffraction study on the oxidation of NiAl (110) surfaces at elevated temperatures. *Thin Solid Films*, 464:52–56, 2004.

[201] M. Yoshitake, T.T. Lay, and W.J. Song. Well-ordered ultra-thin Al_2O_3 film formation on NiAl (110) by high-temperature oxidation. *Surf. Sci.*, 564(1):211–217, 2004.

[202] K.F. McCarty, J.P. Pierce, and C.B. Carter. Translation-related domain boundaries form to relieve strain in a thin alumina film on NiAl (110). *Appl. Phys. Lett.*, 88(14):141902, 2006.

[203] M. Klimenkov, S. Nepijko, H. Kuhlenbeck, and H.-J. Freund. Transmission electron microscopic investigation of an ordered Al_2O_3 film on NiAl (110). *Surf. Sci.*, 385(1):66–76, 1997.

[204] G. Ceballos, Z. Song, J.I. Pascual, H.-P. Rust, H. Conrad, M. Bäumer, and H.-J. Freund. Structure investigation of the topmost layer of a thin ordered alumina film grown on NiAl (110) by low temperature scanning tunneling microscopy. *Chem. Phys. Lett.*, 359:41–47, 2002.

[205] L. Heinke, L. Lichtenstein, G.H. Simon, T. König, M. Heyde, and H.-J. Freund. Structure and electronic properties of step edges in the aluminum oxide film on NiAl (110). *Phys. Rev. B*, 82(7):075430, 2010.

[206] T. Nishimura, Y. Hoshino, T. Okazawa, and Y. Kido. Structure of an ultrathin aluminum oxide layer grown on a NiAl (110) substrate. *Phys. Rev. B*, 77(7):073405, 2008.

[207] N. Nilius, M. Kulawik, H.-P. Rust, and H.-J. Freund. Defect-induced gap states in Al_2O_3 thin films on NiAl (110). *Phys. Rev. B*, 69:121401, Mar 2004.

[208] L. Heinke, L. Lichtenstein, G.H. Simon, T. König, M. Heyde, and H.-J. Freund. Local work function differences at line defects in aluminium oxide on NiAl (110). *ChemPhysChem*, 11(10):2085–2087, 2010.

[209] P. Krukowski, S. Chaunchaiyakul, Y. Minagawa, N. Yajima, M. Akai-Kasaya, A. Saito, and Y. Kuwahara. Anomalous hexagonal superstructure of aluminum oxide layer grown on NiAl (110) surface. *Nanotechnology*, 27(45):455708, 2016.

[210] Z.F. Zhang, L. Li, and J.C. Yang. γ-Al_2O_3 thin film formation via oxidation of β-NiAl (110). *Acta Mater.*, 59(15):5905–5916, 2011.

[211] Z.F. Zhang, K. Jung, L. Li, and J.C. Yang. Kinetics aspects of initial stage thin γ-Al_2O_3 film formation on single crystalline β-NiAl (110). *J. Appl. Phys.*, 111(3):034312, 2012.

[212] V. Maurice, N. Frémy, and P. Marcus. Hydroxylation-induced modifications of the Al_2O_3/NiAl (001) surface at low water vapour pressure. *Surf. Sci.*, 581(1):88–104, 2005.

[213] G. Hamm, C. Becker, and C.R. Henry. Bimetallic PdAu nanocluster arrays grown on nanostructured alumina templates. *Nanotechnology*, 17(8):1943–1947, 2006.

[214] S. Le Pévédic, D. Schmaus, and C. Cohen. Growth of Ni-Al alloys on Ni (111): (I) formation of epitaxial Ni_3Al from ultra-thin Al deposits. *Surf. Sci.*, 600:565–576, 2006.

[215] S. Le Pévédic, D. Schmaus, and C. Cohen. Growth of Ni-Al alloys on Ni (111), from Al deposits of various thicknesses: (II) Formation of NiAl over a Ni_3Al interfacial layer. *Surf. Sci.*, 601(2):395–410, 2007.

[216] S. Le Pévédic, D. Schmaus, and C. Cohen. Formation of a well-ordered ultrathin aluminum oxide film on Ni (111): Determination of its thickness, composition and structure. *Surf. Sci.*, 602:67–76, 2008.

[217] M. Wardé, J. Ledieu, L.N. Serkovic Loli, M. Herinx, M.-C. de Weerd, V. Fournée, S. Le Moal, and M.-G. Barthés-Labrousse. Growth and structure of ultrathin alumina films on the (110) surface of γ-Al_4Cu_9 complex metallic alloy. *J. Phys.: Condens. Matter*, 26(48):485009, 2014.

[218] J.M. Dubois and E. Belin-Ferre. *Complex metallic alloys: fundamentals and applications*. Wiley, 2010.

[219] V. Vonk, C. Ellinger, N. Khorshidi, A. Vlad, A. Stierle, and H. Dosch. *In situ* x-ray study of Fe_3Al (110) subsurface superlattice disordering during oxidation. *Phys. Rev. B*, 78(16):165426, 2008.

[220] D.R. Jennison and A. Bogicevic. Ultrathin aluminum oxide films: Al-sublattice structure and the effect of substrate on ad-metal adhesion. *Surf. Sci.*, 464(2):108–116, 2000.

[221] S. Booyens, L. Gilbert, D. Willock, and M. Bowker. The adsorption of ethene on Fe (111) and surface carbide formation. *Catal. Today*, 244:122–129, 2015.

[222] H.J. Grabke, W. Paulitschke, G. Tauber, and H. Viefhaus. Equilibrium surface segregation of dissolved nonmetal atoms on iron (100) faces. *Surf. Sci.*, 63:377–389, 1977.

[223] R.G. Musket, W. McLean, C.A. Colmenares, D.M. Makowiecki, and W.J. Siekhaus. Preparation of atomically clean surfaces of selected elements: A review. *Appl. Surf. Sci.*, 10(2):143–207, 1982.

[224] G. Panzner and W. Diekmann. The bonding state of carbon segregated to α-iron surfaces and on iron carbide surfaces studied by electron spectroscopy. *Surf. Sci.*, 160(1):253–270, 1985.

[225] W. Arabczyk, F. Storbeck, and H.J. Müssig. Electron spectroscopy studies on carbon segregation from a mono-crystalline α-Fe (111) specimen. *Appl. Surf. Sci.*, 65:94–98, 1993.

[226] C. Hinnen, D. Imbert, J.M. Siffre, and P. Marcus. An *in situ* XPS study of sputter-deposited aluminium thin films on graphite. *Appl. Surf. Sci.*, 78(3):219–231, 1994.

[227] A. Wiltner and Ch. Linsmeier. Formation of endothermic carbides on iron and nickel. *Phys. Status Solidi A*, 201(5):881–887, 2004.

[228] E. Papastavros, P.J. Shea, and M.A. Langell. Oxygen, carbon, and sulfur segregation in annealed and unannealed zerovalent iron substrates. *Langmuir*, 20(26):11509–11516, 2004.

[229] D. Connetable, J. Lacaze, P. Maugis, and B. Sundman. A calphad assessment of Al-C-Fe system with the κ carbide modelled as an ordered form of the fcc phase. *Calphad*, 32(2):361–370, 2008.

[230] J. Fujii, G. Panaccione, I. Vobornik, G. Rossi, G. Trimarchi, and N. Binggeli. C-Fe chains due to segregated carbon impurities on Fe (100). *Surf. Sci.*, 600:3884–3887, 2006.

[231] S.R. Kelemen and A. Kaldor. The interaction of surface sulfur with carbon on Fe (110). *J. Chem. Phys.*, 75(3):1530–1537, 1981.

[232] J. Chipman. Thermodynamics and phase diagram of the Fe-C system. *Metall. Trans.*, 3(1):55–64, 1972.

[233] D.E. Jiang and E.A. Carter. Carbon atom adsorption on and diffusion into Fe (110) and Fe (100) from first principles. *Phys. Rev. B*, 71(4):045402, 2005.

[234] V. Blum, A. Schmidt, W. Meier, L. Hammer, and K. Heinz. Competitive surface segregation of C, Al and S impurities in Fe (100). *J. Phys.: Condens. Matter*, 15:3517–3529, 2003.

[235] G. Panaccione, J. Fujii, I. Vobornik, G. Trimarchi, N. Binggeli, A. Goldoni, R. Larciprete, and G. Rossi. Local and long-range order of carbon impurities on Fe (100): Analysis of self-organization at a nanometer scale. *Phys. Rev. B*, 73(3):035431, 2006.

[236] NIST X-ray photoelectron spectroscopy database. https://srdata.nist.gov/xps/Default.aspx.

[237] Inorganic crystal strcuture database, https://www.fiz-karlsruhe.de/de/leistungen/kristallographie/icsd.html.

[238] A simple sputter yield calculator, https://www.iap.tuwien.ac.at/www/surface/sputteryield.

[239] LEEDpat, Version 4.2, utility by K.E. Hermann (FHI) and M.A. Van Hove (HKBU), Berlin / Hong Kong, 2014; see also http://www.fhi-berlin.mpg.de/KHsoftware/LEEDpat/index.html.

[240] T. Duguet and P.A. Thiel. Chemical contrast in STM imaging of transition metal aluminides. *Prog. Surf. Sci.*, 87:47–62, 2012.

[241] G.P. Das, B.K. Rao, P. Jena, and S.C. Deevi. Electronic structure of substoichiometric Fe-Al intermetallics. *Phys. Rev. B*, 66(18):184203, 2002.

[242] T.E. Madey, W. Chen, H. Wang, P. Kaghazchi, and T. Jacob. Nanoscale surface chemistry over faceted substrates: structure, reactivity and nanotemplate. *Chem. Soc. Rev.*, 37:2310–2327, 2008.

[243] C. Revenant, F. Leroy, G. Renaud, R. Lazzari, A. Letoublon, and T.E. Madey. Structural and morphological evolution of Co on faceted Pt/W (111) surface upon thermal annealing. *Surf. Sci.*, 601(16):3431–3449, 2007.

[244] A. Szczepkowicz, A. Ciszewski, R. Bryl, C. Oleksy, C.-H. Nien, Q. Wu, and T.E. Madey. A comparison of adsorbate-induced faceting on flat and curved crystal surfaces. *Surf. Sci.*, 599(1):55–68, 2005.

[245] J.-S. Lin, H. Cabibil, and J.A. Kelber. S-induced faceting transformations on Fe (111). *Surf. Sci.*, 395(1):30–42, 1998.

[246] G. Kresse and J. Furthmüller. Efficient iterative schemes for *ab initio* total energy calculations using a plane-wave basis set. *Phys. Rev. B*, 54(16):11169, 1996.

[247] G. Kresse and J. Hafner. *Ab initio* molecular dynamics for liquid metals. *Phys. Rev. B*, 47(1):558, 1993.

[248] P.E. Blöchl. Projector augmented-wave method. *Phys. Rev. B*, 50(24):17953, 1994.

[249] G. Kresse and D. Joubert. From ultrasoft pseudopotentials to the projector augmented-wave method. *Phys. Rev. B*, 59(3):1758, 1999.

[250] J.P. Perdew, J.A. Chevary, S.H. Vosko, K.A. Jackson, M.R. Pederson, D.J. Singh, and C. Fiolhais. Atoms, molecules, solids, and surfaces: applications of the generalized gradient approximation for exchange and correlation. *Phys. Rev. B*, 46(11):6671, 1992.

[251] http://www.webelements.com, 2014.

[252] Th. Bertrams, A. Brodde, and H. Neddermeyer. Tunneling through an epitaxial oxide film: Al_2O_3 on NiAl (110). *J. Vac. Sci. Technol. B*, 12(3):2122–2124, 1994.

[253] E. Ozensoy, J. Szanyi, and C.H.F. Peden. Interaction of water with ordered θ-Al_2O_3 ultrathin films grown on NiAl (100). *J. Phys. Chem. B*, 109(8):3431–3436, 2005.

[254] M. Yoshitake, B. Mebarki, and T.T. Lay. Crystallinity and thickness control of well-ordered ultra-thin Al_2O_3 film on NiAl (110). *Surf. Sci.*, 511(1):L313–L318, 2002.

[255] C. Freysoldt, P. Rinke, and M. Scheffler. Ultrathin oxides: bulk-oxide-like model surfaces or unique films? *Phys. Rev. Lett.*, 99(8):086101, 2007.

[256] P. Netzer and A. Fortunelli, editors. *Oxide Materials at the Two-Dimensional Limit*. Springer, 2016.

ABBREVIATIONS

Advanced High-Strength Steel, AHSS
Atomic Force Microscopy, AFM
Auger Electron Spectroscopy, AES
Binding Energy, BE or E_B
Body centred cubic, bcc
Complex Metallic Alloy, CMA
Constant Analyser Energy, CAE
Constant Retard Ratio, CRR
Crystal Truncation Rod, CTR
Density Functional Theory, DFT
Density Of States, DOS
Electron Spectroscopy for Chemical Analysis, ESCA
European Synchrotron Radiation Facility, ESRF
Face centred cubic, fcc
Full Width at Half Maximum, FWHM
Grazing Incidence Small-Angle X-ray Scattering, GISAXS
Grazing Incidence X-ray Diffraction, GIXD
Hexagonal compact, hcp
Highest binding energy, hbe
In situ Nanostructure and Surface, INS
Inelastic Mean Free Path, IMFP
Inorganic Crystal Structure Database, ICSD
Institut des NanoSciences de Paris, INSP
Kinetic Energy, KE or E_K
Local Density Of States, LDOS
Long-Range Order, LRO
Low-Energy Electron Diffraction, LEED
Lowest binding energy, lbe
MonoLayer, ML
Pass energy, E_p
Photo-Ionization Cross Section, PICS

Projector Augmented Wave, PAW
Reciprocal lattice unit, r.l.u
Residual Gas Analyser, RGA
Scanning Force Microscopy, SFM
Scanning Probe Microscopy, SPM
Scanning Tunnelling Microscopy, STM
Short-Range Order, SRO
Spin-Orbit Splitting, SOS
Surface X-Ray Diffraction, SXRD
Tunneling bias, U_b
Tunneling current, I_t
Ultra-High Vacuum, UHV
Ultraviolet Photoelectron Spectroscopy, UPS
Vienna *Ab initio* Simulation Package, VASP
X-Ray Diffraction, XRD
X-ray Photoemission Spectroscopy, XPS
X-Ray Reflectivity, XRR